

INAUGURAL - DISSERTATION
zur
Erlangung der Doktorwürde
der
Naturwissenschaftlich-Mathematischen
Gesamtfakultät der Ruprecht-Karls-Universität
Heidelberg

Vorgelegt von
Jan-Michael Mewes, Master of Science Chemie
Kontakt: janmewes@janmewes.de
geboren am 10. Februar 1986 in Frankfurt am Main

Datum der Mündlichen Prüfung: 5. Februar 2015

**Development and Application of
Methods for the Description of
Photochemical Processes in Condensed
Phase**

December 11, 2014

Meinen Eltern, Evi und Klaus.

Contents

Preface	VII
Foreword – On Theoretical Chemistry	VIII
Abstract	X
Zusammenfassung	XII
1 Theoretical Background	1
<i>First Part:</i>	
Electronic-Structure Theory	2
1.1 Time-Independent Schrödinger Equation	2
1.1.1 Born-Oppenheimer Approximation	3
1.1.2 Solutions for Hydrogen-Like Atoms	4
1.2 Hartree-Fock Theory	6
1.2.1 A Basis of Single-Electron Functions	7
1.2.2 Construction of Many-Electron Functions	8
1.2.3 Optimization of the Slater Determinant	10
1.2.4 Self-Consistent Field Procedure	13
1.2.5 Practical Aspects	16
1.3 Orthogonalization Schemes	19
1.3.1 Gram-Schmidt	19
1.3.2 Symmetric Orthonormalization	19
1.4 Configuration Interaction	21
1.4.1 Electron Correlation	21
1.4.2 Excited States <i>via</i> CIS	24
1.5 Many-Body Perturbation Theory	27
1.5.1 General Rayleigh-Schödinger PT	27
1.5.2 Møller-Plesset PT for Hartree-Fock	29
1.6 The ISR for Correlated Excited States	32
<i>Second Part:</i>	
Photochemistry	39
1.7 Light-Driven Chemistry	39
1.8 Investigation of Photochemical Processes	41
1.9 Characterization of Excited States	42
1.10 Transient Absorption Spectroscopy	43
2 Photo-Decarboxylation of Nitrophenylacetates	45
2.1 Introduction	46
2.2 Time-Resolved UV-Pump Vis-Probe Spectroscopy	48
2.2.1 Methodology	48

2.2.2	Previous Investigations	48
2.2.3	Results	49
2.3	Quantum-Chemical Calculations	51
2.3.1	Methodology	51
2.3.2	Influence and Modeling of the Solvent	52
2.3.3	Ground-State Equilibrium Geometry	56
2.3.4	Singlet Excited States	58
2.3.5	Triplet Excited States	59
2.4	Discussion	61
2.4.1	Summarising Earlier Findings	61
2.4.2	Mechanism of Photo-Decarboxylation	61
2.4.3	Excited-State Hydrogen-Transfer in oNPA	67
2.5	Summary & Conclusion	72
3	HT & ISC in the Photo-Deprotection of oNBA	75
3.1	Introduction	76
3.2	Methodology	79
3.3	Results & Discussion	80
3.3.1	Excited States of oNBA	80
3.3.2	Potential Energy Surface of ESIHT	82
3.4	Summary & Conclusions	86
4	Non-Radiative Decay of Nitrobenzene	89
4.1	Introduction	90
4.2	Previous Investigations of Nitrobenzene	91
4.3	Ground and Excited States of Nitrobenzene	93
4.3.1	Excited Singlet States	93
4.3.2	Triplet States	94
4.3.3	Inter-System Crossing	96
4.4	Results, Methodology and Accuracy	96
4.4.1	Ground-State Equilibrium Geometry	96
4.4.2	Excited States of Nitrobenzene	97
4.4.3	DFT/MRCI	98
4.4.4	CAS-SCF	99
4.4.5	Maximum-Overlap Method	100
4.4.6	Structural Relaxation in the Excited States	102
4.4.7	Technical Details	105
4.5	Mechanism of Non-Radiative Decay	105
4.5.1	Approach	105
4.5.2	Internal Conversion	106
4.5.3	ISC into the Triplet Manifold and IC to the Ground State	107
4.5.4	Inter-System Crossing to the Ground State	109
4.6	Summary & Conclusion	111
5	PCM-Based Corrections for Excitation Energies	115
5.1	Introduction	116
5.2	General Considerations	117
5.2.1	Polarizable Continuum Model	117
5.2.2	Considerations for Excited States	117
5.2.3	Comparing Experimental and Calculated Solvatochromism	119

5.3	Formalism & Implementation	120
5.3.1	Ground-State Equilibrium PCM	120
5.3.2	Vertical Excitations in a PCM Framework	122
5.3.3	Free Energy	123
5.3.4	Electron Correlation in the PCM Framework	124
5.3.5	Perturbative Linear-Response-Type Corrections	125
5.3.6	Excited-State Densities	125
5.3.7	Technical Details of the Implementation	126
5.4	Methodology	126
5.4.1	Technical Details	126
5.4.2	Experimental Data	128
5.5	Results & Discussion	129
5.5.1	Characterization of the Excited States	129
5.5.2	Composition of the xBDSM Set	129
5.5.3	Basis-Set Dependence	130
5.5.4	Composition of Calculated Shifts	131
5.5.5	PTE vs. PTD	134
5.5.6	ptSS and ptLR with ADC and TD-DFT	134
5.5.7	Discussion of the Relation of SS and LR Formalisms	138
5.5.8	Examples Involving Hydrogen Bonding	141
5.5.9	Non-Electrostatic Examples	144
5.6	Summary & Conclusions	145
6	Conclusion	149
6.1	Global Summary & Outlook	150
6.2	Danksagung	156

Preface

On Theoretical Chemistry

Chemistry is defined as the science of the interaction and interconversion of complex atomic systems called molecules, including metals and salts. Since molecules are the subunits of any common matter, chemistry is ubiquitous and has a long history as scientific discipline. In the early 20th century, it was discovered that atoms themselves are not indivisible as their Greek-descending name (*a-tomos*, in-divisible) suggests, but are composed of protons, neutrons and electrons. Nowadays, only the latter are still seen as indivisible, or in other words fundamental with respect to the standard model of particle physics. Protons and neutrons, in contrast consist of even smaller subunits: so-called up and down quarks.

These quarks, which are again fundamental particles, carry fractions of the elementary charge of either plus two thirds (*up* quarks) or minus one third (*down* quarks). Protons consist of two *up* quarks and one *down* quark and thus carry one positive elementary charge ($2 \cdot 0.\bar{6} - 0.\bar{3} = 1$), while for neutrons the charges of one *up* quark and two *down* quarks cancel out ($0.\bar{6} - 2 \cdot 0.\bar{3} = 0$). The very number of quarks that constitute each proton and neutron does, in combination with their fractional charge, lead to an important coincidence: any atomic nucleus consisting of an arbitrary number of protons and neutrons will carry an exact multiple of the elementary charge and can in turn be neutralized by adding the respective number of electrons. Formally, this process yields the neutral atoms that constitute the periodic table of the elements.

Due to the huge binding energy of quarks, which is the result of the so-called strong interaction between them, they can only be observed in groups. Similarly, with the exception of hydrogen, neutrons and protons are fused together in the atomic core, where they are held in place by the very same short-ranged forces of the strong interaction. Despite the 10^5 times smaller size compared to the atom including the electrons, the nucleus contains virtually the complete mass of an atom. The biggest part of this mass is due to the huge binding energy according to Einstein's equation $m = E \cdot c^{-2}$, whereas the resting mass contributes less than 1%.

Ultimately, atoms may be rationalized as the frozen interaction energy of their elementary building blocks carrying a positive charge, which incidentally is a multiple of the elementary charge. Moreover, this charge exclusively determines which chemical element a nucleus belongs to, and gives rise to the Coulomb potential that attracts the much lighter, negatively charged electrons. It is the delicate interplay of many electrons in the field of complex nuclear arrangements which guides the nuclear motion and in turn the whole of chemistry with its vast number of stable molecules and reactions. Following this line of thought, chemistry could formally be categorized as the sub-field of particle physics concerned with the quantum mechanics of the electromagnetic interaction in complex systems composed of electrons and nuclei. However, such a categorization would neither reflect the vast number of thinkable and/or stable molecules emerging from the interplay of electrons in the field of the nuclei, nor the great relevance this discipline had long before the connections to the underlying physical equations were discovered. The sheer infinite possibilities to combine atoms to molecules, investigate their properties in creative ways and find empirical solutions to chemical problems (e.g. acid-base models, lewis-structures) gave rise to an independent scientific discipline. Nevertheless, the utilization of the

laws of quantum-mechanics to establish a first-principles approach for chemical problems is and has been very promising ever since these connections were first discovered at the beginning of the 19th century, as evident from the following quote:

“The underlying physical laws necessary for the mathematical theory of a large part of physics and the whole of chemistry are thus completely known, and the difficulty is only that the exact application of these laws leads to equations much too complicated to be soluble. It therefore becomes desirable that approximate practical methods of applying quantum mechanics should be developed, which can lead to an explanation of the main features of complex atomic systems without too much computation.”

Paul A. M. Dirac, 1929¹

In the past decades ever faster computers in combination with powerful algorithms and wisely chosen approximations made it possible to solve these insoluble equations on a regular basis. Eventually, the empirical top-down models developed by chemists over hundreds of years could for the first time be challenged by a first-principles bottom-up approach providing a new quality of insights into the elementary steps of chemical reactions such electron transfer as well as into the electronic structure of matter. This first-principles approach is what characterizes the field of theoretical chemistry, which emerged from a fruitful collaboration of chemists, physicists, mathematicians and computer scientists over the past hundred years.

Abstract

The interaction of complex molecular systems with light has great relevance in nature as well as for many of the latest technological developments. The process of photosynthesis converts light into chemical energy, thereby providing the primary energy source for life on Earth. Photovoltaic devices, as the technological implementation of this principle, constitute one of the most promising sources of electrical energy for the 21st century, whose application has increased tremendously in the past decade. The reverse process, the controlled emission of light from electronically activated (excited) molecules, is central to many modern technologies, the most prominent of which are presumably the ever smaller yet higher resolving display screens of hand-held computers.

For all these applications, a fundamental understanding of the processes taking place at the atomistic scale is of key relevance to allow for a rational design and improvement of new technologies. However, due to the ultra-short time-scales on which the elementary steps of most light-induced phenomena occur and their inherent complexity, an exclusively experimental investigation is often tedious, in particular concerning the interpretation of the results. Here, the combination of experimental techniques and theoretical models can help to gain insights into the involved processes. For this purpose, the electronic structure of ground and light-activated (excited) states of the involved molecules as well as the interaction with their environment has to be approximated, which is the central topic of this work.

In the first part, namely chapters 2–4, I present applications of the quantum-mechanical methodology introduced in chapter 1 to study light-triggered processes in molecular systems. The so-called caged compounds studied in chapters 2 and 3 constitute an attempt to employ the remarkable spatio-temporal light control of modern lasers to control chemical reactions. For this purpose, the investigated, prototypical molecules nitro-phenylacetate (NPA) and *ortho*-nitrobenzylacetate (oNBA) serve as precursors for the active compounds CO₂ and acetate, respectively. Upon irradiation with UV light, the active compound is released within nano- to microseconds, and may e.g. trigger subsequent reactions. In the above-mentioned sense, my theoretical investigation accompanied and guided an experimental study, which allowed to shed light on the molecular processes and to resolve the detail of the mechanism responsible for the light-induced reactivity.

The common structural motif of NPA, oNBA and many other photo-active systems is the nitroaromatic moiety in the form of its smallest representative nitrobenzene (NB). Due to this prototypical character, the photochemistry of NB is relevant for many photochemical applications. In chapter 4, I report an extensive theoretical investigation of ground and excited states as well as the non-radiative decay of NB, which due to its small size and high symmetry allows for an application of a hierarchy of state-of-the-art quantum-chemical methods. Surprisingly, I found this small molecule to pose a serious challenge to electronic structure theory and consequently, some rather sophisticated *ab initio* methods fail to afford an accurate description, e.g. with respect to the photochemically very important ordering of the lowest triplet states. Nevertheless, I determined the mechanism of non-radiative decay in good agreement with experimental findings and, moreover, suggested an experiment to test my hypothesis.

Although there exist a number of accurate and reliable quantum chemical

methods that allow for an investigation of the ground and excited states of *isolated* systems with the molecular size of NPA, oNBA and NB, the environment often plays a crucial role and may decisively influence the light-induced processes, as e.g. in NPA. Hence, the approximate modeling of molecular environments for quantum-chemical problems in condensed phase is a very active field of research, which culminated in the 2013 Nobel Prize for Chemistry, which was awarded to Karplus, Levitt and Warshel for their pioneering developments in the field of multiscale models for complex chemical systems. To enable a quantum-chemical description of photo-chemical excitation processes in condensed phase, I extended and implemented a quantum-classical polarizable-continuum model (PCM) for calculation of vertical excitation energies, which is described in chapter 5. In general, PCMs allow for an efficient computation of the often dominating electrostatic portion of the solute-solvent interaction by means of the macroscopic descriptors ϵ (dielectric constant) and $\epsilon_{\text{opt}} = n^2$ (optical dielectric or squared refractive index, respectively). The implementation of the method was realized in such a way that its application to any quantum-chemical model that affords electron densities for ground- and excited-states is straightforward. For the systematic evaluation of the method, I composed the first set of experimental Benchmark Data for Solvatochromism in Molecules (xBDSM), and part of the data points were measured by myself. Comparing calculated gas phase to solvent shifts to the xBDSM set, I was able to demonstrate the convincing accuracy of my approach in combination with various levels of electronic structure theory and could shed light on the relation of different flavors of excited state PCMs. Moreover, a close examination of the contributions to the calculated shifts revealed general patterns, which are essential regarding any evaluation of calculated solvent shifts by comparison to the experiment. The implemented methodology will be released with one of the next versions of the Q-CHEM quantum-chemical software package.

Zusammenfassung

Die Wechselwirkung komplexer, molekularer Systeme mit Licht ist sowohl in der Natur, als auch für viele moderne Technologien von großer Bedeutung. Während die photosynthetische Umwandlung von Licht in chemische Energie die primäre Energiequelle für das Leben auf der Erde bildet, verspricht Photovoltaik, als technische Implementierung dieses Prinzips, eine der bedeutendsten Lieferanten elektrischer Energie des 21. Jahrhunderts zu werden. Der inverse Prozess, die gezielte Erzeugung von Licht durch elektrisch angeregte Moleküle, bildet die Grundlage vieler moderner Technologien, wie z.B. die immer kleiner und gleichzeitig hochauflösender werdenden Bildschirme mobiler Computer. Um eine gezielte Verbesserung und Entwicklung dieser Technologien zu ermöglichen, ist ein grundlegendes Verständnis der auf atomarer Ebene ablaufenden Prozesse von entscheidender Bedeutung. Aufgrund der ultrakurzen Zeitskalen auf denen die elementaren Schritte lichtinduzierter Prozesse ablaufen, ist eine rein experimentelle Untersuchung der Phänomene jedoch schwierig. Insbesondere die Interpretation der gewonnenen Daten ist ohne eine Begleitung durch theoretische Modelle schwierig und wird teilweise erst unter Zuhilfenahme solcher Modelle möglich. Die Entwicklung und Anwendung eben dieser theoretischen Modelle für den elektronischen Grundzustand und lichtaktivierte (angeregte) Zustände von molekularen Systemen und die approximative Beschreibung von deren Wechselwirkung mit ihrer Umgebung ist das zentrale Thema dieser Arbeit.

In den Kapiteln 2 und 4 beschreibe ich die Anwendung der in Kapitel 1 vorgestellten Methodik, um lichtinduzierte Prozesse in molekularen Systemen zu untersuchen. Bei den in Kapiteln 2 und 3 untersuchten Systemen Nitrophenylacetat (NPA) und *ortho*-Nitrobenzylacetat handelt es sich um sogenannte Käfigverbindungen, deren Zweck es ist, die bemerkenswerte räumliche und zeitliche Auflösung moderner Laser zu nutzen, um chemische Reaktionen zu steuern. Dafür besitzen Käfigverbindungen die Eigenschaft nach Lichtabsorption an einer Stelle zu „brechen“, wodurch das Molekül in eine aktive Verbindung und einen inerten Rest zerfällt. Im Falle von NPA ist diese aktive Verbindung CO_2 , im Falle von *o*NPA Acetat, wobei *o*NBA prinzipiell zur Freisetzung jedes organischen Moleküls genutzt werden kann, das eine vergleichbar gute Abgangsgruppe bildet. Da die lichtinduzierte Spaltung auf einer Nano- bis Mikrosekundenzeitskala abläuft, lassen sich Folgereaktionen der aktiven Verbindung mit entsprechend höherer Zeitauflösung starten. Im Rahmen einer Kooperation begleitete meine theoretische Untersuchung zunächst eine Reihe von Experimenten. Um die dabei erstellten Modelle und Vorhersagen zu prüfen, wurden anschließend, inspiriert durch die Theorie, weitere Experimente durchgeführt. Schlussendlich lieferten diese Untersuchungen detaillierte Einblicke in den molekularen Mechanismus der lichtinduzierten Spaltung, die in sehr guter Übereinstimmung mit den experimentellen Befunden stehen und für eine gezielte Verbesserung photolabiler Schutzgruppen zur Verfügung stehen.

Ein gemeinsames Strukturelement von NPA und *o*NPA, aber auch vieler andere lichtaktiver Verbindungen ist Nitrobenzol (NB). Daher hat die Photochemie von diesem kleinsten, prototypischen Nitroaromaten allgemein eine große Bedeutung für viele photochemische Anwendungen und macht NB selbst zu einem interessanten Untersuchungsobjekt. Zudem ermöglichen die geringe Größe und hohe Symmetrie des Moleküls die Anwendung einer Reihe hoch-genauer und verlässlicher Methoden, mit deren Hilfe sich die Vorhersagen approximativer Me-

thoden, u.a. für NPA und oNBA eingesetzt wurden, überprüfen lassen. In Kapitel 4 beschreibe ich eine ausführliche Untersuchung der angeregten Zustände und des Grundzustandes von NB, sowie dessen strahlungsloser Deaktivierung. Dabei zeigt sich, dass dieses kleine Molekül eine unerwartete Herausforderung darstellt und selbst verlässlich geglaubte Methoden eine falsche Reihenfolge der für die Photochemie besonders relevanten, niedrigsten Tripletzustände vorhersagen. Nichtsdestotrotz konnte ich den molekularen Mechanismus der strahlungslosen Deaktivierung in guter, quantitativer Übereinstimmung mit den experimentellen Befunden aufklären und zudem weitere Experimente vorschlagen, um meine Hypothese zu überprüfen.

Obwohl eine Reihe von Methoden existiert, die eine genaue und verlässliche Beschreibung des elektronischen Grundzustandes und der angeregten Zustände von *isolierten* Systemen der Größe von NB, NPA und oNBA liefern können, spielt die molekulare Umgebung häufig eine entscheidende Rolle. So z.B. im Falle des anionischen NPA, dessen Eigenschaften durch Wasser als stark polares Lösungsmittel dramatisch verändert werden. Aus diesem Grund ist die Entwicklung von Umgebungsmodellen ein sehr aktives Forschungsgebiet, das 2013 mit dem Nobelpreis für Chemie gewürdigt wurde. Um die Beschreibung vertikaler Anregungsprozesse in Lösung zu ermöglichen, habe ich im Rahmen dieser Arbeit ein Modell aus der Klasse der polarisierbaren Kontinuumsmodelle (PCM) auf Anregungsprozesse erweitert und implementiert. Da das entwickelte Modell zur Berechnung der Energiekorrekturen ausschließlich die Elektronendichte der involvierten Zustände benötigt, ist es leicht auf verschiedene quantenchemische Rechenmethoden übertragbar. Formalismus, Implementierung und Evaluation des Modells stelle ich in Kapitel 5 vor. Grundsätzlich ermöglichen PCMs eine sehr effiziente Berechnung des häufig bedeutsamsten, elektrostatischen Teils der Wechselwirkung eines Moleküls mit seiner Umgebung anhand der makroskopischen Parameter ϵ (Dielektrizitätskonstante) und $\epsilon_{\text{opt}} = n^2$ (optische Dielektrizitätskonstante bzw. quadrierter Brechungsindex). Um das implementierte PCM zu evaluieren, habe ich einen Satz von experimentellen Benchmarkdaten für Solvatochromie von Molekülen (xBDSM) zusammengestellt und teilweise selbst experimentell bestimmt. Der Vergleich zwischen berechneter und experimentell ermittelter Solvatochromie demonstriert die Genauigkeit des PCMs in Verbindung mit verschiedenen quantenchemischen Modellen und erlaubt zudem Einblicke in das Verhältnis verschiedener theoretischer Ansätze zur Beschreibung vertikaler Anregungen im Rahmen eines PCMs. Weiterhin konnte ich in einer detaillierten Aufschlüsselung der einzelnen Beiträge der berechneten Solvatochromie bestimmte Muster identifizieren, die entscheidend sind für eine aussagekräftige Evaluation theoretischer Modelle anhand experimenteller Daten. Das entwickelte Modell wird zusammen mit einer der nächsten Versionen des quantenchemischen Programmpaketes Q-CHEM veröffentlicht.

Chapter 1

Theoretical Background

In the first part of this chapter I introduce and discuss a selection of the methods applied in chapters 2 – 4 to study photochemical processes in molecules. Furthermore, the formalism introduced here will serve as a starting point for the derivation of a quantum-classical model for the calculation of vertical excitations in solution described in chapter 5. Instead of giving a superficial introduction to each of the numerous methods applied in the scope of this work, I decided to focus this theoretical part on a few methods, namely Hartree-Fock, Configuration Interaction as well as Many-Body Perturbation-Theory for the ground state (Møller-Plesset PT) and excited states (Intermediate-State Representation). This enables me to point out central, recurring concepts within the approximate, quantum-mechanical treatment of molecules as well as the relations between the methods. Nevertheless, I want to mention other, prominent quantum-chemical methods which are not explicitly discussed in this chapter. In the scope of this work, also coupled-cluster (CC) theory,² Kohn-Sham density functional theory (KS-DFT),³ and their excited-state versions time-dependent DFT (TD-DFT) and equation-of-motion (EOM-CC) as well as the whole class of multi-configurational self-consistent field (MC-SCF) and complete active-space (CAS) SCF methods⁴ were employed. For detailed reviews and discussions of these methods, please be referred to the cited literature. Practical advantages and drawbacks of the methods applied in chapters 2 – 4 are discussed in the respective methodology sections, in particular in section 4.4.

In the second part of this chapter, beginning with section 1.7, I will give a brief overview about general concepts that help to rationalize the interaction of molecules with light and the subsequent physical and chemical processes. For the sake of brevity, I will limit the discussion to topics that are relevant for the applications described in chapters 2–4. These topics are mainly the characterization of excited states, rules for inter-conversion between excited states of different character and multiplicity and the photochemical and photophysical processes of molecules in excited states and the time-scales thereof.

First Part:

Electronic-Structure Theory

1.1 Time-Independent Schrödinger Equation

The equation underlying the quantum-mechanical description of stationary states of molecular systems is the time-independent Schrödinger equation

$$\mathcal{H}\Psi = \mathcal{E}\Psi . \quad (1.1)$$

While the molecular wave function Ψ contains all coordinates or in other words variables of the system (*i.e.* positions of electrons, nuclei etc.), the Hamiltonian \mathcal{H} collects all interactions that give rise to an energy contribution.

To evaluate this equation, or in other words to compute the energy eigenvalue \mathcal{E} of a wave function, the set of mathematical operations that constitute the Hamiltonian given in eq. (1.2) have to be applied. If the wave function is a solution to this equation, *i.e.* an eigenfunction of the Hamiltonian, application of the Hamiltonian yields a product of the eigenvalues times the wave function. Hence, the task at hand is to find the eigenfunctions that solve this equation. For this purpose, consider the following Hamiltonian of an arbitrary molecule with N nuclei A, B, \dots at the positions R_A, R_B, \dots and n electrons i, j, \dots at the positions r_i, r_j, \dots , which can be written as a sum of electronic terms, nuclear terms and the electron-nuclear interaction.

$$\mathcal{H} = \hat{H}^{elec}(r) + \hat{H}^{nuc}(R) + \hat{H}^{elec-nuc}(r, R) \quad (1.2a)$$

$$= - \sum_{i=1}^n \frac{1}{2} \nabla_i^2 + \sum_{i=1}^n \sum_{j < i}^n \frac{1}{r_i - r_j} \quad (1.2b)$$

$$- \sum_{A=1}^N \frac{1}{2m_A} \nabla_A^2 + \sum_{A=1}^N \sum_{B < A}^N \frac{Z_A Z_B}{R_A - R_B} \quad (1.2c)$$

$$- \sum_{A=1}^N \sum_{i=1}^n \frac{Z_A}{r_i - R_A} \quad (1.2d)$$

For this and all following equations atomic units have been used. Their introduction is described in ref. 5 chapter 2.1.1.

The Schrödinger equation for the given Hamiltonian can not be solved analytically if more than one electron and one nucleus are present. This is due to the complicated electron-electron (second term in (1.2b)) and nuclear-nuclear interactions second term in (1.2c)), which render any molecular Schrödinger equation

a many-body problem. To arrive at soluble equations, a number of approximations have to be introduced. The first one, which simplifies the problem by separation into an electronic and a nuclear part, is termed Born-Oppenheimer approximation.

1.1.1 Born-Oppenheimer Approximation

In the Hamiltonian given in eq. (1.2), the terms have been separated into exclusively electronic contributions (eq. 1.2b), exclusively nuclear contributions (eq. 1.2c) and the interaction between electrons and nuclei (eq. 1.2d). The Born-Oppenheimer (BO) approximation may be regarded as a transfer of the separation of the molecular Hamiltonian described in eq. (1.2a) to the wave function. Accordingly, the latter is split into a product of nuclear and an electronic parts

$$\Psi^{Mol}(r, R) = \Psi^{Elec}(r, \bar{R})\Psi^{Nuc}(R), \quad (1.3)$$

where the bar over the nuclear coordinates on the right hand side this equation indicates a parametric dependence. In other words, the separated electronic wave function depends on the fixed coordinates of the nuclei and in turn, the electrons instantaneously adapt to any change of the nuclear geometry. This approximation can be motivated with large difference between the electronic and the nuclear masses, which in case of the lightest nucleus (hydrogen) is as large as $m_N/m_e > 1850$. Assuming fixed nuclei, the kinetic energy term of the nuclei becomes zero and the nuclear-nuclear interactions become a constant energy contribution. Consequently, the electronic part of the wave function may be solved for a fixed orientation of the nuclei and in turn, the latter are assumed to move in the mean, conservative potential of the electrons. The picture of nuclei moving in a conservative potential gives rise to so-called potential-energy surfaces (PES), whose calculation and investigation is one of the most common tools in quantum-chemistry.

The remaining terms may now be categorized as follows: Two terms depend on one electronic coordinate (kinetic energy of the electrons and the electron-nuclear interaction), one term depends on two electronic coordinates (electron-electron interaction) and third is the constant nuclear repulsion.

$$\mathcal{H} = \hat{H}_1(r, \bar{R}) + \hat{H}_2(r, r') + C(\bar{R}) \quad (1.4a)$$

$$= - \sum_{i=1}^n \frac{1}{2} \nabla_i^2 - \sum_{A=1}^N \sum_{i=1}^n \frac{Z_A}{r_i - R_A} \quad (1.4b)$$

$$+ \sum_{i=1}^n \sum_{j < i}^n \frac{1}{r_i - r'_j} \quad (1.4c)$$

$$+ \sum_{A=1}^N \sum_{B < A}^N \frac{Z_A Z_B}{R_A - R_B} \quad (1.4d)$$

The partition used above is motivated by the level of complexity of the different terms. While all the contributions depending only on the coordinates of one electron can be calculated straightforwardly, the interaction of many electrons constitutes a many-body problem. A large part of quantum chemistry is concerned with finding efficient and practical approximations, since the accuracy of quantum-chemical models stands or falls by the description of the

electron-electron interaction. Many of these approaches are based on Hartree-Fock theory, which, in a nutshell, provides an approximate description of the electron-electron interaction by turning the n -electron problem into n coupled single-electron problems.

For the purpose of building an approximate, molecular many-particle function, the structure of the solutions for a hydrogen-like atom, *i.e.* a single electron in the Coulomb potential of a nuclei is instructive. Hence, I will first discuss the analytical solutions for the single particle, which can subsequently be used as a starting point for the construction of a molecular many-body wave function.

1.1.2 Solutions for Hydrogen-Like Atoms

For a single, non-relativistic electron at the position r interacting with the electric field $V(r)$ of an atomic nucleus at the position R with the atomic number Z , the electronic part of the general molecular Hamiltonian given in eq. (1.2) reduces to

$$\hat{H}_{\text{elec}} = \hat{T}(r) + \hat{V}(r, R) = \frac{1}{2} \nabla_r^2 - \frac{Z}{|r - R|}, \quad (1.5)$$

where I have separated the Hamiltonian into the kinetic energy operator $\hat{T}(r)$ and the potential energy operator $\hat{V}(r, R)$. While the kinetic energy of the electrons is related to the curvature of the functions and thus computed *via* double differentiation with respect to the position, the potential energy of the electrons is due to the presence of the Coulomb potential of the nucleus and thus depends on the electron-nuclear distance and the nuclear charge. Due to energy conservation, the sum of the two is constant.

Solutions for an eigenvalue problem such as the Schrödinger equation are called eigenfunctions. To be a solution, the function must apart from a pre-factor be recovered when the Hamiltonian is applied, *i.e.* when it is derived twice, which hints to exponential or trigonometric functions and thus explains for the term “wave function”. The analytical solutions of the hydrogen-problem are closely related to the so-called Slater orbitals. The analytical expression for the Slater function with the lowest energy ($1s$ orbital) is given in eq. (1.7). In general, these solutions are products of a radial part $R_n(r)$ and an angular part $Y_l^m(r)$

$$\phi_{\text{STO}}(r, n, l, m) = R_n(r) Y_l^m(r) \quad (1.6a)$$

$$R_n(r) = (2\zeta)^n \sqrt{\frac{2\zeta}{(2n)!}} r^{(n-1)} e^{-\zeta r}, \quad (1.6b)$$

where ζ is the exponent determining the compactness of the orbital and $Y_l^m(r)$ can be identified as the spherical harmonics of degree l and order m . In the context of atomic orbitals, n , l and m correspond to the principle (shell), orbital (s, p, d, f etc.) and magnetic (discriminating between p_x, p_y, p_z etc.) quantum numbers, respectively. Note that for the case of a single electron, the energy is determined solely by the principle quantum number, and hence all orbitals of one shell (e.g. $2s, 2p$ as well as $3s, 3p$ and $3d$ orbitals) are perfectly degenerate. Only for the element-like atoms with n electrons in the field of an n -tuply charged core, the usual energetic ordering of the atomic orbitals, which gives rise to the structure of the periodic table of the elements, is recovered. The shape of the resulting orbitals is shown for a neutral argon-atom in fig. 1.1.

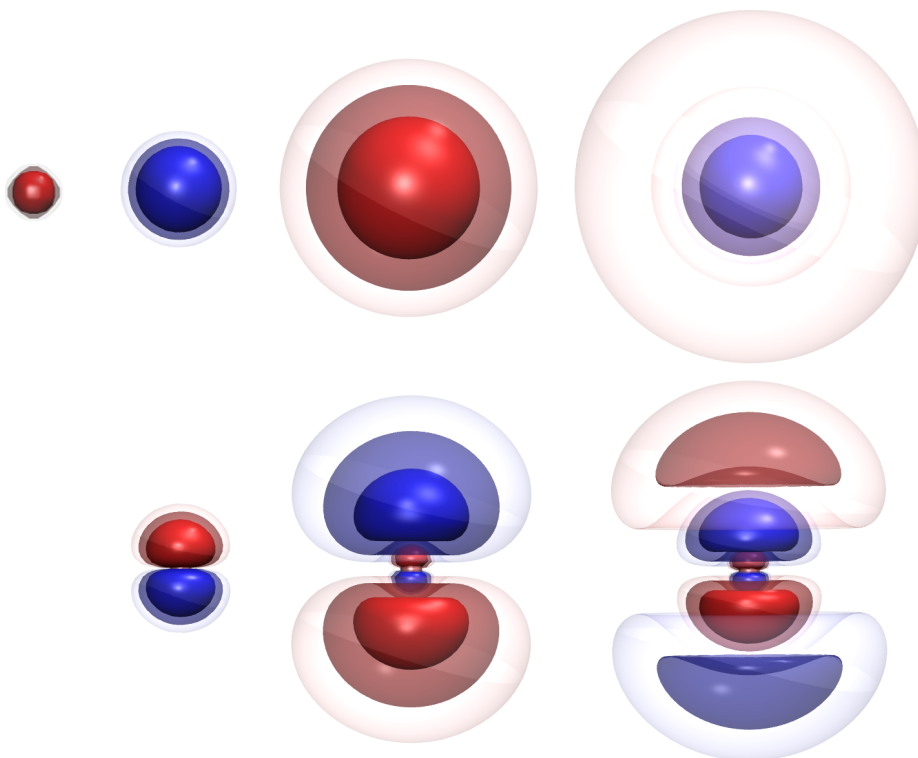


Figure 1.1: Shape of (from left to right) $1s$, $2s$, $3s$ and $4s$ as well as one of the (below) $2p$, $3p$ and $4p$ orbitals of elemental Argon calculated at the Hartree-Fock/def2-TZVP level of theory and visualized using isovalue surfaces. The latter are a very common tool for visualization of densities in quantum-chemistry. Each of the three surfaces encases a specific fraction of the global density of the respective orbital (solid surface: 80%, transparent: 90% and diffuse: 95%) and furthermore, all points of one surface have the same local value of the density (isovalue). The plots nicely show the internal nodal structure of the orbitals with increasing principle quantum number n , which is due to the $r^{(n-1)}$ term in the radial part of the orbital. Also, the orbitals become more and more diffuse, as indicated by the increase of transparent and diffuse surfaces in the higher orbitals to the right.

The (approximate) solutions or eigenfunctions for any quantum mechanically treated system may be categorized according to their energy expectation values. The one eigenfunction with the lowest energy expectation value is referred to as the ground state, while the solutions with higher energy are termed excited states. For a single electron in the spherical Coulomb field of an atom, the ground state corresponds to the $1s$ orbital, whereas the excited states are represented by the orbitals with higher quantum numbers ($2s, 2p, 3s, 3p$).

In general, any function that fulfils the Schrödinger equation and in addition a certain set of physical conditions like e.g. the anti-symmetry principle for fermions, is a valid wave function. The conditions for the wave function are dictated by the so-called axioms or postulates of quantum mechanics. The first of these postulates states the existence of the wave function and its nature, while the others describe a framework for the mathematical structure of the wave function as well as operator algebra. Loosely spoken, the postulates constitute a manual how to set up the wave function and Schrödinger equation.

1.2 Hartree-Fock Theory

According to the first postulate of quantum mechanics, all molecular properties can be calculated from the molecular wave function. Hence, the quest for practical procedures to obtain molecular wave functions is one of the central topics in quantum-chemistry. Since all chemically relevant systems are, however, inherently complicated many-body problems, all practical procedures for the calculation of molecular wave function are of approximate nature. A common approach underlying such methods is to assume a structure for the wave function based on the analytically known solutions for a single particle, form an educated guess of the respective parameters and then optimize the latter using a numerical procedure.

What is nowadays referred to as Hartree-Fock (HF) and/or self-consistent-field (SCF) theory is a combination of numerous ideas and concepts that enable an efficient, numerical procedure to obtain an approximate electronic wave function for the molecular ground state in the framework of the BO approximation. Central to this formalism are the approximate treatment of the interaction of electrons using an effective single-particle potential as well as the application of functional variation to derive a systematic procedure for optimizing the wave function. However, also the expansion of the many-body wave function in a basis of one-electron functions (Roothaan equations) and the application of efficient numerical techniques for the evaluation of so-called electron-repulsion integrals as well as the diagonalization of large, sparse matrices are crucial ingredients to the actual numerical HF-SCF procedure. Owing to the major relevance of the HF method in modern day quantum chemistry and the illustrative character of its derivation, I will in this section give a rather detailed introduction skipping only lengthy derivations, for which I will refer to the book “Modern Quantum-Chemistry” by A. Szabo and N. Ostlund.⁵

I will present the HF method pursuing a rather unusual bottom-up approach, starting with the discussion with the explicit mathematical structure of the the smallest building blocks of the HF wave function, the so-called one electron functions or orbitals. Subsequently, I will describe how the single electron functions can be combined to a many-electron function (Slater determinant) that obeys

the anti-symmetry principle and how this choice affects the treatment of the electron-electron interaction. Eventually, I will present the variational procedure used to systematically optimize such a many-electron wave function and close this section with a discussion of practical aspects of HF-SCF calculations.

1.2.1 A Basis of Single-Electron Functions

An apparent choice for the single-electron functions in the context of an approximate method like HF are the atom-centered functions ϕ_i that constitute analytical solutions for a single electron in the field of a hydrogen-like atom introduced in section 1.1.2. The analytical form of a Slater function for a 1s orbital is

$$\phi_{1s}^{Slater}(\zeta, r_i - R_A) = \sqrt{\frac{\zeta^3}{\pi}} e^{-\zeta(r_i - R_A)}. \quad (1.7)$$

From a numerical perspective, however, Slater functions are impractical. In the HF equations, the electron-electron interaction is computed using so-called electron-repulsion integrals (ERIs), which are introduced in section 1.2.4. Evaluated between Slater-functions, the calculation of the ERIs is very expensive, *i.e.* requires a lot of computer time. Gaussian functions (eq. 1.8), on the other hand, which qualitatively resemble Slater functions, are about 4 orders of magnitude cheaper (faster) to integrate. Consequently, in most modern quantum-chemistry programs Gaussian functions are used to approximate the Slater functions.

$$\phi_{1s}^{Gauss}(\alpha, r_i - R_A) = \sqrt[4]{\left(\frac{2\alpha}{\pi}\right)^3} e^{-\alpha(r_i - R_A)^2} \quad (1.8)$$

For very small and very large electron-nuclear distances, however, the behaviour of Gaussian and Slater functions is quite different as illustrated in fig. 1.2. To account for these differences, linear combinations of multiple Gaussians, which are fitted to resemble Slater functions are used in practice (e.g. the so-called minimal-basis STO-3G $n = 3$; $c_1 = 0.44$, $\alpha_1 = 0.17$, $c_2 = 0.54$, $\alpha_2 = 0.62$, $c_3 = 0.15$ and $\alpha_3 = 3.43$, shown in fig. 1.2).

$$\phi^{STO-nG} = \sum_{i=1}^n c_i \phi^{Gauss}(\alpha_i) \quad (1.9)$$

Eventually, each single electron-function (orbital) in a molecular many-electron wave function is represented by at least one, but usually a linear combination of many STO- n G type basis functions. The linear combination coefficients c_i of the n so-called *primitive* Gaussian functions are usually fixed and the flexibility in the wave function is due to the expansion of each single-electron function ψ_i in a number of different STO- n G type functions ϕ_μ according to:

$$\psi_i = \sum_{\mu=1}^K C_{i\mu} \phi_\mu^{STO-nG} \quad (1.10)$$

The resulting, so-called Gaussian basis sets can be categorized according to the number of independent functions used to describe a single orbital. Basis sets with two independent functions are termed double- ζ basis, with three triple- ζ basis and so on. Practical aspects of the choice of basis sets are discussed in section 1.2.5.

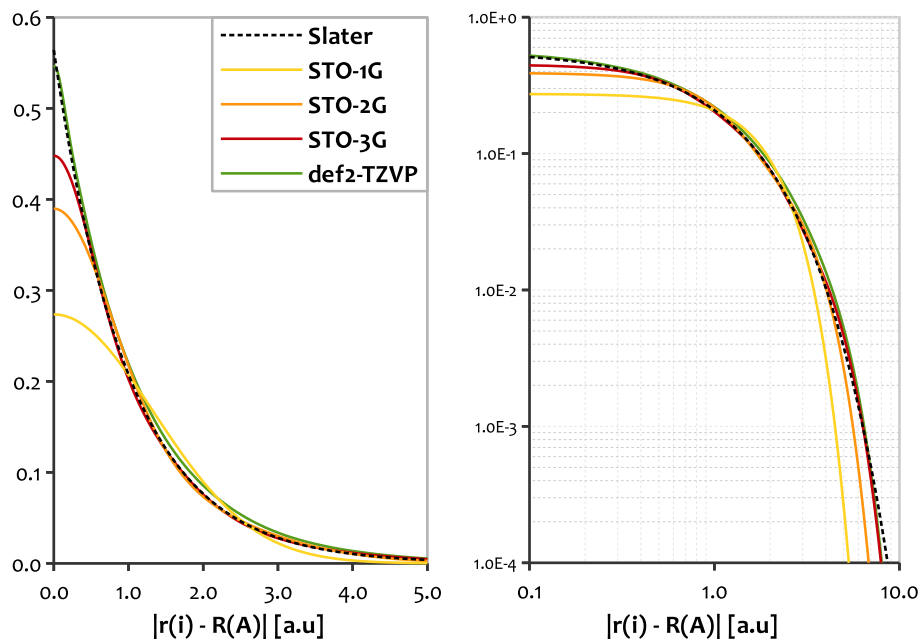


Figure 1.2: Comparison between the Slater-type and Gaussian (STO-1G) $1s$ orbital for the hydrogen atom (eq. 1.7) as well as linear combinations of two (STO-2G) to five (def2-TZVP) primitive Gaussian functions according to eq. (1.9). While the linear plot on the left exposes the different shape of the Slater and Gaussian functions close to the core, the logarithmic plot on the right also shows differences for large electron-nuclear distances.

1.2.2 Construction of Many-Electron Functions

A self-evident ansatz for a many-electron wave function is to simply take a product of single-electron functions introduced in the last section, which is termed Hartree-product

$$\Psi^{HP}(r_1, r_2, \dots, r_n) = \prod_{i=1}^n \psi_i(r_i). \quad (1.11)$$

However, since electrons are fermions, an electronic wave function has to obey the Pauli or anti-symmetry principle. It states that the wave function must only change sign when two particles exchange positions. Obviously, the Hartree-product given in eq. (1.11) does not fulfil this condition as it is neither invariant nor anti-symmetric with respect to an exchange of two particles. To satisfy this condition, an anti-symmetrized product of one electron functions can be used. Illustrated for the case of two electrons, the anti-symmetrization yields

$$\Psi^{SD}(r_1, r_2) = \frac{1}{\sqrt{2}}(\psi_1(r_1) * \psi_2(r_2) - \psi_2(r_1) * \psi_1(r_2)). \quad (1.12)$$

The product in the equation above can be identified as determinant of a 2×2 matrix, in which the index of the electrons r_1, r_2, \dots, r_n runs in the columns

and the index of the single-electron functions $\psi_1, \psi_2, \dots, \psi_n$ runs in the rows

$$\Psi^{\text{SD}}(r_1, r_2, \dots, r_n) = \frac{1}{\sqrt{n!}} \cdot \det \begin{pmatrix} \psi_1(r_1) & \psi_2(r_1) & \dots & \psi_n(r_1) \\ \psi_1(r_2) & \psi_2(r_2) & \dots & \psi_n(r_2) \\ \vdots & \vdots & \ddots & \vdots \\ \psi_1(r_n) & \psi_2(r_n) & \dots & \psi_n(r_n) \end{pmatrix}. \quad (1.13)$$

This so-called Slater determinant constitutes an appropriate molecular wave function that is in agreement with the anti-symmetry principle. Since the number of terms of a given Slater determinant is given by the factorial of the number of electrons, the following bra-ket short-hand notation illustrated will be used

$$\Psi^{\text{SD}}(r_1, r_2, \dots, r_n) \equiv |\psi_1 \psi_2 \dots \psi_n\rangle. \quad (1.14)$$

Although the Slater determinant is of the correct symmetry for a fermionic wave function, it does not constitute a full basis in which the exact ground-state wave function can be represented. Within the HF approach that makes use of a single reference, only the averaged interaction of electrons in the occupied one-electron basis-functions (orbitals) is taken into account, while the explicit correlation of the electronic movement is neglected. This will become evident from the HF-equations derived in the course of this section, which only include terms accounting for the interaction of one electron with the averaged field of all electrons, but not a single term that explicitly depends on the distance r_{ij}^{-1} between pairs of electrons. Per definition, electron-correlation refers to the difference between the mean-field treatment of the electron-electron interaction in HF theory and the exact interaction between explicit electrons. Accordingly, the energetic impact of electron correlation, the so-called correlation energy E_{corr} , is the difference between HF energy E^{HF} and the exact energy \mathcal{E} .

$$E_{\text{corr}} = \mathcal{E} - E_{\text{HF}} \quad (1.15)$$

To compute the exact energy, one has to allow for the explicitly correlated motion of multiple electrons. This can be realized by including so-called excited Slater determinants, which can be obtained from the (supposedly known) HF solution by interchanging 1 to n electrons or in other words the respective, occupied one-electron functions (orbitals) (i, j, \dots) with unoccupied (so-called virtual) orbitals (a, b, \dots). Ultimately, the exact ground-state wave function Φ^0 is represented as a linear combination of all possible determinants

$$\Phi^0 = c_0 \Psi_0^{\text{HF}} + \sum_{i,a} c_i^a \Psi_i^a + \sum_{i,j,a,b} c_{ij}^{ab} \Psi_{ij}^{ab} + \dots, \quad (1.16)$$

whereas the energetic impact of each of the possible correlated motions or in other words excited determinants is contained in the respective linear combination coefficients. The above-described ansatz is termed configuration interaction and discussed in section 1.4.

In general, the use of such a linear combination of Slater determinants as starting point in a numerical procedure is, however, impractical. Besides the fact that the numerical complexity of such an exact ansatz grows with the factorial of the number of particles (electrons), there is the more fundamental problem of a missing reference. Hence, the common approach is to *first* obtain an approximate solution using a single Slater determinant *via* e.g. the HF procedure, and subsequently approach the exact wave function with the HF solutions serving as starting point.

1.2.3 Optimization of the Slater Determinant

Having defined the wave function down to the explicit mathematical structure of orbitals, I may now describe the derivation of a procedure for its systematic optimization. For this purpose, one needs to obtain an explicit expression for the energy of the wave function represented by a single Slater determinant.

As mentioned before concerning eq. (1.4), the Hamiltonian can be split into three terms. The constant nuclear repulsion $C(\bar{R})$, a one-electron energy that depends on one electronic coordinate $\hat{H}_1(r, \bar{R})$ as well as a third part that describes the electron-electron interactions and thus depends on two electronic coordinates $\hat{H}_2(r, r')$. Inserting the mathematical structure of the wave function, one can derive explicit expressions for the expectation values of the one- and two-electron part of the Hamiltonian, or in a more general sense the expectation values for one- and two-electron operators. A detailed derivation of the integrals using the so-called Slater-Condon rules can be found in ref. 5 chapter 2.3.4. Here, I will continue with the discussion of the results. For the integrals over one electron-operators that need to be evaluated in the HF framework, the derivation yields:

$$\begin{aligned}
 \langle \Psi^{\text{SD}} | \hat{H}_1 | \Psi^{\text{SD}} \rangle &= - \sum_{i=1}^n \int \psi_i^*(r_1) \left(\frac{1}{2} \nabla_i^2 + \sum_{A=1}^N \frac{Z_A}{r_{iA}} \right) \psi_i(r_1) dr_1 \\
 &= - \sum_{i=1}^n \langle \psi_i | \hat{h}_1 | \psi_i \rangle \\
 &\equiv - \sum_{i=1}^n \langle i | \hat{h}_1 | i \rangle
 \end{aligned} \tag{1.17}$$

Apparently, the one-electron energy of a Slater determinant is just the sum of the one-electron energies of all electrons.

For the two-electron operator, which accounts for the inter-electronic repulsion r_{ij}^{-1} , one obtains the following result.

$$\begin{aligned}
 \langle \Psi^{\text{SD}} | \hat{H}_2 | \Psi^{\text{SD}} \rangle &= \frac{1}{2} \left(\sum_{i,j}^n \int \psi_i^*(r_1) \psi_i(r_1) \frac{1}{r_{12}} \psi_j^*(r_2) \psi_j(r_2) dr_1 dr_2 \right. \\
 &\quad \left. - \sum_{i,j}^n \int \psi_i^*(r_1) \psi_j(r_1) \frac{1}{r_{12}} \psi_j^*(r_2) \psi_i(r_2) dr_1 dr_2 \right) \\
 &= \frac{1}{2} \sum_{i,j}^n \int \psi_i^*(r_1) \psi_i(r_1) \frac{1}{r_{12}} (1 - \mathcal{P}_{12}) \psi_j^*(r_2) \psi_j(r_2) dr_1 dr_2
 \end{aligned} \tag{1.18}$$

Considering Born's rule, which basically states that the squared amplitude of the wave function can be interpreted as a probability, the first term in eq. (1.18) apparently constitutes the quantum analog of the classical Coulomb interaction. Integrated over all space, it yields the Coulomb repulsion (r_{12}^{-1}) of the electrons weighted by the probability to find them in the respective volume elements dr_1 and dr_2 . In a classical picture, this corresponds to the interaction of the charge density of electron 1 in ψ_i with electron 2 in ψ_j .

For the second term, there exists no such simple classical interpretation. As evident from ref. 5 chapter 2.3.4, it is a direct result of the anti-symmetric nature of the wave function. Consequently, it is commonly referred to as exchange

interaction. A conceivable physical interpretation of this term may be derived considering the anti-symmetry or in other words the Pauli-exclusion principle. The latter states that two fermions with the same spin may never occupy the same point in space. Consequently, this term could be interpreted as the energetic contribution arising from the fact that same-spin electrons perfectly evade each other, thereby reducing the Coulomb repulsion between them. Since there is no analog term between opposite-spin electrons, the treatment of the electron-electron interaction is spin-dependent and thus imbalanced at the HF level of theory.

In the last line of (1.18), I have made use of the so-called permutation operator \mathcal{P}_{12} to compact the equations. Formally, this operator permutes the indices of the MO of electron 1 and the complex conjugate MO of electron 2, thereby turning a Coulomb integral into an exchange integral. For the sake of compactness, Coulomb and exchange integrals given in eq. (1.18) will from now on be depicted using the so-called physicists notation, in which the complex conjugates are collected on the left hand side of the operator.

$$\begin{aligned}
 \langle \Psi^{\text{SD}} | \hat{H}_2(r_1, r_2) | \Psi^{\text{SD}} \rangle &= \frac{1}{2} \sum_{i,j}^n \int \psi_i^*(r_1) \psi_j^*(r_2) \frac{1}{r_{12}} (1 - \mathcal{P}_{12}) \psi_i(r_1) \psi_j(r_2) dr_1 dr_2 \\
 &= \frac{1}{2} \sum_{i,j}^n \left(\langle \psi_i \psi_j | \psi_i \psi_j \rangle - \langle \psi_i \psi_j | \psi_j \psi_i \rangle \right) \\
 &\equiv \frac{1}{2} \sum_{i,j}^n \left(\langle ij | ij \rangle - \langle ij | ji \rangle \right) \\
 &\equiv \frac{1}{2} \sum_{i,j}^n \langle ij || ij \rangle
 \end{aligned} \tag{1.19}$$

Eventually, the expectation value of a Slater determinant for the Hamiltonian becomes

$$E(\Psi^{\text{SD}}) = \langle \Psi^{\text{SD}} | \hat{H}_1 + \hat{H}_2 | \Psi^{\text{SD}} \rangle = \sum_i^n \langle i | h_1 | i \rangle + \frac{1}{2} \sum_{i,j}^n \langle ij || ij \rangle. \tag{1.20}$$

Having obtained an explicit expression for the energy expectation value, one can employ the mathematical technique of functional variation described in chapter 1.3 of ref. 5 to establish a procedure, which will eventually enable an iterative optimization of the wave function. For this purpose, energy expressions given in eqs. (1.17) and (1.18) are differentiated with respect to the orbitals ψ_i , which in practice depend on the linear combination coefficients $C_{i\mu}$. Furthermore, one has to constrain the orbital-basis to stay orthonormal ($\langle i | j \rangle - \delta_{ij} = 0$), since this condition was used for the derivation of the energy expression given in (1.20). For this purpose, one employs Lagrange's methods of undetermined multipliers yielding the following ansatz:

$$\mathcal{L}[\psi_i] = \delta E^{\text{HF}}[\psi_i] - \sum_{i,j} \epsilon_{ij} (\langle i | j \rangle - \delta_{ij}) \tag{1.21}$$

I will skip the actual derivation continue with the discussion of the resulting Hartree-Fock eigenvalue equation. A detailed derivation can be found in ref. 5

chapter 3.2. Nonetheless, I want to point out a key aspect of the technique, which is that an approach derived by means of functional variation will yield an upper boarder for the exact energy of the system. In turn, it is possible to judge any modification of the numerical procedure (e.g. using a different basis set) by means of the energy change it induces, whereas any modification (e.g. of the AO-basis functions) that lowers the energy constitutes an improvement.

The result of the ansatz described in eq. (1.21) is a non-linear eigenvalue equation for the molecular orbitals (MOs) ψ_i such as the Schrödinger equation. In general, there is an infinite number of sets of MOs that fulfil this equation, which are related to each other *via* so-called unitary transformations. There is, however, only one set of MOs for which the eigenvalues ϵ_i correspond to orbital energies. This is the canonical form of the Hartree-Fock equations, which states that the Fock operator f working on a molecular orbital ψ_i yields the orbital energy ϵ_i times the orbital.

$$f(r_1)\psi_i(r_1) = \epsilon_i\psi_i(r_1) \quad (1.22)$$

Originating from the energy derivative in eq. (1.21), the Fock operator can be separated into a one-electron part $h(1)$ and two-electron part v^{HF} , of which the latter can be split-up further into a Coulomb operator \mathcal{J} and an exchange operator \mathcal{K} .

$$f = h_i(1) + v_i^{HF}(1) = h_i(1) + \mathcal{J}_i(1) - \mathcal{K}_i(1) \quad (1.23)$$

$$h_i(1) = \frac{1}{2}\nabla_i^2 + \sum_{A=1}^N \frac{Z_A}{r_{iA}} \quad (1.24)$$

$$\mathcal{J}_i(1) = \int \psi_i^*(r_2) \frac{1}{r_{12}} \psi_i(r_2) dr_2 \quad (1.25)$$

$$\mathcal{K}_i(1) = \int \psi_i^*(r_2) \frac{1}{r_{12}} \psi_j(r_2) dr_2 = \int \psi_i^*(r_2) \frac{\mathcal{P}_{12}}{r_{12}} \psi_i(r_2) dr_2 \quad (1.26)$$

Since all terms that depend on the second electron in eqs. (1.25) and (1.26) are integrated out, the Fock operator effectively depends on a single electronic coordinate that shows up in the r_{12}^{-1} term. Eventually, the many-electron problem of a molecular system is turned in an effective one-electron problem in HF theory, whereas the interaction between the electrons is taken into account implicitly *via* an averaged, mean-field potential v^{HF} .

To be able to solve them numerically, the set of i spatio-integro-differential equations for the i MOs given in eq. (1.22) needs to be turned into a set of algebraic equations. For this purpose, the explicit mathematical structure of the MOs as linear combinations of atom-centered basis functions ϕ_μ (eq. 1.10) is inserted into eq (1.22). After left-multiplication with the complex conjugate of the respective basis functions and integration over the electronic coordinate r_1 the eigenvalues are isolated on the right hand side of the equation.

$$\sum_{\nu}^K C_{\nu i} \int dr_1 \phi_{\mu}^*(r_1) f(r_1) \phi_{\nu}(r_1) = \epsilon_i \sum_{\nu}^K C_{\nu i} \int dr_1 \phi_{\mu}^*(r_1) \phi_{\nu}(r_1) \quad (1.27)$$

In the resulting equation, one can identify the linear-combination coefficients that transform a set of AOs ϕ_{ν} into a set of MOs ψ_i as elements of a transformation matrix \mathbf{C} with the dimension $\nu \times i$. Since a linear combination of K AOs

always yields the same number of MOs, \mathbf{C} is usually a square matrix (exceptions occur if the basis functions are not linearly independent). Also, the integrals on the left and right hand sides of eq. (1.27) can be identified as elements of matrices of the same dimension:

$$\mathbf{F}_{\mu\nu} = \int dr_1 \phi_\mu^*(r_1) f(r_1) \phi_\nu(r_1) \quad (1.28)$$

$$\mathbf{S}_{\mu\nu} = \int dr_1 \phi_\mu^*(r_1) \phi_\nu(r_1) \quad (1.29)$$

Using these definitions of the so-called Fock matrix \mathbf{F} (1.28) and overlap matrix \mathbf{S} (1.29), the canonical Hartree-Fock equation (1.27) becomes

$$\sum_\nu \mathbf{F}_{\mu\nu} \mathbf{C}_{\nu i} = \epsilon_i \sum_\nu \mathbf{S}_{\mu\nu} \mathbf{C}_{\nu i}, \quad (1.30)$$

which is a set of coupled eigenvalue equations, that can be rewritten in matrix form

$$\mathbf{FC} = \epsilon \mathbf{SC}. \quad (1.31)$$

1.2.4 Self-Consistent Field Procedure

Assuming an orthonormal basis ($\mathbf{S} = \mathbf{1}$), the matrix equation (1.31) can be solved numerically by diagonalizing the Fock matrix. For this purpose, explicit expressions for the Fock-matrix elements are required and need to be evaluated. Since the Fock matrix is just the representation of the Fock operator (eq. 1.23) in the AO-basis, it may in analogy to the Fock operator be divided into a one-electron part, the so-called core-Hamiltonian H^{core} and a two-electron part termed G .

$$\mathbf{F}_{\mu\nu} = H_{\mu\nu}^{\text{core}} + G_{\mu\nu} \quad (1.32)$$

The expectation value of the core-Hamiltonian corresponds to the energy of independent electrons in the respective AO-basis functions ϕ_ν and ϕ_μ , which is the sum of the kinetic energy termed $T_{\mu\nu}$ and the electron-nuclear interaction $V_{\mu\nu}^{\text{nucl}}$.

$$H_{\mu\nu}^{\text{core}} = T_{\mu\nu} + V_{\mu\nu}^{\text{nucl}} \quad (1.33)$$

$$T_{\mu\nu} = \int \phi_\mu^*(1) \left[-\frac{1}{2} \nabla_1^2 \right] \phi_\nu(1) dr_1 \quad (1.34)$$

$$V_{\mu\nu}^{\text{nucl}} = \int \phi_\mu^*(1) \left[-\sum_A^N \frac{Z_A}{|r_1 - R_A|} \right] \phi_\nu(1) dr_1 \quad (1.35)$$

To arrive at an explicit expression for the core-Hamiltonian, one has to replace the generic functions ϕ_ν and ϕ_μ with the fixed linear combination of Gaussian functions that constitute an STO- n G basis set given in eqs. (1.8) and (1.9) and carry out the integration over the electronic coordinates. A detailed description of the analytical integration of one-electron integrals using common Gaussian basis functions can be found in appendix A of ref. 5. Inserting the system-specific values for the nuclear charges Z_A and distances determined by the molecular geometry into the integrated expressions yields a set of K^2 numbers corresponding to the matrix elements of $H_{\mu\nu}^{\text{core}}$. Apparently, the core-Hamiltonian does not depend on the linear combination coefficients collected in

the matrix $C_{\nu i}$. Since only the latter are varied during the SCF procedure, the core-Hamiltonian does not change and has to be calculated only once.

The two-electron part of the Fock matrix corresponds to the representation of the Coulomb and exchange operators given in eqs. (1.25) and (1.26) in the AO-basis set.

$$G_{\mu\nu} = \sum_i^n \int \phi_\mu^*(1) [\mathcal{J}_i(1) - \mathcal{K}_i(1)] \phi_\nu(1) dr_1 \quad (1.36a)$$

$$= \sum_i^n \int \phi_\mu^*(1) \left[\int \psi_i^*(2) (1 - \mathcal{P}_{12}) \frac{1}{|r_{12}|} \psi_i(2) dr_2 \right] \phi_\nu(1) dr_1 \quad (1.36b)$$

These equations describe the interaction of an electron in the AO-basis functions ϕ_ν and ϕ_μ with the molecular orbital ψ_i via the Coulomb and exchange operators. To obtain an explicit expression, ψ_i is expanded in atomic basis functions (eq. 1.10), which yields

$$\begin{aligned} G_{\mu\nu} &= \sum_i^n \int \phi_\mu^*(1) \left[\int \sum_\lambda C_{\lambda i} \phi_\lambda^*(2) (1 - \mathcal{P}_{12}) \frac{1}{|r_{12}|} \sum_\sigma C_{\sigma i} \phi_\sigma(2) dr_2 \right] \phi_\nu(1) dr_1 \\ &= \sum_{\lambda, \sigma} \sum_i^n C_{\lambda i} C_{\sigma i}^* \int \phi_\mu^*(1) \left[\int \phi_\lambda^*(2) (1 - \mathcal{P}_{12}) \frac{1}{|r_{12}|} \phi_\sigma(2) dr_2 \right] \phi_\nu(1) dr_1 \\ &= \sum_{\lambda, \sigma} \sum_i^n C_{\lambda i} C_{\sigma i}^* \int \int \phi_\mu^*(1) \phi_\nu(1) (1 - \mathcal{P}_{12}) \frac{1}{|r_{12}|} \phi_\lambda^*(2) \phi_\sigma(2) dr_2 dr_1 \end{aligned}$$

Apart from the summation over μ and ν as well as the respective linear-combination coefficients, this result can be identified as the two-electron energy of the Slater determinant given in eq. (1.18). Hence, the short-hand notation introduced in eq. (1.19) may be used to compact the equations yielding

$$G_{\mu\nu} = \sum_{\lambda, \sigma} \sum_i^n C_{\lambda i} C_{\sigma i}^* \langle \mu\nu || \lambda\sigma \rangle \quad (1.38a)$$

$$= \sum_{\lambda, \sigma} P_{\lambda\sigma} \langle \mu\nu || \lambda\sigma \rangle. \quad (1.38b)$$

In the lower equation, I have made use of the so-called (one particle reduced) density matrix $P_{\mu\nu}$. It allows for a mapping between an electron density $\rho(r)$ and the linear combination coefficients and moreover constitutes a powerful tool for the purpose of analyzing and interpreting results of HF and post-HF calculations. To derive this relation between a given electron density and the respective $C_{\nu i}$,

the density $\rho(r)$ is expanded in the AO-basis.

$$\rho(r) = \sum_i^n \psi_i^*(r) \psi_i(r) \quad (1.39a)$$

$$= \sum_i^n \sum_\nu C_{\nu i} \phi_\nu^*(r) \sum_\mu C_{\mu i} \phi_\mu(r) \quad (1.39b)$$

$$= \sum_{\nu, \mu} \left[\sum_i^{n/2} C_{\lambda i} C_{\sigma i}^* \right] \phi_\nu^*(r) \phi_\mu(r) \quad (1.39c)$$

$$= \sum_{\mu, \nu} P_{\mu\nu} \phi_\nu^*(r) \phi_\mu(r) \quad (1.39d)$$

To obtain explicit expressions for the so-called electron-repulsion integrals (ERIs) given in eq. (1.38) that constitute the two-electron part of the Fock operator, one inserts the explicit Gaussian basis functions and integrates the resulting terms over the electronic coordinates. Together with the system specific parameters as well as the the linear-combination coefficients, the explicit expressions afford numerical values for the elements of the Fock matrix. The computational effort for the evaluation of an ERI is comparable to that for the integrals of the core-Hamiltonian. However, due to the double summation over μ and ν , each of the K^2 elements of the Fock matrix apparently contains K^2 ERIs and consequently, a total of $K^4/8$ of these integrals has to be evaluated (the factor 8 is due to the permutation symmetry of the ERIs). Due to their sheer number, the evaluation of the ERIs constitutes the bottleneck of the HF-SCF procedure and determines the scaling of the HF-SCF calculation to be proportional to the fourth power of the number of primitive basis functions. Since furthermore the two-electron part of the Fock operator does in contrast to the one-electron part obviously depend on the linear combination coefficients, it has to be evaluated in every step.

Additionally, and this is one of the key aspects of Hartree-Fock, the dependence of the Fock operator (eq. 1.28) on the linear-combination coefficients or in other words the density matrix $\mathbf{P} = \mathbf{C}\mathbf{C}^\dagger$ introduces a non-linearity into the equations. Loosely spoken, the Fock operator turns a given set of MOs determined by \mathbf{C} into an effective averaged potential. Subsequent diagonalization of the Fock operator yields a new set of MOs (eigenvectors) as well as orbital energies (eigenvalues), which correspond their interaction. Including this non-linearity, the Roothaan equation becomes

$$\mathbf{F}(\mathbf{P}^i) \mathbf{C}^{i+1} = \epsilon^{i+1} \mathbf{S} \mathbf{C}^{i+1} . \quad (1.40)$$

As such, this non-linear equation has to be solved iteratively. For this purpose, the Fock matrix is build using an educated, initial guess (iteration $i = 0$) for the \mathbf{C}^i matrix, e.g. using the core-Hamiltonian or a superposition of pre-calculated atomic densities, which is mapped onto the coefficient matrix using the density matrix formalism (eq. 1.39). Presupposing an orthonormal basis (1.45), for which the overlap matrix is unity ($\mathbf{S} = \mathbf{1}$), a new, improved set of coefficients can be obtained by diagonalizing the Fock matrix

$$\mathbf{F}(\mathbf{P}^i) \mathbf{C}^{i+1} = \epsilon^{i+1} \mathbf{C}^{i+1} , \quad (1.41)$$

which yields the orbitals energy matrix ϵ^{i+1} and an updated set of coefficients (eigenvectors) \mathbf{C}^{i+1} . Using the latter, a new Fock matrix can be build and diagonalized. This procedure is repeated until the coefficients and/or the orbital energies are converged with respect to a certain threshold, which then correspond to the eigenfunctions of the Fock operator, the so-called HF-MOs.

For the above described procedure, an orthonormal set of basis functions was presupposed. Although, the basis functions of common atom-centered basis sets are normalized, they are not orthogonal and thus have to be orthogonalized prior to application of the above-described procedure. Since the orthogonalization of a set of basis functions is of general relevance for many quantum-chemical methods, I will describe and discuss orthogonalization schemes separately in section 1.3.

1.2.5 Practical Aspects

In practice, the above-described approach of iteratively building and diagonalizing the Fock operator until convergence is archived is neither numerically efficient nor stable. One major problem of this approach is that it tends to oscillate between solutions that are not eigenfunctions of the Fock operator. A common and efficient way to suppress these oscillations is to add to the latest eigenvectors of step n a number of k solutions from former steps

$$\mathbf{C}^n = \frac{1}{k} \sum_{i=0}^k \mathbf{C}^{n-i}, \quad (1.42)$$

which is the so-called damping. More involved schemes like the direct inversion of iterative subspace (DIIS) or the Newton-Raphson procedure systematically accelerate the convergence, e.g. by circumventing a complete recalculation of the Fock operator in every step. Since the computational effort for the diagonalization of the Fock operator scales with the third power of the number of basis functions, it may become the bottleneck of HF calculations for larger systems, in which many of the ERIs, whose evaluation usually constitutes the bottleneck, are zero. Hence, the development and evaluation of convergence accelerators is an active field of research. A recent comparison between various flavors of the DIIS method can be found in ref. 6.

After convergence of the SCF procedure, the eigenfunctions the Fock operator can be used to calculate the total Hartree-Fock energy. It corresponds to the expectation value of the HF wave function with respect to the Hamiltonian.

$$E^{\text{HF}} = \langle \Psi^0 | \mathcal{H} | \Psi^0 \rangle = \sum_i \langle i | h | i \rangle + \frac{1}{2} \sum_{i,j} \langle ij || ij \rangle = h_{ii} + \frac{1}{2} \sum_{i,j} \langle ij || ij \rangle. \quad (1.43)$$

Note that this expression is not equal to sum of orbital energies, or in other words the expectation value of the HF wave function with respect to the Fock operator (eqs. (1.22) and (1.23)). The difference between the two is a factor of one half in front of the two-electron part in eq. (1.43), which avoids double counting of the electron-electron interaction in the HF energy. Actually, the HF energy can be obtained as first-order energy when perturbation theory is applied to the HF solution as described in section 1.5.2, while the zeroth-order result corresponds to the sum of orbital energies.

Essentially, a HF-SCF calculation is an optimization of the linear expansion coefficients $C_{i\mu}$ of the atomic orbitals in order to obtain the set of MOs with the

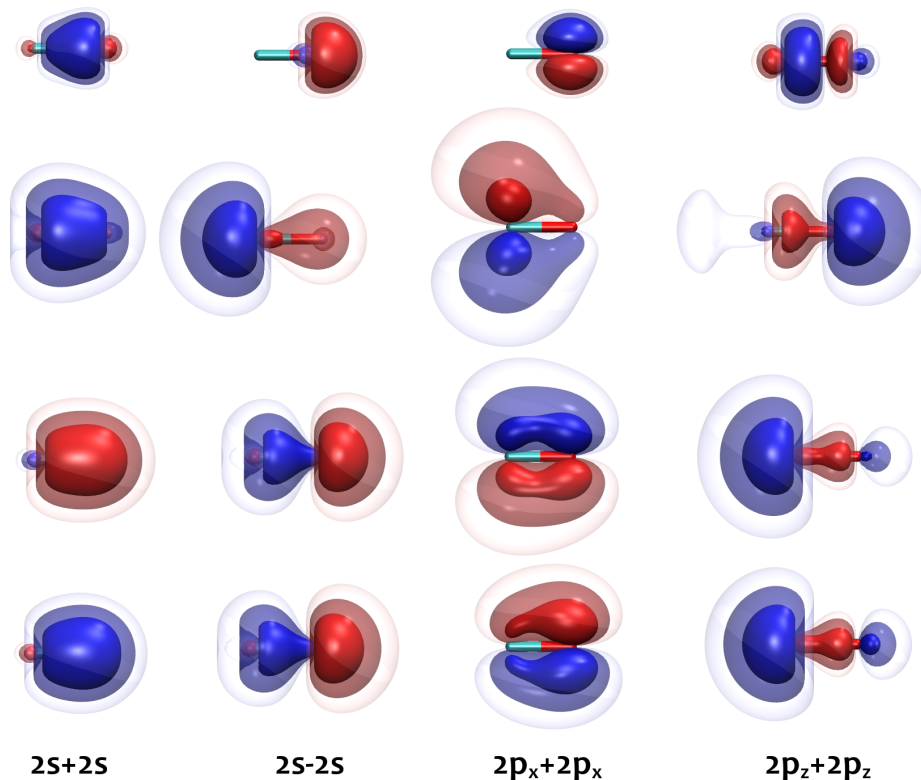


Figure 1.3: Selected valence molecular orbitals of CO (carbon left, oxygen right) during a HF-SCF/def2-TZVP calculation using the DIIS algorithm. The first row corresponds to the initial guess, which was in this case obtained using only the one-electron part of the Hamiltonian (H^{core}). Apparently, in absence of the inter-electronic repulsion the electrons accumulate at the oxygen atom due to its higher nuclear charge, which causes the oxygen atom to accumulate a (Mulliken) charge of -1.4 (Löwdin -2.1). In the first SCF step including also the mean-field potential depicted in the second row, this is over-corrected and the center of the electron-distribution is shifted to the carbon atom. Already the orbitals from the second step including v^{HF} shown in the third row closely resemble the final, converged MOs (after 12 further steps, convergence threshold 10^{-6} Hartree) shown in the last row. This can be regarded as a demonstration of the efficiency of the DIIS algorithm. Note that the phases of the orbitals change randomly during the calculation and the coloring is thus inconsistent.

lowest energy. Hence, the accuracy of the result but also the dimensionality of the problem and in turn the computational effort for its numerical solution grows with the number of primitive basis functions. The effort depends on both, the number of Gaussian functions n combined to STO- n G functions, which is the so-called contraction depth, as well as the number m of STO- n G functions used to describe each molecular orbital (see section 1.2.1). While the number of primitive functions only affects the number of ERIs that have to be evaluated in an SCF calculation, the number of contracted functions determines the dimensionality of the SCF problem (\mathbf{C} matrix), since the respective linear combination coefficients are optimized during the SCF procedure.

Since the flexibility of the basis set is critical for the accuracy of the calculation, it is practice to make use of at least two independent, contracted basis functions for each valence orbital, even in exploratory calculations. Such a basis set is called a split-valence or double- ζ basis. Furthermore, since Gaussians are so cheap to integrate, typical fixed STO- n G type linear combinations involve 5 primitive functions for a single carbon $1s$ orbital and two more, uncontracted functions for the $2s$ valence orbital (def2-SV: $(7s, 4p) \rightarrow [3s, 2p]$, number of primitive functions in parenthesis, number of contracted function in brackets). To obtain accurate results close to the basis-set limit, one should at least employ thoroughly polarized triple- ζ basis sets (e.g. def2-TZVP, for carbon $(11s, 6p, 2d, 1f) \rightarrow [5s, 3p, 2d, 1f]$). Polarization functions are of higher angular momentum, e.g. the d and f functions for the carbon $2p$ -orbital in the def2-TZVP set, which allows to shift (polarize) the orbital. A detailed description of polarization and also diffuse functions can be found in chapter 3.6 of ref. 5. A brief and instructive discussion focusing on the practical aspects can be found in chapter 7 of the manual of the ORCA 3.0.1 program package.⁷

To this point, I have only discussed the electronic part of the wave function and neglected the constant nuclear repulsion as well as the kinetic energy of the nuclei (1.2c). Adding back in the nuclear repulsion one arrives at the so-called electronic energy at the Hartree-Fock level of theory for a given basis set, abbreviated e.g. HF/STO-3G. Since HF is variational, this number corresponds to an upper limit for the energy of the given number of electrons in the nuclear arrangement compared to the situation where all these particles are at infinite distance to each other.

For an actual molecule at any temperature, this electronic energy neglects the kinetic energy stored in the nuclear degrees of freedom, which can be split up into translational, rotational and vibrational contributions. Even at zero temperature, the kinetic energy of the nuclei is non-zero, which is due to the zero-point vibration. A calculation of the kinetic energy of the nuclei requires information about the shape of the potential-energy surface, which needs the first and second derivatives of the electronic energy with respect to the nuclear coordinates to be evaluated. Since the computational effort for the evaluation of these derivatives is much higher than for the HF calculation itself, the kinetic energy of the nuclei is often neglected.

1.3 Orthogonalization Schemes

Apparently, atom-centered STO- n G basis functions (eq. 1.9) do overlap when placed in a molecular system. Their overlap gives rise to the overlap matrix

$$\int \phi'_i(r)^* \phi'_j(r) dr = S_{ij} , \quad (1.44)$$

which shows up in the Roothaan equation (1.27). For an orthonormal basis the overlap becomes a delta function

$$\int \phi_\mu(r)^* \phi_\nu(r) dr = \delta_{\mu\nu} , \quad (1.45)$$

and consequently the overlap-induced inhomogeneity in the Roothaan equation vanishes ($\mathbf{S} = \mathbf{1}$) and it becomes a simple eigenvalue equation. Hence, it is desirable to orthogonalize the basis in a SCF calculation. For this purpose, a number of methods exist, of which I will discuss the intuitive, sequential Gram-Schmidt scheme and afterwards the so-called symmetric orthonormalization.

1.3.1 Gram-Schmidt

The concept of the Gram-Schmidt scheme is to obtain a set of n orthogonal basis functions ϕ_μ from a non-orthonormal, linearly independent set of n functions ϕ'_i . For this purpose, the normalized overlap ($|\phi_n\rangle\langle\phi_i|\phi_i\rangle^{-1}$) between the functions of the old set is subsequently subtracted using the projection operator $\hat{P}_{i'} = |\phi'_i\rangle\langle\phi'_i|$.

$$\phi_1 = \phi'_1 \quad (1.46a)$$

$$\phi_2 = \phi'_2 - |\phi'_1\rangle \frac{\langle\phi'_1|\phi'_2\rangle}{\langle\phi'_1|\phi'_1\rangle} \quad (1.46b)$$

$$\phi_n = \phi'_n - \sum_{i=1}^{n-1} |\phi'_i\rangle \frac{\langle\phi'_i|\phi'_n\rangle}{\langle\phi'_i|\phi'_i\rangle} \quad (1.46c)$$

The simplicity of this scheme is compromised by disadvantages, which are due to its sequential character. Since each of the original basis functions is treated separately and changed by a different amount, the Gram-Schmidt procedure fails to preserve many properties (e.g. symmetry) of the original basis. This renders the scheme impractical for the use in the SCF procedure, or more general when a class of equivalent basis functions has to be orthogonalized against each other. If, however, there are different classes of basis functions that have to be orthogonalized against each other, like e.g. those forming singly, doubly and n -tuply excited determinants in eq. (1.16), the scheme may be well-suited.

1.3.2 Symmetric Orthonormalization

In contrast to Gram-Schmidt, the symmetric orthonormalization does preserve many properties of the original basis. This is achieved by transforming all basis functions using the same transformation matrix \mathbf{X} , whose structure can be derived from a systematic analysis of the problem. Obviously, one wants to

transform the non-orthogonal basis function ϕ'_i into a set of orthogonal functions ϕ_μ , which may be achieved by multiplication with the a transformation matrix \mathbf{X}

$$\phi_\mu = \sum_{\mu} X_{\mu i} \phi'_i . \quad (1.47)$$

Substituting this transformation in the expression for the overlap one obtains

$$\int \phi'_i(r)^* \phi'_j(r) dr = \int \sum_{\mu} X_{\mu i}^* \phi_\mu^*(r) \sum_{\nu} X_{\nu j} \phi_\nu(r) dr \quad (1.48a)$$

$$= \sum_{\mu, \nu} X_{\mu i}^* \int \phi_\mu^*(r) \phi_\nu(r) dr X_{\nu j} \quad (1.48b)$$

$$= \sum_{\mu, \nu} X_{\mu i}^* S_{\mu \nu} X_{\nu j} = \delta_{ij} \quad (1.48c)$$

$$= \mathbf{X}^\dagger \mathbf{S} \mathbf{X} = \mathbf{1} , \quad (1.48d)$$

where the last line contains the requirements for the transformation matrix. Supposing a set of linearly independent basis functions as well as $\mathbf{X} = \mathbf{X}^\dagger \neq \mathbf{0}$, multiplication with \mathbf{X}^{-1} from both sides yields

$$\mathbf{S} = \mathbf{X}^{-2} \quad (1.49a)$$

$$\mathbf{X}^2 = \mathbf{S}^{-1} \quad (1.49b)$$

$$\mathbf{X} = \mathbf{S}^{-1/2} . \quad (1.49c)$$

Apparently, the inverse square root of the overlap matrix is a suitable transformation matrix. Hence, to transform a non-orthogonal basis set into an orthogonal one, the overlap matrix has to be diagonalized, manipulated and re-transformed to obtain the transformation matrix $\mathbf{S}^{-1/2}$.

1.4 Configuration Interaction

1.4.1 Electron Correlation

The concept underlying configuration interaction has already been brought up in the discussion about a formally exact ansatz for the wave function in section 1.2.2, eq. (1.16). In full configuration interaction (FCI), the exact ground-state wave function Φ^0 is represented as a linear combination of all possible permutations of n electrons in the $2K$ spin-orbitals of the HF wave function Ψ_0^{HF}

$$\Phi^0 = c_0 \Psi_0^{\text{HF}} + \sum_{i,a} c_i^a \Psi_i^a + \sum_{i>j,a>b} c_{ij}^{ab} \Psi_{ij}^{ab} + \dots, \quad (1.50)$$

where the permutations are referred to as *configurations* $\Psi_\mu \in \{\Psi_i^a, \Psi_{ij}^{ab}, \dots\}$, with the indices i, j, k, l referring to the occupied orbitals and a, b, c, d to the virtual orbitals that have been exchanged in the respective configuration.

Since the eigenfunctions (MOs) of a hermitian operator (Fock operator, which is hermitian for real basis functions) form a complete basis, one can represent the exact solution as linear combination of all possible configurations. Hence FCI is, in theory, exact within the respective set of AO-basis functions employed in a calculation. However, FCI has serious practical limitations due to the huge number of configurations, which amount to

$$\binom{2K}{n} = \frac{2K!}{(2K-n)!n!} \quad (1.51)$$

when permutation symmetry like e.g. $\Psi_{ij}^{ab} = \Psi_{ji}^{ab}$ is neglected. Even with permutation symmetry, this number is very large already for diatomic molecules with a decent polarized double- ζ basis set. Consequently FCI is impractical for an investigation of chemically relevant systems. Nevertheless, since the procedure yields the exact correlation energy for a given set of basis functions, FCI can be used as a benchmark to evaluate the quality of efficient, approximate approaches to calculate the correlation energy, e.g. perturbation theoretical approaches or truncated CI schemes like CI singles and doubles (CISD), like e.g. in ref. 8.

The derivation of an expression for the FCI energy follows the same scheme that was applied in case of HF theory. Application of functional variation to minimize the energy of eq. (1.16) with respect to the linear combination coefficients yields the FCI matrix. Using the following short-hand notation indicated in the following

$$c_0 \Psi^0 = c_0 0 \quad (1.52a)$$

$$\sum_{i,a} c_i^a \Psi_i^a = c_s S \quad (1.52b)$$

$$\sum_{i,j,a,b} c_{ij}^{ab} \Psi_{ij}^{ab} = c_d D, \quad (1.52c)$$

the general structure of the CI matrix is

$$\begin{pmatrix} \langle 0|\mathcal{H}|0\rangle & \langle 0|\mathcal{H}|S\rangle & \langle 0|\mathcal{H}|D\rangle & \langle 0|\mathcal{H}|T\rangle & \langle 0|\mathcal{H}|Q\rangle & \cdots \\ \langle S|\mathcal{H}|0\rangle & \langle S|\mathcal{H}|S\rangle & \langle S|\mathcal{H}|D\rangle & \langle S|\mathcal{H}|T\rangle & \langle S|\mathcal{H}|Q\rangle & \cdots \\ \langle D|\mathcal{H}|0\rangle & \langle D|\mathcal{H}|S\rangle & \langle D|\mathcal{H}|D\rangle & \langle D|\mathcal{H}|T\rangle & \langle D|\mathcal{H}|Q\rangle & \cdots \\ \langle T|\mathcal{H}|0\rangle & \langle T|\mathcal{H}|S\rangle & \langle T|\mathcal{H}|D\rangle & \langle T|\mathcal{H}|T\rangle & \langle T|\mathcal{H}|Q\rangle & \cdots \\ \langle Q|\mathcal{H}|0\rangle & \langle Q|\mathcal{H}|S\rangle & \langle Q|\mathcal{H}|D\rangle & \langle Q|\mathcal{H}|T\rangle & \langle Q|\mathcal{H}|Q\rangle & \cdots \\ \vdots & \vdots & \vdots & \vdots & \vdots & \ddots \end{pmatrix}. \quad (1.53)$$

In this matrix, each of the integrals $\langle I|\mathcal{H}|J\rangle$ represents a block of elements, whose size is determined by the number of configurations in I times the number of configurations in J . Hence, while $\langle 0|\mathcal{H}|0\rangle$ corresponds to a single element, the singles/singles block itself is a square matrix of the dimension $i \times a$, the doubles/doubles block $i^2 \times a^2$ and so on, where I have for once used i and a as the number of occupied and virtual orbitals instead of the indices. Obviously, this matrix needs to be truncated in order to deal with it on a real computer in practical time. But first, one can make use of the fact that many of the off-diagonal blocks are zero, which simplifies the matrix. According to the Slater-Condon rules, matrix elements for a two-particle operator like the Hamiltonian between configurations that differ by more than two spin-orbitals are zero

$$\langle 0|\mathcal{H}|T\rangle = \langle T|\mathcal{H}|0\rangle = 0, \langle S|\mathcal{H}|Q\rangle = \langle Q|\mathcal{H}|S\rangle = 0. \quad (1.54)$$

Furthermore, Brillouin's theorem states that singly excited determinants do not mix with the HF ground state

$$\langle 0|\mathcal{H}|S\rangle = \langle S|\mathcal{H}|0\rangle = 0, \quad (1.55)$$

and in turn the CI matrix becomes a diagonally dominated matrix

$$\begin{pmatrix} \langle 0|\mathcal{H}|0\rangle & 0 & \langle 0|\mathcal{H}|D\rangle & 0 & 0 & 0 \\ 0 & \langle S|\mathcal{H}|S\rangle & \langle S|\mathcal{H}|D\rangle & \langle S|\mathcal{H}|T\rangle & 0 & 0 \\ \langle D|\mathcal{H}|0\rangle & \langle D|\mathcal{H}|S\rangle & \langle D|\mathcal{H}|D\rangle & \langle D|\mathcal{H}|T\rangle & \langle D|\mathcal{H}|Q\rangle & 0 \\ 0 & \langle T|\mathcal{H}|S\rangle & \langle T|\mathcal{H}|D\rangle & \langle T|\mathcal{H}|T\rangle & \langle T|\mathcal{H}|Q\rangle & \ddots \\ 0 & 0 & \langle Q|\mathcal{H}|D\rangle & \langle Q|\mathcal{H}|T\rangle & \langle Q|\mathcal{H}|Q\rangle & \ddots \\ 0 & 0 & 0 & \ddots & \ddots & \ddots \end{pmatrix}. \quad (1.56)$$

In order to obtain an expression for the FCI correlation energy, the respective FCI wave function is inserted into the Schrödinger equation and the HF energy is subtracted, which yields

$$(\mathcal{H} - E^{\text{HF}})|\Phi^0\rangle = (\mathcal{E} - E^{\text{HF}})|\Phi^0\rangle \quad (1.57a)$$

$$(\mathcal{H} - E^{\text{HF}})|c_0\Psi^0 + \sum_{i,a} c_i^a \Psi_i^a + \sum_{i,j,a,b} c_{ij}^{ab} \Psi_{ij}^{ab} + \cdots\rangle = E_{\text{corr}}|\Phi^0\rangle. \quad (1.57b)$$

Presupposing so-called intermediate normalization $\langle \Psi^0|\Phi^0\rangle = 1$ and consequently $\langle \Psi^0|\Psi_\mu\rangle = 0$ (for more detail see eq. (1.71) and the following), left

multiplication with the HF reference yields the correlation energy on the right hand side of the equation. On the left hand side of the equation the HF energy cancels out, the terms involving singly excited configurations are zero because of Brillouin's theorem as well as all terms involving triply- and higher-excited configurations due to Slater-Condon rules.

$$\langle \Psi^0 | (\mathcal{H} - E^{\text{HF}}) | c_0 0 + c_s S + c_d D + \dots \rangle = E_{\text{corr}} \langle \Psi^0 | \Phi^0 \rangle \quad (1.58a)$$

$$c_0 (\langle 0 | \mathcal{H} | 0 \rangle - E^{\text{HF}}) + c_s \langle 0 | \mathcal{H} | S \rangle + c_d \langle 0 | \mathcal{H} | D \rangle + \dots = E_{\text{corr}} \quad (1.58b)$$

$$c_d \langle 0 | \mathcal{H} | D \rangle = E_{\text{corr}} \quad (1.58c)$$

$$\sum_{i,j,a,b} c_{ij}^{ab} \langle \Psi^0 | \mathcal{H} | \Psi_{ij}^{ab} \rangle = E_{\text{corr}} \quad (1.58d)$$

Apparently, and this is a very general and important result, only doubly excited configurations contribute to the ground-state energy weighted by the respective linear combination coefficients, which in this context are referred to as amplitudes. In turn, all that is required to compute the exact energy are the doubles amplitudes. To obtain a conditional equation for these amplitudes, eq. (1.57) is left-multiplied with the doubly excited configurations and E^{HF} is replaced by \mathcal{E} , yielding

$$\langle D | (\mathcal{H} - \mathcal{E}) | c_0 0 + c_s S + c_d D + \dots \rangle = 0 \quad (1.59a)$$

$$c_0 \langle D | \mathcal{H} | 0 \rangle + c_s \langle D | \mathcal{H} | S \rangle + c_d \langle D | \mathcal{H} - \mathcal{E} | D \rangle + c_t \langle D | \mathcal{H} | T \rangle + \dots = 0. \quad (1.59b)$$

It turns out that the doubles amplitudes c_d are coupled to all other singles, triples etc. amplitudes and consequently, to compute the FCI energy according to eq. (1.58), one has to solve a coupled system of n equations for all n singles, n^2 doubles, n^3 triples amplitudes etc., whereas n is the highest possible excitation in the system, which in case of FCI is equal to the number of electrons. Since this is not practical, all CI and CI-related methods for the calculation of correlation energy of actual molecules are truncated. Since only doubly-excited configuration contribute to the correlation energy, truncated CI methods are in general approximate approaches to compute doubles amplitudes. In CI Singles and Doubles (CISD), for example, the first three terms in eq. (1.59b) are kept while all terms involving triply- and higher-excited determinants are neglected.

Although the computational effort for a CISD calculation is large compared to the preceding HF-SCF calculation, it recovers a large fraction of about 95% of the correlation energy of small molecules near the equilibrium geometry (compared to FCI).⁸ More importantly, the CISD energy represents an upper boundary to the exact energy, *i.e.* CISD is variational. For molecular arrangements far from the equilibrium structure, however, e.g. in bond-breaking situations, the influence of quadruply excited determinants (onto the doubles amplitudes) has to be taken into account, which corresponds to CISDTQ. In a nutshell, the reason is that far from the equilibrium geometry, doubly excited determinants become near-degenerate to the HF ground state and are thus important, which means large values for c_{ij}^{ab} show up in the expansion eq. (1.16). In analogy to the HF ground state, which is correlated *via* an inclusion of doubly excited determinants, doubly excited determinants themselves are correlated *via* quadruply excited determinants. Eventually, the fraction of the correlation energy recovered with CISD drops sharply as one moves away from the equilibrium, while the fraction recovered by CISDTQ is very constant at about 99%.⁸ Compared

to doubly and quadruply excited determinants, the singly- and triply-excited determinants are not as important for the ground-state energy. They are, however, very relevant for the correlation of singly-excited determinants, which build electronically excited states. Unfortunately, CISDTQ and even CISDT are impractical for most chemically relevant problems due to their immense computational cost.

Apart from the appealing properties of being conceptually simple and variational, truncated CI approaches have a fundamental drawback. They are not size-consistent, which means the correlation energy is not extensive with respect to system size. This problem is a result of the excitation-level based truncation scheme and may be illustrated for a calculation of a dimer compared to the calculation of the monomer. Since a double-excitation of both monomers corresponds to a quadruple excitation of the respective dimer, the calculation of the dimer is truncated differently than the calculation of the monomer. Since size-consistency seriously complicates many investigations of chemical problems, truncated CI is hardly used in practice. Instead, size consistent post-HF methods are used, such as related quadratic configuration interaction (QCI) or coupled-cluster (CC), or many-body perturbation theory (MBPT), which are size consistent, but no longer variational.

1.4.2 Excited States *via* CIS

Apart from the application to the electronic ground state, CI can be used to describe electronically excited states,⁹ which can be identified as the higher eigenvalues and respective eigenvectors of the CI matrix. If the CI matrix is truncated after single excitations, the resulting CI singles (CIS) method is, in contrast to any other truncated CI scheme, size consistent. The formalism of CIS is related to HF in the sense that the aim of both methods is to find a diagonal, first-order representation of the Hamiltonian. In contrast to HF, the CIS problem is linear, since the Hamiltonian is independent of the basis of singly-excited HF determinants. The respective part of the FCI matrix given in eq. (1.56) is the 2×2 matrix in the top left corner. Expanding the block represented by $\langle S|\mathcal{H}|S\rangle$ yields the CIS matrix, which is hermitian if, as usual, real basis functions are employed.

$$\begin{pmatrix} \langle \Psi^0|\mathcal{H}|\Psi^0\rangle & 0 & 0 & \dots \\ 0 & \langle \Psi_i^a|\mathcal{H}|\Psi_i^a\rangle & \langle \Psi_j^b|\mathcal{H}|\Psi_i^a\rangle & \dots \\ 0 & \langle \Psi_i^a|\mathcal{H}|\Psi_j^b\rangle & \langle \Psi_j^b|\mathcal{H}|\Psi_j^b\rangle & \dots \\ \vdots & \vdots & \vdots & \ddots \end{pmatrix} \quad (1.60)$$

Because of Brillouin's theorem, the HF ground state does not couple to any of the CIS excited states and all the respective coupling elements are zero. On the diagonal, one finds matrix elements of the form

$$\langle \Psi_i^a|\mathcal{H}|\Psi_i^a\rangle = E^{\text{HF}} - h_{ii} + h_{aa} - \sum_k \langle ki||ki\rangle + \sum_k \langle ka||ka\rangle - \langle ia||ia\rangle \quad (1.61a)$$

$$= E^{\text{HF}} - F_{ii} + F_{aa} - \langle ia||ia\rangle \quad (1.61b)$$

$$= E^{\text{HF}} - \epsilon_i + \epsilon_a - \langle ia||ia\rangle, \quad (1.61c)$$

which apparently correspond to the energy of a HF determinant with all interactions of an electron in i replaced by those of an electron in a .

Furthermore, there are off-diagonal elements that couple singly excited determinants, which may differ by one or two indices, yielding

$$\langle \Psi_i^a | \mathcal{H} | \Psi_i^b \rangle = h_{ab} + \sum_{k \in \{\text{occ}\} \setminus \{i\}} \langle ak || bk \rangle = F_{ab} - \langle ai || bi \rangle \quad (1.62a)$$

$$\langle \Psi_i^a | \mathcal{H} | \Psi_j^a \rangle = h_{ij} + \sum_{k \in \{\text{occ}\} \cup \{a\}} \langle ik || jk \rangle = -F_{ij} - \langle ia || ja \rangle \quad (1.62b)$$

$$\langle \Psi_i^a | \mathcal{H} | \Psi_j^b \rangle = \langle aj || ib \rangle, \quad (1.62c)$$

where the off-diagonal elements of the Fock matrix F_{ij} and F_{ab} are zero for HF references (Brillouin's theorem). Using Kronecker deltas and supposing the orbitals to be real-valued ($\langle aj || ib \rangle = -\langle ja || ib \rangle$), one obtains the following general expression

$$\langle \Psi_i^a | \mathcal{H} | \Psi_j^b \rangle = E^{\text{HF}} \delta_{ij} \delta_{ab} - F_{ij} \delta_{ab} + F_{ab} \delta_{ij} - \langle aj || ib \rangle, \quad (1.63)$$

and for the special case of a closed-shell HF reference

$$\langle \Psi_i^a | \mathcal{H} | \Psi_j^b \rangle = E^{\text{HF}} \delta_{ij} \delta_{ab} + (\epsilon_a - \epsilon_i) \delta_{ij} \delta_{ab} - \langle aj || ib \rangle. \quad (1.64)$$

Since all diagonal matrix elements of the CIS matrix apparently contain the HF energy, one may subtract it prior to diagonalization, which yields the shifted CIS matrix. The eigenvalues and eigenvectors of the shifted CIS matrix only correspond to excitation energies and excited-state wave functions. For a closed-shell HF reference, the CIS excitation energy of an excited state I denoted ω_I can be expressed as a function of the singles amplitudes

$$\omega_I = \sum_{i,a} (\chi_I^{ia})^2 (\epsilon_a - \epsilon_i) + \sum_{i,j,a,b} \chi_I^{ia} \chi_I^{jb} \langle aj || ib \rangle. \quad (1.65)$$

Carrying out the summation over the amplitudes for each MO, the last term in this expression yields the interaction of the excited electron and the "hole" it left behind. Supposed there exists an excited state which is fully characterized by a single-orbital transition and thus $i = j = n$ (highest occupied molecular orbital, HOMO) and $a = b = (n+1)$ (lowest unoccupied molecular orbital, LUMO) with $\chi_I^{ia} = \chi_I^{jb} = 1$, with all other amplitudes being zero. For such a state, the term below corresponds to the inverse of the interaction of an electron in orbital a with an electron in i ,

$$\langle ia || ia \rangle = \langle ia | ia \rangle - \langle ia | ai \rangle, \quad (1.66)$$

which has been discussed in detail in eq. (1.18). If furthermore, electron and hole are regarded as quasi-particle, the so-called exciton,¹⁰ this term can be regarded as the exciton binding energy. This picture of excitons is often used in the field of organic semiconductors and photovoltaics. Apparently, the exciton binding energy depends on the overlap of the involved orbitals as well as their distance. For large i - a separations the exchange-like term of the anti-symmetrized integral becomes zero and in turn the exciton binding energy approaches the classical Coulomb interaction between a positive (hole) and a negative charge (electron).

Eventually, the problem that remains is to find the excited-state vectors x_I consisting of the respective amplitudes χ_I^{ia} that diagonalize the CIS matrix.

Usually one is interested in the lowest eigenvectors and the corresponding eigenvalues that correspond to the first excitation energies. In matrix form, the CIS eigenvalue problem can be written as

$$\mathbf{HX} = \mathbf{X}\omega, \quad (1.67)$$

where \mathbf{X} is the matrix whose columns correspond to the excited-state vectors x_I . For the purpose of calculating the lowest eigenvalues and corresponding eigenvectors of large matrices, iterative, numerical approaches like the Davidson¹¹ or Lanczos¹² algorithms exist. Common to these approaches is that they iteratively build the state vectors from an initial set of guess vectors. An obvious choice for such a guess vector would be the HOMO to LUMO transition. During the actual procedure, these guess vectors are optimized iteratively by including additional columns until a convergence is achieved.

Since the virtual orbital energies from HF calculations are obtained for the $n + 1$ electron system, the orbital energy difference as zeroth-order term in the CIS equations yields too high excitation energies. Although the change of the interactions of the excited electron itself, or in other words the exciton binding energy is accounted for, the relaxation of the remaining electrons is neglected at the CIS level of theory. Hence, CIS excitation energies are usually too high, which can e.g. be seen for nitrobenzene in fig. 4.3. However, the error of CIS is usually systematic and foreseeable. The only case for which CIS completely fails are doubly (and higher) excited states, in which two (or more) electrons are promoted to virtual orbitals at once. This is a result of the absence of the respective, doubly excited determinants in the CIS matrix.

A nearby solution to improve the accuracy of CIS would be to include higher excited configurations, like e.g. doubles and triples yielding CISD and CISDT, respectively. However this would not only increase the computational cost, but also and more importantly sacrifice the size-consistency of the method. Hence, despite the great success of CIS-based methods, CISD and higher-order variants are hardly used in practice, neither for correlated ground-state calculations, nor for the description of electronically excited states. To conserve the size-consistency of CIS, the CIS vectors can be corrected perturbatively like e.g. in CIS(D), which constitutes an *a posteriori* correction to the CIS excitation energies (eigenvalues). The state vectors themselves, however, remain unaltered. An alternative approach that also improves the state vectors or in other words the excited-state wave function can be obtained by postulating an orthonormal basis of correlated, n -tuply excited determinants, the so-called intermediate-state basis. The resulting approach is termed intermediate-state representation (ISR) and is conceptually related to CI differing only in the basis of determinants. For the ISR of first order, the two methods coincide. For higher orders, the respective, correlated basis functions for the matrix elements are obtained *via* perturbation theory and subsequent orthonormalization. Because of its first derivation using diagrammatic techniques, this method is also termed algebraic-diagrammatic construction (ADC) of n^{th} order. To create a framework for the discussion of ISR/ADC in section 1.6, I will introduce many-body perturbation theory and its application to HF in the next section.

1.5 Many-Body Perturbation Theory

By means of many-body perturbation theory (MBPT), one may derive an approach to calculate the correlation energy for an arbitrary, uncorrelated reference state. Here, I will first introduce the general concept termed Rayleigh-Schrödinger perturbation theory (RSPT) up to second order and then apply it to the HF ground state, which yields a perturbative estimate of electron-correlation, which is referred to as Møller-Plesset perturbation theory (MP). Moreover, by combining the concepts of RSPT and the shifted CI matrix, one can derive the intermediate-state representation (ISR), which is more efficient and practical method for calculation of correlated excited states than CI itself. The ISR formalism is described in section 1.6.

1.5.1 General Rayleigh-Schrödinger Perturbation Theory

The general concept of RSPT is a partitioning of the exact Hamiltonian \mathcal{H} into two parts. The first part \hat{H}_0 , whose exact eigenfunctions are known and the second part \hat{V} , which resembles the so-called perturbation.

$$\mathcal{H}|\Phi_i\rangle = (\hat{H}_0 + \hat{V})|\Phi_i\rangle = \mathcal{E}_i\Phi_i \quad (1.68)$$

If the perturbation and consequently the difference between the exact and approximate eigenfunctions is small, perturbation theory usually works very well and exhibits fast convergence to the exact result. If, however, the reference (the i^{th} of the complete set of eigenfunctions f of \hat{H}_0 depicted $f_i^{(0)} \equiv i^{(0)}$) is qualitatively wrong and in turn the perturbation is large, RSPT may not work at all and the perturbation series may oscillate or diverge. To improve the eigenvalues of a well-behaved reference using RSPT, one introduces the formal ordering parameter λ into the Hamiltonian

$$\mathcal{H} = \hat{H}_0 + \lambda\hat{V} , \quad (1.69)$$

and develops the eigenvalues and eigenfunction Φ_i of the exact Hamiltonian in a Taylor series

$$\mathcal{E}_i = E_i^{(0)} + \lambda E_i^{(1)} + \lambda^2 E_i^{(2)} \quad (1.70a)$$

$$|\Phi_i\rangle = |i^{(0)}\rangle + \lambda|i^{(1)}\rangle + \lambda^2|i^{(2)}\rangle . \quad (1.70b)$$

To compute the n^{th} order corrections to eigenvalues and eigenfunctions, these quantities have to be expressed in terms of the known, unperturbed (zeroth-order) reference wave function. For the following derivations, it will prove very helpful to invoke intermediate normalization

$$\langle i^{(0)}|\Phi_i\rangle = 1 . \quad (1.71)$$

Since also the zeroth-order wave function is normalized

$$\langle i^{(0)}|i^{(0)}\rangle = 1 , \quad (1.72)$$

the unperturbed wave function has to be orthogonal to any of the higher-order eigenfunctions, which becomes evident from left-multiplication of eq. (1.70b) with $\langle i^{(0)}|$

$$\langle i^{(0)}|\Phi_i\rangle = \langle i^{(0)}|i^{(0)}\rangle + \lambda\langle i^{(0)}|i^{(1)}\rangle + \lambda^2\langle i^{(0)}|i^{(2)}\rangle . \quad (1.73)$$

For this equation to hold, $\langle i^{(0)} | i^{(n)} \rangle$ has to be zero.

Eventually, Taylor expansion given in eq. (1.70) is inserted into the respective Schrödinger eq. (1.68). Sorting the resulting terms according to the order in perturbation represented by the exponent of λ , one arrives at the following relations between the n^{th} order eigenvalues and eigenfunctions

$$\hat{H}_0 |i^{(0)}\rangle = E_i^{(0)} |i^{(0)}\rangle \quad (1.74a)$$

$$\hat{H}_0 |i^{(1)}\rangle + \hat{V} |i^{(0)}\rangle = E_i^{(0)} |i^{(1)}\rangle + E_i^{(1)} |i^{(0)}\rangle \quad (1.74b)$$

$$\hat{H}_0 |i^{(2)}\rangle + \hat{V} |i^{(1)}\rangle = E_i^{(0)} |i^{(2)}\rangle + E_i^{(1)} |i^{(1)}\rangle + E_i^{(2)} |i^{(0)}\rangle . \quad (1.74c)$$

Each of these equations is left-multiplied with $|i^{(0)}\rangle$, which in combination with the intermediate normalization yields expressions for the n^{th} order energy

$$E_i^{(0)} = \langle i^{(0)} | \hat{H}_0 |i^{(0)}\rangle \quad (1.75a)$$

$$E_i^{(1)} = \langle i^{(0)} | \hat{V} |i^{(0)}\rangle \quad (1.75b)$$

$$E_i^{(2)} = \langle i^{(0)} | \hat{V} |i^{(1)}\rangle . \quad (1.75c)$$

The n^{th} order energy correction can be obtained from the $(n-1)$ order wave function. However, since only the eigenfunctions of the unperturbed Hamiltonian, or in other words the zeroth-order eigenfunctions $f^{(0)}$ are known, the higher-order wave functions have to be expressed in terms of the zeroth-order quantities. For this purpose, eq. (1.74b) is rearranged such that the first-order wave function is isolated on the left-hand side

$$(E_i^{(0)} - \hat{H}_0) |i^{(1)}\rangle = (\hat{V} - E_i^{(1)}) |i^{(0)}\rangle . \quad (1.76)$$

Remembering the eigenfunctions of zeroth-order Hamiltonian form a complete, orthonormal basis, one can attempt to express first-order wave function of the i^{th} eigenfunction of the exact Hamiltonian \mathbf{H} in terms of the eigenfunctions of the unperturbed Hamiltonian \hat{H}_0 .

$$|i^{(1)}\rangle = \sum_k c_{ki}^{(1)} |f_k^{(0)}\rangle , \quad (1.77)$$

where the expansion coefficients are determined by left-multiplying this equation with the respective eigenfunctions

$$\langle f_k^{(0)} | i^{(1)} \rangle = c_{ki}^{(1)} . \quad (1.78)$$

Due to intermediate normalization, the i^{th} coefficient is zero and may thus be excluded from the summation. Inserting the definition of the coefficients from above yields

$$|i^{(1)}\rangle = \sum_{k \setminus \{i\}} |f_k^{(0)}\rangle \langle f_k^{(0)} | i^{(1)} \rangle . \quad (1.79a)$$

Next, left-multiplication of eq. (1.76) with the n^{th} zeroth-order eigenfunction $f_n^{(0)} \equiv n^{(0)}$ eliminates the first-order energy on the right-hand side of the equation due to orthogonality of the eigenfunctions. Subsequently, the expansion of

the first-order wave function is inserted

$$\langle n^{(0)} | E_i^{(0)} - \hat{H}_0 | i^{(1)} \rangle = \langle n^{(0)} | (\hat{V} - E_i^{(1)}) | i^{(0)} \rangle \quad (1.80a)$$

$$E_i^{(0)} \langle n^{(0)} | i^{(1)} \rangle - \sum_{k \setminus \{i\}} \langle n^{(0)} | \hat{H}_0 | f_k^{(0)} \rangle \langle f_k^{(0)} | i^{(1)} \rangle = \langle n^{(0)} | \hat{V} | i^{(0)} \rangle, \quad (1.80b)$$

where due to orthogonality of the basis functions only the n^{th} element of the sum over k survives. After further rearrangements

$$E_i^{(0)} \langle n^{(0)} | i^{(1)} \rangle - \langle n^{(0)} | \hat{H}_0 | n^{(0)} \rangle \langle n^{(0)} | i^{(1)} \rangle = \langle n^{(0)} | \hat{V} | i^{(0)} \rangle \quad (1.81a)$$

$$(E_i^{(0)} - E_n^{(0)}) \langle n^{(0)} | i^{(1)} \rangle = \langle n^{(0)} | \hat{V} | i^{(0)} \rangle \quad (1.81b)$$

$$\langle n^{(0)} | i^{(1)} \rangle = \frac{\langle n^{(0)} | \hat{V} | i^{(0)} \rangle}{(E_i^{(0)} - E_n^{(0)})}, \quad (1.81c)$$

one finally obtains an expression that may be used to substitute the unknown first-order wave function in the second-order energy expression (eq. 1.75c) with known eigenfunctions of the unperturbed Hamiltonian

$$E_i^{(2)} = \langle i^{(0)} | \hat{V} | i^{(1)} \rangle = \langle i^{(0)} | \hat{V} | n^{(0)} \rangle \langle n^{(0)} | i^{(1)} \rangle = \sum_{n \setminus \{i\}} \frac{\langle i^{(0)} | \hat{V} | n^{(0)} \rangle \langle n^{(0)} | \hat{V} | i^{(0)} \rangle}{(E_i^{(0)} - E_n^{(0)})}. \quad (1.82)$$

As intended, the second-order energy is expressed in terms of zeroth-order quantities. In a very similar but much longer derivation this also works for the third- and higher-order contributions, which are not discussed here. Before I apply the second-order formalism to HF theory, I want to point out a general drawback of perturbation theory which becomes evident already from this general expression for the second-order energy. Since the denominator apparently contains the difference between the eigenvalues of the unperturbed Hamiltonian, it will approach zero for degenerate eigenvalues, which will in turn yield an unphysically large (infinite) correction. In such a case also the high-order perturbation theory will not help to improve the zeroth-order description, as mentioned in the beginning of this section.

1.5.2 Møller-Plesset Perturbation Theory for Hartree-Fock

To improve upon the HF description of molecules, the effects of the explicitly correlated motion of electrons can be treated perturbatively, which was first suggested by C. Møller and M.S. Plesset.¹³ Although MP theory of n^{th} order is, in contrast to CI, not variational, it is size-consistent at any order, which is more important in practice. Moreover, due its reasonable computational cost and the existence of efficient, highly parallel implementations, MP theory of second order (MP2) has become one of the working horses of modern quantum chemistry for the calculation of ground-state energies and structures. In recent years, due to the availability of very efficient implementations and ever faster computers, also MP theory of third and higher order became applicable to study the intermolecular interaction between relatively large systems, such as e.g. DNA base pairs. It seems, however, that higher-order perturbation theory does not necessarily yield more accurate results. It has been found that ground-state properties calculated at the MP2 level of theory are in many cases more accurate than those obtained at MP theory of higher order.

Attempts to empirically improve the accuracy of MP led to a development of spin-component scaled (SCS) variants by Grimme and coworkers.^{14;15} In SCS-MP2, the correlation contributions originating between same-spin electrons are scaled down (in the original version by a factor of 0.6), while those contributions arising for electrons of opposite spin are scaled up by a factor of 1.3. Presumably due to imbalances in the treatment of same- and opposite-spin electrons at the HF level of theory, spin-component scaling has been found to significantly improve the results of MP methods with respect to more accurate calculations and experimental data.¹⁶ This seems to apply in particular to systems, for which rigorous MP theory experiences difficulties, like e.g. transition metal complexes.¹⁷ Recently, an intriguingly simple scaled variant of MP3 termed MP2.5 has been demonstrated to achieve a remarkable accuracy for weakly-bound systems, for which the scaled variants of MP2 are not well-suited. It can be obtained from original MP3 by scaling down the MP3 correction by a factor of 0.5.^{18;19}

In the original formulation by C. Møller and M.S. Plesset, \hat{H}_0 in eq. (1.68) is identified as the Fock operator \hat{F} , while the perturbation \hat{V} is the difference between the HF mean-field interaction and the exact r_{12}^{-1} operator.

$$\mathcal{H} = \hat{F} + \hat{V} \equiv \left[\sum_i (h(i) + v^{\text{HF}}(i)) \right] + \left[\sum_{i<j} r_{ij}^{-1} - \sum_i v^{\text{HF}}(i) \right] \quad (1.83)$$

In the context of many-body perturbation theory, HF may be regarded as a method required to transform a set of non-orthogonal, AO-basis functions into a complete, orthonormal set of eigenfunctions (i.e. the MOs) of an unperturbed, approximate Hamiltonian (i.e. the Fock operator), thereby providing a proper starting point for a perturbation theoretical treatment. Following this line of thought, the difference between the expectation value of the Fock-operator $E^{(0)}$ and Hartree-Fock energy E^{HF} , which was just presupposed in section 1.2.5, can be explained. With the MP of the partition of the Hamiltonian, the zeroth-order energy corresponds to the sum of orbital energies

$$E_i^{(0)} = \langle i^{(0)} | \hat{H}_0 | i^{(0)} \rangle = \sum_i^n \langle \psi_i | f(i) | \psi_i \rangle \equiv \sum_i^n \langle i | f(i) | i \rangle = \sum_i^n \epsilon_i, \quad (1.84)$$

and in turn, the zeroth-order eigenfunction are identified as the HF MOs and the orbital energies as the respective eigenvalues. The first-order energy can be expressed as

$$\begin{aligned} E_i^{(1)} &= \langle i^{(0)} | \hat{V} | i^{(0)} \rangle = \langle i | \sum_{i<j} r_{ij}^{-1} - \sum_i v^{\text{HF}}(i) | i \rangle \\ &= \langle i | \sum_{i<j} r_{ij}^{-1} | i \rangle - \langle i | \sum_i v^{\text{HF}}(i) | i \rangle, \end{aligned}$$

where expectation value of HF MOs w.r.t. r_{ij}^{-1} is the anti-symmetrized two-electron integral, which has already been derived in eq. (1.19). The expectation value of a HF MO w.r.t. $v^{\text{HF}}(i)$ is the same integral but without the factor of 0.5 as derived in eq. (1.38a). Eventually, the first-order energy becomes

$$E_i^{(1)} = \sum_{i,j} (0.5 \langle ij || ij \rangle - \langle ij || ij \rangle) \quad (1.86a)$$

$$= -\frac{1}{2} \sum_{i,j} \langle ij || ij \rangle, \quad (1.86b)$$

which is just the difference between the expectation value of the Fock operator and the Hartree-Fock energy E^{HF} . Consequently, the sum of zeroth and first-order energies is equivalent to the HF energy and the first correction to HF is obtained at second order. Regarding the general form of the second-order energy derived in the last section

$$E_i^{(2)} = \sum_{n \setminus \{i\}} \frac{\langle i^{(0)} | \hat{V} | n^{(0)} \rangle \langle n^{(0)} | \hat{V} | i^{(0)} \rangle}{(E_i^{(0)} - E_n^{(0)})} = \sum_{n \setminus \{i\}} \frac{|\langle i^{(0)} | \hat{V} | n^{(0)} \rangle|^2}{(E_i^{(0)} - E_n^{(0)})}, \quad (1.87)$$

the task at hand is to assign $|n^{(0)}\rangle$ and $E_n^{(0)}$ to the respective quantities in the HF framework. Since $|i^{(0)}\rangle$ and $E_i^{(0)}$ correspond to the HF wave function and its zeroth-order energy, a nearby assumption would be that $|n^{(0)}\rangle$ can be identified as n -tuply excited determinants. Since the latter are composed of HF MOs, they are also eigenfunctions of the Fock operator or in other words the zeroth-order Hamiltonian, as supposed in the derivation of RSPT. Because of Brillouin's theorem and Slater-Condon rules, however, only doubly excited determinants will give a non-zero energy correction, which has already been established in the framework of CI (eq. 1.58). Inserting the doubly excited determinants for $|n^{(0)}\rangle$ yields

$$E^{(2)} = \sum_{\substack{i < j \\ a < b}} \frac{|\langle \Psi^0 | r_{12}^{-1} | \Psi_{ij}^{ab} \rangle - \langle \Psi^0 | v^{\text{HF}} | \Psi_{ij}^{ab} \rangle|^2}{\langle \Psi^0 | \hat{F} | \Psi^0 \rangle - \langle \Psi_{ij}^{ab} | \hat{F} | \Psi_{ij}^{ab} \rangle}$$

for the second-order energy. The second term in the numerator is zero because the v^{HF} is a one-electron operator but the determinants differ by two indices, and the terms in the denominator are just the differences of the sums of orbital energies (eq. 1.84). Hence, one obtains

$$E^{(2)} = \sum_{\substack{i < j \\ a < b}} \frac{|\langle ij || ab \rangle - 0|^2}{E^{(0)} - (E^{(0)} - \epsilon_i - \epsilon_j + \epsilon_a + \epsilon_b)}$$

$$E^{(2)} = \sum_{\substack{i < j \\ a < b}} \frac{|\langle ij || ab \rangle|^2}{\epsilon_i + \epsilon_j - \epsilon_a - \epsilon_b},$$

which corresponds to an excitation of each unique pair of electrons into each unique pair of virtual orbital. Since the numerator is zero for $a = b$ or $i = j$ and furthermore the result is invariant w.r.t. an interchange of ij and ab when using real orbitals, one can drop the restriction in the summation and write

$$E^{(2)} = \frac{1}{4} \sum_{i,j,a,b} \frac{|\langle ij || ab \rangle|^2}{\epsilon_i + \epsilon_j - \epsilon_a - \epsilon_b}. \quad (1.90)$$

Ultimately, one may expand the anti-symmetrized integral into regular two-electron integrals, which yields

$$E^{\text{MP2}} = \frac{1}{2} \sum_{i,j,a,b} \left(\frac{\langle ij | ab \rangle \langle ab | ij \rangle}{\epsilon_i + \epsilon_j - \epsilon_a - \epsilon_b} - \frac{\langle ij | ab \rangle \langle ab | ji \rangle}{\epsilon_i + \epsilon_j - \epsilon_a - \epsilon_b} \right), \quad (1.91)$$

Apparently, the final expression for the electron-correlation correction at the MP2 level of theory has a structure similar to the expectation value of the two-electron part of the (derived from eq. (1.19) for a closed-shell determinant)

$$\langle \Psi^0 | \hat{H}_2(r_1, r_2) | \Psi^0 \rangle = \frac{1}{2} \sum_{i,j}^n \left(\langle ij | ij \rangle - \langle ij | ji \rangle \right).$$

Both expressions involve a Coulomb term as well as an exchange term. In accordance with HF, the second term in eq. (1.91) takes into account an exchange of the orbitals a and b , which is a direct result of the anti-symmetry of the wave function, or in other words the indistinguishability of electrons.

If the Hartree-Fock energy is, in the sense of Brillouin's theorem, regarded as an approximation to the exact energy that can not be lowered by an uncorrelated manipulation of single electrons, MP2 improves on this energy by approximating the energetic impact of a simultaneous excitation of two electrons in i and j into the virtual orbitals a and b . For eq. (1.90) to give a sizeable correction, there has to be significant overlap between i and j in a region close to where the product between a and b is also large. Furthermore, the difference between the sums $\epsilon_i + \epsilon_j$ and $\epsilon_a + \epsilon_b$ has to be small, since otherwise the denominator is large. In a physical picture, this means that pairs of electrons, which occupy the same portion of space ($|ij\rangle$) are allowed to avoid each other by a formal excitation into the less "crowded" region of space provided by the virtual orbitals a and b . Since the virtual orbitals are apparently of particular relevance for this correction, the quality of the MP2 correction is more sensitive with respect to the flexibility (size) of the basis set than HF theory. Also, it is more expensive to evaluate than HF energy, since it involves a sum over all unique pairs of occupied and virtual orbitals.

1.6 The Intermediate-State Representation for Correlated Excited States

The intermediate-state representation (ISR) is a method which unites the concepts of the shifted CI matrix from section 1.4.2 and Rayleigh-Schrödinger perturbation theory (RSPT) introduced in section 1.5 to provide an accurate (correlated), numerically efficient and size-consistent description of excited states. The starting point for its derivation is the postulation of a basis of correlated, n -tuply excited intermediate states (IS), which are formally obtained *via* n -tuple excitations of the exact ground-state wave function Φ^0 . In a way, the IS of the ISR approach take the role of the uncorrelated, n -tuply excited determinants generated from the HF ground state Ψ^0 , which form the basis for CI (see section 1.4). Ultimately, the lowest eigenvalues of the resulting ISR-matrix correspond to the excitation energies, whereas the eigenvectors provide a representation of the excited-state wave functions Φ^I in the IS basis. In accordance to CI, eigenvalues and eigenvectors may be obtained *via* partial diagonalization with approximate schemes like the Davidson or Lanczos algorithms.

The inherent advantage of the ansatz underlying the ISR over common CI is due to the formally separated treatment of electron correlation and excitation. This is achieved by the formal trick of initially postulating the existence of the unknown, exact ground state and IS basis, in which the excited states are

expanded. When one finally employs Rayleigh-Schrödinger PT to approximate the formally exact ground and intermediate states, the resulting equations afford a more balanced and computationally efficient description of electron-correlation than the simple, excitation-class based truncation underlying any practical CI method. The reasons for the poor convergence of CI have been outlined at the end of section 1.4.1. For an extensive discussion of the relation of CI, coupled-cluster and the ISR, please be referred to the work of Schirmer and Mertins.²⁰ Since the ISR has first been derived using algebraic-diagrammatic construction techniques as an approximation to the second-order polarization propagator,²¹ it is usually referred to as ADC(n). In this work, the abbreviations ADC and ISR are used interchangeably. For an evaluation of the accuracy of ISR up to third order of PT see ref. 22 (large benchmark of theoretical best estimates) and ref. 23 (small benchmark set of FCI results).

In the following derivations, I will make use of second quantization creation-annihilation operator algebra. A detailed introduction to this formalism, which constitutes a more elegant way of writing down equations that show up in the ISR framework can be found in chapter 2.4 of ref. 5. In second-quantization, the HF ground state determinant $|\Psi^0\rangle$ with n electrons is formally generated by creating the respective number of particles (here electrons) in the vacuum state $|\rangle$ using the creation operator a^\dagger associated with a HF orbital ϕ_i .

$$|\Psi^0\rangle = \sum_i^n a_i^\dagger |\rangle = |\phi_1\phi_2\cdots\phi_n\rangle \quad (1.92)$$

Accordingly, an n -tuply excited determinant can be obtained from an arbitrary ground state wave function by annihilation of n electrons in occupied orbitals i, j and creation of n electrons in unoccupied orbitals a, b

$$a_a^\dagger a_i |\Phi^0\rangle = c_a^i |\Phi^0\rangle = |\Phi''^a_i\rangle \quad (1.93a)$$

$$-a_b^\dagger a_j a_a^\dagger a_i |\Phi^0\rangle = a_b^\dagger a_a^\dagger a_j a_i |\Phi^0\rangle = c_{ij}^{ab} |\Phi^0\rangle = |\Phi''^{ab}_{ij}\rangle, \quad (1.93b)$$

where I have introduced the excitation operators $c_i^a = a_a^\dagger a_i$, $c_{ij}^{ab} = a_b^\dagger a_a^\dagger a_j a_i$, which are associated with the respective occupied MOs ϕ_i and ϕ_j as well as the virtual MOs ϕ_a and ϕ_b . Per definition, these operators always refers to a string with all annihilation operators collected on the right-hand side with increasing index. This specification is necessary to reflect the properties of the Slater determinant

$$|\phi_i\phi_j\rangle = a_i^\dagger a_j^\dagger |\rangle = -|\phi_j\phi_i\rangle = -a_j^\dagger a_i^\dagger |\rangle, \quad (1.94)$$

in second quantization algebra, due to which a string of operators changes sign upon exchange of two operators next to each other.

Since by definition the excitation operators are specifically associated with HF MOs, while the choice of the ground state used in eqs. (1.92) and (1.93) is arbitrary, one has to mind that this formalisms may only yield orthogonal excited determinants for the HF ground state Ψ^0 , like e.g. in the CI expansion. In the framework of the ISR, however, it is employed in combination with the formally exact ground state Φ^0 with the aim of generating a set of correlated excited states, the so-called intermediate states (IS). The generation of the latter consequently requires a multi-step procedure, whose first step is the generation

of a non-orthogonal set of so-called precursor states ϕ''_μ via n -tuple excitation of the correlated ground state Φ_0

$$|\Phi''_\mu\rangle = \hat{C}_\mu |\Phi^0\rangle, \quad (1.95)$$

where the index μ of the general excitation operator \hat{C} refers to the excitation class

$$\hat{C}_\mu \in \{c_i^a\}^{\mu=1}, \{c_{ij}^{ab}; i < j, a < b\}^{\mu=2}, \dots \quad (1.96a)$$

$$\hat{C}_1 |\Phi^0\rangle = c_i^a |\Phi^0\rangle = |\Phi''_i^a\rangle \quad (1.96b)$$

$$\hat{C}_2 |\Phi^0\rangle = c_{ij}^{ab} |\Phi^0\rangle = |\Phi''_{ij}^{ab}\rangle. \quad (1.96c)$$

Subsequently, the precursor states are orthonormalized. At first, Gram-Schmidt orthogonalization discussed in section 1.3.1 is used to subtract the overlap with all lower excitation classes including also the ground state

$$|\Phi'^a_i\rangle = |\Phi''^a_i\rangle - |\Phi_0\rangle \frac{\langle \Phi_0 | \Phi''^a_i \rangle}{\langle \Phi_0 | \Phi_0 \rangle} \quad (1.97a)$$

$$|\Phi'^{ab}_{ij}\rangle = |\Phi''^{ab}_{ij}\rangle - \sum_{k,c} |\Phi'^c_k\rangle \frac{\langle \Phi'^c_k | \Phi''^{ab}_{ij} \rangle}{\langle \Phi'^c_k | \Phi'^c_k \rangle} - |\Phi_0\rangle \frac{\langle \Phi_0 | \Phi''^{ab}_{ij} \rangle}{\langle \Phi_0 | \Phi_0 \rangle}. \quad (1.97b)$$

Secondly, all IS within the same excitation class are orthogonalized against each other *via* symmetric orthonormalization introduced in section 1.3.2

$$|\Phi^a_i\rangle = \sum_{j,b} |\Phi^b_j\rangle \mathbf{S}_{ia,jb}^{-1/2} \quad (1.98a)$$

$$|\Phi^{ab}_{ij}\rangle = \sum_{\substack{k < l \\ c < d}} |\Phi'^{cd}_{kl}\rangle \mathbf{S}_{ijab,klcd}^{-1/2}, \quad (1.98b)$$

where $\mathbf{S}^{-1/2}$ is the overlap matrix for all precursor states within a certain class of excitations

$$\mathbf{S}'_{ia,jb} = \sum_{\substack{i,a \\ j,b}} \langle \Phi'^a_i | \Phi'^b_j \rangle \quad (1.99a)$$

$$\mathbf{S}'_{ijab,klcd} = \sum_{\substack{i < j, a < b \\ k < l, c < d}} \langle \Phi'^{ab}_{ij} | \Phi'^{cd}_{kl} \rangle. \quad (1.99b)$$

Ultimately, the IS within a certain excitation class are orthonormal with respect to each other and orthogonal to the ground state and all lower excitation classes

$$\begin{aligned} S_{ia,jb} &= \langle \Phi^a_i | \Phi^b_j \rangle = \delta_{ij} \delta_{ab} \\ S_{ijab,klcd} &= \langle \Phi^{ab}_{ij} | \Phi^{cd}_{kl} \rangle = \delta_{ik} \delta_{jl} \delta_{ac} \delta_{bd} \\ \langle \Phi^a_i | \Phi_0 \rangle &= 0 \\ \sum_{k,c} \langle \Phi^{ab}_{ij} | \Phi^c_k \rangle &= \langle \Phi^{ab}_{ij} | \Phi_0 \rangle = 0, \end{aligned}$$

and thus constitute a proper basis in which any excited state Φ^I can be expanded

$$\Phi^I = \sum_{\mu} \chi_I^{\mu} |\Phi_{\mu}\rangle = \sum_{i,a} \chi_I^{ia} \Phi_i^a + \sum_{i,j,a,b} \chi_I^{ijab} \Phi_{ij}^{ab} + \dots \quad (1.101)$$

where the $\chi_{I\mu}$ are identified as amplitudes, which in accordance with CI determine the contribution of each IS to the excitation vector. Inserting this expansion into the Schrödinger equation, one arrives at an eigenvalue equation for the excited state I

$$\mathbf{H}\mathbf{x}_I = \omega_I \mathbf{x}_I, \quad (1.102)$$

where, \mathbf{x}_I is the eigenvector or state vector containing the amplitudes $\chi_{I\mu}$. Including all other excited states, one arrives at a matrix representation of the shifted Hamiltonian in analogy to CIS (eq. 1.67)

$$\mathbf{H}\mathbf{X} = \mathbf{X}\mathbf{\Omega} \quad \text{with} \quad \mathbf{X}\mathbf{X}^{\dagger} = \mathbf{1}, \quad (1.103)$$

with \mathbf{H} being the hermitian secular matrix composed of the elements

$$H_{\nu\mu} = \langle \Phi_{\nu} | \mathcal{H} - \mathcal{E}_0 | \Phi_{\mu} \rangle, \quad (1.104)$$

and \mathbf{X} a column matrix, whose I^{th} column \mathbf{x}_I corresponds to the I^{th} eigenvector of \mathbf{H} . Accordingly $\mathbf{\Omega}$ is a diagonal matrix, whose diagonal elements can be identified as excitation energies ω_I .

So far, the presented formalism is exact since no approximations have been introduced. However, to arrive at numerically soluble equations, the problem or more specifically the ISR matrix, which formally has the same size as the FCI matrix, has to be truncated. Instead of an excitation-class based truncation scheme of classical CI, one makes use of Rayleigh-Schrödinger perturbation theory (RSPT) of n^{th} order, which yields the following perturbation expansion of the secular matrix

$$\mathbf{H} = \mathbf{H}^{(0)} + \mathbf{H}^{(1)} + \mathbf{H}^{(2)} + \mathbf{H}^{(3)} + \dots, \quad (1.105)$$

while the application to the ground state yields MP of n^{th} order as discussed in section 1.5.2. Subsequently, the intermediate states can be obtained from the respective MP ground state *via* second-quantization algebra.

Although the addends to the ISR matrix $\mathbf{H}^{(n)}$ increase in dimension with increasing order of PT, the dimension grows much slower than that of CI and nonetheless affords a superior truncation behaviour. In other words, despite a smaller matrix, any given class of excitations (e.g. singly and doubly excited states) is treated formally correct through higher order of perturbation theory with the ISR than with CI. This may be illustrated for the example of singly excited states, for which CI requires an inclusion of triply-excited determinants to afford a description that is correct through second order of PT. Using the ISR, however, the correlation of singly-excited determinants is perturbatively folded into the singles (and doubles) blocks, which causes the resulting states to be correct to second order of perturbation already for the much smaller ISR matrix of second order. Even the ISR of third order, which affords a third-order treatment of singly-excited states, does not require an extension of the ISR matrix, but only a modification of existing sub-blocks of the ISR matrix of second order. Only for the already somewhat academical ISR of fourth order, a zeroth-order (diagonal) triples block would have to be included.

		{p-h}	{p-h}	{2p-2h}		(a)	(b)	(c)
{p-h}	$\mathbf{H}_{11}^{(a)}$	$\mathbf{H}_{11}^{(a)}$	$\mathbf{H}_{12}^{(b)}$		ISR(0)	0	-	-
					ISR(1)	0-1	-	-
{2p-2h}		$\mathbf{H}_{21}^{(b)}$	$\mathbf{H}_{22}^{(c)}$		ISR(2)	0-2	1	0
					ISR(3)	0-3	1-2	0-1

Figure 1.4: Block-structure of the hermitian ISR matrix of zeroth and first order (left) as well as second and third order (middle). Apparently, the zeroth and first-order matrix as well as the second- and third-order matrix have an identical structure. The differences between these levels of theory arise from the order of perturbation theory at which the matrix elements in the singles (a), doubles (c) and coupling blocks between singles/doubles (b) are obtained, which is shown for ISR(0) through ISR(3) in the table on the right.

The structure of the ISR matrix as well as the perturbation-theoretical level at which the sub-blocks are obtained is shown in fig. 1.4. While the ISR(0) corresponds to a diagonal matrix with the elements

$$\langle \Phi_i^a | \mathcal{H} | \Phi_j^b \rangle = (\epsilon_i - \epsilon_a) \delta_{ij} \delta_{ab} \quad (1.106)$$

the excitation energy can be obtained simply by carrying out the matrix-vector multiplication in eq. (1.102), yielding

$$\omega^{(0)} = \mathbf{x}_I^\dagger \mathbf{H}_{11}^{(0)} \mathbf{x}_I = \sum_{i,a} (\chi_I^{ia})^2 (\epsilon_a - \epsilon_i). \quad (1.107)$$

The first-order ISR matrix is identical to the CIS matrix described in section 1.4.2 and the ground state is in agreement with the result obtained in section 1.5.2 for the HF ground state. For a closed-shell HF reference, the elements of the first-order ISR matrix take the form

$$\langle \Phi_i^a | \mathcal{H} | \Phi_j^b \rangle = (\epsilon_a - \epsilon_i) \delta_{ij} \delta_{ab} - \langle a j || i b \rangle, \quad (1.108)$$

whereas the excitation energies become

$$\omega^{(1)} = \mathbf{x}_I^\dagger \mathbf{H}_{11}^{(1)} \mathbf{x}_I = \sum_{i,a} (\chi_I^{ia})^2 (\epsilon_a - \epsilon_i) + \sum_{i,j,a,b} \chi_I^{ia} \chi_I^{jb} \langle a j || i b \rangle. \quad (1.109)$$

For ISR(2), the ground state is identified as the MP2 ground state and the ISR matrix includes an additional doubles (2p-2h) block at zeroth order, which only has diagonal elements. A matrix element of the singles block has additional

second-order terms originating from $\mathbf{H}_{11}^{(2)}$ and becomes

$$\langle \Phi_i^a | \mathcal{H} | \Phi_j^b \rangle = (\epsilon_a - \epsilon_i) \delta_{ij} \delta_{ab} - \langle aj || ib \rangle \quad (1.110a)$$

$$+ \frac{1}{2} \sum_{k,c} (t_{acik} \langle kj || cb \rangle + t_{kjcb} \langle ac || ik \rangle) \quad (1.110b)$$

$$+ \delta_{ij} \frac{1}{4} \sum_{k,l,c} (t_{klbc} \langle ac || kl \rangle + t_{ackl} \langle kl || bc \rangle) \quad (1.110c)$$

$$+ \delta_{ab} \frac{1}{4} \sum_{k,c,d} (t_{jkcd} \langle cd || ik \rangle + t_{cdik} \langle jk || cd \rangle), \quad (1.110d)$$

where I have introduced the so-called t -amplitudes, which provide a short-hand notation for the recurring combination of anti-symmetrized integrals divided by the respective orbital energies

$$t_{pqrs} = \frac{\langle pq || rs \rangle}{(\epsilon_r + \epsilon_s - \epsilon_p - \epsilon_q)}. \quad (1.111)$$

To illustrate the physical meaning of the second-order terms, one may expand the first of the three second-order ISR terms (eq 1.110b) for a diagonal element ($b = a, j = i$),

$$= \frac{1}{2} \sum_{k,c} \left(\frac{\langle ac || ik \rangle \langle ki || ca \rangle}{(\epsilon_i + \epsilon_k - \epsilon_a - \epsilon_c)} + \frac{\langle ac || ik \rangle \langle ki || ca \rangle}{(\epsilon_k + \epsilon_i - \epsilon_c - \epsilon_a)} \right) \quad (1.112a)$$

$$= \sum_{k,c} \frac{\langle ac || ik \rangle \langle ki || ca \rangle}{(\epsilon_i + \epsilon_k - \epsilon_a - \epsilon_c)}, \quad (1.112b)$$

and compare it to general MP2 ground state correlation energy (eq. 1.90)

$$E^{(\text{MP2})} = \frac{1}{4} \sum_{i,j,a,b} \frac{\langle ab || ij \rangle \langle ij || ab \rangle}{\epsilon_i + \epsilon_j - \epsilon_a - \epsilon_b}.$$

Apparently, this second-order ISR term is closely related to the respective ground-state term. The ISR term seems to account for the change in correlation energy due to the excitation of one of the electrons, either from the orbital i or j to an orbital a or b , which in other words corresponds to the difference between the correlation contribution for the ground state and an excited (intermediate) state. Consequently, the ISR is sometimes referred to as the equivalent of MP theory for excited states.

The additional (2p-2h) block $\mathbf{H}_{22}^{(2)}$ only has diagonal elements of the form

$$\langle \Phi_{ij}^{ab} | \mathcal{H} | \Phi_{kl}^{cd} \rangle = F_{ac} + F_{bd} - F_{ij} - F_{jl} \quad (1.113a)$$

$$= (\epsilon_a + \epsilon_b - \epsilon_i - \epsilon_j) \delta_{ac} \delta_{bd} \delta_{ik} \delta_{jl}, \quad (1.113b)$$

whereas the elements of the (p-h)/(2p-2h) coupling blocks $\mathbf{H}_{12}^{(2)} = \mathbf{H}_{21}^{(2)}$ become

$$\langle \Phi_i^a | \mathcal{H} | \Phi_{jk}^{bc} \rangle = \delta_{ab} \langle jk || ci \rangle - \delta_{ac} \langle ik || bi \rangle - \delta_{ij} \langle ak || bc \rangle + \delta_{ik} \langle aj || cb \rangle. \quad (1.114)$$

Eventually, the second-order excitation energy reads

$$\omega^{(2)} = \mathbf{x}_I^\dagger \mathbf{H}_{11}^{(2)} \mathbf{x}_I + 2 \mathbf{x}_I^\dagger \mathbf{H}_{12}^{(2)} \mathbf{x}_I + \mathbf{x}_I^\dagger \mathbf{H}_{22}^{(2)} \mathbf{x}_I, \quad (1.115)$$

where

$$\mathbf{x}_I^\dagger \mathbf{H}_{11}^{(2)} \mathbf{x}_I = \sum_{i,a} (\chi_I^{ia})^2 (\epsilon_a - \epsilon_i) + \sum_{i,j,a,b} \chi_I^{ia} \chi_I^{jb} \langle aj || ib \rangle \quad (1.116a)$$

$$+ \frac{1}{2} \sum_{i,j,a,b} \chi_I^{ia} \chi_I^{jb} (t_{acik} \langle kj || cb \rangle + t_{kjcb} \langle ac || ik \rangle) \quad (1.116b)$$

$$+ \frac{1}{4} \sum_{\substack{i,k,l \\ a,b,c}} \chi_I^{ia} \chi_I^{ib} (t_{kibc} \langle ac || kl \rangle + t_{ackl} \langle kl || bc \rangle) \quad (1.116c)$$

$$+ \frac{1}{4} \sum_{\substack{i,j,k \\ a,c,d}} \chi_I^{ia} \chi_I^{ja} (t_{jkcd} \langle cd || ik \rangle + t_{cdik} \langle jk || cd \rangle) \quad (1.116d)$$

$$\mathbf{x}_I^\dagger \mathbf{H}_{12}^{(2)} \mathbf{x}_I = \sum_{\substack{i,j,k \\ a,b,c}} \chi_I^{ia} \chi_I^{jbc} (\delta_{ab} \langle jk || ci \rangle - \delta_{ac} \langle ik || bi \rangle - \delta_{ij} \langle ak || bc \rangle + \delta_{ik} \langle aj || cb \rangle) \quad (1.116e)$$

$$\mathbf{x}_I^\dagger \mathbf{H}_{22}^{(2)} \mathbf{x}_I = \sum_{\substack{i,j,k,l \\ a,b,c,d}} \chi_I^{ijab} \chi_I^{jkcd} (\epsilon_a + \epsilon_b - \epsilon_i - \epsilon_j) \delta_{ac} \delta_{bd} \delta_{ik} \delta_{jl} . \quad (1.116f)$$

The number of indices of the sums in combination with the number of additional terms compared to the first-order result allows to estimate the increased complexity of the equations and in turn, the increase in computational demand for solving them. Formally, the computational demand for the calculation of the energy of each ISR(2) state-vector scales with the fifth power of the number of basis functions.

Having defined all the matrix elements and resulting energy for the ISR of second order, the matrix can ultimately be diagonalized. For actual molecules, however, a full diagonalization is usually not feasible due to the huge dimension of the matrix. However, a full diagonalization is usually not required, since one is usually interested mainly in the low-lying excited states, which correspond to the lowest eigenvectors. Hence, in practice, one makes use of e.g. the Davidson algorithm,¹¹ which is well suited for the purpose of computing the lowest eigenvalues of a diagonally dominated matrix. The respective numerical procedure consists of guessing an initial vector (e.g. the HOMO to LUMO transition), which is subsequently optimized in a series of matrix-vector multiplications. Eventually, within usually tens of iterations, the initial guess vectors converge to the eigenvectors \mathbf{x}_I .

Second Part: Photochemistry

1.7 Light-Driven Chemistry

Molecules can interact with light in manifold ways. Depending on the energy of the photon and the presence of resonant transitions in the molecule, either elastic processes like scattering or inelastic processes like absorption may occur. The focus of this work is on inelastic processes that involve the absorption of the photon and in turn an energy transfer to the molecule, which is called excitation. Molecular transitions susceptible to an excitation by light or more general electromagnetic radiation can be categorized according to the excitation energy. This categorization coincides with the degrees of freedom, which are excited with the energy of the photon. From lowest to highest energy, these are translational, rotational and vibrational as well as electronic degrees of freedom. While the former three exclusively involve the nuclear degrees of freedom and occur at energies below that of visible light (photon energy < 1.5 eV), above this limit an excitation of the electronic degrees of freedom, or in other words an excitation of outer (valence) electrons can occur. Since the valence electrons largely determine the chemistry of a molecule, such an electronic transition usually changes and/or increases the reactivity, which gives rise to the field of photochemistry. Moreover, any excitation of a resonant, high-lying (e.g. electronic) transition usually causes all lower-lying transitions to be excited as well. Hence, electronic transitions and spectra of the latter are sometimes referred to as “vibronic”, indicating that electronic as well as vibrational (and rotational etc.) transitions take part and determine the shape of the observed absorption spectrum. Eventually, after absorption of a visible or ultraviolet (vis/UV) photon, molecules are vibrationally excited and particularly reactive, which typically causes photochemical reactions to occur with much higher rate constants or in other word on much shorter femto- and picosecond time-scales compared to classical, thermochemical reactions. Light-induced processes in molecule are usually depicted using so-called Jablonski-diagrams (see e.g. figs. 2.12, 3.2 and 4.9).²⁴

In general, the processes taking place after an optical excitation may be categorized as photochemical or photophysical. While the photochemical processes are those involving a rearrangement of bonds e.g. an inter-molecular excited-state hydrogen transfer, photophysical processes are e.g. interconversions between excited states and the ground state (e.g. internal conversion (IC) or inter-system crossing (ISC)) along molecular coordinates that do not involve a formation or cleavage of bonds. An example for exclusively photophysical pro-

cesses after light absorption is the non-radiative decay of nitrobenzene, which is covered in chapter 4. In closely related *ortho*-nitrobenzylic (oNB) compounds, on the contrary, very similar initial photophysical processes are succeeded by a cascade of photochemically induced transformations, which are topic of chapters 2 and partially also 3.

The light-induced reactivity of molecules depends on the character of the orbitals involved in the electronic transition as well as on the structure of the molecules. This can be illustrated using the two examples given above. Despite the fact that the lowest electronically excited states of nitrobenzene and oNB compounds are essentially identical as they involve the promotion of a non-bonding electron to the anti-bonding π^* orbital at the nitro group (referred to as $\text{NO}_2(n \rightarrow \pi^*)$ excited state), only oNB compounds undergo photochemical transformations. Here, the vibronically excited nitro group behaves like an oxygen-radical and abstracts a hydrogen atom from the neighboring benzylic substituent. In nitrobenzene, the absence of neighbouring substituents prevents the radicalic reactivity of the nitro-group to culminate in an intra-molecular excited-state hydrogen transfer. Instead, nitrobenzene decays to the ground state *via* a cascade of ISC and IC processes along vibrational modes of the nitro group. Apparently, the non-reactive decay of nitroaromatics is too slow to compete with the intramolecular hydrogen-abstraction, but fast enough to prevent large fractions of the initially excited population to undergo hydrogen abstraction reactions with solvent molecules, i.e. intermolecular hydrogen-transfer. Although the latter can in general be observed for nitrobenzene, it is only a minor side reaction with a quantum yield of a few percent. In the context of photochemistry, the quantum yield refers to the fraction of initially excited molecules that undergo a certain reaction.

The competition between various processes based on their rates or in other words their time-scales is a very typical aspect of photochemistry and draws a border to common ground-state chemistry. The causative difference is that in ground-state chemistry, the mechanism and product formation is usually determined by the relation of the available energy (temperature) to barrier heights (kinetically controlled reactions) or the final free energy of products (thermodynamically controlled reaction). In photochemical reactions, however, the vibrational excess energy present in the first few picoseconds (ps) after the initial excitation serves as activation energy and is typically sufficient to overcome many barriers and in turn, many different products can usually be observed. However, it is only the first few picoseconds after the absorption of a photon before most of the excess vibrational energy is dissipated in the environment.²⁵ The main product or main “channel” of product formation is often determined rather by the bare speed at which the respective processes can occur. This does strongly favor simple, straightforward processes with a ballistic character like, e.g. electron or proton-transfer over more involved reactions like, heavy-atom transfer and in general any large-scale nuclear rearrangements. Figuratively spoken, the initial photochemistry as a non-equilibrium process is rather determined by the diameter of the reactive funnels than by their energetic position.

Besides the equilibration with the environment, also the internal vibrational redistribution (IVR) of energy takes a finite amount of time, as it usually occurs on a time-scale of few hundreds of femtoseconds (fs), which is relevant in photochemical processes. To assign these time-scales to a molecular, mechanistic picture, they can be expressed in terms of periods of typical molecular

vibrations. Within one picosecond, a typical stretching vibration of a H-X bond of 3000 cm^{-1} loops through 90 periods, a frequency of 300 cm^{-1} corresponds to 9 periods and so on. Apparently, for any processes that occurs on a sub-ps time-scale, the concept of temperature breaks down even within a molecule. In turn, for photochemical questions concerning such ultra-fast processes, one has to explicitly consider the energy stored in each molecular degree of freedom when judging possible mechanisms to explain for a certain experimental observation. Even the direction of the initial gradient in the excited state can be of relevance for the outcome of a reaction, which in such a case rather corresponds to a ballistic process than a classical chemical equilibrium.

Regarding these considerations, photochemistry may be subdivided into a non-equilibrium and an equilibrium regime. While the presence of a large amount of vibrational excess energy in the few picoseconds after the initial excitation is characteristic for the non-equilibrium regime, the following regime of equilibrium photochemistry is basically like classical thermochemistry with the difference that it occurs on the potential energy surface of the excited state. In condensed phase, the transition from the non-equilibrium to the equilibrium regime typically occurs a few to a few tens of picoseconds after the initial excitation depending on the molecule and environment.

1.8 Investigation of Photochemical Processes

In this section I briefly describe typical photochemical and photophysical reaction cascades from a practical point of view, *i.e.* I will outline how they may be investigated by means of quantum-chemical calculations. For this purpose, I will state a set of rules that may be derived from typical time-scales of photochemical and photophysical processes. A common problem would be the interpretation of time-resolved experiments (e.g. transient absorption data).

After the initial excitation to a bright excited state, the fastest process is usually the internal conversion (IC) to the lowest excited state *via* conical intersections (CIs). Since the latter are ubiquitous in potential-energy surfaces of polyatomic molecules (see e.g. the PES of nitrobenzene in section 4.5) IC is usually unrivalled fast and completed within few vibrational periods. This gives rise to Kasha's rule,²⁶ which was derived from the observation that fluorescence with significant quantum yield usually occurs exclusively from the lowest excited state. Thus, the conversion to this state must be orders of magnitude faster than the fluorescence from higher-lying states. Since fluorescence, or in other words spontaneous emission occurs on a time-scale of $0.5 - 20\text{ ns}$, it is rather slow compared to typical photochemical processes, this rule may not necessarily be transferable. However, exceptions from Kasha's rule are scarce. They occur when there are no accessible CIs between the excited states, which can be the case for energetically well separated states. An exception from Kasha's rule is azulene, which undergoes fluorescence from the second excited singlet state. Another example for a violation of Kasha's rule is the ultrafast release of CO_2 from *meta*- and *ortho*-nitrophenylacetate, which is the topic of chapter 2.

Nevertheless, as a rule of thumb photochemical conversions can be expected to occur from the lowest excited singlet state, keeping in mind that there might be exceptions. Consequently, the first task should be to characterize the lowest excited state using quantum-chemical methodology. Important questions are

(1): How far below the Franck-Condon point (energy of the excited state at the ground-state equilibrium) lies the minimum of the S_1 , and (2): Are there any apparent/intuitive reactive channels below the initial excitation energy, or in other words with barriers below the available vibrational excess energy? If this is the case, the possible channels should be investigated and the height of the respective barriers calculated. Also, one should identify the vibrational modes which exhibit the largest difference between ground-state minimum and S_1 -relaxed geometry, as well as those relevant for the reactive channel. Since the Franck-Condon (FC) active modes will receive a majority of the initial vibrational excess energy, any reaction involving this modes will overcome barriers more easily in the first few picoseconds after the initial excitation.

If no suitable reactive channels exist or a participation of triplet states has been determined experimentally, the next question should be (3): are there triplet states energetically degenerate to the S_1 that may allow for efficient inter-system crossing (ISC)? To answer this question qualitatively one should consider El-Sayed's qualitative rules,²⁷ which state that states of different local symmetry (e.g. singlet $n \rightarrow \pi^*$ to triplet $\pi \rightarrow \pi^*$ and *vice versa*) can exhibit fast ISC on a time-scale of picoseconds. If ISC in accordance with El-Sayed's rules is possible, one should explicitly calculate the spin-orbit coupling (SOC) between the respective states. The ISC rate is inversely proportional to the SOC. As a rule of thumb, a SOC on the order of $10 - 100 \text{ cm}^{-1}$ translates into an ISC on a timescale of $10 - 1 \text{ ps}$, respectively. The actual rate might vary by a factor of 10, because ISC largely depends on the dynamics of the system. Succeeding ISC, IC to the lowest triplet state will occur again on a sub-ps time-scale. For this process, the same rules as before apply. The vibrational excess energy available to the molecules right after ISC roughly equals the difference between S_1 and T_1 minima and one should consider all possible reactions that involve vibrational modes along which the equilibrium geometries of lowest singlet and triplet states differ the most.

Regardless of the multiplicity, after tens of picoseconds in the lowest excited state the molecules will have dissipated the vibrational excess energy and hence arrive in the equilibrium regime of photochemistry. Here, the same rules as in classical ground-state thermochemical reactions apply.

1.9 Characterization of Excited States

Since the vast majority of quantum-chemical methods for the description of excited states make use of a Hartree-Fock (HF) reference, quantum-chemists think of excited states in terms of the involved molecular orbitals (MOs). In particular the low-lying excited states of molecules, which are of major relevance for the photochemistry are usually well-described by a single or a few one-electron transition(s) from an occupied to a virtual orbital. Since moreover, the zeroth-order approximation of the respective excitation energy is orbital-energy difference, the transition of an electron from the highest occupied MO (HOMO) to the lowest unoccupied MO (LUMO) constitutes the main contribution of lowest excited state of many molecules. Accordingly, excited states can be characterized based on the energetic ordering of the orbitals involved in the largest transition, which affords terms like e.g. $S(\text{HOMO} \rightarrow \text{LUMO})$ for the singlet state involving the HOMO to LUMO transition.

In the so-called adiabatic picture, one takes this energy-based characterization a step further and refers to excited states on the basis of their excitation energy. This yields the names S_1, S_2, S_3, \dots for the first, second etc. singlet excited state, and accordingly T_1, T_2, T_3, \dots for the respective triplet states. This has the drawback that the nomenclature does not only depend on the molecular geometry, which usually affects the ordering of the excited states, but also on the level of theory. Hence, I find this adiabatic nomenclature to be impractical and have only used it in situations in which I want to emphasize the energetic position of the respective state and the ordering of the excited states is without a doubt.

Besides an energy-based characterization, one may categorize the excited states according to the character of the orbitals. In this context, the term “character” refers to a combination of local symmetry (e.g. σ, π) and bonding (i.e. anti-bonding, non-bonding) properties (e.g. π^* for a anti-bonding orbital with π symmetry, or n_π for a non-bonding orbital with π symmetry). To give an example for this nomenclature, an excited singlet state, which involves the transition from a π orbital to a π^* orbital is termed $S(\pi \rightarrow \pi^*)$, a triplet states in which an electron is promoted from an n to a π^* orbital $T(n \rightarrow \pi^*)$. This characterization with respect to the properties and structure of the underlying orbitals has two advantages over the characterization based on the energetic ordering. At first, the character of orbitals is usually rather independent with respect to changes in the geometry of the molecule, while the energetic ordering of orbitals and states readily changes. Therefore, the characterization with respect to the structure of the involved orbitals is more universal. Moreover, there are certain properties associated with excited states that depend on the character of the involved orbitals, like e.g. the general rule that $n \rightarrow \pi^*$ excited states are usually dark and also El-Sayed’s rules,²⁷ which allow for a qualitative estimation of the inter-system crossing rate between singlet and triplet states depending on their character. Hence, the character-based nomenclature for excited states has the advantage of implicitly containing information about the photochemical and photophysical reactivity.

1.10 Transient Absorption Spectroscopy

Often, the initial photochemical processes are succeeded by reactions in the ground state. For example in oNB photo-labile protecting groups, the initial excited-state intra-molecular hydrogen-transfer initiates a reaction cascade that culminates in the cleavage of the oNB moiety from the active compound. To investigate the initial, ultra-fast photochemical steps of this reactions on ps and sub-ps time-scales, very fast experimental techniques are required. Transient absorption pump-probe spectroscopy constitutes one of the few methods that allows to track ultra-fast photochemical reactions in detail. For this purpose, an ultra-short light pulse is generated using e.g. a Nd:YAG solid state laser and split in two using a semi-transparent mirror. One of the pulses is made into a pump pulse, whose purpose is to excite the molecules in the sample at a given wavelength. For an UV excitation as in case of the experiment discussed in chapters 2 and 3, the frequency of the pulse can be tripled using non-linear optics prior to focusing the pulse into the sample. The other pulse, termed probe, is used to the read out information from the sample at a specific time delay with

respect to the pump pulse. For this purpose, the infra-red light originating from the Nd:YAG laser may either be employed directly to obtain information on the molecular vibrations, or turned into a white-light pulse to gain information related to the electronic part of the molecular spectrum. Anyway, the probe pulse has to be delayed with respect to the pump pulse for a very specific amount of time. This can be realized using an optical delay pathway on a micrometer (μm) scale (a delay of 3 ps corresponds roughly to 1 μm). Ultimately, a number of pump-probe experiments is carried out for each given delay time to get an average, which is then repeated for each of the desired time delays. Put together, the data from these experiments yields a transient absorption spectrum, which is basically the evolution of the absorption after an optical excitation. Using this technique, one can achieve a time resolution of few tens of femtoseconds. The experiments on ortho-nitrobenzylic compounds discussed in this work had a time resolution of about 100 fs.

Chapter 2

Photo-Decarboxylation of Nitrophenylacetates

In this chapter, I present an investigation of the photo-decarboxylation (PDC) mechanism of *ortho*, *meta* and *para*-nitrophenylacetate (NPA) employing quantum chemical calculations as well as time-resolved UV-pump vis-probe spectroscopy. In the course of this investigation I demonstrate that for a proper theoretical description of the excited states of anionic NPA in aqueous solution a careful consideration of the influence of the solvent is indispensable. In this sense, NPA constitutes a prototypical example that demonstrates how character and lifetime of excited states in combination with the choice of the solvent-model (*i.e.* equilibrium and non-equilibrium solvation) exert a major influence onto excited-state energies and in turn the photochemical processes. Eventually, an ultra-fast decay channel *via* a repulsive, excited singlet state is found to be responsible for observed, ultra-fast CO₂ release, while another very efficient but slower CO₂ release channel could be traced back to the presence of a repulsive triplet state. Most notably, the much smaller quantum yield of CO₂ release from the *ortho*-isomer oNBA is due to an alternative excited-state intermolecular hydrogen-transfer channel, which may occur along a triplet or singlet pathway.

Complementing the research of my master thesis, this joint experimental and theoretical work was the first project of my Ph.D. It was carried out in cooperation with the experimental Group of J. Wachtveitl, namely E. Pepler, who conducted the experiments described herein. Interpretation of the results and design of the experiment was closely accompanied by my theoretical work. An initial investigation of the PDC of NPA conducted in the framework my master thesis based on UV-pump IR-probe data is published elsewhere.^{28;29} The work presented in this chapter has been published in *the Journal of Physical Chemistry A*, volume 116 (2012), pages 11846-11862 (ref. 30). The article has been written and composed by myself and includes only editorial contributions from the co authors.

2.1 Introduction

Photo-labile protecting groups allow for light-triggered release of chemically or biologically active compounds, which is commonly called uncaging. In combination with the control achieved by modern lasers, so-called caged-compounds offer remarkable spatio-temporal control over the release of active species. In general, the unique prospects of light-controlled reactions allow for new experimental techniques and caused development and application of such photo-labile protecting groups (cages) to become a vastly growing research field.^{31–33} The first synthesis of photo-labile protecting groups was already reported in the 1960s.³⁴ In a first application, molecular cages were employed for the controlled release of ATP to study the kinetics and mechanism of ATPases.³⁵ The idea and chemistry of caged-compounds was developed only weeks earlier.^{36;37}

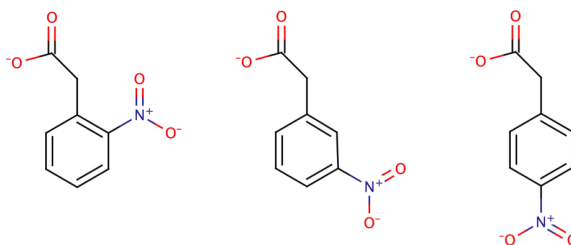


Figure 2.1: Molecular structure of anionic *ortho*-, *meta*- and *para*-nitrophenylacetate.

Despite promising alternatives,^{38;39} the most prominent structural motif in caged-compounds still is the *ortho*-nitrobenzyl (oNB) group, which is presumably due to a straightforward synthetic access. The photochemistry of *ortho*-nitrobenzyl compounds was discovered as early as in 1901.⁴⁰ In the context of oNB cages, the three isomers of nitrophenylacetate (*n*PA, fig. 2.1) can be regarded as a caged CO₂, as they are known to undergo ultra-fast photo-decarboxylation (PDC), *i.e.* they release CO₂ when irradiated with UV light.⁴¹ Indeed, *meta*-NPA (mNPA) has already been successfully applied as caged CO₂ to study the kinetics of the enzyme Ribulose-1,5-bisphosphate carboxylase oxygenase (RuBisCO), which is the central protein involved in CO₂ fixation of green plants.⁴² Note that only the *ortho*-isomer of NPA (oNPA) possesses the structural motif of typical oNB cages but exhibits the lowest uncaging quantum yield of only 4%, whereas *m*- and *p*NPA exhibit remarkably high quantum yields of 63% and 59%.⁴¹ Hence, at least for *m*- and *p*NPA the PDC will most certainly occur *via* an alternative mechanistic pathway compared to uncaging from typical oNB cages, for which quantum yields of at most 10% have been observed for the unmodified oNB cage.³¹

The molecular mechanism of CO₂ release from NPA was recently studied using time-resolved UV-pump IR-probe spectroscopy in combination with quantum chemical calculations.^{28;29} For that objective, the decarboxylation was triggered with an UV photon and the emerging CO₂ was observed at its main IR band around 2345 cm⁻¹ with a time resolution of approximately 150 fs. The obtained absorption transients reveal a complex picture of the CO₂ release kinetics: while the majority of CO₂ is released from *m*- and *p*NPA with an identical time con-

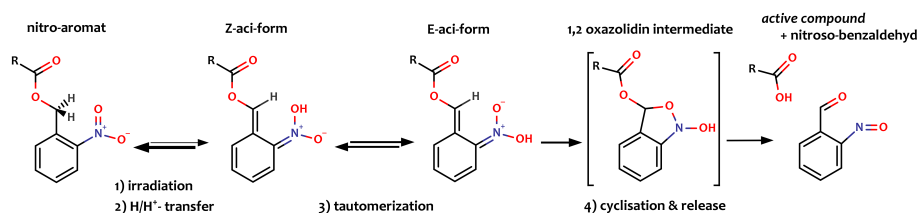


Figure 2.2: Generic deprotection-mechanism of photo-labile protecting groups (cages) of the *ortho*-nitrobenzyl type

stant of about 200 ps, the *meta*-isomer exhibits an additional, ultra-fast channel of CO₂ release, which causes a significant presence of CO₂ after only 0.5 ps. While this ultra-fast component is absent in pNPA, it is, on the contrary, the major CO₂ release channel in oNPA. For the latter, the slow component is almost completely suppressed, hinting towards an alternative fast deactivation channel quenching the PDC. These findings are complemented by additional UV-pump VIS-probe experiments, which are described in section 2.2.

NPA as caged-CO₂ represents a suitable candidate for a thorough theoretical investigation of the underlying photochemistry at a high-level of electronic structure theory, since its modest molecular size allows for application of reliable *ab initio* wave-function based theory. Nevertheless, a comprehensive quantum chemical description of anionic NPA in aqueous solution and, in particular, the theoretical study of the PDC mechanism is a challenge to theory in a series of aspects. An appropriate model of solvation is indispensable even for a qualitatively correct description, since the electronic structure of anionic NPA is largely influenced by a strong dielectric like water. Hence, prior to the investigation of the uncaging mechanism of NPA, various theoretical methodologies and explicit molecular model systems have been developed and evaluated in section 2.3.2.

Having established a suitable theoretical methodology, the electronic structure of NPA, its ground and excited state properties as well as the photo-initiated PDC reaction mechanism are studied in detail in sections 2.3.3 – 2.3.5. Based on calculated potential energy surfaces and new experimental evidence, a detailed molecular mechanism of the PDC proceeding in the different NPA isomers is derived in section 2.4. The mechanism explains differences and similarities in the kinetics of CO₂ release from the NPA isomers and sheds light on the ultra-fast H-transfer channel of oNPA quenching PDC. This ultra-fast quenching channel turns out to be relevant for the early photochemistry and in particular for the uncaging quantum yield of related oNB caged compounds as discussed in section 2.5.

2.2 Time-Resolved UV-Pump Vis-Probe Spectroscopy

2.2.1 Methodology

A Clark CPA 2001 laser system with a repetition rate of 1 kHz was used for the generation of 170 fs laser pulses with a central wavelength of 775 nm and 800 J output power. In the UV-pump-UV/VIS-probe experiments, the 258 nm excitation pulses were generated by frequency tripling of the laser fundamental. The broadband probe pulses with a spectral range from 350 nm to 700 nm were created by focusing the laser fundamental into a 3 mm CaF₂ crystal. The angle between pump and probe polarization was adjusted to the “magic angle” (54.7°). The sodium phosphate buffered aqueous solutions (pH 8.5) of 10 mM NPA isomers (Sigma Aldrich, Germany) were circulated through a flow cell with an optical path length of 0.5 mm. Due to the generation of solvated electrons in water, pure buffer solutions were measured separately in order to subtract the solvent transients from the NPA measurements. Finally, the transients were globally fitted using a sum of four exponential functions. The experimental methods for the pump-probe measurements in the IR region are described in ref. 28.

2.2.2 Previous Investigations

The mechanism of uncaging CO₂ from NPA has recently been studied using time-resolved UV-pump IR-probe spectroscopy.²⁸ In these experiments, decarboxylation was triggered with UV-laser pulses with photon energies of 4.3 eV and 4.8 eV. Subsequently the emerging CO₂ was monitored at its strong IR band around 2345 cm⁻¹. The results for o-, m- and pNPA reveal a complicated picture of the CO₂ release kinetics with similarities but also striking differences. In general two channels for CO₂ release exist: a dominant one on a time-scale of 200 ps and an ultra-fast one on a time-scale of 0.5 ps. An additional time constant of 3 ps was needed to globally fit the experimental data. However, the occurrence of the two channels of CO₂ release varies for the different isomers. While for pNPA the ultra-fast channel is completely absent, it is present for mNPA to a minor extend and the only channel of CO₂ release for oNPA. On the contrary, the slow component of CO₂ release is completely suppressed in oNPA, while it is the dominant or, respectively, the only one for the other two isomers.

In view of the much lower quantum yield for CO₂ release from oNPA compared to mNPA and pNPA, it is clear that an additional, efficient non-radiative decay channel must exist for the *ortho*-isomer, which diminishes the ultra-fast and completely suppresses the slow component. Earlier quantum chemical calculations corroborated the hypothesis of intra-molecular excited-state H-transfer (ESIHT),²⁹ which has first been suggested by Margerum and coworkers.⁴¹ Based on calculations and comparison to experimental data for nitrobenzene and other nitroaromatics, arguments were provided that the ultra-fast component of CO₂ release occurs from a repulsive singlet state. The 3 ps time constant most likely corresponds to inter-system crossing (ISC), i.e. formation of a triplet state. Hence, the slow component with the 200 ps time constant will most certainly occur from a triplet precursor state, as inferred in ref. 43.

Table 2.1: Summary of the time-constants derived from the global fit analyses of o-, m- and pNPA.

	τ_1/ps	τ_2/ps	τ_3/ps	τ_4
oNPA	0.2	4.1	178	∞
mNPA	0.15	2.1	261	∞
pNPA	0.13	2.3	156	∞

2.2.3 Results

Time-resolved UV-pump VIS-probe transient absorption experiments corroborate the earlier findings of the UV-pump IR-probe experiments. In these new experiments, all three isomers were initially excited with light of 258 nm (4.8 eV) to trigger PDC. The changes in absorption have then been probed by white light continuum pulses recording the complete transient absorption spectrum between 350 and 700 nm with an overall temporal resolution of 170 fs. These UV-pump VIS-probe transient absorption experiments offer complementary information on the species involved in the PDC processes. While in the previous experiment CO₂ was monitored exclusively, in the VIS spectrum only signals resulting from the nitrobenzyl caging group can be observed.

The measured transients of the three isomers, o-, m- and pNPA were globally fitted using a sum of four exponential functions. In excellent agreement with the previous experiment, an ultra-short time constant τ_1 of 0.13 – 0.2 ps below the time-resolution of the experiment, a short time constant τ_2 of 2.1 – 4.1 ps, a long time constant τ_3 of 156 – 261 ps and an infinite time τ_4 are required to satisfyingly fit the kinetics of all three isomers (tab. 2.1). While the first time τ_1 can not be interpreted in detail, both τ_1 and τ_2 are most likely associated with processes occurring in singlet excited states. While the first presumably describes the decay of singlet excited-state absorption, τ_2 most certainly represents the ISC into a triplet state. Regarding previous results, τ_3 clearly corresponds to the slow decarboxylation from the triplet precursor state.

To further illuminate the role of the triplet states for the slow release of CO₂ from the different NPA isomers, it is instructive to analyze their corresponding kinetic traces recorded at a wavelength of 667 nm (fig. 2.3). It is well known that the triplet state exhibits a prominent absorption at this wavelength.⁴⁴ At early times, however, these kinetic traces contain contributions from excited singlet-state absorption, which decays either *via* fast CO₂ release or *via* inter-system crossing within 2 – 4 ps generating excited triplet state absorption. The latter eventually decays *via* the slow decarboxylation on a 150 – 250 ps time-scale depending on the isomer. Although the slow decay of the 667 nm absorption of oNPA exhibits the same characteristics as for m- and pNPA, no formation of CO₂ was detected in the UV-pump IR-probe experiments. As a consequence, the decay of this signal of oNPA is not related to decay *via* CO₂ release but rather to the alternative H-transfer decay channel, which results in the formation of the so-called aci-form. The latter is known to absorb around 400 nm,⁴⁵ which is in good agreement with the calculations that predict an excitation of aci-form of oNPA at 403 nm. Due to overlap with the broad triplet and excited-

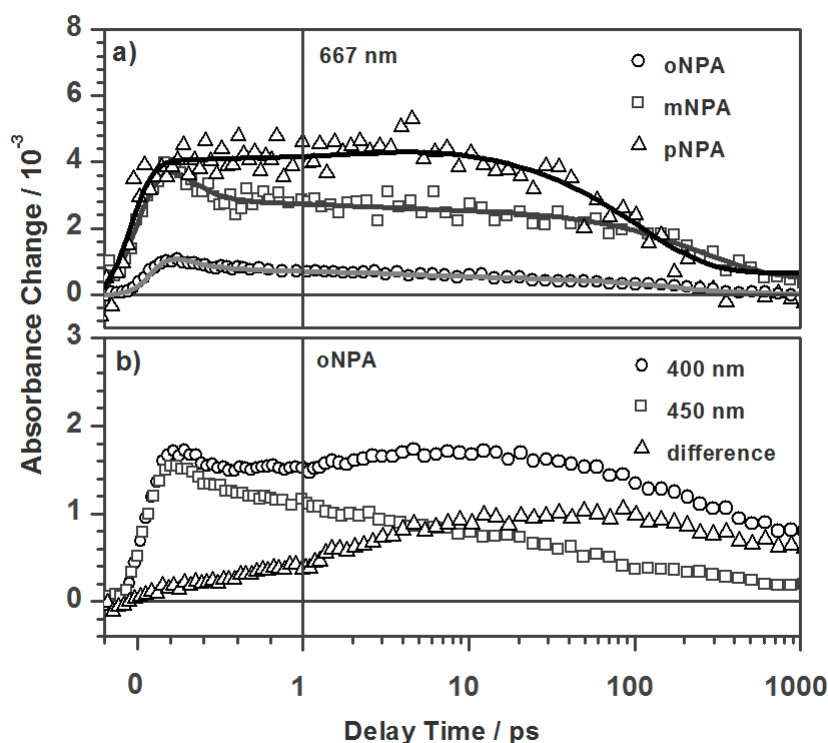


Figure 2.3: a) Absorption transients of o-, m-, and pNPA at the characteristic triplet absorption of 667 nm. b) Absorption transients of oNPA at 450 and 400 nm as well as their difference.

state absorption along the complete time-scale of the experiments, however, the interpretation of the 400 nm transients is more involved. To estimate the aci-formation despite these complications, the difference of the zero-point corrected transients at 400 nm and 450 nm was calculated (see fig. 2.3) to eliminate a large fraction of the other overlapping contributions. Eventually, the formation of the aci-form seems to occur *via* two channels, of which the faster one takes place on a sub-picosecond time-scale, while the slower one occurs on a 10 – 100 ps time-scale. As far as this rough estimate allows for quantification, it seems that the fast channel contributes equal or a little less to the formation of the aci-form than the slow channel, which is in good agreement with results for related compounds described in ref. 45.

The initial singlet excited state absorption exhibits an additional decay channel for o- and mNPA, which is not present for pNPA. Assuming this decay relates to the fast component of CO₂ release, the results of the UV-pump VIS-probe experiments fully support the earlier experimental findings.

2.3 Quantum-Chemical Calculations

2.3.1 Methodology

For the theoretical description of the photochemistry of NPA, I employed the approximate second-order coupled-cluster method exploiting the resolution-of-the-identity (ri) approximation (riCC2)^{46;47} as implemented in TURBOMOLE⁴⁸ 5.10 and 6.3.1 as the standard theoretical model because of its efficient parallel implementation featuring excited-state gradients^{49;50} and the conductor-like screening model (COSMO).⁵¹ Although COSMO is implemented in TURBOMOLE only for the SCF calculation, which corresponds to the frozen reaction field approximation for the calculation of vertical excitation energies, I extensively tested it as described in section 2.3.2 and found it to be sufficiently accurate for our purposes.

In addition, I employed configuration-interaction singles with perturbative doubles (CIS(D))⁵² together with spin-component-scaled Møller-Plesset perturbation theory of second order using the ri-approximation (SCS-riMP2)⁵³ as implemented in ORCA 2.8,⁵⁴ since this program allows for appropriate non-equilibrium treatment of solvation effects for vertical excitation energies in the framework of the COSMO solvation model.

To investigate the effects of equilibrium solvation onto the low-lying triplet states of NPA, I employed ground-state unrestricted Kohn-Sham density functional theory (DFT) using the functional PBE0,^{55;56} and COSMO as implemented in ORCA 2.8. In particular for the ground and excited triplet states, the results obtained at DFT/PBE0 level agree well with those obtained at the riCC2 and SCS-MP2 levels of theory. A broad application of unrestricted SCS-MP2 for the investigation of equilibrium solvation was not possible due to convergence issues and large spin-contamination, which originate from the complicated electronic structure of the anionic NPA.

Nuclear geometries used to calculate excitation energies have at all times been optimized at the theoretical level corresponding to the excited-state calculation, i.e. riCC2 for linear-response riCC2, SCS-riMP2 for CIS(D), and DFT for linear-response time-dependent DFT (TD-DFT). Unless mentioned otherwise, the def2-TZVP⁵⁷ basis set has been used in all calculations.

The lowest excited state of common nitroaromatics and thus the key to understand their photochemistry is a local $n \rightarrow \pi^*$ excited state at the nitro group $\text{NO}_2(n \rightarrow \pi^*)$ with a vertical excitation energy of about 3.8 eV, which readily mixes with slightly higher lying excitations involving charge transfer (CT states). The extent of this mixing and hence also character and reactivity of this $\text{NO}_2(n \rightarrow \pi^*)$ state strongly depend on the energy difference to the respective CT excitations. Hence, a balanced description of the local excitations at the nitro group and the low-lying CT excitations is essential for a thorough theoretical investigation of the photochemistry of nitro-aromatic compounds. For this purpose, it is generally advisable to avoid TD-DFT for the investigation of the photochemistry of oNB compounds. Regarding the special case of NPA this is even more important, since these low-lying charge-transfer (CT) excitations significantly contribute to the excited states relevant for the PDC of NPA.

In case TD-DFT is unavoidable one should at least use exchange-correlation (xc) functionals with large to very large fractions of non-local HF-exchange. In case of NPA, even Becke's half-and-half xc-functional (BHandH-LYP)⁵⁸ with

50% HF-exchange fails to find the correct bound minimum structure for the lowest $\text{NO}_2(n \rightarrow \pi^*)$ excited singlet and triplet states due to admixture of artificially low-lying and reactive $\text{COO}(s,n) \rightarrow \text{NO}_2(\pi^*)$ CT states. Double hybrid functionals including the perturbative doubles correction of CIS(D) in the excitation energies and particularly B2K-PLYP with 72% exact exchange yield acceptable results.⁵⁹ Nonetheless, even with double hybrid or range-separated functionals the description of a system exhibiting low-lying CT states like NPA is based on fortuitous and unreliable compensation of errors and should be avoided. In order to obtain a physically correct and more reliable description, correlated *ab initio* methods like CIS(D) and/or (lr)CC2 are more appropriate.

2.3.2 Influence and Modeling of the Solvent

For comparison with experimental spectra obtained in aqueous solution, a suitable model of solvation is undoubtedly required within the computation, since the electronic structure of the NPA anion is strongly affected by a polar and protic solvent like water. This is illustrated by a first example compiled in tab. 2.2, which shows vertical excitation energies of the energetically four lowest excited states of mNPA and neutral *meta*-nitrophenylacetic acid (mNPAA) calculated with and without COSMO at the CIS(D)/def2-TZVP level of theory.

Table 2.2: Vertical excitation energies (ω_{ex}) [eV] and oscillator strength (f , in parenthesis) as well as character^a of the first four excited states of mNPA and mNPAA with and without COSMO at the CIS(D)/def2-TZVP level of theory.

mNPA				
State	gas phase		COSMO	
	ω_{ex} (f)	char ^a	ω_{ex} (f)	char ^a
S_1	3.51 (0.00)	$\text{COO}(n')$	3.90 (0.02)	$\text{NO}_2(n)$
S_2	3.97 (0.03)	$\text{COO}(n'')$	4.42 (0.05)	$\text{Bz}(\pi)$
S_3	3.98 (0.13)	$\text{NO}_2(n)$, $\text{Bz}(\pi)$	4.65 (0.01)	$\text{NO}_2(n')$
S_4	4.04 (0.23)	$\text{Bz}(\pi)$, $\text{NO}_2(n)$	5.23 (0.14)	$\text{Bz}(\pi')$
mNPAA				
S_1	3.84 (0.00)	$\text{NO}_2(n)$	3.88 (0.01)	$\text{NO}_2(n)$
S_2	4.50 (0.00)	$\text{NO}_2(n')$	4.59 (0.02)	$\text{Bz}(\pi)$ $\text{NO}_2(n)$
S_3	4.92 (0.04)	$\text{Bz}(\pi)$	4.70 (0.02)	$\text{NO}_2(n')$ $\text{Bz}(\pi)$
S_4	5.76 (0.12)	$\text{Bz}(\pi')$	5.36 (0.16)	$\text{Bz}(\pi')$

^aFor the characterization of the excited states only the electron origin is relevant, since the four lowest excitations correspond to transitions into the LUMO, which is a linear combination of the π^* orbitals of the aromatic ring and the nitro group.

For the neutral mNPAA as well as for the anion applying the COSMO model for water solvation, the lowest four electronically excited states consist of two local $n \rightarrow \pi^*$ excited states at the nitro group and two $\pi \rightarrow \pi^*$ excited states of the nitrobenzylic moiety. The latter are mainly characterized as $\text{Bz}(\pi) \rightarrow \pi^*$ and $\text{Bz}(\pi') \rightarrow \pi^*$ transitions, which involve the aromatic π -orbitals ($\text{Bz}(\pi)$ and $\text{Bz}(\pi')$) as well as the low-lying π^* -orbital of the nitro group. The negatively

charged carboxylate is hardly involved in the lower lying excited states of NPAA. In mNPA using COSMO only a relatively small contribution of a $\text{COO}^-(\sigma, n)$ orbital to the $\text{Bz}(\pi)$ and concomitantly to the $\text{Bz}(\pi) \rightarrow \pi^*$ excited state can be found. This $\text{COO}^-(\sigma, n)$ orbital mainly resembles an oxygen lone pair of the carboxylate but has also significant binding character with respect to the bond between the benzylic and the carboxylate carbon atoms. Not surprisingly, for the anionic mNPA without the COSMO solvation model the ordering and character of the excited states as well as of the frontier orbitals is completely different. Due to the missing electrostatic stabilization of the anionic carboxylate n -orbital, they constitute the HOMO to HOMO-2, whereas the aromatic $\text{Bz}(\pi)$ orbitals are now found as HOMO-4 and HOMO-5. Consequently, the lowest two excited states of mNPA in the gas phase are CT states in which an electron is transferred from the charged carboxylate to the LUMO, followed by two states which are linear combinations of the $\text{Bz}(\pi) \rightarrow \pi^*$ and a local $n \rightarrow \pi^*$ excitation of the nitro group (tab. 2.2). Inclusion of a solvent model like COSMO causes a strong stabilization of the anionic charge at the carboxylate and leads to a strong blue-shift of the corresponding CT states, while local excitations are little affected.

In the conjugated acid mNPAA without COSMO, the additional proton has a similar but more pronounced influence compared to the COSMO for water. The carboxylate lone pairs as well as the adjacent benzene π -orbitals shift to even lower energies and the states involving these orbitals consequently exhibit a larger blue shift than mNPA with COSMO. Nevertheless, the excited states obtained for mNPAA without COSMO agree much better to the experimental values (tab. 2.5) and with the results obtained for mNPA with COSMO than the excited states calculated for mNPA without COSMO. This holds for all isomers and methods. Therefore, if no solvation model is available, the corresponding protonated acid mNPAA resembles the electronic structure of solvated NPA much better than isolated, anionic NPA itself. NPAA has been employed successfully as model for solvated NPA in a previous preliminary investigation.^{28;29} The agreement between NPA and NPAA is further increased, if COSMO is applied to both systems. The largest influence of COSMO on the excitation energies of NPAA is found for the excited states with CT-character, which are red-shifted by 0.33 eV ($\text{Bz}(\pi) \rightarrow \pi^*$) and 0.4 eV ($\text{Bz}(\pi') \rightarrow \pi^*$), respectively.

The results presented in tab. 2.2 were obtained at the CIS(D)/def2-TZVP level of theory, because its implementation in ORCA 2.8 features a consistent treatment of solvation effects with COSMO for vertical excitation energies, which at present is not available at riCC2 level. In case of the latter, COSMO is applied to the Hatree-Fock (HF) SCF calculation and the resulting SCRf-RHF orbitals are used to calculate the correlation correction. This is equivalent to the non-iterative “energy only” scheme, the so-called PTE approach, at the MP2 level of theory.^{60;61} However, for excited-state properties this approach is generally incomplete, since it lacks the dynamic answer of the solvent electron density to the excitation. The time-independent ground state COSMO describes the static interaction between the solute and the solvent due to all three components of solvent polarization (orientation-, nuclear-, and electronic polarization). For optical excitations, these components split into fast electronic parts and slow nuclear parts, of which usually only the electronic component can adapt to the changes in the charge-distribution of the solute at the time-scale of the electronic excitation. Hence, nuclear polarization components (orientation- and nuclear polarization) have to be kept frozen for CI-like excited-state calculations, whereas

the electronic component has to be recalculated using the excited-state charge-distribution. An elucidating discussion of the importance of polarization effects in the framework of QM/MM approaches can be found in chapter 5 or ref. 62.

However, freezing all components of the polarization can be a reasonable approximation as long as the fast electronic component is small compared to the slow nuclear components. In our case of charged NPA in water the fast component, which is related to the squared refractive index (1.77 for water) is much smaller than the slow one, which is related to the dielectric constant (approx. 78 in water). Consequently, the contribution of the fast term is only -66 meV and -49 meV for the $Bz(\pi) \rightarrow \pi^*$ and $Bz(\pi') \rightarrow \pi^*$ states involving CT character and -37 meV and -22 meV for the local $n \rightarrow \pi^*$ and $n \rightarrow \pi^*$ states of mNPA at the CIS//SCS/MP2/def2-TZVP level of theory, which is identical to CIS(D)//SCS-MP2 regarding the COSMO part of the calculation. In contrast, the influence of the slow term shifts CT states involving the COO^- group upwards by as much as 3 eV, while the $Bz(\pi) \rightarrow \pi^*$ and $Bz(\pi') \rightarrow \pi^*$ states of solvated NPA are shifted by 0.5 – 1 eV. However, the numbers for the slow term are approximate since they can only be obtained indirectly by comparison of calculations with and without COSMO, which in case of mNPA leads to a qualitatively different picture as discussed in the beginning of this section.

After all, the application of COSMO to the HF-ground state wavefunction drastically improves the description of the ground state as well as the calculated vertical excitation energies at the riCC2 level of theory. Actually, the excitation energies and oscillator strengths f calculated using this approach show remarkable agreement with the experimental spectra with deviations mostly below 0.2 eV. Compared to the qualitatively wrong results from the calculations without any model for solvation this is a huge improvement, which is achieved despite the complete neglect of the fast term. This is most likely due to the practically state-independent stabilization of the anionic charge at the carboxylate due to orientation polarization, the by far most important consequence of solvation, which is quantitatively captured at the HF/COSMO level of the calculation.

However, for the calculation of excited state properties like equilibrium structures, the use of COSMO evaluated for the ground state is certainly not the physically correct approach, but what would be? For any excited-state geometry optimization, the solvent relaxation must to some extent be taken into account.⁶³ For a hypothetical, infinitely slow process solvent molecules can completely adapt to the structural changes of the solute. Therefore, recalculation of the COSMO field using the relaxed excited-state density for each optimization step is necessary. This is generally called equilibrium approach, since the solvent is allowed to fully equilibrate at each step. For a hypothetical, infinitely fast process the solvent would not be able to relax at all. Hence, one should use the frozen COSMO charges from the ground state calculation along the reaction coordinate investigated within the so-called non-equilibrium approach. Since all chemically relevant processes are intermediates of the two extreme cases discussed above the approach chosen is system- and process-dependent and not immediately clear. Besides the time-scales of the processes also the character of the excited state is crucial for the error introduced by an incomplete model for solvation. On the one hand, for locally excited states (e.g. $NO_2(n \rightarrow \pi^*)$) exhibiting charge distributions similar to that of the ground state, equilibrium and non-equilibrium approaches will presumably yield similar results. On the other

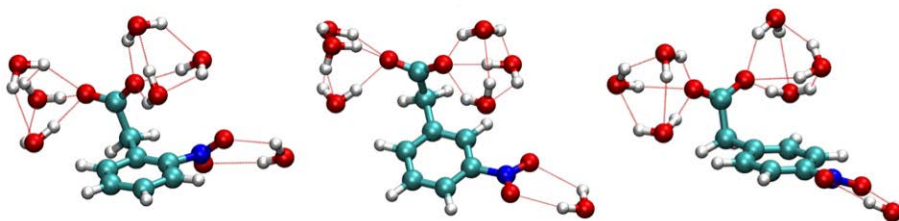


Figure 2.4: Coordination geometries of micro-solvated clusters of (from left to right) oNPA, mNPA and pNPA including seven water molecules.

hand, for states exhibiting CT character (e.g. $Bz(\pi) \rightarrow \pi^*$ state), for which the charge distribution significantly differs from the one of the GS, solvent relaxation may significantly affect the electronic structure.

In the scope of this work, chemical processes on different time-scales that involve excited states of different character are addressed, e.g. ultra-fast excited-state intramolecular hydrogen-transfer, ultra-fast PDC from hot, short-lived singlet states, but also PDC from long-lived triplet states. The first two of these (processes) occur on a sub-picosecond time-scale and are thus too fast to allow for extensive equilibration of the solvent. Hence, for these cases I decided to employ non-equilibrium solvation as standard approach, being aware that the errors due to the complete neglect of solvent relaxation may vary. However, this approach makes the treatment at higher level of $riCC2$ theory instead of TD-DFT possible, which is mandatory due to the large charge-transfer character of the excited states of NPA. In case of the slow release of CO_2 , which will turn out to involve long-lived triplet states with substantial CT character as well as locally excited triplet states, solvent relaxation can no longer be neglected. Hence, I additionally studied the respective triplet states within an equilibrated solvent field using unrestricted ground-state DFT and MP2 in combination with COSMO, which corresponds to the equilibrium approach.

Besides the continuum solvation models, also the influence of explicit solvation has been extensively studied including successively up to 7 water molecules. In principle the molecular complexes provide results comparable to those obtained employing COSMO, which are essentially converged with respect to changes of the coordination geometry and the number of water molecules when seven water molecules are included. The key advantage of this explicit approach is that the influence of solvent molecules present in the calculation is fully included at the level of theory of the underlying quantum chemical calculation. In tab. 2.3, the vertical excitation energies of the four lowest excited states of the three isomers of NPA are compiled as calculated for model systems including 7 explicit water molecules (fig. 2.4).

However, explicitly solvated model systems are impractical, since the potential energy surfaces of such molecular complexes are flat and exhibit countless local minima that complicate geometry optimizations. In addition, these model systems including explicit water are impractical for the calculation of the PES along a certain reaction coordinate, since the reorganization of the incomplete solvent-shell will be different at each point of the PES. As a final test, I combined explicit solvation with the COSMO model. For this purpose, the geometry of the explicitly solvated systems was re-optimized including two and seven water

Table 2.3: Vertical excitation energies (ω_{ex}) [eV] and oscillator strengths (f , in parenthesis) of the first four excited singlet states of o-, m- and pNPA*7 H₂O at the ground state equilibrium geometries at the riCC2/def2-TZVP(-f) level of theory.

	oNPA	mNPA	pNPA
e ⁻ origin	ω_{ex} (f)	ω_{ex} (f)	ω_{ex} (f)
NO ₂ (n)	3.74 (0.01)	3.78 (0.01)	3.74 (0.03)
NO ₂ (n')	4.37 (0.00)	4.32 (0.01)	4.37 (0.00)
Bz(π)	4.51 (0.02)	4.51 (0.01)	4.41 (0.29)
Bz(π')	5.37 (0.14)	4.9 (0.15)	4.63 (0.01)

molecules using the COSMO solvation model and the differences in the excitation energies were investigated. Neither the coordination of the nitro group nor that of the carboxylate with explicit water molecules alter the vertical excitation energies significantly compared to the results of calculations when only COSMO was employed. The changes in the excitation energies due to explicit solvent molecules are below 0.1 eV for all isomers and excitations. In other words, explicit solvation does not significantly improve the results justifying the increased computational effort discussed above.

Table 2.4: Influence of the model of solvation on the vertical excitation energies (ω_{ex}) [eV] and oscillator strengths (f , in parenthesis) of mNPA at the riCC2/def2-TZVP(-f) level of theory. The calculations were performed with and without COSMO (C) for bare mNPA as well as the complex including two and seven explicit water molecules.

	gas phase	Cosmo (C)	2 H ₂ O	2 H ₂ O + C	7 H ₂ O	7 H ₂ O + C
e ⁻ origin	ω_{ex} (f)					
NO ₂ (n)	3.74 (0.01)	3.80 (0.00)	3.76 (0.00)	3.77 (0.00)	3.78 (0.01)	3.76 (0.00)
NO ₂ (n')	4.38 (0.00)	4.46 (0.00)	4.39 (0.00)	4.48 (0.00)	4.32 (0.01)	4.44 (0.00)
Bz(π)	2.86 (0.02)	4.01 (0.02)	3.02 (0.02)	4.11 (0.03)	4.51 (0.01)	4.13 (0.02)
Bz(π')	3.70 (0.14)	4.60 (0.20)	3.17 (0.05)	4.55 (0.17)	4.9 (0.15)	4.58 (0.24)

2.3.3 Ground-State Equilibrium Geometry

In general, the ground-state equilibrium geometry used in the calculations and the vibrational motion of the molecules at ambient temperature can have a significant influence on the observed absorption spectra and thus need to be considered comparing experimental and theoretical spectra. To address effects like spectral shapes and vibronic effects like intensity borrowing, in principle nuclear dynamics simulations are required. Here these effects are only estimated using static electronic structure calculations.

Excitation energies and oscillator strengths of all relevant excitations of the NPA isomers depend on the dihedral angle $d(\text{C-C-N-O})$ between the nitro group and the benzene ring. The motion along this angle strongly affects the overlap between the π^* orbitals of the nitro group and the benzene ring, whose linear combinations form the LUMO and LUMO+2, of which at least one is populated in all relevant excitations.

For m- and pNPA only one ground state equilibrium structure exists with an in-plane nitro group and the carboxylate pointing away from the plane of the benzene ring. The PES of the torsional out-plane motion of the nitro group is flat, allowing for a tilt of 30° at a cost of only $2 - 3$ kJ/mol, which is possible at room temperature. This explains the contribution of the local $n \rightarrow \pi^*$ excitation to the experimental spectrum in terms of a small peak around 3.8 eV, although the transition is calculated to be virtually dark ($f < 0.001$) at the equilibrium geometry (tab. 2.5). However, along this vibration f increases up to 0.02 at a torsional angle of 40° .

Also the excitation energies of the CT states are affected by the dihedral motion of the nitro group, because the energy of the LUMO, which is the symmetric combination of the π^* orbitals at the nitro group and those at the benzene ring, depends on the overlap of these orbitals. Consequently, the tilt of the nitro group reducing this overlap yields increasing energy of the symmetric combination (LUMO) and decreasing energy of the anti-symmetric combination (LUMO+2), which is reflected in the excitation energy of the states.

The energy of the local $n \rightarrow \pi^*$ excitations, on the other hand, are much less affected by the dihedral motion of the nitro group, because they correspond to linear combinations of determinants in which LUMO and LUMO+2 are populated. The expansion coefficients are such that orbital contributions from the benzene $\text{Bz}(\pi^*)$ orbital cancel out, and the states correspond to $n \rightarrow \pi^*$ excitations exclusively localized at the nitro group (for a visualization of the respective attachment and detachment densities for the parent compound nitrobenzene see fig. 4.1). After all, one may conclude that the similarity of the local excited states of the nitro group for all the isomers investigated here is responsible for the similar photochemical reactivity of nitrobenzylic compounds.

In the case of oNPA, the proximity of the nitro group and the carboxylate causes its ground state PES to exhibit multiple local minima corresponding to different stable conformers of comparable total energy but with different absorption behaviours. Two local minima exist with the carboxylate pointing either towards (conformer 1) or away (conformer 2) from the nitro group, whereas conformer 1 is favored by only 0.1 eV. Due to this small difference it is not clear which of the two dominates in aqueous solution, therefore both will be considered in the further discussion. Both isomers exhibit a 40° tilt of the nitro group, which causes the excitation energies of the CT states as well as the f of the $n \rightarrow \pi^*$ excitation to be significantly higher than in m- and pNPA. Since this is the case for the equilibrium geometry, it affects the UV/VIS spectrum of oNPA and oNPAA much more than the vibrational intensity borrowing of m- and pNPA. Consequently, the absorption at around 3.8 eV is more pronounced for oNPA than for m- and pNPA. When the nitro group is forced into the plane, a transition state (conformer 3) 0.2 eV above the favored conformer 1 with excitation energy and f similar to m- and pNPA is obtained, in particular for the bright $\text{Bz}(\pi') \rightarrow \pi^*$ excited state. Another consequence of the spatial proximity of the nitro and carboxylate groups in oNPA is that CT states originating

from the n -orbitals at the carboxylate that populate the LUMO enter the low energy region below the $Bz(\pi') \rightarrow \pi^*$ excited state, in particular for conformer 1 (tab. 2.5).

Table 2.5: Vertical calculated excitation energies (ω_{ex}) [eV] and oscillator strengths (f , in parenthesis) of the first four excited singlet states of o-, m- and pNPA at their equilibrium geometries at the riCC2/def2-TZVP level of theory.

Occ. orb.	oNPA			mNPA	pNPA
	conf. 1	conf. 2	conf. 3		
	ω_{ex} (f)				
$\text{NO}_2(n)$	3.78 (0.02)	3.75 (0.02)	3.68 (0.00)	3.80 (0.00)	3.79 (0.00)
$\text{NO}_2(n')$	4.55 (0.02)	4.43 (0.00)	4.37 (0.00)	4.46 (0.00)	4.48 (0.00)
$Bz(\pi)$	4.29 (0.02)	4.54 (0.02)	4.38 (0.00)	4.01 (0.02)	4.21 (0.35)
$Bz(\pi')$	5.24 (0.08)	5.30 (0.11)	4.91 (0.20)	4.60 (0.20)	4.47 (0.01)
$\text{COO}^-(\sigma, n)$	4.93 (0.00)	4.86 (0.00)	4.84 (0.00)	4.89 (0.07)	5.23 (0.04)
$\text{COO}^-(n_\pi)$	4.37 (0.02)	5.01 (0.01)	4.60 (0.02)	5.24 (0.06)	4.71 (0.00)

2.3.4 Singlet Excited States

All isomers of NPA exhibit two practically dark, local excited states at the nitro group with excitation energies of 3.8 eV ($n \rightarrow \pi^*$) and 4.4 eV ($n' \rightarrow \pi^*$) and $f < 0.001$. These excitations are mainly characterized by the transition of an electron from one of the nonbinding (n) orbitals at the nitro group to its π^* orbital. Due to their local character they are closely related to the 1^1A_2 and 1^1B_2 state of nitrobenzene in C_{2v} symmetry. For a summary of the excited states of the parent compound nitrobenzene including symmetry, molecular orbitals as well as attachment and detachment densities see fig. 4.1. In case of nitrobenzene the $n \rightarrow \pi^*$ excitation is symmetry allowed but dark due to missing orbital overlap, whereas the $n' \rightarrow \pi^*$ excitation is symmetry forbidden. Within the triplet manifold these local excited states are found with almost unchanged character at approximately 0.3 eV lower energies.

The third possible $n \rightarrow \pi^*$ excitation at the nitro group originating from the energetically most unfavorable n -orbital with local π -symmetry (from now on referred to as n_π -orbital) is counter-intuitively found at much higher excitation energies of about 6 eV within the singlet manifold. Within the triplet manifold, however, this $n_\pi \rightarrow \pi^*$ state is lower in energy than the $n' \rightarrow \pi^*$ state and has about the same energy as the $n \rightarrow \pi^*$ state in the singlet manifold (S_1). This degeneracy will turn out to be important as a prerequisite for the unusually fast inter-system crossing (ISC) preceding the slow release of CO_2 (see below).

Besides the local excitations at the nitro group, two energetically low-lying states with CT character have been identified, each corresponding to single electron transitions from occupied orbitals at the benzene ring (HOMO and $Bz(\pi')$) to the LUMO, which are mainly located at the nitro group. At the level of riCC2, one of them is almost dark, while the other one is bright. Compared to nitrobenzene, these states are closely related to the 1^1B_1 (symmetry forbidden,

dark, $Bz(\pi) \rightarrow L$, 4.8 eV) and 2^1A_1 state (allowed, bright, $Bz(\pi') \rightarrow L$, 5.3 eV) of the parent compound.

While the order of these states is the same for all isomers of NPAA, for *o*- and *m*NPA and for nitrobenzene, it differs for *p*NPA. For the latter, the bright state is the energetically lower-lying $Bz(\pi) \rightarrow \pi^*$ state, while the $Bz(\pi') \rightarrow \pi^*$ state is dark. Close analysis of the orbitals and difference density plots reveals that this is due to the particular substitution pattern of *p*NPA. Obviously, the relative position of the substituents favors the former $Bz(\pi')$ of nitrobenzene over the $Bz(\pi)$ in such a way that these orbitals as well as the respective excited states swap order. The absence of this swap in *p*NPAA is probably due to the smaller impact of a neutral acetic acid group onto orbital energies than of the anionic carboxylate in NPA. Nevertheless, the orbital energies of $Bz(\pi)$ and $Bz(\pi')$ of *p*NPAA are more similar with a difference of only 0.05 eV than the corresponding ones of *o*- and *m*NPAA with a difference of 0.3 eV.

Again, this is also reflected in the excitation energies of the respective CT states ($Bz(\pi) \rightarrow \pi^*$ and $Bz(\pi') \rightarrow L$) originating from these orbitals. The different impact of the charged carboxylate versus the neutral carboxylic acid becomes even more evident from a comparison of these CT states of NPA to those of NPAA. While for NPAA excitation energies of both CT states are very close to those of the respective isomer of nitro-toluene (NT), these states are strongly red-shifted in NPA. In the orbital picture, the reason for this influence can be found in a contribution of the $COO^-(\sigma, n)$ -orbital to the $Bz(\pi)$. Due to the excess charge at the acetate group these usually low lying oxygen *p*-orbitals at the carboxylate energetically encounter the benzene π -orbitals resulting in mutual exchange of character. This is the case for all three isomers of NPA and also NPAA and it becomes apparent from the difference-density plots of the respective excited state (fig. 2.5).

Since the $COO^-(\sigma, n)$ -orbital has a binding contribution with respect to the $H_2C - CO_2$ bond, one may assume that a depopulation of the $Bz(\pi)$ within the $Bz(\pi) \rightarrow \pi^*$ excited state reduces the barrier for decarboxylation. To corroborate this assumption, the geometry of the isomers has been optimized in the $Bz(\pi) \rightarrow \pi^*$ excited state yielding equilibrium structures of *m*- and *p*NPA with $H_2C - CO_2$ bond lengths of about 180 pm and 170 pm, respectively. Compared to a bond length of 155 pm in the ground state, this equilibrium structure of the $Bz(\pi) \rightarrow \pi^*$ state of *m*- and *p*NPA clearly exhibits a pre-dissociated bond. Although the difference density of the $Bz(\pi) \rightarrow \pi^*$ state of *o*NPA is similar to *m*- and *p*NPA, the geometry optimization of *o*NPA in this state did not yield such a converged equilibrium structure. Since the reason for this failure is directly connected to the competing photochemical pathway of *o*NPA it will be analyzed and discussed in detail below.

2.3.5 Triplet Excited States

Let us now turn to the triplet states, which are crucial for the photochemistry of NPA and nitrobenzyl compounds in general due to their unusually fast and efficient ISC occurring on a time-scale of a few ps with triplet quantum yields >0.6 .^{64;65} In general, the triplet states calculated at the Franck-Condon (FC) point are very similar to the singlet states, thus allowing for direct comparison. The $n \rightarrow \pi^*$ (T_1) and $n' \rightarrow \pi^*$ (T_4) excited states are both about 0.3 eV lower in energy than their corresponding singlet-states. As already mentioned, the

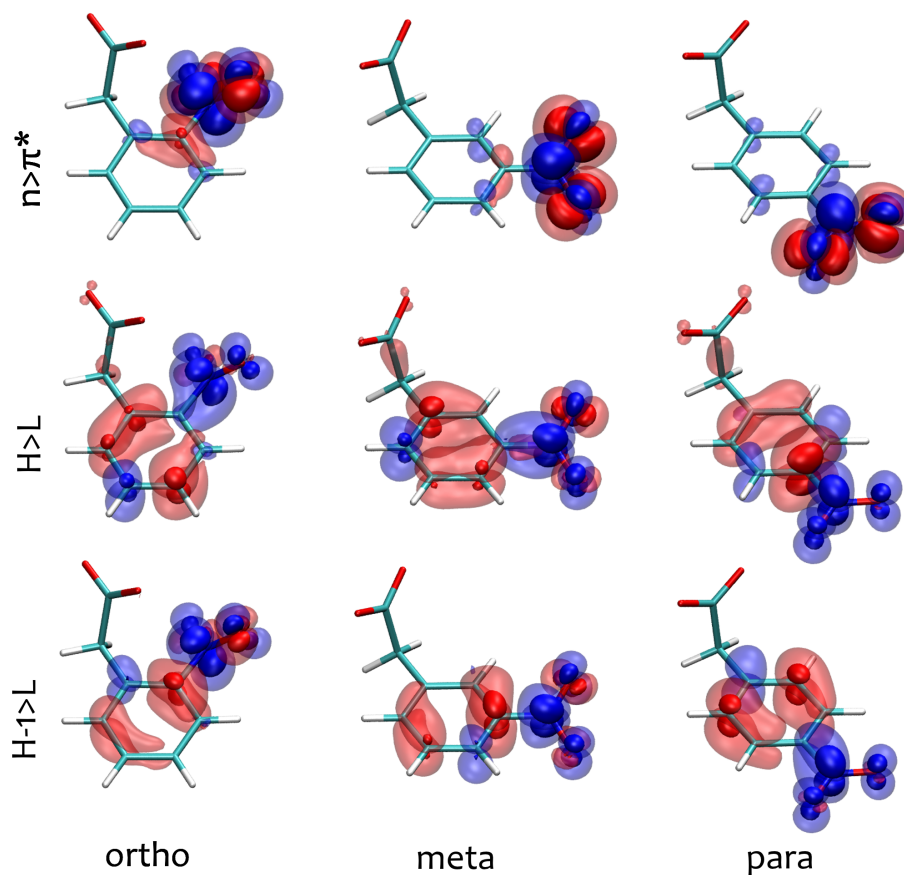


Figure 2.5: Difference-density plots of the $n \rightarrow \pi^*$ (top), $Bz(\pi) \rightarrow \pi^*$ (middle) and $Bz(\pi') \rightarrow \pi^*$ (bottom) state of *o*-, *m*- and *p*NPA (from left to right) at the CIS/def2-TZVP level of theory. The transparent surfaces are rendered using an isovalue of 0.002 (to include minor contributions), while the opaque surfaces correspond to an isovalue of 0.01 (to show major contributions). Regions of increasing density are blue, while red areas show a decrease in density.

$n_\pi \rightarrow \pi^*$ state (T_3) exhibits a much larger singlet/triplet-splitting of about 3 eV, placing it at an excitation energy of 3.7 eV in the triplet manifold.

The unusually fast ISC of nitrobenzylic compounds can be explained considering El Sayed’s rules.²⁷ According to El Sayed $S_n(n \rightarrow \pi^*)$ to $T_n(\pi \rightarrow \pi^*)$ or $S_n(\pi \rightarrow \pi^*)$ to $T_n(n \rightarrow \pi^*)$ ISC is usually fast, whereas $S_n(n \rightarrow \pi^*)$ to $T_n(n \rightarrow \pi^*)$ or $S_n(\pi \rightarrow \pi^*)$ to $T_n(\pi \rightarrow \pi^*)$ ISC is about three orders of magnitude slower. The analysis of the character of the excited states possibly involved in the ISC process of NPA and nitrobenzylic compounds in general reveals that all exhibit a local $n_\pi \rightarrow \pi^*$ excited triplet state at the nitro group, which is practically degenerate with the $n \rightarrow \pi^*$ excited S_1 state. Computations along various vibrational modes of the nitro group further show that these two states of different multiplicity intersect readily. Thus, all requirements for fast ISC obeying El-Sayed’s rule are met for ISC from S_1 ($n \rightarrow \pi^*$) to the ($n_\pi \rightarrow \pi^*$) triplet state. Subsequently, ultra-fast internal conversion to T_1 takes place within a few picoseconds as can be seen from the increase of the $T_1 \rightarrow T_n$ absorption in the 667 nm transients (fig. 2.3). The characteristic, broad triplet excited state absorption of the nitrobenzylic moiety at 450 nm and 650 nm visible in the experiment can be assigned at the level of riCC2. While the absorption at 650 nm corresponds to the excitation from the T_1 state to the excited ($n' \rightarrow \pi^*$) triplet state, the excited state absorption at 450 nm originates from an excitation into the $Bz(\pi') \rightarrow \pi^*$ triplet state.

2.4 Discussion

2.4.1 Summarising Earlier Findings

The previous UV-pump IR-probe²⁸ and the new UV-pump VIS-probe experiments demonstrate that the evolution of the absorption transients is completed after about two nanoseconds, which roughly equals the lifetime of the excited triplet state of the parent nitrobenzene (see chapter 4). The low-lying triplet state has been inferred to be the precursor state of slow CO_2 release from pNPA⁴³ and probably also from o- and mNPA. The fast release of CO_2 from o- and mNPA observed experimentally after less than one picosecond can originate only from vibronically excited singlet states, since neither vibrational cooling with a typical time-scale of 1–10 ps²⁵ nor ultra-fast ISC of nitroaromatic compounds with a similar time-scale can compete. The same argument applies to the quenching processes responsible for the ten times lower quantum yield of CO_2 release from oNPA. To efficiently compete with ISC and fast CO_2 release this deactivation channel must take place at least on the same sub-picosecond time-scale, thus excluding sophisticated equilibration with the environment as well as ISC processes.

2.4.2 Mechanism of Photo-Decarboxylation

Let me first turn to the discussion to mNPA, since this isomer exhibits both channels of CO_2 release. Subsequently, the absence of the fast component in pNPA as well as the quenching pathway responsible for the low uncaging quantum yield in oNPA will be explained. Eventually, since the competing H-transfer pathway represents the initial step of the uncaging reaction of conventional oNB caging groups, I will close the discussion with implications and predictions for

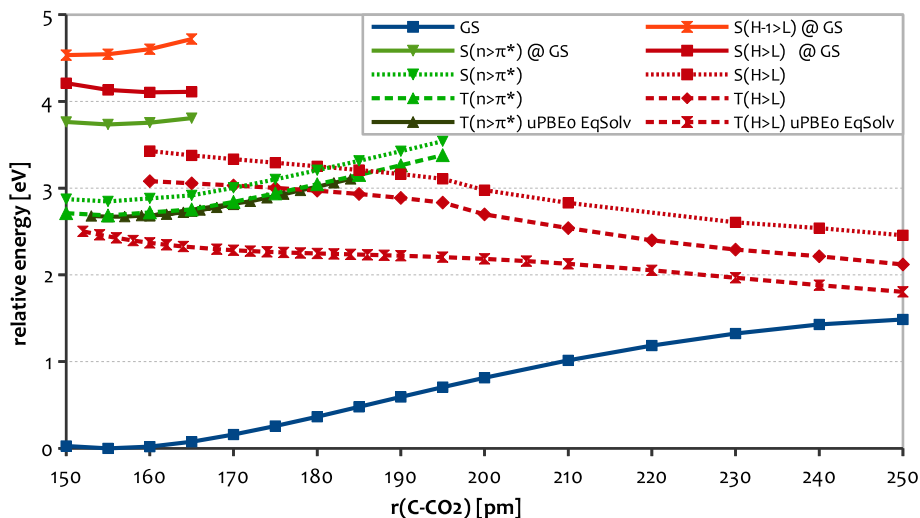


Figure 2.6: Cut through the relaxed potential energy surfaces along the decarboxylation coordinate of mNPA. The Figure includes the ground state (blue) as well as $Bz(\pi) \rightarrow \pi^*$ (termed $S(H>L)$, red) and $n \rightarrow \pi^*$ (green) excited singlet (dotted) and triplet (dashed) states at the riCC2/def2-TZVP/COSMO level of theory and furthermore the $Bz(\pi) \rightarrow \pi^*$ (termed $T(H>L)$) and $n \rightarrow \pi^*$ triplet states at the uPBE0/def2-TZVP level of theory. Except for the excited states close to the Franck-Condon point, the curves correspond to the relaxed surfaces obtained using non-equilibrium solvation for riCC2 and equilibrium solvation for uPBE0. All curves are shown relative to the optimized ground state geometry.

the design of improved oNB caging groups. To provide a first framework for the discussion, the time-scale of the fast CO_2 release within 500 fs can be related to relevant molecular vibrations. In this simple picture, it corresponds to just 20 periods of the normal mode resembling the decarboxylation coordinate (1600 cm^{-1}), which is mainly the stretching of the C-CO₂- bond.²⁸ Obviously, such fast processes cannot involve a complicated molecular mechanism but rather take place within a single step. As already mentioned, the $Bz(\pi) \rightarrow \pi^*$ excited state of NPA is a possible candidate for fast CO_2 release, since it exhibits a pre-dissociated bond between the carboxylate and the remaining molecule and might therefore allow for fast, barrierless decarboxylation in a single step. Although it is not the energetically lowest state at the FC point but rather the second one, it is located only slightly above the lowest state ($n \rightarrow \pi^*$) for m- and pNPA (by 0.2 eV). However, within the first 500 fs after the initial UV excitation of mainly the bright $Bz(\pi') \rightarrow \pi^*$ state, the excited state population will be distributed over all excited states below the initially excited one, also including the reactive $Bz(\pi) \rightarrow \pi^*$ state.

To further investigate the possibility of fast CO_2 release from this $Bz(\pi) \rightarrow \pi^*$ excited state, relaxed scans of the singlet PES have been calculated along the decarboxylation coordinate (fig. 2.6). As expected, the surface of the $Bz(\pi) \rightarrow \pi^*$ excited state (S_2) facilitates a barrierless, exothermic decarboxylation.

However, ultra-fast decarboxylation from the minimum of the first $n \rightarrow \pi^*$ excited state (S_1) possibly *via* a conical intersection (CI) between the $n \rightarrow \pi^*$

and $\text{Bz}(\pi) \rightarrow \pi^*$ excited states is very unlikely because of a high energy barrier. This can be estimated from the difference of more than 2 eV between the energies of the $n \rightarrow \pi^*$ and $\text{Bz}(\pi) \rightarrow \pi^*$ states at the $n \rightarrow \pi^*$ equilibrium geometry (not shown in Fig. 5). Nevertheless, considering the ultra-fast experimental time-scale of this early decarboxylation, cooling and internal conversion into the S_1 state will most certainly be incomplete prior to decarboxylation. Instead, the excited-state population will rather still be distributed over all the different electronic states below the bright $\text{Bz}(\pi') \rightarrow \pi^*$ state, which includes the reactive $\text{Bz}(\pi) \rightarrow \pi^*$ state, in which ultra-fast decarboxylation can compete with further relaxation into S_1 .

Regarding the PES and time-scale of the fast release of CO_2 , the following mechanism can be postulated. Upon initial excitation into the bright $\text{Bz}(\pi') \rightarrow \pi^*$ state, a minor part of excited mNPA molecules undergoes fast decarboxylation *via* the $\text{Bz}(\pi) \rightarrow \pi^*$ state yielding ground-state CO_2 and an electronically excited *meta*-nitrotoluene anion. In the meantime, the majority of the excited-state population cools down into the minimum of the $n \rightarrow \pi^*$ excited singlet state, from where ISC efficiently takes the molecules into the triplet manifold. This is corroborated by the UV-pump VIS-probe experiments on NPA (Section 2), where the transients recorded at 667 nm demonstrate the rising triplet excited-state absorption with a time-scale of approx. 2-4 ps, depending on the isomer. As already mentioned in the previous section, this excited-state absorption at 667 nm can be assigned to the $T_1(n \rightarrow \pi^*)$ to $T_3(n' \rightarrow \pi^*)$ excited-state absorption according to riCC2 calculations.

Assuming that almost every molecule undergoing ISC subsequently undergoes decarboxylation, the typical triplet yield of nitrobenzylic compounds of 0.6-0.8 agrees nicely with the measured quantum yield of CO_2 release of m- and pNPA of 0.6. The time-scales of ISC and the occurrence of slow CO_2 release however do not. Although the excited-state population will have crossed into the triplet manifold almost completely after only 10 ps, slow CO_2 release occurs with a time-scale of about 200 ps. This is surprising, since at first glance the triplet PES facilitates decarboxylation more than the respective singlet PES, which is due to the larger singlet/triplet-splitting of the $\text{Bz}(\pi) \rightarrow \pi^*$ excited state compared to the $n \rightarrow \pi^*$ excited state. Consequently, the reactive state is energetically closer to the lowest triplet and one would expect a formation of CO_2 within the first few picoseconds after ISC in analogy to the fast release from the singlet manifold. However, to arrive in the reactive $\text{Bz}(\pi) \rightarrow \pi^*$ excited triplet state from the $n \rightarrow \pi^*$ excited T_1 a crossing between the respective states has to be reached. In contrast to the fast release from the singlet manifold, the assumption that the population is distributed over the lower states is no longer valid. Instead, as suggested by the 667 nm excited-state absorption, the population has already dissipated a large fraction of the initial vibrational excess energy into the surrounding and is localized in the minimum of the $n \rightarrow \pi^*$ excited T_1 state. At this equilibrium geometry, the reactive $\text{Bz}(\pi) \rightarrow \pi^*$ state is energetically almost 1 eV above the relaxed minimum, which obviously prevents instantaneous decarboxylation.

If, however, an excited-state optimization of the $\text{Bz}(\pi) \rightarrow \pi^*$ state is carried out at riCC2 level, the energy gap between T_1 and $\text{Bz}(\pi) \rightarrow \pi^*$ triplet state is reduced to 0.3 eV. Arguing with these energies, one has to keep in mind that for the excited-state optimizations the non-equilibrium approach, i.e. the frozen ground state COSMO-field, was employed. As already discussed in section

3, one can expect a state like the $\text{Bz}(\pi) \rightarrow \pi^*$ excited state with substantial CT character and thus exhibiting a significantly different charge distribution to profit more from the relaxation of the solvent shell than the locally excited T_1 state. To estimate this impact of the relaxation of the solvent field onto the different states, the geometries of both states were optimized using unrestricted ground state DFT (uPBE0) together with the equilibrium COSMO approach. Finally, relaxed PES along the decarboxylation coordinate for both $\text{Bz}(\pi) \rightarrow \pi^*$ and $n \rightarrow \pi^*$ states employing equilibrium solvation at the PBE0/def2-TZVP/COSMO level of theory have been obtained.

The result of these calculations is as expected. Within a completely equilibrated solvent shell, the relaxed surface of the reactive $\text{Bz}(\pi) \rightarrow \pi^*$ excited state is energetically significantly below the $n \rightarrow \pi^*$ excited state throughout the PES of the PDC (fig. 2.7). After all, it seems that the delay of the slow release of CO_2 is caused by an efficient trapping of the population in the minimum of the $n \rightarrow \pi^*$ excited triplet state. With the remaining vibrational energy of the molecules being too low to directly access the reactive $\text{Bz}(\pi) \rightarrow \pi^*$ state, this trapping may only be broken by thermal fluctuations of solvent shell and molecular geometry that cause the $\text{Bz}(\pi) \rightarrow \pi^*$ state to become energetically accessible. Obviously these fluctuations cause slow CO_2 release to take place on a time-scale of 200 ps.

Let me turning to pNPA, where fast CO_2 release is absent while the slow component is essentially identical to mNPA. To explain this difference, I calculated the PES of the relevant excited singlet-states along the decarboxylation coordinate. Comparing the corresponding minimum energy pathways for the $\text{Bz}(\pi) \rightarrow \pi^*$ state of m- and pNPA uncovers that the shape of the singlet $\text{Bz}(\pi) \rightarrow \pi^*$ state is different. While a repulsive curve was found for the $\text{Bz}(\pi) \rightarrow \pi^*$ state of mNPA, the singlet $\text{Bz}(\pi) \rightarrow \pi^*$ optimized surface of pNPA is virtually flat. This difference between the PES of m- and pNPA can be traced back to the conjugation of the aromatic p -orbitals of the benzylic CH_2 -group and the nitro group through the π -system, which is possible in o- and pNPA but not in mNPA. To understand the complete absence of the fast component in pNPA, one has to recall that even for the much more repulsive $\text{Bz}(\pi) \rightarrow \pi^*$ excited state of mNPA only a minor part of the population undergoes fast decarboxylation. Obviously, for the essentially flat $\text{Bz}(\pi) \rightarrow \pi^*$ state of pNPA, competing internal conversion and inter-system crossing are more efficient than early decarboxylation *via* the $\text{Bz}(\pi) \rightarrow \pi^*$ excited singlet state. In an earlier work,²⁹ I suggested that the absolute energy of the repulsive $\text{Bz}(\pi) \rightarrow \pi^*$ state, which is about 0.2 eV lower in mNPA (tab. 2.5), causes the mNPA molecules to have larger vibrational excess energy, which thus undergo fast decarboxylation more readily than pNPA. However, my new calculations involving explicit as well as continuum solvation, this difference of 0.2 eV vanishes completely.

In contrast to the singlets, the shape of the PES of the $\text{Bz}(\pi) \rightarrow \pi^*$ excited triplet state as well as the other triplet states is virtually identical to mNPA. Thus, it is clear that after ISC the photochemistry of pNPA is the same as proposed for mNPA, explaining the similar timings of slow CO_2 release observed.

Let me finally turn to oNPA. Here, the observed over-overall quantum yield of CO_2 release is almost 15-fold lower than in m- and pNPA. The experiments show almost complete suppression of the slow release, whereas the fast release exists even though the amount of CO_2 released *via* this channel is small. Already in 1969, Magerum et al. inferred a proton-transfer from the benzylic methylene

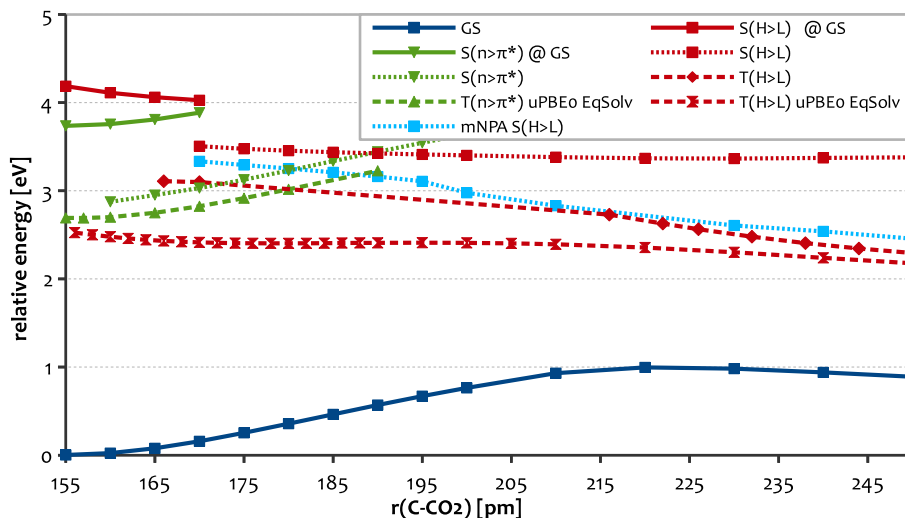


Figure 2.7: Cut through the relaxed potential energy surfaces along the decarboxylation coordinate of pNPA. Displayed is the ground state (blue) as well as Bz(π) \rightarrow π^* (termed, S(H>L), red) and $n \rightarrow \pi^*$ (green) excited singlet (dotted) and triplet (dashed) states at the riCC2/def2-TZVP/COSMO level of theory and furthermore the Bz(π) \rightarrow π^* (termed, T(H>L)) and $n \rightarrow \pi^*$ triplet states at the uPBE0/def2-TZVP level of theory. Except for the excited states close to the Franck-Condon point, the curves correspond to the relaxed surfaces obtained using non-equilibrium solvation for riCC2 and equilibrium solvation for uPBE0. All curves are shown relative to the optimized ground state geometry.

group to the nitro group to provide an alternative deactivation channel.⁴¹ However, according to Turro’s Rule, $n \rightarrow \pi^*$ excited carbonyl groups are by no means bases, but exhibit a similar reactivity as oxygen-centered radicals, which readily undergo H-abstraction.⁶⁶ Consequently, the competing reaction is presumably a H-abstraction at the benzylic position by the $n \rightarrow \pi^*$ excited nitro group, or in other word an intramolecular excited-state hydrogen-transfer (ESIHT).

For clarification, minimum energy pathways for H-transfer and decarboxylation were computed on the singlet- and triplet $n \rightarrow \pi^*$ and Bz(π) \rightarrow π^* excited state surfaces. In contrast to m- and pNPA, the minimum energy pathway for decarboxylation in the Bz(π) \rightarrow π^* excited state could not be obtained since the numerical procedures did not converge. The investigation of this failure was instructive, as it delivered an explanation for the high quenching efficiency *via* excited-state H-transfer. If the geometry of oNPA is optimized in the Bz(π) \rightarrow π^* excited state, the nitro group turns into the plane of the benzene ring. The planarization of the conjugated system consisting of nitro group and benzene ring causes the nitro group and in particular the $\text{NO}_2(n)$ orbital to approach the benzylic methylene group. Due to the resulting steric interaction the energy of this n -orbital and in particular of the contributing p -orbital of one of the oxygen atoms increases, finally leading to an admixture of $\text{NO}_2(n)$ character to the Bz(π). Consequently, the Bz(π) \rightarrow π^* excited state gains increasing $n \rightarrow \pi^*$ character, which in combination with the spatial proximity of the benzylic hydrogen to the nitro group readily causes the optimization to run into the H-transfer

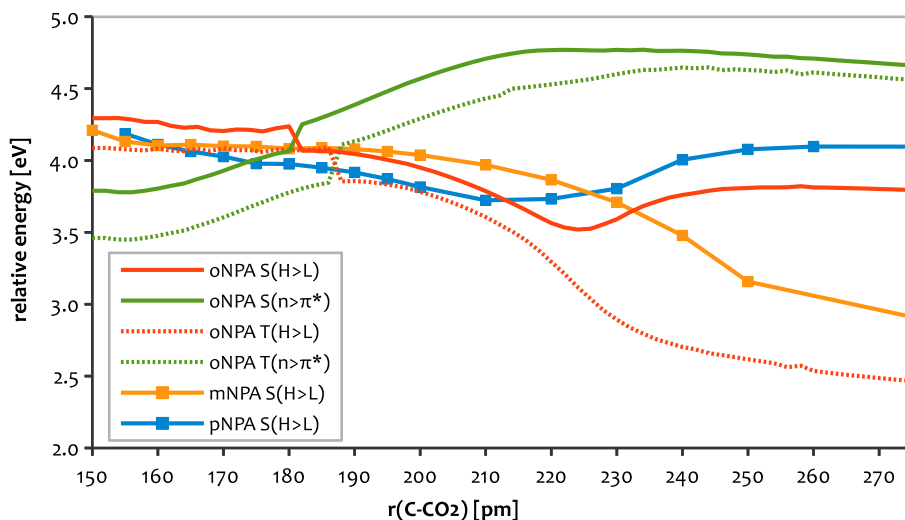


Figure 2.8: Cut through the ground-state optimized potential energy surface of $Bz(\pi) \rightarrow \pi^*$ excited (red curves) and $n \rightarrow \pi^*$ excited (green curves) singlet (solid curves) and triplet (dashed curves) states along the decarboxylation coordinate of oNPA at the riCC2/def2-TZVP/COSMO level of theory using non-equilibrium solvation.

coordinate instead of the desired decarboxylation coordinate. In conclusion, the geometry relaxation on the surface of the precursor state for decarboxylation also facilitates and thereby triggers the competing H-transfer, which also justifies the very efficient quenching.

Since I was unable to obtain the relaxed $Bz(\pi) \rightarrow \pi^*$ excited-state surface for oNPA due to the issues discussed above, the discussion is restricted to either unrelaxed or ground-state relaxed PES for the investigation of the decarboxylation. From a comparison of the analogous surfaces of mNPA with the corresponding $Bz(\pi) \rightarrow \pi^*$ relaxed one, it becomes apparent that the ground-state optimized PES resembles the actual $Bz(\pi) \rightarrow \pi^*$ optimized surface much better than the non-relaxed curves. This is most certainly due to the absence of two energetically very important relaxation processes, which in a similar fashion seem to occur in the ground and relevant excited states. These processes are the formation of CO_2 from the carboxylate (linearization) as well as the change in hybridization of the benzylic carbon from sp^3 to sp^2 accompanied by an in-plane motion of the two benzylic H-atoms.

In general, the ground-state optimized PES of the PDC of oNPA is very similar to that of pNPA. It exhibits a similar minimum at $r(CC) = 220$ pm, whereas the triplet state is repulsive equivalent to the respective states of m- and pNPA. In contrast to m- and pNPA, the singlet and triplet $Bz(\pi) \rightarrow \pi^*$ and $n \rightarrow \pi^*$ excited states do not really intersect but rather exhibit an avoided crossing. This can be traced back to the mentioned admixture of the $Bz(\pi)$ and the respective n -orbital, which is absent for m- and pNPA due to the larger energetic distance between these orbitals. For oNPA, instead of the excited states, the involved orbitals consecutively change character, thereby avoiding a direct intersection of the surfaces.

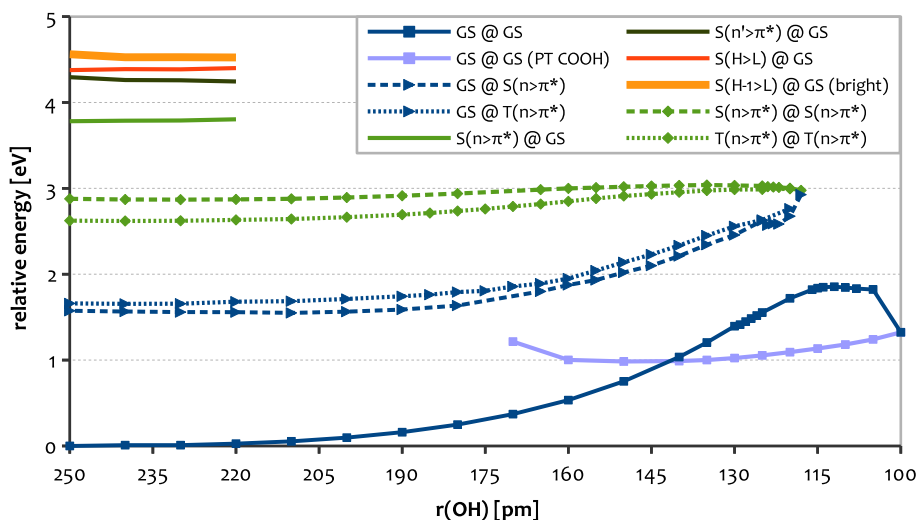


Figure 2.9: Cut through the relaxed potential energy surface along the H-transfer coordinate of oNPA. Singlet as well as triplet $n \rightarrow \pi^*$ excited states allow for an almost barrierless H-transfer eventually leading to a conical intersection with the electronic ground state.

Considering the similarities of the PES of o- and pNPA one would expect oNPA to exhibit the same photochemistry as pNPA, when actually the opposite is the case. This has been traced back to an efficient, competing H-transfer channel. However, due to the issues preventing a calculation of the full PES of oNPA and the ambiguous picture comparing calculated and measured excitation energies the picture of the PDC of oNPA is incomplete in contrast to m- and pNPA and should be taken with a grain of salt. To further corroborate this picture of the PDC of oNPA and quantify the relation of H-transfer and PDC quantum-dynamical simulations of nuclear motion would in principle be necessary.

2.4.3 Excited-State Hydrogen-Transfer in oNPA

The excited-state H-transfer quenching the PDC in oNPA is the initial uncaging step of typical oNB caged compounds and thus of wider interest. The discussion of the H-transfer channel in oNPA is carried out in the background of the findings for related oNB compounds, while it is assumed that the similarities of the molecules and the PES of the H-transfer allow for a direct comparison. Considering the strictly local character of the involved excited-states of the nitro group, this assumption is certainly satisfied.

Several experimental and theoretical investigations of this H-transfer reaction have been carried out for related oNB compounds, demonstrating that this H-transfer reaction can occur from the singlet manifold as well as from the triplet manifold.⁴⁵ In these most recent studies the formation of the aci-form, i.e. the hydrogen transfer, of *ortho*-nitrotoluene (oNT) and *ortho*-nitrobenzylacetate (oNBA) was investigated using UV-pump Raman-probe as well as VIS-probe spectroscopy with 200 fs time resolution. It is suggested that the formation of

the aci-form in oNT and oNBA occurs on a 1-10 ps and another 2 ns time-scale, corresponding to singlet and triplet channels. For oNBA it was further established that both channels equally contribute to the formation of the reactive aci-form.

As shown in fig. 2.9, the minimum-energy pathway for H-transfer in oNPA is very flat and exhibits only a small barrier, which is 0.2 eV on the singlet surface and 0.3 eV on the triplet surface at the theoretical level of riCC2. Starting at $r(\text{OH}) = 250$ pm and following the $n \rightarrow \pi^*$ optimized surface to the right, it directly leads into a conical intersection with the ground state at $r(\text{OH}) = 120$ pm. The origin of this interaction is a change in hybridization (sp^3 to sp^2) of the benzylic carbon due to hydrogen abstraction. Consequently, the excited-state H-transfer inevitably forces the singlet excited-state population back in the electronic ground state, accompanied by a rearrangement of the π -system. Thereby the aromatic conjugation is broken and two new double bonds, one to the former benzylic carbon and another to the nitrogen, are established. The resulting system of six conjugated double bonds now includes the carboxylate as well as the nitro group (fig. 2.10). The configuration of the generated C=C double bond can take both, E or Z configuration depending on the starting geometry of the H-transfer pathway (conformer 1 leads to Z, conformer 2 leads to E). The energy difference of these pathways is the same as for the conformers and its value of about 0.1 eV is small enough to expect a formation of both isomers. The new C=N bond on the contrary will always exhibit Z configuration if the H-transfer takes place in the singlet manifold, since this configuration is the direct result of the H-transfer. Subsequent isomerization by CN rotation or O-to-O proton transfer can most certainly be excluded, since these would have to take place in the ground state, where both exhibit a huge barrier >1 eV according to riCC2 and uPBE0. The triplet population undergoing H-transfer is, however, trapped in its spin state. This prevents relaxation to the ground state as can already be seen at the long-lived triplet absorption at 667 nm of oNPA. Here, the H-transfer product rather exhibits a double-radical character instead of the terminal double bonds (fig. 2.10). Analysis of the singly occupied molecular orbitals (SOMOs) shows that the unpaired electrons are mainly located at the nitrogen and the benzylic carbon with significant contributions at the oxygen atom of the nitro group and further small contributions distributed amongst the whole conjugated backbone. A very similar electronic structure has been found for oNT.⁴⁵ In such a system the barrier for rotation around the bonds to the benzylic and nitro groups is much lower (for CN 0.1 eV and for CC 0.3 eV), which in contrast to the singlet route allows for formation of all possible aci-isomers. Regarding available vibrational excess energy and barrier heights (fig. 2.9), one would initially expect the triplet H-transfer products to be in a dynamic equilibrium between all isomers, mainly yielding the thermodynamically most stable EE and ZE-aci-isomers after cooling and subsequent ISC to the GS.

In addition to the configuration of the double bond, the NOOH group can take two different conformations for each isomer, in which the hydrogen is either pointing outwards (anti, ONOH dihedral 180) or inwards (syn, ONOH dihedral 0). The syn-conformation is more favorable by about 0.1 eV with a 0.2 eV barrier towards anti. Considering the amount of vibrational excess energy left (over) from the initial excitation and subsequent relaxation processes, one can expect syn and anti-conformation to be in a dynamic equilibrium with the vast majority

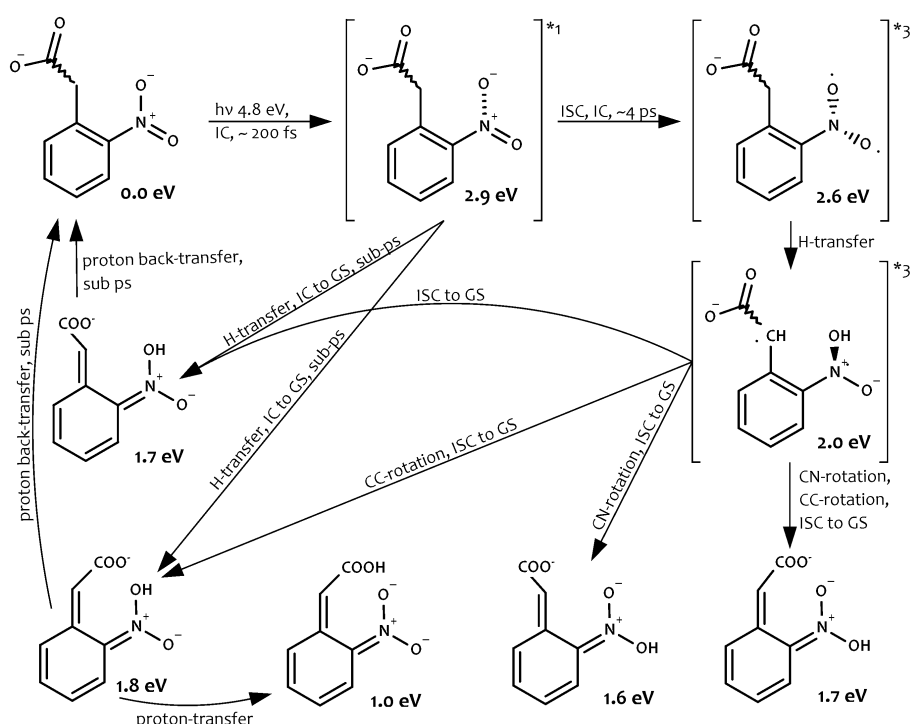


Figure 2.10: Suggested photochemistry of oNPA after UV excitation. Although H-transfer may occur *via* a singlet or triplet pathway, mainly the triplet route yields stable aci-isomers, while the initial photo products of singlet H-transfer largely undergo proton-backtransfer.

of the population exhibiting syn-conformation. Due to these circumstances I will not consider these rotamers explicitly in the following discussion and usually refer to the more favorable syn-conformation if not mentioned otherwise.

After H-transfer and subsequent IC or ISC the molecules reach the GS, where a number of subsequent reactions are possible depending on the conformation of the double bonds formed and the available vibrational excess energy. The latter will be much higher for the molecules originating from the singlet pathway, since they will presumably reach the electronic ground state within a few picoseconds after the initial excitation. The molecules undergoing triplet H-transfer, however, will reach the GS after several hundreds of picoseconds as follows from the late, second increase of the 400 nm aci-signal in the experiments. Thus they will have spent much more time cooling and equilibrating with the solvent.

Molecules exhibiting a E (C=C) Z (C=N) configuration (EZ-aci) will almost completely undergo proton-backtransfer, which becomes evident from a comparison of the shallow minimum of the EZ-aci form (barrier < 0.3 eV) with the large amount of vibrational excess energy available (singlet/triplet surface > 1 eV above GS surface) and furthermore the largely exothermic energy balance of the proton-backtransfer (> 1.5 eV).

The ZZ-aci isomers can be stabilized *via* an ionic intramolecular H-bridge, which is readily formed between the aci-proton (requires anti-conformation of

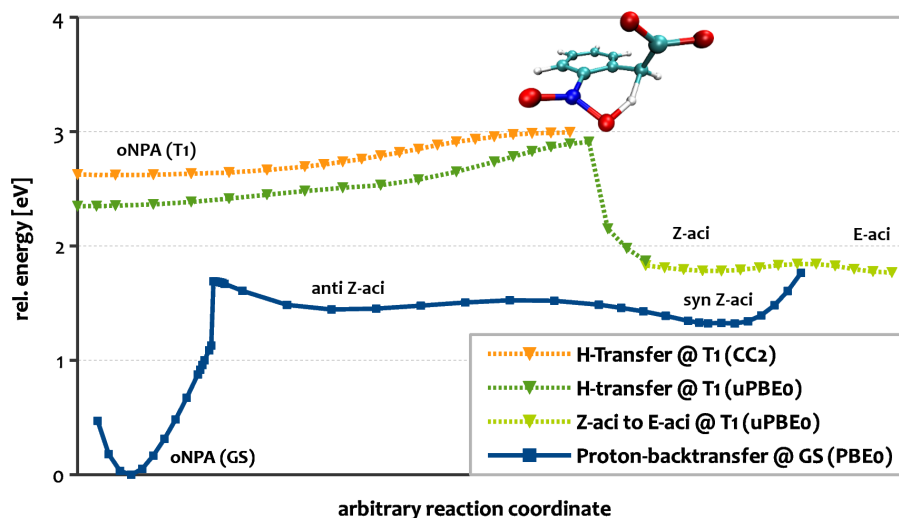


Figure 2.11: Energy profile of the H-transfer (O-H scan) and C=N rotation (CCNO dihedral scan from EZ-aci to ZE-aci) in T_1 as well as proton-backtransfer including syn-EZ-aci to anti-EZ-aci isomerization (C-H scan) in the GS for oNPA at the uPBE0/def2-TZVP level of theory using COSMO equilibrium solvation. For comparison, the results of corresponding CC2 calculations using non-equilibrium solvation are also shown (orange curve). In the top-right corner the maximum-energy structure along the H-transfer coordinate is given.

NOOH) and the carboxylate group. Following the formation of this H-bridge, barrierless proton-transfer to the carboxylate and further relaxation may occur, which would yield a total stabilization of almost 1 eV compared to the original EZ-aci form (fig. 2.11). Nevertheless, it seems that a majority of the population of the ZZ-aci form will also undergo proton-backtransfer, which can be concluded from the UV pump VIS probe experiments. There, a strong absorption ($f = 0.2$) of the stabilized photoproduct which riCC2 predicts at 530 nm (2 eV) is not detected. Exclusively originating from the triplet pathway, ZE-aci and EE-aci isomers are the only ones for which proton-backtransfer is kinetically impossible in the ground state. Hence, one may suggest that the final yield of the aci-form depends on the part of the molecules undergoing triplet H-transfer and subsequent isomerization of the C=N double bond.

These predictions agree with experimental findings for oNT and *ortho*-nitro phenyl-methylether (oNPME), in which after UV excitation in an argon or nitrogen matrix almost exclusively the corresponding syn-EZ-aci and syn-EE-aci isomers were detected and identified by means of their calculated IR-absorption.⁶⁷ To explain the formation of ZE and EE-aci-isomers the isomerization of the double bond was suggested to occur in a triplet state, which is now confirmed by my calculations for oNPA.

Let me finally summarize the results for oNPA and relate them to the photochemistry of oNB compounds in general. Despite similar PES like pNPA, both channels of decarboxylation are efficiently suppressed. This suppression results from an excited-state intramolecular H-transfer, which occurs in the singlet as well as in the triplet manifold. Considering the much smaller amplitude of the

$T_1 \rightarrow T_n$ absorption of oNPA compared to m- and pNPA (fig. 2.3), I conclude that singlet H-transfer is by far the dominant pathway, while only a minor fraction undergoes triplet H-transfer. However, for the very efficient suppression of CO₂ release, the presence of both H-transfer pathways turns out to be essential. While the singlet H-transfer channel efficiently diminishes the singlet excited-state population prior to ISC, the remaining fraction of molecules undergoing ISC is further quenched by triplet H-transfer. In principle, decarboxylation and H-transfer are again competing in the triplet-manifold, as can be seen from the relatively slow but efficient CO₂ release from m- and pNPA *via* the Bz(π) \rightarrow π^* excited state, which also exists in oNPA. Here, in contrast to m- and pNPA the $n \rightarrow \pi^*$ excited T_1 is also a reactive state. Thus, instead of being trapped in T_1 until slow CO₂ release takes place as in case of m- and pNPA, the complete triplet population of oNPA undergoes H-transfer and subsequently ISC into the ground state takes place. In summary, this double quenching mechanism nicely explains the diminished quantum yield of fast CO₂ release in oNPA as well as the complete suppression of slow release and shows very good agreement with the UV-pump VIS-probe experiments.

Although the yield of the different EE, EZ, ZE and ZZ-aci-isomers is irrelevant for the decarboxylation of oNPA, it is of great relevance for the photochemistry of related oNB caged compounds, in particular with respect to the overall uncaging yield. It has been suggested that the formation of the aci-isomer is the yield-limiting step, because the subsequent steps starting with the aci-form exhibit a quantum yield of practically unity.^{31;45} In most of the recent studies on caged compounds it is generally assumed that only molecules with a Z-configured C=N bond reach the ground-state surface and further isomerization occurs *via* proton-exchange with solvent molecules.³¹ This contradicts findings of the matrix-isolation experiments,⁶⁷ in which exclusively E-aci isomers were detected. Furthermore, O-to-O proton transfer exhibits a barrier >1 eV in the ground state, while proton exchange is only possible in protic solvents and would furthermore occur on a time-scale of 100 ns in water at pH 7.43.

To estimate the aci-yield for the singlet and triplet channel in oNPA, the characteristic aci-absorption has to be investigated, which is predicted to occur at 400 nm (excitation energy=3.05 eV, $f=0.3$) for EZ and EE-aci-oNPA at the theoretical level of riCC2 (fig. 2.3). Indeed, the 400 nm transients for oNPA exhibit the expected characteristics: a very fast increase on a sub-ps time-scale corresponding to singlet H-transfer and another increase on a 10-100 ps time-scale which can most certainly be assigned to triplet H-transfer and inter-system crossing. However, these features cannot be quantitatively analyzed since they overlap with the long-lived, broad triplet absorption (maximum at 450 nm) and with the short-lived, broadband excited-state absorption. To roughly estimate the quantities of the aci-form generated *via* each channel, the 450 nm signal was directly subtracted from the 400 nm signal. The resulting double difference spectrum, which roughly relates to the concentration of the aci-form clearly shows that the vast majority is formed on longer time-scales *via* the triplet route, while there is only a small contribution from the fast singlet channel. This is explained by the calculations for oNPA, which established the existence of a proton-back transfer channel, which is readily accessible for molecules undergoing ultra-fast singlet H-transfer. Since further preliminary calculations for related compounds yielded similar results, triplet H-transfer is most likely the main channel for the formation of the reactive aci-form, while singlet H-transfer acts as loss channel

quenching uncaging.

Although it might seem contrary at first glance, my suggestions are in good agreement with results for oNBA.⁴⁵ It was reported that singlet and triplet H-transfer contribute both to aci-formation from oNBA to equal amounts. Considering that singlet H-transfer is much faster (0.1–1 ps) than ISC (2–4 ps) and that thus a much larger fraction of molecules undergoes singlet H-transfer and not ISC and subsequent triplet H-transfer, it is clear that triplet H-transfer is more efficient in forming the aci-form. To estimate the ratio of oNPA molecules undergoing singlet pathway versus those taking the triplet pathway, one may compare the 667 nm transients of oNPA with those of pNPA, for which no competing pathways exist in the singlet manifold. If it is further assumed that the triplet-absorption of both isomers exhibits similar f and fast decarboxylation of oNPA does not significantly contribute to the quenching, the at least four times larger amplitude of the triplet absorption of pNPA suggests that at the minimum 75% of the population of oNPA is quenched *via* singlet H-transfer prior to ISC. Assuming that these values are similar for oNBA, the aci-yield of the triplet H-route has to be about four times larger than the yield of the singlet route to explain the similar contribution of both.

Finally, I suggest focusing on the higher aci-yield of the triplet H-transfer pathway for the purpose of creating oNB cages with higher uncaging quantum yields, or in other words higher sensitivity. For that objective, the fraction of molecules undergoing ISC instead of singlet H-transfer needs to be increased, which can either be achieved by an acceleration of ISC or by constraining singlet H-transfer. To further increase the ISC of oNB compounds, an introduction of aromatic substituents containing heavy atoms that exhibit a large spin-orbit coupling (e.g. bromine, iodine) might help. To slow down singlet H-transfer, one might substitute one of the benzylic hydrogens by an inert, sterically demanding group. Although this also slows down H-transfer in the triplet case, this is not a problem since along this triplet pathway H-transfer is not the rate-limiting step. The second suggestion has already been employed trying to improve the water solubility of oNB cages, when a carboxylic group in alpha position was introduced, yielding so-called alpha-carboxy oNB (CNB) cages.⁶⁸ The latter indeed show an almost doubled uncaging yield compared with the original oNB cages,⁶⁸ which further substantiates the mechanistic picture presented here and suggests additional investigations of this possibility to improve the uncaging quantum yield.

2.5 Summary & Conclusion

Nitrophenylacetates (NPA) release CO₂ upon UV excitation, or in other words, undergo photo-decarboxylation (PDC). The *para*-isomer has recently been used as caged-CO₂ in biochemical investigations. Surprisingly the different structural isomers *ortho*-, *meta*- and *para*-NPA exhibit very different CO₂ release kinetics and quantum yields. Time-resolved pump-probe measurements revealed two different CO₂ release channels, a fast one on a sub-ps time-scale and a second slower channel on a time-scale of about 200 ps. While mNPA exhibits both fast and slow CO₂ release channels, pNPA releases CO₂ exclusively *via* the slow channel. For m- and pNPA the quantum yields of CO₂ release are about 0.6, whereas oNPA has a CO₂ yield of less than 0.1, which is exclusively emitted

via the fast channel. Obviously, most of the excited oNPA is quenched *via* an alternative decay channel efficiently competing with photodecarboxylation.

In this work, approximate coupled-cluster theory of second order (riCC2), configuration-interaction singles with perturbative doubles (CIS(D)) as well as ground-state unrestricted DFT in combination with the PBE0 xc-functional have been employed in combination with the COSMO solvation model to study the low-lying singlet and triplet excited states of the solvated NPA isomers. Since quantum chemical investigations of anionic NPA with and without solvent models revealed a critical influence of solvation, a thorough evaluation of various implicit, explicit, and combined solvation models has been conducted. It turned out that the COSMO model applied to the HF ground-state wave function provides surprisingly accurate results for ground and in particular excited states. It was further inferred that the accuracy of this simplified approach can be traced back to the fact that in the case of anionic NPA the main task of a solvation model is to describe the stabilization of the charge due to the polarization of the solvent, which is sufficiently well accomplished in the HF/COSMO approach.

Due to the different time-scales of the studied excited-state processes, neither equilibrium nor non-equilibrium descriptions of the solvent polarization are appropriate. Therefore, both approaches were employed. In case of the fast CO₂ release and the competing excited-state intramolecular H-transfer the non-equilibrium approach was used and proved to be sufficient to gain a consistent picture of the underlying mechanism. In case of the slow CO₂ release, for which long-lived charge-transfer as well as local triplet excited states are of crucial importance, equilibrium solvation had to be additionally applied to conclusively explain the surprisingly slow time-scale of 200 ps.

For the investigation of the PDC mechanism, relaxed scans of the excited-state potential energy surfaces (PES) have been performed along the decarboxylation coordinate at the riCC2/COSMO level for all three isomers of NPA. The obtained PES allow for a comprehensive explanation of the PDC mechanism. It was demonstrated that the ultra-fast decarboxylation in mNPA and oNPA proceeds *via* the pre-dissociated S_2 (Bz(π) \rightarrow L) state before the vibronically excited molecules undergo internal conversion into the minimum of the S_1 ($n \rightarrow \pi^*$) excited state. In pNPA, the corresponding S_2 (Bz(π) \rightarrow L) state is almost flat along the decarboxylation coordinate and within the model system also slightly higher in energy. With this state not being repulsive, fast CO₂ release is obviously not possible. From the local S_1 ($n \rightarrow \pi^*$) minimum, fast and efficient ISC takes the remaining population into the triplet manifold (fig. 2.12).

From the character of the excited states we concluded that according to El Sayed rules, a transition from the S_1 ($n \rightarrow \pi^*$) into the energetically degenerate T_3 state with local $n_\pi \rightarrow \pi^*$ symmetry appears most likely, followed by ultra-fast internal conversion to the relaxed minimum of the $n \rightarrow \pi^*$ excited T_1 . These processes are responsible for the increase of the excited-state absorption of the T_1 state at 667 nm, which takes place on a time-scale of 2 ps for m- and pNPA.

At the T_1 equilibrium structure, the reactive Bz(π) $\rightarrow \pi^*$ excited triplet state is found almost 1 eV higher in energy, causing the triplet population of m- and pNPA to be trapped in this state. If relaxed structures for T_1 and for the repulsive Bz(π) $\rightarrow \pi^*$ states are calculated in an equilibrated solvent shell, the energetic order of these states is inverted. This leads to the conclusion that due to thermal fluctuations of solvent shell and molecular structure the Bz(π) $\rightarrow \pi^*$ state at some point becomes energetically accessible from the relaxed $n \rightarrow \pi^*$

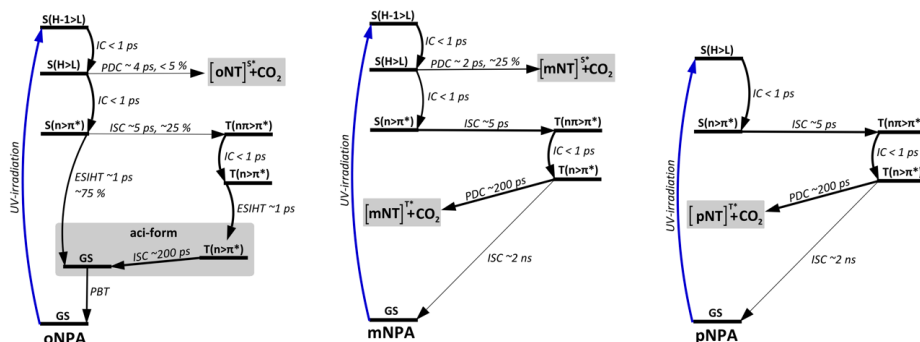


Figure 2.12: Reaction schemes for the photo-decarboxylation of oNPA (left), mNPA (middle) and pNPA (right). The time-scales are estimated based on computational and experimental results. (ESIHT: excited-state intra-molecular hydrogen-transfer, IC: internal conversion, ISC: inter-system crossing, PBT: proton back-transfer).

surface, which leads to decarboxylation at the observed time-scale of 200 ps (fig. 2.12).

In case of oNPA the 15-fold lower quantum yield of CO₂ release was traced back to a very fast and efficient quenching *via* intramolecular excited-state H-transfer. It was established that this reaction can occur in the triplet manifold as well as in the singlet manifold. Due to a small energy barrier in relation to the excess vibrational energy available, this H-transfer pathway can efficiently diminish the excited singlet population prior to inter-system crossing and thereby prevent slow decarboxylation in the triplet manifold. Together, these competing H-transfer reactions nicely explain the reduced yield of fast CO₂ release as well as the complete annihilation of the slow component (fig. 2.12).

Considering *ortho*-nitrobenzylic cages in general, arguments were provided that these singlet and triplet H-transfer pathways are a common feature and the initial and yield limiting step of the uncaging reaction. Therefore, the reaction cascade following H-transfer was studied with respect to the expected photo-products, though these are of little relevance for the PDC of oNPA. It turned out that despite the similarities of the corresponding singlet and triplet PES the distribution of photo-products and in particular the yield of the aci-form differs significantly for the two H-transfer pathways, which is underpinned by various experimental data. It is suggested that mainly due to much larger vibrational excess energy in combination with the readily accessible proton back-transfer channel in the ground state, singlet H-transfer corresponds to a quenching channel, while triplet H-transfer generates aci-molecules with much higher efficiency and longer lifetimes. Considering experimental results and recent literature data, it was proposed that formation of aci-isomers *via* the triplet pathway is at least four times more efficient than *via* the singlet pathway. Finally, it is proposed to modify oNB cages in such a way that inefficient singlet H-transfer is suppressed to allow a larger fraction of the excited-state population to undergo ISC and subsequent triplet H-transfer. Following this simple strategy, the overall uncaging quantum yield of oNB cages can be largely increased.

Chapter 3

Hydrogen-Transfer and Inter-System Crossing in the Photo-Deprotection of *ortho*-Nitrobenzyl Cages

In the following, I describe the investigation of the mechanism of light-induced deprotection of *ortho*-nitrobenzylacetate (oNBA), which is one of the smallest so-called “caged-compounds” utilizing the famous *ortho*-nitrobenzyl caging group. A key step of this uncaging process of, here, acetate from oNBA, is the formation of the protonated aci-form of the nitro-group, which may occur *via* excited-state intramolecular hydrogen transfer (ESIHT) in the lowest $n \rightarrow \pi^*$ excited singlet or the respective triplet state. Taking into account the results of high-level *ab-initio* calculations and experimental findings for oNBA and related *ortho*-nitrophenyl compounds, I suggest that the majority of excited molecules undergoes singlet ESIHT and only a minority undergoes inter-system crossing and triplet ESIHT. However, only the triplet-route leads to a formation of kinetically stable E-aci isomers, which in turn undergo photo-cleavage with higher quantum yield than the Z-aci isomers formed via the singlet-route. After all, based on the mechanism which conclusively explains experimental findings, I suggest modifications for the improvement of the efficiency of the caging-group based on a rational design strategy.

This work was motivated by earlier research on the photodecarboxylation of NPA and in particular oNPA. It constitutes the attempt to shed light on the initial steps of the uncaging process of common *ortho*-nitrobenzyl cages circumventing the complications resulting from the anionic charge of oNPA. It has been published in the *Journal of Physical Chemistry and Chemical Physics*, volume 15 (2013), pages 6691-6698 (ref. 69). The article has been written and composed by myself and includes only editorial contributions from the co-authors. Eventually, I contributed to an experimental investigation of another cage of the oNB type, which has been published in the *Journal of the American Chemical Society* (2014).⁷⁰

3.1 Introduction

The ortho-nitrobenzylic (oNB) moiety is one of the most prominent structural motifs for photolabile protecting groups for use in so-called caged-compounds. Although there are promising alternatives superior to oNB with respect to certain properties,^{38;39} straightforward synthetic access and commercial availability promote oNB to one of the most commonly used caging groups. However, one of the major drawbacks of oNB compounds is their small quantum yield for the light-induced deprotection (uncaging) of 0.02 – 0.2, where other, structurally related caging groups exhibit yields > 0.5.^{33;39}

It is well established that the yield limiting step in this uncaging process is the initial excited-state intramolecular hydrogen transfer (ESIHT), which generates the protonated aci-form of the nitro group, whereas the subsequent steps are assumed to exhibit quantum yields close to unity.³¹ It is also widely accepted that the initial ESIHT takes place in both singlet and triplet excited states owing to an ultra-fast and efficient inter-system crossing (ISC) of nitroaromatics on a time-scale of 1-10 ps and a triplet yield of nitro-benzene > 0.5.³¹ However, despite the knowledge of the relevance of both ESIHT channels as initial steps of the uncaging process, differences between these channels considering photo-product distribution and in particular their respective yields of the aci-form have hardly been addressed yet. To the best of my knowledge, only one experimental and one theoretical study have been published investigating the influence of the spin state.^{45;71}

In their theoretical work,⁷¹ Schaper and coworkers calculated vertical excitation energies for singlet and triplet states of 2-nitrobenzylacetate (ortho-nitrobenzylacetate, oNBA) and its 4,5-dimethoxy-substituted derivative. In doing so, they find a supposedly non-reactive triplet state exhibiting charge-transfer (CT) below the reactive triplet state in the dimethoxy-substituted compound, but not in the parent oNBA. On the basis of this finding, they explain a long-lived species observed in time-resolved experiments on dimethoxy-oNBA. The energies they considered were, however, only vertical excitation energies. For long-lived triplet states with charge-transfer character, however, the vibrational equilibration with the environment and the concomitant relaxation is most certainly very important. In particular with respect to the polar solvent acetonitrile used in the respective experiment,⁴⁵ such an investigation should involve at least an estimation of the influence of solvent relaxation.

In the experimental investigation of Schmierer and coworkers,⁴⁵ the contributions of singlet and triplet ESIHT leading to formation of the reactive aci-nitro form have been estimated for oNBA. For this objective, equal contributions of both channels have been assumed and the ratio of molecules undergoing either singlet or triplet ESIHT was not considered. Therefore, a reliable estimation of the respective aci-yield for each spin state was generally not possible. For the photo-decarboxylation of 2-(nitrophenyl)-acetates (NPA), the ratio of singlet vs. triplet ESIHT was directly determined by comparison of the characteristic triplet excited-state absorption at 667 nm of 2-(2-Nitrophenyl)-acetate (ortho-nitrophenylacetate, oNPA) to the one of the corresponding meta- (mNPA) and para-isomers (pNPA).³⁰ For mNPA as well as for pNPA, ESIHT is not possible in the lowest excited singlet state (S_1). Hence, the amplitude of the triplet excited-state absorption can be directly related to the fraction of the initially singlet excited-state population undergoing ISC, if the oscillator strength (f)

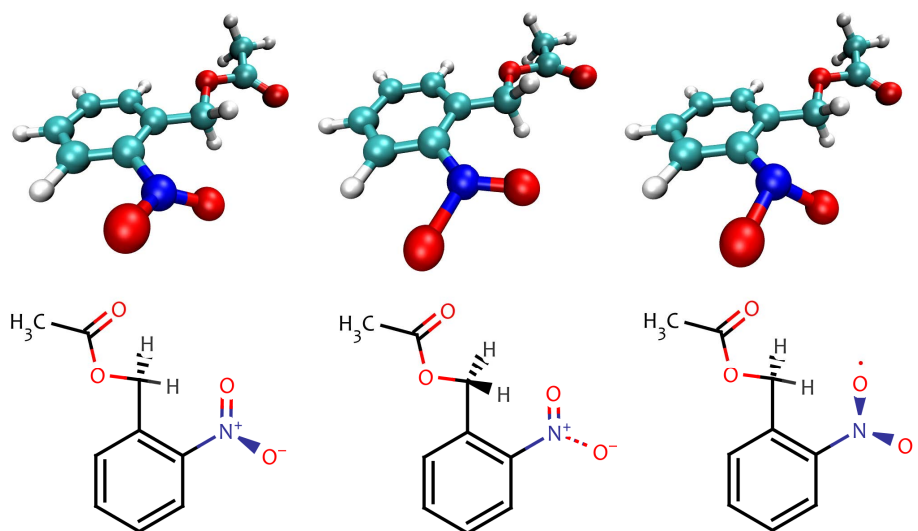


Figure 3.1: Molecular equilibrium structures of ortho-nitro-benzylacetate (oNBA) in its electronic ground state (left), the first excited singlet S_1 (middle) and triplet T_1 (right) states obtained at the riCC2/def2-TZVP(-f) level of theory. The radical character of the lowest excited states can be related to the structural changes in the nitro-group. Compared to the ground-state structure, one of the NO bonds is significantly stretched in S_1 due to a reduced bond order, while in T_1 both NO bonds are elongated and the oxygen-atoms are furthermore bent out-of-plane hinting towards a free electron-pair at the nitrogen atom.

of the relevant excited-state absorption is similar, which is indeed suggested by theory.^{28;30} For NPA, experiments revealed a four times smaller amplitude of triplet absorption for the ortho-isomer. Hence, only approximately 25% of the excited oNPA molecules undergo ISC and subsequent triplet- instead of singlet H-transfer. The results of Schmierer and coworkers, which show an equal contribution of both ESIHT channels to uncaging in combination with a three-fold larger number of molecules undergoing singlet ESIHT, hint towards a much larger efficiency of triplet channel with respect to uncaging.

Although 2-(nitro-phenyl)-acetates (NPA) do not represent typical oNB-caged compounds, the mechanism of photo-decarboxylation (PDC) of NPA offers valuable information about the initial ESIHT of oNB caging groups in general. For NPA, ESIHT corresponds to an undesired deactivation channel quenching CO_2 release in oNPA, hence causing a 15-fold reduction of decarboxylation yield in the oNPA (0.04) as compared to mNPA and pNPA (~ 0.6).^{28;29} In other words, almost the complete excited-state population of oNPA is quenched *via* efficient ESIHT. However, also the aci-form of oNPA, which is the direct product of ESIHT is detected only in very small amounts (quantum yield < 0.2). The conflict between these findings can be resolved postulating the presence of a conical intersection (CI) between the electronic ground state and the S_1 state along the ESIHT reaction coordinate, which would enable ultra-fast, non-radiative decay to the electronic ground state *via* subsequent proton back-transfer (PBT) from the protonated nitro group (aci-form) to the benzylic carbon.^{29;30} Intermolecular

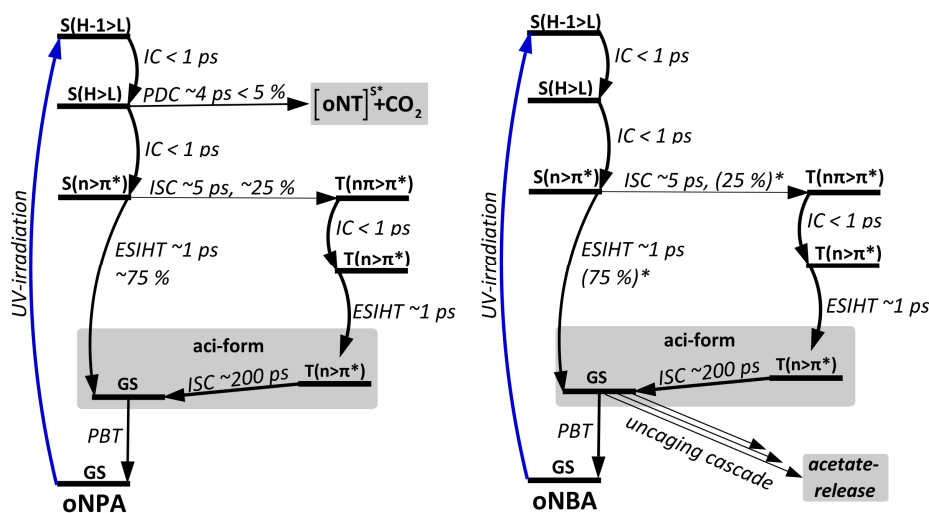


Figure 3.2: Comparison of the photochemical processes of oNPA (left) and oNBA (right) after excitation. The given time constants and yields marked with a star (*) are estimates for NBA based on experimental data for oNPA showing similar theoretical results. In both cases the main channel is the deactivation via internal conversion (IC), excited-state intramolecular hydrogen-transfer (ESIHT) and finally proton back-transfer (PBT). For oNPA it was inferred that a fraction of approximately 25% of the excited molecules undergo inter-system crossing (ISC) into the triplet manifold instead of ESIHT from S_1 . Since these photochemical processes are a common feature of the *ortho*-nitrobenzyl moiety, they are relevant for all oNB cages in general, since the subsequent formation of the aci-form is more efficient in the triplet manifold.

proton exchange with solvent molecules can be excluded as alternative explanation for the given experimental conditions ($\text{pH} > 7$) owing to its three orders of magnitude slower kinetics.³¹

This hypothesis of quenching of the excited-state population of oNPA *via* a molecular H-ping-pong mechanism is corroborated by the calculations of the potential energy surfaces along the ESIHT reaction coordinate in oNPA for the ground and excited states at the approximate coupled-cluster of second order (CC2) level of theory.³⁰ While the nitro-form is energetically strongly favoured in the ground state lying energetically about 1.5 eV below the aci-form, the aci-form is energetically more stable by about 0.7 eV in the lowest triplet T_1 state. On both surfaces, the energy barrier of ESIHT (0.2 – 0.4 eV) is small compared to the excess vibrational energy stemming from the initial photo excitation, which is as large as 3 eV. Since ESIHT in the singlet channel occurs on a sub-ps time-scale and within a few ps in the triplet channel, energy dissipation is not completed a large fraction of the excess energy is available to promote ESIHT.

Here, the results of quantum-chemical calculations for 2-nitrobenzylacetate (oNBA) are reported, which is the smallest prototypical representative of oNB-caged compounds. The investigation is focused on the initial ESIHT process and the formation of the aci-nitro form triggering the subsequent uncaging process.

3.2 Methodology

The modest molecular size of NBA allows for a thorough treatment of electron correlation with *ab initio* methods. Here, the approximate coupled cluster method of second order exploiting the resolution-of-the-identity approximation (riCC2)^{46;47} as implemented in TURBOMOLE 6.3.1 is employed as standard theoretical model,⁴⁸ which has been chosen because of its efficient parallel implementation featuring excited-state gradients and transition moments between excited-states.^{49;50;72}

As basis sets for the riCC2 calculations, a slightly modified version of the updated (def2) Ahlrichs triple-zeta basis sets was used, in which the polarisation functions of highest angular momentum (f-shell) were removed (def2-TZVP(-f)) to reduce computational effort.⁵⁷ The use of diffuse functions has been omitted since they cause Rydberg states to enter the low energy spectrum and moreover since all of the corresponding experiments are carried out in solution, where spatially extended Rydberg orbitals do not exist due to the presence of solvent molecules.

For density functional theory (DFT) and time-dependent-DFT (TD-DFT) calculations the ORCA 2.9 program package was used.⁵⁴ The PBE0 functional⁵⁶ in combination with the def2-TZVP basis was found to afford very reasonable agreement with riCC2 for the low-lying $n \rightarrow \pi^*$ excited triplet and ground state. In particular, the description of the lowest triplet state with unrestricted DFT/PBE0 is very useful due to its reliable SCF convergence. Here, all other tested single-reference methods suffered either from spin-contamination, convergence issues or both. The influence of solvation onto the ESIHT mechanism has been investigated at the DFT/PBE0 level of theory using the conductor-like screening model (COSMO)⁵¹ as implemented in ORCA 2.9.

Relaxed scans of the potential energy surfaces (PES) along the ESIHT coordinate for the ground state as well as the reactive singlet and triplet $n \rightarrow \pi^*$ excited states have been computed by constrained geometry optimization in each state along the O-H distance ($r(\text{OH})$). Optimized geometries of the excited singlet and triplet states obtained at TD-DFT/PBE0 and DFT/PBE0, respectively, served as input for the riCC2/def2-TZVP(-f) optimizations. While the scan along the ESIHT coordinate can be obtained from 90 pm to 240 pm for the ground state with DFT and CC2 as well as for the triplet excited T_1 state with unrestricted DFT, the calculations on the S_1 surface do not converge as soon as $r(\text{OH})$ approaches 120 pm. This is most likely due to the proximity of a conical intersection (CI) between the $n \rightarrow \pi^*$ excited state and the ground state.

Besides the proximity of the CI, also the electronic structure of the aci-form may explain the convergence issues faced here. At the relaxed ground-state geometry of the aci-form, the T_1 state is energetically only 0.6 eV above the ground state, which indicates possible multi-configurational character. A comprehensive theoretical description of the photochemistry of oNBA using accurate multi-reference methods is beyond the scope of this work.

To further explore the electronic structure, the multi-reference ground-state wave function of the aci-form of oNBA at the riCC2 optimized singlet and triplet ground-state geometries was calculated using a state-averaged complete-active-space self-consistent field (SA-CAS-SCF(2,2)). Thereby, the orbitals were averaged for ground state, S_1 and T_1 using an active space of two electrons in

two orbitals and a cc-pVDZ basis set within the COLUMBUS program package.⁷³ Subsequently, ground and excited states were calculated employing a multi-reference configuration-interaction singles and doubles ansatz (MR-CISD) based on the same active space as reference space. According to these computations, S_0 and T_1 are largely dominated by a single reference configuration at their corresponding equilibrium geometries. For the triplet, the next largest reference contributes $\sim 0.1\%$, while for the singlet ground state the second largest contribution with 9% is the doubly excited determinant. Only the lowest excited singlet state at the equilibrium structure of the T_1 state exhibits a pronounced multi-configurational character with 30% contribution from the doubly excited determinant and 50% from the HF ground state. The lowest triplet state at the ground-state geometry has again a clear single-reference character with other configurations $< 1\%$.

From a practical perspective, accuracy and reliability of riCC2 can also be checked by comparison to experimental results. Here, the computed absorption spectra of the singlet and triplet aci-forms of oNBA at the CC2 level agree nicely with the experimentally observed absorption of the aci-form at 400 nm as well as the triplet excited-state absorption at 450 and 600 nm.⁴⁵ After all, the single-reference riCC2 method is appropriate for the description of the photochemistry of oNB compounds.

3.3 Results & Discussion

3.3.1 Excited States of oNBA

Prior to the investigation of the mechanism of the initial ESIHT in oNBA, the relevant energetically low-lying excited states have been computed and characterized at the riCC2/def2-TZVP level of theory. The results of these calculations are compiled in tab. 3.1.

Table 3.1: Excitation energies (ω_{ex}) and oscillator strengths (f) of the energetically lowest singlet and triplet states of oNBA at its ground-state equilibrium structure at the riCC2/def2-TZVP and EOM-CCSD level of theory. For the triplet states, also the energy difference to the corresponding singlet state is given.

e ⁻ origin	State	singlets		triplets		Δ singlet
		ω_{ex}	CC2 (CCSD)	f	ω_{ex} CC2 (CCSD)	
NO ₂ (n)	S_1/T_1 (T_2)	3.77	(3.92)	0.01	3.44 (3.48)	-0.33
NO ₂ (n')	S_2/T_3	4.32	(4.41)	0	4.07	-0.35
Bz(π)	S_3/T_5	4.83	(4.99)	0.021	4.6	-0.23
Bz(π')	S_4/T_4	5.48	(5.89)	0.172	4.21	-1.27
NO ₂ (n_π)	S_6/T_2 (T_1)	6.12		0.001	3.77 (3.22)	-2.35

Both, the energetically lowest singlet and triplet states, S_1 and T_1 , correspond in the molecular orbital picture to a single-electron transition from an oxygen

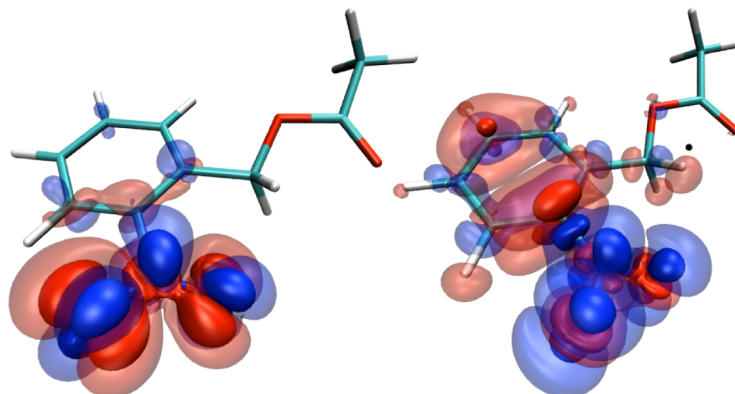


Figure 3.3: Relaxed difference density (negative part: red; positive part: blue) of the lowest singlet $S(n \rightarrow \pi^*)$ state (left) and $S(\pi' \rightarrow \pi^*)$ state (right) of oNBA obtained at the riCC2/def2-TZVP(-f) level of theory. These plots clearly show the purely local character of the S_1 as well as the charge-transfer character of initially excited S_4 state.

lone-pair orbital of the nitro group to the π^* orbital located exclusively at the nitro group. The difference density of the S_1 state is displayed in fig. 3.3. Accordingly, I refer to these states as $\text{NO}_2(n \rightarrow \pi^*)$ excitations. The population of an anti-bonding π orbitals in combination with a half-occupied non-binding orbital is the origin of the radical-like character of the oxygen in these electronic states, which in turn causes a low energy barrier for ESIHT reaction. The electronic structure of the $n \rightarrow \pi^*$ excited nitro group is very similar to an $n \rightarrow \pi^*$ excited carbonyl group and can hence be seen as a carbonyl analogue. Thus, the reactivity of the singlet and triplet $\text{NO}_2(n \rightarrow \pi^*)$ excited states can be expected to be similar to oxygen-centered radicals according to Turro's rule.⁶⁶

The S_2 state of oNBA also corresponds to an $n \rightarrow \pi^*$ excited state located at the nitro group but is 0.55 eV higher in energy than the closely related S_1 state. Since the excited electron stems from a different lone-pair orbital, the electronic structure of the S_2 state will be characterized as $\text{NO}_2(n' \rightarrow \pi^*)$. The corresponding triplet $\text{NO}_2(n' \rightarrow \pi^*)$ state is identified as T_3 .

Furthermore, two valence excited singlet states with partial charge-transfer (CT) character have been identified as S_3 and S_4 , each corresponding to single-electron transitions from an occupied π -orbital (HOMO) and π' (HOMO-1) at the benzene ring to the LUMO, which is a π^* -orbital mainly located at the nitro group with significant contributions from the benzene π^* orbital. While S_3 exhibits practically no oscillator strength, S_4 is bright possessing an oscillator strength of 0.172 and most certainly corresponds to the state which is initially excited in the photochemical uncaging process. The difference density of the S_4 state is displayed in fig. 3.3. These two $\pi \rightarrow \pi^*$ states are closely related to the 1^1B_1 and 2^1A_1 states of the parent compound nitrobenzene, respectively, where they have similar properties (see section 4.4). At the theoretical level of CC2, the 1^1B_1 state of nitrobenzene also corresponds to the HOMO \rightarrow LUMO transition, has an excitation energy of 4.8 eV, is symmetry forbidden and exhibits thus no oscillator strength. The bright 2^1A_1 state is characterized by the HOMO-1 \rightarrow LUMO transition and has an excitation energy of 5.2 eV. Since the

photochemical reactivity of oNBA takes place exclusively in S_1 and T_1 states, a further investigation of these high-lying states is omitted here. A detailed analysis of these states for the closely related oNPA was conducted previously in chapter 2.

The energetic ordering of the triplet states T_2 to T_6 is different compared to the corresponding singlet states (tab. 3.1). Due to a relatively large singlet-triplet splitting of the $\text{NO}_2(n_\pi \rightarrow \pi^*)$ state, the singlet $\text{NO}_2(n_\pi \rightarrow \pi^*)$ occurs as S_6 while the corresponding triplet $\text{NO}_2(n_\pi \rightarrow \pi^*)$ is the T_2 . As a result, the singlet $\text{NO}_2(n \rightarrow \pi^*)$ and triplet $\text{NO}_2(n_\pi \rightarrow \pi^*)$ states are energetically almost degenerate, which is presumably the cause for ultrafast inter-system crossing of nitrobenzylic compounds in accordance with El-Sayed’s rule (for a detailed analysis, see chapter 4, section 4.5).²⁷

3.3.2 Potential Energy Surface of ESIHT

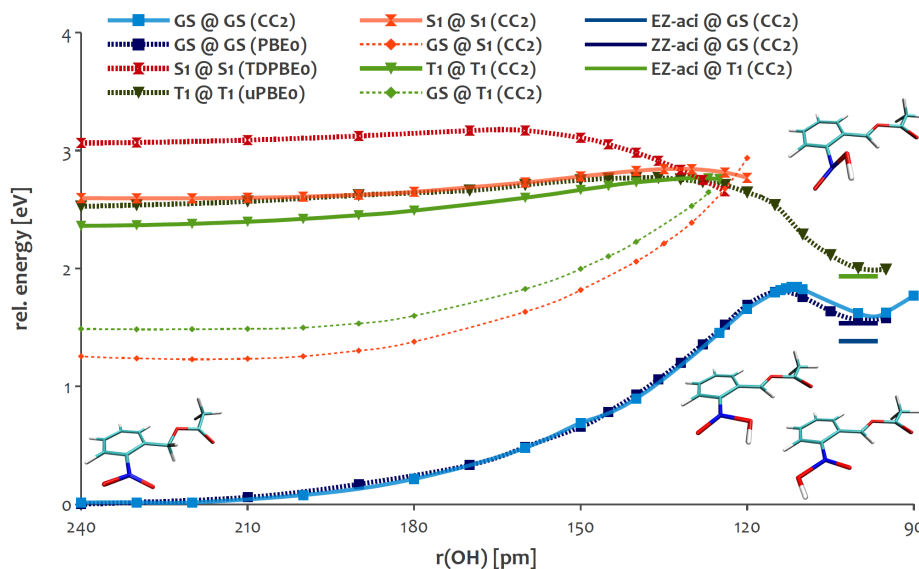


Figure 3.4: Relaxed scans of the potential energy surfaces of the electronic ground state, S_1 and T_1 along the ESIHT coordinate of oNBA at the riCC2-def2-TZVP level of theory. S_1 as well as T_1 are $n \rightarrow \pi^*$ excited states and allow for ESIHT (from left to right) eventually leading to crossings with the electronic ground state (GS). On the right, fully relaxed energies of the H-transfer products EZ- and ZZ-aci-oNBA are given for GS and T_1 . For comparison, also the curves obtained at the uPBE0/def2-TZVP level of theory for GS, S_1 and T_1 are plotted, which are similar to those obtained with riCC2. The shown structures refer to the ground-state optimized nitro-aromat, Z-aci-isomer and E-aci-isomer (bottom from left to right) as well as the triplet-optimized Z-aci-isomer (top right).

For the investigation of the ESIHT process that initiates the uncaging process, relaxed scans of potential energy surfaces of the electronic ground state as well as of S_1 and T_1 states have been computed and are shown in figs. 3.4 and 3.5. For the investigation of ESIHT, consideration of only the S_1 and T_1 states

is sufficient, since the internal conversion from the initially excited S_4 state to S_1 occurs on a sub-picosecond time-scale, and the inter-system crossing to T_1 within a few picoseconds. Hence, ESIHT takes place either in S_1 or in T_1 .

From the calculated relaxed scans of S_1 and T_1 along the ESIHT reaction, it is readily apparent that energy barriers of 0.25 eV and 0.4 eV exist in the S_1 and T_1 states at this level of theory, respectively. However, the initially excited S_4 state exhibits an excitation energy of 5.48 eV at the applied riCC2 level of theory, which lies almost 3 eV above the equilibrium structures of the reactive S_1 and T_1 states, which have relaxed energies of 2.69 eV and 2.47 eV above the ground-state minimum, respectively. Since the relaxation of the initial excited state population into S_1 and T_1 is fast compared to usual time-scales for vibrational equilibration with the immediate environment of typically ten picoseconds for a rigid molecule like NBA,²⁵ this excess energy is certainly not dissipated completely prior to reaching S_1 and T_1 . Thus, sufficient excess energy is available to easily overcome the involved energy barriers in the course of the ESIHT processes. A short glimpse at the optimized equilibrium structures of the S_1 and T_1 states shown in fig. 3.1 reveals pronounced structural changes of the nitro group. In particular the elongated NO bonds hint towards a radical character at the respective oxygen-atoms and thereby explain for the high reactivity with respect to H-abstraction from the benzylic position further motivating the low energy barriers for hydrogen abstraction from the benzylic position.

As can be seen in fig. 3.4, the S_1 as well as the T_1 surfaces intersect with the ground-state surface along the ESIHT coordinate at an elongated O-H bond length distance of about $r(\text{OH}) = 120$ pm. At this point, the HOMO and LUMO become energetically degenerate and interchange positions, which explains the observed state crossings. In the case of S_1 , this crossing corresponds to a conical intersection,⁷⁴ a so-called "photo-chemical funnel" allowing for ultra-fast, non-radiative decay of the excited molecules from S_1 to the electronic ground state. Since this transition is spin-allowed, most of the excited molecules will pass through the conical intersection into the ground state, where the nitro-form of oNBA is the global minimum being 1.5 eV more stable than the aci-form of oNBA. Ultimately, regeneration of the original oNBA is most certainly the main channel in case of the singlet ESIHT, or in other words, quenching of the excitation energy *via* a double H/H⁺-transfer mechanism. In turn, the yield of the aci-form of oNBA, which can react further in the uncaging process, will be very low for this singlet channel.

The shape of the potential energy curve of the reactive T_1 state along the ESIHT coordinate is very similar and it also exhibits a crossing with the electronic ground state. However, the transition from T_1 to the ground state is spin-forbidden and thus orders of magnitude slower than in the singlet ESIHT case, which holds even if there is significant spin-orbit coupling between these states. This is in good agreement with the experimentally determined lifetime of the triplet species, which has been established to be about 200 ps in the case of oNPA,^{28;30} and on the order of one nanosecond for nitrobenzene and nitrotoluene.⁶⁵ For the time-scale of the uncaging reaction of oNB-caged compounds, one may conclude that practically all triplets formed *via* S_1 to T_2 ISC remain in the triplet manifold and establish an equilibrium between nitro- and aci-form of oNBA on the T_1 surface. Here, in contrast to the electronic ground state, the aci-form is more stable than the nitro-form by about 0.8 eV and will thus be the main product of this triplet ESIHT channel.

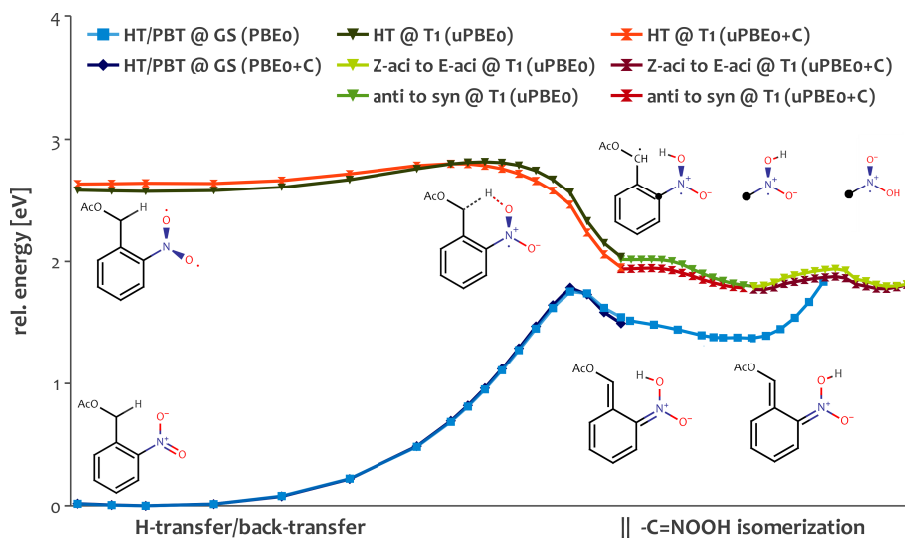


Figure 3.5: Energy profile of the ESIHT process (O-H scan) and subsequent C=NOOH isomerization, which includes N-OH rotation (CNOH dihedral scan from anti (180°) to syn (0°)) and C=NOOH rotation (CCNOH dihedral scan from EZ-aci to EE-aci) in T_1 and GS at the uPBE0/def2-TZVP level of theory with and without COSMO equilibrium solvation. The syn-anti isomerization is possible in both states, whereas the Z-aci to E-aci conversion can only take place in T_1 . Here, the double-radical character of the molecule allows for C=NOOH rotation yielding EE-aci isomers. This can not occur in the electronic ground state, since it would involve the rotation of a double bond.

Prior to the relaxation to the electronic ground state *via* ISC, the oNBA molecules are trapped in the triplet aci-form, an excited state exhibiting two singly occupied molecular orbitals (SOMO). The energetically lower SOMO is located at the nitro group and the other at the benzyl position. These positions can thus also be seen as radical centers, and the bonds from the phenyl ring to the nitro group and the benzyl position correspond to freely rotatable single bonds. Accordingly, one finds multiple, inter-connected local minima for the aci-form with very similar energy on the T_1 surface. These correspond to the E and Z isomers of the above mentioned C-C and C-N bonds, whose isomerization is energetically feasible (0.1 eV for C=N, 0.3 eV for C=C) as long as the system is in its triplet state. Consequently, one would expect a dynamic equilibrium between all of these isomers.

Besides the distinction of E- and Z-aci isomers, also the conformation of the transferred hydrogen atom with respect to the nitro group is relevant. Immediately after ESIHT, the hydrogen is in anti-position, i.e. the H-O-N-O dihedral angle amounts to 180° , and the generated aci-form would be referred to anti-Z(CN). Inspecting fig. 3.5 reveals the corresponding syn-Z(CN) with a H-O-N-O dihedral angle of 0° to be more stable in the T_1 state, which will thus be readily formed. From there, isomerization around the CN bond yielding the syn-E(CN) conformer exhibits only a small energy barrier of 0.1 eV.

All our calculations discussed to this point were carried out without any solvent model (*i.e.* in gas phase). However, the experiments mentioned above have

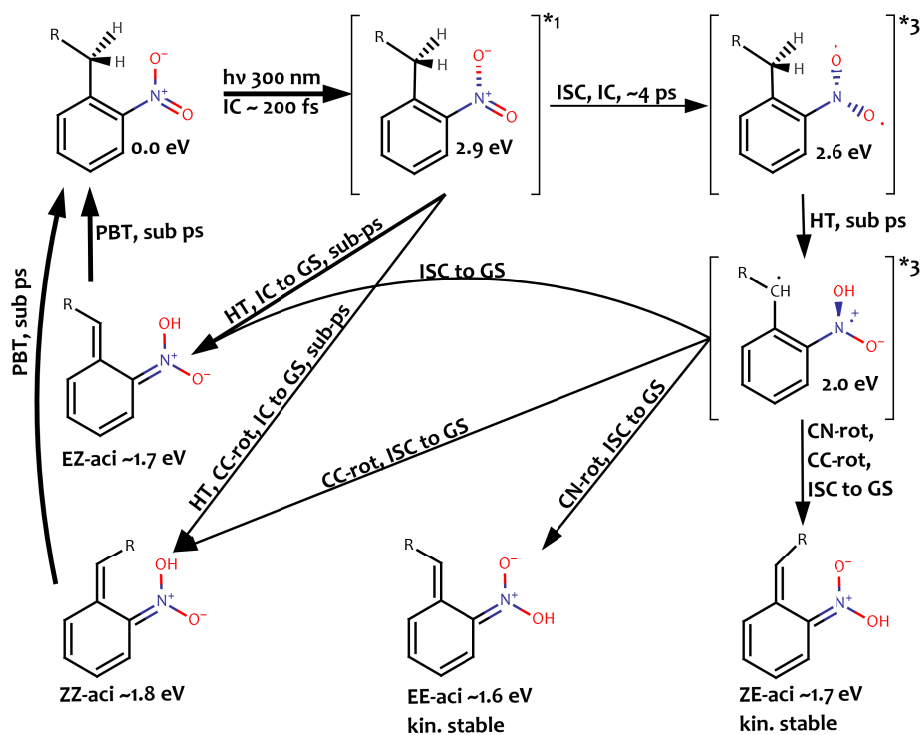


Figure 3.6: Photochemistry of oNBA after UV excitation into S_4 . Although ESIHT can occur via both singlet and triplet pathways, only the triplet route yields kinetically stable aci-isomers. The singlet route, on the contrary, leads into a conical intersection and thus mainly to non-radiative decay to the electronic ground state.

been conducted in polar acetonitrile,⁴⁵ and the oNB cage is mostly applied in aqueous solution.^{31;33} To estimate the influence of solvent, analog calculations were performed at the PBE0/def2-TZVP level of theory using COSMO with the parameters simulating aqueous solution. Since the triplet state is long-lived compared to solvent relaxation time-scales, equilibrium solvation was applied, i.e. the COSMO image charges were allowed to adapt to the ESP of the respective triplet-state of oNBA at each point of the calculated relaxed scan along the triplet ESIHT coordinate shown in fig. 3.5. Apparently, the influence of solvation is rather small. Although the curves are unevenly shifted by 0.1 – 0.2 eV along the H-transfer coordinate, the overall picture remains the same and the changes are small with respect to vibrational excess energy expected at these time-scales. One may conclude that these initial steps of the uncaging reaction are almost independent of the solvent.

It is important to point out here that a proper description of solvation is not generally negligible for the uncaging reaction of oNB compounds. For the closely related, anionic NPA, the influence of the solvent is huge and must be accounted for to obtain a qualitatively correct description.³⁰

3.4 Summary & Conclusions

2-Nitrobenzylacetate (oNBA) is the one of the smallest prototypical caged-compounds releasing acetate upon irradiation, which exploits the most widely used oNB cage. The uncaging process of oNBA is initiated by the absorption of a UV photon, exciting the molecule into S_4 state. Ultra-fast internal conversion takes the excited-state population efficiently into the $\text{NO}_2(n \rightarrow \pi^*)$ excited S_1 state, where most of the molecules undergo excited-state intra-molecular hydrogen transfer (ESIHT) from the benzylic position to the nitro group leading directly into a conical intersection (CI) between the S_1 and the electronic ground state prior to formation of the aci-form on the S_1 surface. The CI allows ultra-fast non-radiative relaxation into the electronic ground state, in which the nitro form of oNBA is by far the most stable conformer. Consequently, practically all molecules going through the CI will undergo thermal back-proton transfer recovering the original oNBA.

Besides ESIHT, excited oNBA molecules also undergo efficient inter-system crossing (ISC) from the S_1 state via the almost degenerate $\text{NO}_2(n_\pi \rightarrow \pi^*)$ into the $\text{NO}_2(n \rightarrow \pi^*)$ state. Owing to the very similar electronic structure of S_1 and T_1 , ESIHT is also possible in this triplet state. Also T_1 shows a intersection with the electronic ground state along the ESIHT coordinate, however, the transition into the electronic ground state is spin-forbidden, and thus slower than the formation of the aci-conformer of oNBA in the triplet state, which is energetically favored over the nitro-form by about 0.8 eV. Hence, the T_1 excited-state population ends up in four local minima associated with the aci-form, i.e. EE-, EZ-, ZE- and ZZ-aci isomers of oNBA, which are separated by only small energy barriers of 0.1 eV and 0.3 eV. In particular, aci-isomers with an E-configuration of the C=N double bond are kinetically stable with respect to proton back-transfer in the electronic ground state, since it involves the rotation around a double bond. In general, formation of mainly EE- and ZE-aci isomers can be expected, since those are about 0.1 eV more stable than their EZ- and ZZ-aci counterparts.

This picture is consistent with the large reduction in photo-decarboxylation and triplet yield observed for the related 2-(2-nitrophenyl)-acetate (oNPA) and the low yield of the aci-form as photo product.³⁰ In general, the similarity of the potential energy surfaces (PES) of the relevant excited singlet and triplet states of oNBA and oNPA is remarkable. This suggests that also for other caged-compounds, the relevant excited states will exhibit similar PES, and as a consequence a very similar initial ESIHT process. My findings also agree with experimental results for ortho-nitrotoluol (oNT) and ortho-nitrophenyl-methylether (oNPME). Here, UV irradiation in an argon or nitrogen matrix yields almost exclusively the corresponding syn-EZ-aci and syn-EE-aci isomers.⁶⁷ To explain the formation of ZE and EE-aci-isomers, the isomerization of the double bond was suggested to occur in a triplet state, which is now confirmed by the reported calculations for oNBA. Though seemingly contrary at first glance, the suggestion of a much higher efficiency of the triplet channel with respect to aci-formation is also in good agreement with the experimental findings for oNBA.⁴⁵ They reported singlet and triplet H-transfer to contribute equally to aci-formation of oNBA. However, taking into account that a much larger fraction of the population undergoes singlet ESIHT instead of ISC, subsequent triplet ESIHT, and formation of kinetically stable aci-isomers, it is clear that triplet ESIHT has to be much more efficient in aci-formation to contribute equally.

Finally, one may suggest to improve the yield of uncaging by fine-tuning the competition between singlet ESIHT and ISC towards the latter. This can in principle be done in two ways. On the one hand, one could directly try to increase the ISC rate by substituting hydrogen with heavier atoms (e.g. iodine, bromine) at the aromatic core. It is, however, questionable whether this would have the desired effect since ISC of nitro-aromatic compounds is already very fast. On the other hand, one could aim at reducing the probability of singlet ESIHT. This may only affect the ratio of ESIHT and ISC in S_1 , since after ISC into T_1 no competing processes has been found besides triplet ESIHT resulting in formation of the reactive aci-form.

Chapter 4

Non-Radiative Decay of Nitrobenzene

In this chapter, I present an investigation of the mechanism of non-radiative decay of nitrobenzene (NB) employing a hierarchy of state-of-the-art quantum-chemical methods. Eventually, I suggest a complete mechanistic picture for the conversion from the bright singlet state to the electronic ground state. This proposed mechanism involves internal conversion and inter-system crossing along three dominating internal coordinates of the nitro group and consistently explains the experimental findings. Relaxation from the lowest triplet state via inter-system crossing occurs along the out-of-plane bending coordinate of the nitro group, while initial IC as well as ultra-fast inter-system crossing into the triplet manifold take place along symmetric NO stretching and ONO bending modes that have not been considered before. The investigation is based on high-level single- and multi-reference electronic structure calculations employing ADC(3), MOM-CCSD(T), EOM-CCSD, DFT/MRCI and CAS-SCF/NEVPT2 level of theory, which is, as I will demonstrate, absolutely necessary to assure a reliable and accurate theoretical description of NB. The need for a first-order treatment of doubly excited states will be traced back to the large double-excitation character of the second excited singlet state of NB. Methods featuring a zeroth-order treatment of double excitations like approximate coupled-cluster of second order (CC2), algebraic-diagrammatic construction of second order (ADC(2)) and partially even (EOM)-CCSD yield a qualitatively wrong picture of the excited states. Presumably due to problems with singly excited contributions, already the description of the ground-state geometries is problematic at the CC2 level of theory.

To answer questions arising from the investigations of NPA and oNBA and the prototypical nature of NB for many photo-active systems, I conducted this extensive investigation of the photochemical processes. The investigation was conducted in cooperation with the group of C. Marian, namely Vladimir Jovanović, who contributed the calculations with DFT/MRCI. It has been published in the journal *Physical Chemistry Chemical Physics*, volume 16 (2014), pages 12393-12406 (ref. 75). The article has been written and composed by myself and includes only editorial contributions from the co-authors.

4.1 Introduction

As early as in 1900, Ciamician and Silber first reported on their experiments on light-induced reactivity of various compounds. A large group of these compounds consisted of substituted nitroaromatics e.g. *ortho*-nitrobenzaldehyde, which is converted to nitroso-benzoic acid in the presence of UV-light.^{40;76} Since then, nitroaromatics and their photo-reactivity have been investigated in numerous studies and found countless applications as photochemical reagents as well as in photoswitches and photolabile protecting groups.^{31-33;39;77} In particular for the latter applications, a profound knowledge of the character of the ground and low-lying excited states as well as of the very first photophysical processes taking place after excitation is indispensable to allow for rational design. In general, the photochemical processes and excited states of nitrobenzene (NB) as the most simple and prototypical nitroaromat are of fundamental academical interest. This is reflected by about 180 000 hits obtained by searching for the term nitrobenzene on google scholar. There exists, however, neither detailed knowledge along which molecular coordinates of the NB molecule the ultra-fast photophysical processes like internal conversion (IC) and inter-system crossing (ISC) take place nor even common agreement on the character of the lowest excited states has been achieved yet.

From an experimental point of view, one of the reasons for this knowledge gap for such a simple molecule is the non-radiative character of almost all photophysical processes in NB. It is non-fluorescent, non-phosphorescent⁶⁵ (other sources report a very weak phosphorescence with a very low quantum yield $< 10^{-3}$)⁶⁴ and shows only a broad, unstructured excited-state absorption with maxima at 400 and 650 nm.⁴⁴ For NB vapor, there is only one strongly absorbing singlet state below 6 eV, which is a $\pi \rightarrow \pi^*$ excitation at 5.16 eV (240 nm) and two much weaker absorptions, one of which is visible only in the gas-phase spectrum around 4.42 eV (280 nm) and another only evident in solution at approximately 3.8 eV (326 nm).⁷⁸

For practically all theoretical investigations of chemical compounds containing the nitrobenzoic moiety reported so far usually either DFT methods (e.g. B3-LYP/6-31G*) or perturbative coupled cluster of second-order (CC2) have been used,^{69;71} which, as we will demonstrate, do not even provide a qualitatively correct description of NB and presumably nitroaromatics in general. The coupled-cluster based CC2 predicts an inaccurate ground-state geometry for NB, which is largely improved with MP2 or DFT/B3-LYP. The latter, however, yields far too low excitation energies for any compound including the nitrobenzoic moiety and electron donating groups, which is due to the well known charge-transfer error of TD-DFT.⁷⁹⁻⁸¹ In fact, most *ortho*-nitrobenzylic photolabile protecting groups do contain additional electron donation groups such as e.g. 4,5-dimethoxy substituents or alpha-carboxy groups, which have the purpose to shift the absorption to longer wavelengths and increase solubility in water.³¹

The difficulties determining the character of the lowest excited triplet state of NB most certainly result from the fact that there are two or three low-lying states with similar energy that require a balanced description of local $n \rightarrow \pi^*$, local $\pi \rightarrow \pi^*$ and charge-transfer character, which are in addition differently influenced by solvation. Moreover, the relative energies of these states strongly depend on the geometrical parameters such as the NO bond length and ONO bending angle. In particular the computed values of these parameters exhibit

large deviations from the experimental ones even at high coupled-cluster level of theory (see section 4.4, ground-state equilibrium geometry).

With this work, I attempt to shed light on the photo-physical and photo-chemical processes of NB, which is the smallest representative for nitroaromatic compounds. Due to its small size and high C_{2v} symmetry, even highest level single- and multi-reference *ab initio* calculations (ADC(3), CCSD(T), CAS(14/11)) with reasonably large basis sets (def2-TZVP, cc-pVTZ) are feasible. This allows for a thorough investigation of the character of the lowest triplet state, which is of utmost importance for the reactivity of nitroaromatics.

In an attempt to make this chapter accessible for theoreticians as well as experimentalists, the theoretical details of the somewhat extensive search for a suitable methodology are collected in section 4.4. Readers that are mainly interested in the mechanism of non-radiative relaxation of NB will find a short summary of electronic structure of NB ground and excited states in section 4.3 and may skip section 4.4 to continue with section 4.5, which covers mechanistic aspects of non-radiative decay.

This chapter is arranged as follows: in section 4.2, a short summary of existing experimental and theoretical literature will be given to create a starting point for our investigation. In section 4.3, relevant singlet and triplet excited states of NB will be characterized and summarized foreclosing the conclusion from the next section. In section 4.4, results, accuracy and reliability of various methods (CIS, CIS(D), CC2, CCSD, EOM-CCSD, ADC(2), ADC(3), DFT/MRCI, CAS-SCF/NEVPT2 and MOM-CCSD(T)) for ground and excited states will be discussed in detail to explain problems concerning theoretical description of NB. At the end of section 4.4, technical details of programs and methods are summarized. In section 4.5, the relevant internal coordinates of the NB molecule will be investigated regarding possible pathways for non-radiative relaxation processes based on relaxed potential-energy-surface scans along ONO bending, symmetric NO stretching and ONCO out-of-plane bending coordinates calculated at the ADC(3)//EOM-CCSD and DFT/MRCI//EOM-CCSD levels of theory.

4.2 Previous Investigations of Nitrobenzene

The very first photochemical experiments on NB and nitroaromatic compounds were conducted by Ciamician and Silber in the beginning of the 20th century. For their investigations, they exposed solutions of NB and various *ortho*-substituted nitroaromatics (e.g. *o*-nitrotoluene, *o*-nitrobenzaldehyde) to sunlight over long periods of time (days to years).^{40;76} In doing so, they discovered the photooxidative reactivity of the nitro group with respect to neighboring substituents and also solvent molecules.

After investigating the vapor-phase photochemistry of NB, Hurley and Testa were the first to infer that hydrogen-abstraction by the electronically excited nitro group may be a key step in the manifold photochemistry of nitrobenzylic compounds.⁶⁴ In the same work, they also found that ISC plays a crucial role in NB photochemistry. By means of quenching experiments, they determined the triplet yield to be as big as $67 \pm 10\%$. Moreover, they concluded that the strong concentration dependence of many photochemical reactions of NB in solution has to be a result of an unusually short lifetime of the lowest triplet state of NB compared to other nitroaromatics and does not originate from a low triplet

yield. From their experiments, they suggested a triplet lifetime < 1 nanosecond, which was, as it turned out later (see below), a very good estimate.

To determine the character of the excited state responsible for the experimental absorption peak around 5.1 eV, Nagakura and coworkers recorded an absorption spectrum of NB vapour and in various solvents of increasing polarity.⁷⁸ In combination with very basic molecular-orbital theory considerations, they suggested the strongly absorbing singlet state at 5.16 eV to be a charge-transfer (CT) state of A_1 symmetry, in which an electron is transferred from the benzene ring to the nitro group. Another weakly absorbing state that is found at about 3.8 eV was suggested to be the lowest $n \rightarrow \pi^*$ excitation because of its solvatochromatic blue shift. Although this state is symmetry forbidden at the strictly C_{2v} symmetric ground-state equilibrium geometry, it can gain an oscillator strength (f_{osc}) of 0.02 when the symmetry is broken for example by thermal tilting of the nitro group with respect to the benzene ring. The weak absorption exhibiting vibrational fine structure at around 4.42 eV, which is observed only in the gas-phase spectra, was attributed to the $1^1B_1 \pi \rightarrow \pi^*$ excited state by comparison to a peak with similar vibrational structure observed for benzene.⁷⁸

To investigate the gas-phase structure of NB, Domenicano and coworkers carried out electron diffraction experiments on NB vapor.⁸² According to these experiments, the geometry is planar but due to a low rotational barrier, the nitro group carries out a large amplitude-tilting motion, causing the unsigned average tilting angle (CCNO dihedral) in the gas phase at 300 K to be about 13° . The critical NO bond length is (122.3 ± 0.3) pm, the CN bond length is (148.6 ± 0.4) pm and the ONO-angle $(125.3 \pm 0.2^\circ)$.

Later, Takezaki and coworkers investigated the relaxation of UV excited NB by means of photoacoustic spectroscopy.⁶⁵ The latter allows to detect the changes in optical density caused by temperature change in the molecular environment during the non-radiative relaxation processes. They calculated the triplet yield to be $(80 \pm 4)\%$, which is slightly higher than the one reported by Hurley and Testa. Furthermore, due to the high time resolution of the photoacoustic transient grating and population grating techniques employed, they were able to determine an upper limit for the time-scale of the fastest process of 100 fs as well as the time-scale of ISC into the triplet manifold to be 6 ps.⁸³ They found the triplet population to decay in the nanosecond time regime (*i.e.* 480-900 ps lifetime depending on solvent and temperature) to give back ground-state NB. Surprisingly, the lifetime of the triplet hardly depends on solvent polarity, but rather on the chain length of the alkane solvent and temperature. A lower bound for the energy of the relaxed triplet state was determined to be at 2.55 eV by quenching experiments. Based on preliminary CAS-SCF calculations, they suggested the IC and ISC processes to take place along the ONCO out-of-plane coordinate of the nitro group (fig. 2 in ref. 83). For the CAS-SCF investigation of NB, they used a small basis set with polarization functions only on the nitrogen atom and a small active space.⁸⁴ Although they find similar ordering and character of the lowest excited states, the energies they report are too low by about 1 eV compared to the experiment.

Quenneville and coworkers investigated the photochemical processes in NB theoretically by means of quantum-chemical calculations employing a mixture of MRQDPT, CAS-SCF and TD-DFT.⁸⁵ They optimized the S_1/S_0 conical intersection (CI) using CAS-SCF yielding a geometry that is, apart from the tilting angle of the nitro group also found in this work (intersection of S_1 and

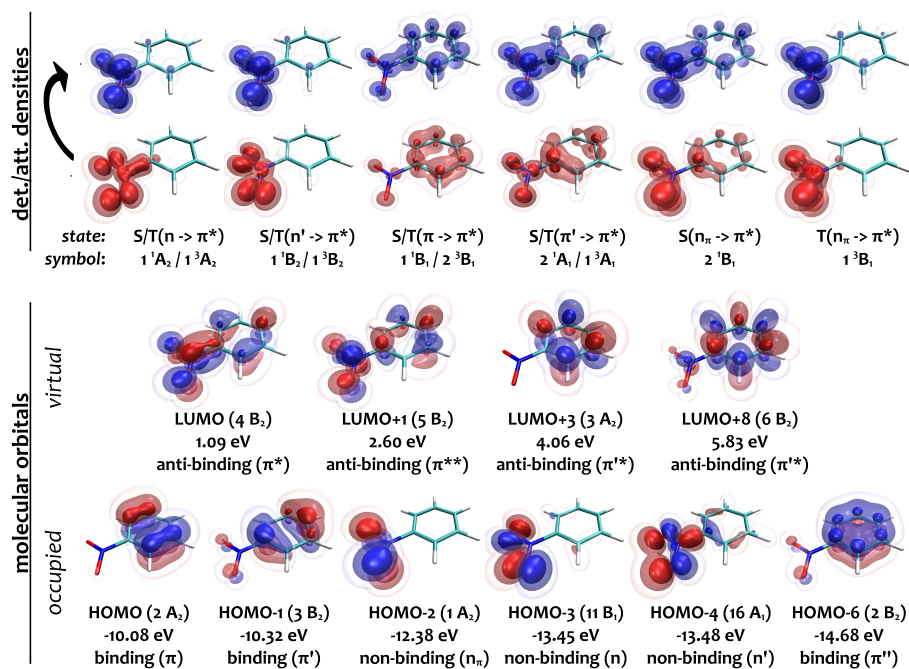


Figure 4.1: Isosurfaces for attachment (top, blue) and detachment (top, red) densities for the energetically lowest excited singlet states and the $n_\pi \rightarrow \pi^*$ triplet state at the ADC(3) level of theory as well as the relevant molecular orbitals (bottom) of nitrobenzene calculated with the def2-TZVP basis for the B2-PLYP/def2-TZVP geometry. For all states apart from the $n_\pi \rightarrow \pi^*$ state, attachment and detachment densities of singlet and respective triplet states are hardly distinguishable. The isosurfaces were rendered with the isovalues 0.018 (opaque), 0.006 (colored transparent) and 0.002 (transparent) for the att./det. densities and 0.1, 0.05 and 0.025 for the orbitals. The use of three surfaces instead of only one allows to distinguish between major contributions (opaque surfaces) and minor ones and furthermore to estimate the gradient of the density from the distance of the three surfaces.

ground state in fig. 4.8). Based on this result, they suggested the internal conversion to take place along this ONCO out-of-plane and CCNO dihedral coordinate.

4.3 Ground and Excited States of Nitrobenzene

4.3.1 Excited Singlet States

According to the calculations, the lowest excited singlet state with large oscillator strength (f_{osc}) of about 0.25 is a $\pi \rightarrow \pi^*$ excited state with CT character as suggested by Nagakura and coworkers.⁷⁸ Since this bright state with the same symmetry as the ground state (A_1) is characterized by an excitation from the second highest occupied π orbital (HOMO-1), it will be referred to as $S(\pi' \rightarrow \pi^*)$ state. Like for all excited states discussed here, the biggest components

of the excitation vector of the $S(\pi' \rightarrow \pi^*)$ state are excitations to the LUMO, which is a mixture of mainly the π^* orbital at the nitro group with significant contributions from a benzene π^* orbital. For the rather local $n \rightarrow \pi^*$, $n' \rightarrow \pi^*$ and $n_\pi \rightarrow \pi^*$ states (see attachment/detachment densities in fig. 4.1), excitations to the LUMO+1 are included in the excitation vector as well, but with opposite sign. Eventually, the contributions from LUMO and (phase-inverted) LUMO+1 cancel out at the carbon atoms while they add up at the nitro group, yielding the locally excited states.

At the Franck-Condon (FC) point there are four dark singlet excited states energetically below the bright $\pi' \rightarrow \pi^*$ excited state. These include two $n \rightarrow \pi^*$ and two $\pi \rightarrow \pi^*$ excited states, which will be termed $S(n \rightarrow \pi^*)$ (term symbol: 1^1A_2 , main contribution from the HOMO-3), $S(n' \rightarrow \pi^*)$ (1^1B_2 , HOMO-4), $S(\pi \rightarrow \pi^*)$ (1^1B_1 , HOMO) and $S(n_\pi \rightarrow \pi^*)$ (2^1B_1 , HOMO-2). The latter state is termed $S(n_\pi \rightarrow \pi^*)$ because it is involving the HOMO-2, which is a non-bonding orbital of π -symmetry located at the nitro group. The excitation vector of this state exhibits large contribution from double excitations (see fig. 4.2). Hence, the energy of this state is significantly overestimated by any first- and second-order method. Since this is not the case for the corresponding triplet state, which is largely dominated by single electron excitations, one obtains a huge, artificial singlet-triplet splitting of 2 – 3 eV with any first or second-order method. Eventually, this state will turn out to be essential for the photochemistry of NB, which complicates the investigation since any accurate and reliable theoretical description of an excited state with significant double excitation character requires a reasonable description of doubly excited states.

The 1^1B_1 $S(\pi \rightarrow \pi^*)$ state is characterized exclusively by the HOMO→LUMO excitation exhibiting very limited *fosc*. The 1^1B_2 $S(n' \rightarrow \pi^*)$ is located at the nitro group and also dark. These $S(n' \rightarrow \pi^*)$ and $S(\pi \rightarrow \pi^*)$ states are of limited relevance for NB photochemistry as they cannot become the lowest excited states but rather play a role as intermediate ladder steps during IC in the singlet manifold.

The lowest 1^1A_2 $S(n \rightarrow \pi^*)$ excited state is strictly localized at the nitro group. It can obtain little but significant *fosc* of about 0.02 if the nitro group is tilted with respect to the aromatic ring and hence shows up in the experimental spectra recorded in solution at $T = 300$ K as a small shoulder at about 3.8 eV.

4.3.2 Triplet States

In the triplet manifold, the three lowest excited states have a similar energy and may thus become photochemically relevant. Concluding the results of all calculations for unsubstituted NB in vacuum, the lowest triplet state at the ground-state equilibrium structure is most likely the $T(n_\pi \rightarrow \pi^*)$ state, whereas the $T(n \rightarrow \pi^*)$ and $T(\pi' \rightarrow \pi^*)$ states are only little higher in energy (0.2–0.5 eV depending on the method, for a detailed analysis see section 4.4).

In contrast to its singlet analog, the 1^3B_1 $T(n_\pi \rightarrow \pi^*)$ state is characterized mainly by single-electron transitions, the largest of which is originating from the HOMO-2 (fig. 4.2). Surprisingly, this does not eliminate the problems concerning the accuracy of its theoretical description. Even for this $T(n_\pi \rightarrow \pi^*)$ state, at least EOM-CCSD level of theory is required to obtain a qualitatively correct picture in agreement with higher-order single-reference and multi-reference methods such as ADC(3) and MOM-CCSD(T), whereas CC2 as well as all second-order

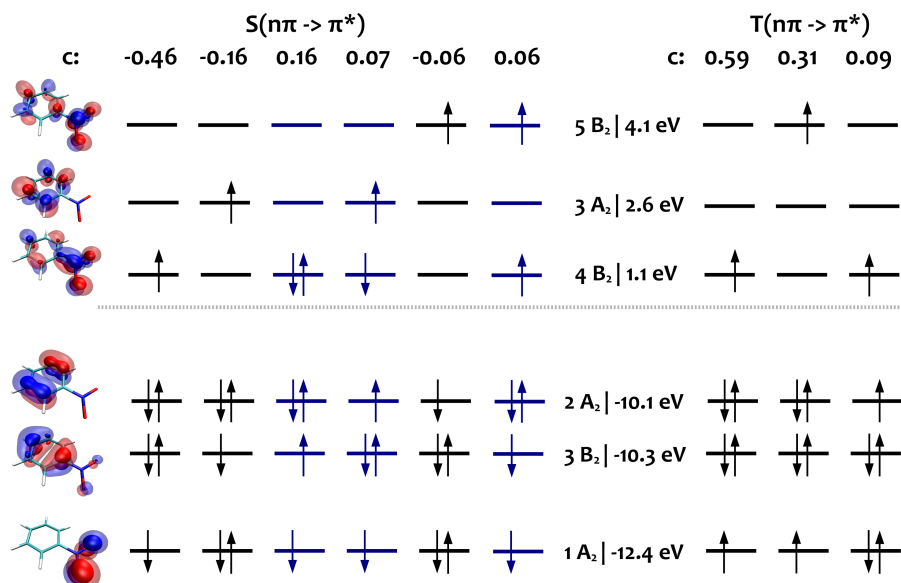


Figure 4.2: Composition of the $n_\pi \rightarrow \pi^*$ excited singlet and triplet states ADC(3)/def2-TZVP//B2-PLYP/def2-TZVP level of theory. Doubly excited determinants are shown in blue. Over-all, they make up for about 50% of the contributions to the excitation vector of this state.

methods yield a wrong order of the lowest triplet states (*i.e.* $n \rightarrow \pi^*$ far below $n_\pi \rightarrow \pi^*$). This becomes even more evident from the magnitude of the triples correction to MOM-CCSD, which is about 0.3 eV for this state (singlet -0.3 eV and triplet $+0.3$ eV), while for most other states its well below 0.1 eV (see fig. 4.4, bright and dark blue bars).

The analog of the lowest singlet state with A_2 symmetry, the $T(n \rightarrow \pi^*)$ state, is the second lowest triplet state at the FC point. A key property of these lowest triplet states is the different position of their respective minima along the ONO bending coordinate (see table 4.1), which causes the singlet and triplet $n \rightarrow \pi^*$ states to intersect with $T(n_\pi \rightarrow \pi^*)$ state at small ONO bending angles. For even smaller ONO angles, these states also cross the ground-state surface (see fig. 4.7). These seams and crossings between the $T(n_\pi \rightarrow \pi^*)$ and $T(n \rightarrow \pi^*)$ states along the ONO bending coordinate will turn out to be of great importance for the IC and ISC processes in UV excited NB.

If a very polar solvent is present, also the $1\ ^3A_1\ T(\pi' \rightarrow \pi^*)$ state can become the global energy minimum of the triplet manifold due to its CT character. Although this is presumably impossible for NB, it becomes feasible if substituents with $+m$ effect are introduced in the meta and/or para positions. Practical examples are 4,5-dimethoxy-*ortho*-nitrobenzylic caged compounds, for which it is well established that the triplet population can be trapped in a long-lived triplet state under these conditions, reducing the quantum yield for the uncaging reaction from around 10% to 1–2%.^{70;71;86} Here, the initial hydrogen abstraction that has been shown to take place in the singlet and triplet $n \rightarrow \pi^*$ states, is prevented by trapping the population in the low lying $T(\pi' \rightarrow \pi^*)$ minimum.^{45;69}

For a more detailed analysis of the energetics of the lowest triplet states

explicitly discussing the results of various single- and multireference methods the reader is referred to section 4.4.

4.3.3 Inter-System Crossing

For NB, the probability of transitions between singlet and triplet states *via* spin-orbit coupling (SOC) can be derived qualitatively from El-Sayed’s rules.²⁷ According to the latter, ISC is fast between states involving orbitals of different symmetry, e.g. $n \rightarrow \pi^*$ to $\pi \rightarrow \pi^*$, while it is slow between states of the same orbital symmetry. Hence, concerning NB, it may be concluded that ISC takes place between the lowest $S(n \rightarrow \pi^*)$ and $T(n_\pi \rightarrow \pi^*)$ states, while the ISC rates between $n \rightarrow \pi^*$ singlet and triplet states should be three orders of magnitude smaller. This qualitative picture is substantiated by DFT/MRCI and CAS-SCF/NEVPT2 calculations of SOC, which are around 60 cm^{-1} (DFT/MRCI) and 100 cm^{-1} (CAS(14/11)/NEVPT2) between $S(n \rightarrow \pi^*)$ and $T(n_\pi \rightarrow \pi^*)$ states and exactly zero between the states of same symmetry at the C_{2v} symmetric ground-state equilibrium structure. For ISC from the triplet manifold back to the ground state the same rules apply and consequently, SOC is large between $n \rightarrow \pi^*$ excited states and the ground state, while for $\pi \rightarrow \pi^*$ or $n_\pi \rightarrow \pi^*$ states SOC with the singlet ground state vanishes. This, however, changes when the molecule is distorted out of its C_{2v} symmetry. Along the ONCO out-of-plane coordinate for example, the SOC of the $T(n_\pi \rightarrow \pi^*)$ state with ground state increases to 65 cm^{-1} at an ONCO out-of-plane angle of 40° ($T(n_\pi \rightarrow \pi^*)$ relaxed structure), while the SOC between $T(n \rightarrow \pi^*)$ and the ground state is reduced to 15 cm^{-1} (see fig. 4.8).

4.4 Results, Methodology and Accuracy

4.4.1 Ground-State Equilibrium Geometry

During a preliminary theoretical investigation of NB using the approximate coupled cluster theory of second-order (CC2), it was found that this method predicts a ground-state geometry that is significantly different from the experimental vapor geometry. The most substantial deviation is observed for the NO bond length, which is 122.3 pm in the experiment compared to 124.6 pm at the CC2/def2-TZVP level of theory. At first glance, this deviation of 2.3 pm seems negligible and is inconspicuous due to a fortuitous error compensation between the CC2 geometry and linear-response (LR)-CC2 excitation energies, which are actually much closer to experimental values for the faulty geometry. Surprisingly, CCSD/def2-TZVP and CCSD/cc-pVTZ do not perform much better as they overcompensate the error, both yielding a bond length of 121.5 pm , which is significantly too short compared to the experiment. If one compares excitation energies calculated for ground-state geometries obtained with CC2 and CCSD, the impact of this erroneous bond length becomes evident: Since CC2 and CCSD deviate in opposite directions, the differences add up and the excitation energies of some of the states differ by as much as 0.5 eV . The reason is that between 120 pm and 125 pm , the vertical excitation energies of the excited states localized at the nitro group are extremely sensitive with respect to this bond length and are shifted by as much as 0.13 eV/pm (see fig. 4.6), while the other excited states are hardly affected. Due to the state-dependent shift, the

use of the CC2 ground-state geometry introduces a systematic error not only to absolute, but also to relative state energies in the order of 0.25 – 0.3 eV with respect to the experimental geometry.

The agreement between experimental structure and CCSD may be improved by using the smaller double zeta SVP or cc-pVDZ basis sets yielding 122.1 pm, which is at least within the error bars of the experiment. Further investigating this issue, it was found that simple MP2, SCS-MP2 and double-hybrid DFT/B2-PLYP in combination with the def2-TZVP basis set yield NO bond lengths of 122.7 pm, 122.6 pm and 122.5 pm, respectively. In particular B2-PLYP shows an extremely good agreement with experimental data considering other structural parameters such as ONO angle and CC bond lengths as well as excitation energies, whereas the calculations take a small fraction of the computational resources required for CCSD. After all, I decided to use the B2-PLYP geometry as basis for the rigid scans as well as vertical excitation energy calculations.

4.4.2 Excited States of Nitrobenzene

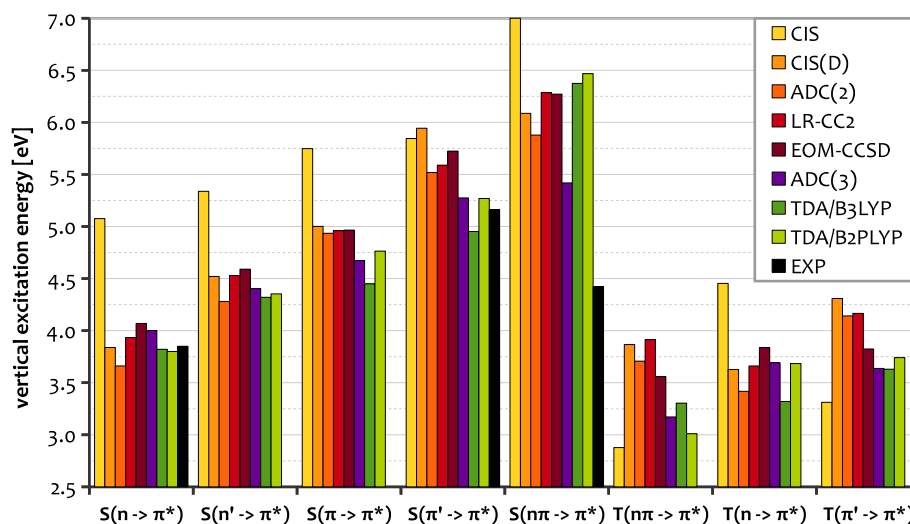


Figure 4.3: Plot of the vertical excitation energies calculated with single-reference methods of increasing accuracy. The level of theory increases from yellow (first order) over red (second-order) to purple (third order), DFT results are green. Regarding the states for which experimental data is available, ADC(3) outperforms EOM-CCSD. For the $S(n \rightarrow \pi^*)$ excited state, ADC(3) yields excitation energies that are little too high and ADC(2) is superior. All calculation were carried out for the B2-PLYP/def2-TZVP equilibrium geometry with the def2-TZVP basis set.

The quality of the theoretical description of NB is remarkably different for each of the lowest five excited electronic states. Therefore, I employed a large variety of methods to calculate vertical excitation energies from CIS through MOM-CCSD(T) as well as various multi-reference methods and DFT to allow for an estimation of trends and to investigate the convergence of the results with respect to the level of theory. Furthermore, my results may help guide the choice

of methods for future studies of molecules containing the nitrobenzylic moiety. For reasons of clarity, I will firstly discuss the results of the single-reference excited-state methods (fig. 4.3), secondly the results of the multi-reference methods DFT/MRCI and CAS-SCF and finally the calculations employing the maximum-overlap method (MOM) in combination with CCSD(T) (fig. 4.4).

For all states discussed below except the $n_\pi \rightarrow \pi^*$ singlet and triplet and partially also the $S(\pi' \rightarrow \pi^*)$ state, the calculated vertical excitation energies are virtually converged at CIS(D) level of theory. CC2, EOM-CCSD, ADC(2) and ADC(3) and B2-PLYP give results within 0.3 eV as can be seen in fig. 4.3. For the afore-mentioned $n_\pi \rightarrow \pi^*$ state, however, this agreement breaks down as ADC(3) predicts an excitation energy significantly lower than any other method. Even TDA/B2-PLYP, which is within 0.1 eV from the ADC(3) result for any other state, gives a much higher energy for the $S(n_\pi \rightarrow \pi^*)$ state. Foreclosing the result of MOM-CCSD(T) (fig. 4.4), one finds that the excitation energy of this state is actually even lower at this highest level of theory and with 4.42 eV more than 1 eV below the ADC(3) result. Although the $n_\pi \rightarrow \pi^*$ singlet state is of limited relevance for the processes investigated in this work, the corresponding $T(n_\pi \rightarrow \pi^*)$ state is supposedly the global minimum of the triplet manifold. Hence, a reliable and accurate description of the $T(n_\pi \rightarrow \pi^*)$ state and the neighboring $T(n \rightarrow \pi^*)$ and $T(\pi' \rightarrow \pi^*)$ states is the key to understanding the non-radiative relaxation processes of NB. Despite the fact that the $T(n_\pi \rightarrow \pi^*)$ state exhibits no double-excitation character like its singlet analog, its description is comparably problematic with the single-reference methods being spread over almost 1 eV and the triples correction to MOM-CCSD amounting to 0.3 eV. As a result, the ordering of the lowest triplet states changes multiple times when going from CIS to the approximate second-order methods (CIS(D), ADC(2), CC2) and once more regarding EOM/MOM-CCSD and ADC(3) and DFT.

To clarify this matter, additional calculations were carried out with methods known to yield a good description of highly correlated states with double-excitation and/or multi-reference character. These are DFT/MRCI and state-averaged (SA) CAS-SCF/NEVPT2 to investigate the multi-reference character as well as the maximum-overlap method (MOM) in combination with CCSD and CCSD(T) (MOM-CCSD, MOM-CCSD(T)) to obtain a converged description of the doubly excited $S(n_\pi \rightarrow \pi^*)$ state.

4.4.3 DFT/MRCI

Unfortunately, the results of DFT/MRCI suffer from admixture of low-lying doubly-excited intruder states with four open shells, which artificially lower the energy of the physical excited states (see fig. 4.4). Although this is a known problem of DFT/MRCI, it seems to be particularly pronounced in the case of NB and especially the $S(n \rightarrow \pi^*)$ excited state. An explanation might be the fact that there are indeed low-lying excited states with large double excitation character. Nevertheless, the results of the DFT/MRCI calculations allow for a qualitative comparison of relative energies. Compared to ADC(3), the ordering of the states is the same and especially for the $S(n_\pi \rightarrow \pi^*)$ state DFT/MRCI agrees with ADC(3). In particular for the difference between the two lowest triplet states DFT/MRCI and ADC(3) agree quite well.

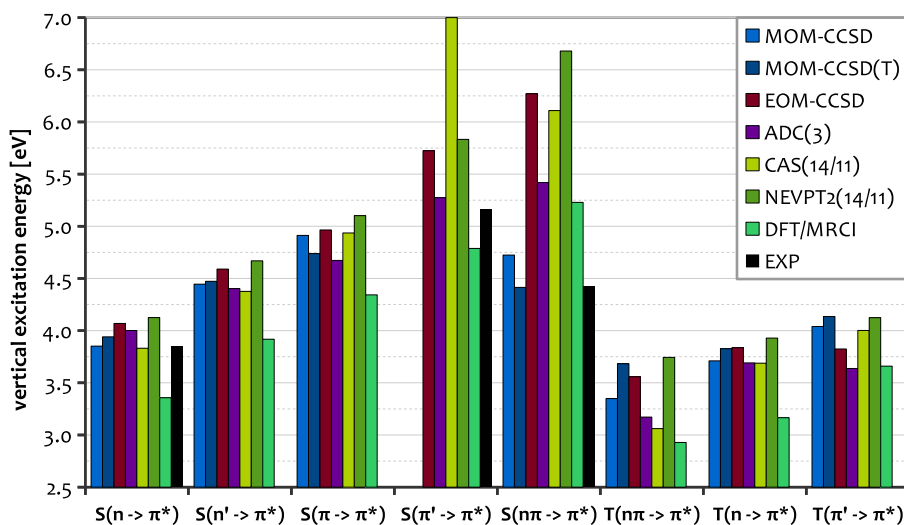


Figure 4.4: Vertical excitation energies calculated with the maximum-overlap method in combination with CCSD/CCSD(T) as well as DFT/MRCI and CAS-SCF/NEVPT2 for the B2-PLYP/def2-TZVP equilibrium geometry. While all methods shown here predict the $T(n_{\pi} \rightarrow \pi^*)$ state to be the lowest triplet state, the critical energy gap to the next higher $T(n \rightarrow \pi^*)$ state varies from 0.13 eV (MOM-CCSD(T)) to 0.72 eV (NEVPT2) with ADC(3) (0.52 eV) and EOM-CCSD (0.3 eV) in between.

4.4.4 CAS-SCF

To obtain an initial guess for the CAS-SCF calculation, MP2/def2-TZVP natural orbitals were generated and reordered according to the choice for the active space (AS) (see below). Concerning the look of their isovalue surface plots, the final CAS-SCF orbitals are virtually indistinguishable from the MP2 natural orbitals and the HF MOs shown in fig. 4.1.

The CAS-SCF calculations were carried out using three different choices for the AS: The largest AS consists of 14 electrons in 11 orbitals (CAS(14/11)), which includes all ten orbitals shown in fig. 4.1 and additionally the lowest bonding π -orbital of the nitro group (lowest orbital of B_2 symmetry, -19.56 eV). This largest AS includes all orbitals with π symmetry as well as all n -orbitals of the nitro group, which should allow for a reasonable description of primary relaxation effects already at the CAS-SCF level of theory. To systematically investigate the importance of each of these orbitals for the relaxation effects, I successively reduced the AS. For the next smaller AS including 12 electrons in 10 orbitals, the π -orbital at the nitro group was removed from the AS. Finally, also the highest and lowest π - and π^* -orbitals of the benzene ring were removed to obtain a CAS(10/8), which only includes orbitals primarily involved in the excitations. In all cases, state-averaging (SA) was done over all states discussed above with equal weights for each. To quantify the influence of the SA scheme, the weights were varied by shifting them either more to the localized $n \rightarrow \pi^*$ excited states of the nitro group or to the $\pi \rightarrow \pi^*$ excited states. These variations of the SA scheme, for which no distinct rules exist, uncovered that the influence of

these choices onto the excitation energies is up to 0.2 eV, which is quite significant regarding the small energy gap between the states of interest. However, the relative energies of the lowest triplet states are less affected by the SA scheme.

For the largest CAS(14/11), the excitation energies calculated at the CAS-SCF and NEVPT2 level are very similar for the unproblematic excited states (all but $n_\pi \rightarrow \pi^*$ and $\pi' \rightarrow \pi^*$). Hence, one may conclude that the primary relaxation effects for these state are well described within the orbitals included in the AS. Already for the CAS(12/10) calculations (data not shown, please be referred to the supporting information of ref. 75) this is no longer true for any of the excited states, leading to the conclusion that all of the orbitals in the CAS are required.

For the $n_\pi \rightarrow \pi^*$ and $\pi' \rightarrow \pi^*$ states CAS-SCF and NEVPT2 excitation energies differ significantly. Hence, for these states an even larger AS would be required. This is, however, not feasible since an even larger AS would lead to prohibitively expensive calculations. As soon as perturbation theory is applied to the CAS-SCF(14/11) calculation *via* the NEVPT2 approach (CAS-NEVPT2), one yields very reasonable agreement with the other high-level calculations for nearly all excited states. Once more, solely the description of the $S(n_\pi \rightarrow \pi^*)$ is poor and worsens from CAS-SCF to NEVPT2 (see fig. 4.4).

Regarding the lowest triplet states, the energy difference predicted at the CAS-NEVPT2 level of theory with the largest AS is only 0.18 eV, which is the second-lowest difference after MOM-CCSD(T) (see below). Furthermore, the CAS calculations can reveal the multi-reference character of the ground state, which is a critical quantity for accuracy and reliability of all single-reference methods. Using CAS(14/11) with the B2-PLYP geometry, the ground state is dominated by a single reference with a contribution of 81%. The next larger contribution is that of the doubly excited ($n_\pi \rightarrow \pi^*$) determinant with 5%. All other contributions are below 2%. For the problematic $n_\pi \rightarrow \pi^*$ excited singlet state on the other hand, the largest determinant has a contribution of only 23% followed by four similar contributions of 19%, 18%, 12% and 10%, explaining the problems concerning its theoretical description. The corresponding $T(n_\pi \rightarrow \pi^*)$ state, however, mainly consists of a singly excited determinant contributing 85% with only one other small admixture from a triply excited determinant with 2.5%, which may explain for the large difference between CCSD and CCSD(T) levels of theory. All singlet and triplet $n \rightarrow \pi^*$ and $n' \rightarrow \pi^*$ excited states show the same pattern of one big and one small contribution. The bigger one making up for about 70 – 75% of the wave function and the smaller one 10 – 15%, while any other contributions are 2% or less.

4.4.5 Maximum-Overlap Method

In principle, the MOM approach allows for a balanced description of the excited states, independent of their character. For this purpose, the SCF is tweaked to converge on the excited state by manipulation of the guess orbitals and application of the MOM algorithm.⁸⁷ Unfortunately, this only works for states, which have no or very little overlap between the involved orbitals, since otherwise the SCF converges back to the ground state. Thus, the MOM approach is not applicable to excited states with large transition moments, which are usually those for which experimental data is available. Hence, the excitation energy of the $S(\pi' \rightarrow \pi^*)$ state of NB could not be obtained since the SCF calculation falls

back to the ground state within the first few iterations. In general, the orbitals resulting from the MOM-SCF are optimized for the respective state, which in combination with high-level CCSD(T) correlation treatment applied here yields very accurate energies of the excited states. Since each state is calculated separately within the MOM approach, this method does not allow for a straightforward calculation of transition moments or any other property involving two or more states.

There is, however a general drawbacks that may reduce accuracy and reliability of the MOM approach: The formally incorrect description of the open-shell singlet state and secondly, spin contamination of the unrestricted Hatree-Fock (UHF) reference. A formally correct open-shell singlet wave function is a linear combination of two determinants. Within the MOM approach, however, only one determinant is used that constitutes a 50:50 mixture of the singlet and triplet ($m_s = 0$) eigenfunctions. Consequently, the S^2 expectation value for this single open-shell determinant is 1.0, whereas a formally correct open-shell singlet state has an expectation value of 0.0. For triplet states with $m_s = \{-1, 1\}$, for which a single reference is sufficient, the S_2 expectation value is 2.0.

For both, singlet and triplet states an UHF calculation is required to obtain the spin-contaminated open-shell reference wave function. At the MOM-CCSD(T) level of theory this problem is compensated by the coupled cluster correlation treatment, which corrects the spin-contamination of the reference wave function to some extent for most of the states. This becomes obvious from a comparison of the $\langle S^2 \rangle$ values for the UHF reference and CCSD wave function, which are:

$$\begin{aligned} S(n \rightarrow \pi^*) & 1.59, 0.94; \\ T(n \rightarrow \pi^*) & 2.60, 1.94; \\ S(n_\pi \rightarrow \pi^*) & 1.52, 0.23; \\ T(n_\pi \rightarrow \pi^*) & 2.51, 1.91; \\ S(\pi \rightarrow \pi^*) & 1.14, 0.82; \\ T(\pi \rightarrow \pi^*) & 2.04, 2.02; \\ T(\pi' \rightarrow \pi^*) & 2.33, 1.98; \end{aligned}$$

The issue of CCSD in combination with spin-contaminated UHF references has previously been investigated in ref. 88. The study reports negligible deviations between the CCSD energies for the doublet state of e.g. the NO_2 molecule calculated with strongly spin-contaminated UHF and spin-pure ROHF references. Nevertheless, the results may be less accurate and less reliable than one would expect from a CCSD(T) calculation for a well-behaved reference and should be taken with grain of salt.

However, aside from these theoretical considerations, one may judge the accuracy and reliability of the MOM approach from a pragmatic point of view, *i.e.* by comparison with experimental values and/or the ADC(3) results. Indeed, ADC(3) and the MOM approach show remarkable agreement, even for those states exhibiting large spin contamination ($dE < 0.1$ eV for $S(n \rightarrow \pi^*)$ and $S(n' \rightarrow \pi^*)$). Hence, I conclude that the MOM approach can, despite the formal problems, be considered to be very accurate.

Additional information that can be obtained from the MOM-CCSD(T) calculation is contained in the magnitude of the triples correction, which may serve as a diagnostic for the importance of correlation effects for each individual excited state. Not surprisingly, the triples correction is more than two times larger

for the $S(n_\pi \rightarrow \pi^*)$ (-0.31 eV) and $T(n_\pi \rightarrow \pi^*)$ ($+0.33$ eV) excited states than for any other state. The next largest correction is found for the $S(\pi \rightarrow \pi^*)$ state, which amounts to 0.16 eV, while it is <0.1 eV for any other state.

After all, the most surprising result of the MOM-CCSD(T) calculations is the energy of the $S(n_\pi \rightarrow \pi^*)$ excited state of 4.4 eV, which is almost 2 eV lower than EOM-CCSD and 1 eV below the ADC(3) and DFT/MRCI results (see fig. 4.4). This huge difference is most likely due to the poor description of doubly excited states at the EOM-CCSD level of theory, which is improved at the ADC(3) level. Due to the conceptual differences in the MOM approach, which involves orbital optimization for each state, doubly-excited states are treated with the same accuracy as any other excited state and the ground state.

Combining the energy of MOM-CCSD(T) with the *fosc* predicted by ADC(3) (0.037) and EOM-CCSD (0.026), the $S(n_\pi \rightarrow \pi^*)$ state should be visible in the absorption spectrum. In fact, the gas-phase spectrum of NB published by Nagakura and coworkers shows a peak with vibrational fine-structure that is found exactly at the predicted energy of 4.42 eV (280 nm).⁷⁸ By comparison to unsubstituted benzene, Nagakura and coworkers attributed this peak to the $S(\pi \rightarrow \pi^*)$ transition. They corroborate their suggestion with the vibrational progression of the peak which was determined to be 860 cm^{-1} in NB compared to 930 cm^{-1} in benzene. However, the $S(\pi \rightarrow \pi^*)$ state has virtually no *fosc* in NB (0.0002 at the ADC(3) and 0.007 at the EOM-CCSD levels of theory) and furthermore a significantly higher energy of 4.7 eV according to ADC(3) and MOM-CCSD(T) and 5 eV according to EOM-CCSD. Also the $S(n' \rightarrow \pi^*)$ state, whose energy of 4.45 eV would be suitable, has negligible *fosc* according to ADC(3) (0.0002) and EOM-CCSD (0.0003) that does not increase along any of the molecular coordinates investigated in section 4.5.

The measured vibrational splitting is identical to the frequency of the ONO bending mode (868 cm^{-1} at CCSD/SVP level, 864 cm^{-1} at B2-PLYP/def2-TZVP level) along which the $S(n_\pi \rightarrow \pi^*)$ state exhibits the largest nuclear gradient at the Franck-Condon point of the ground state. Considering these results and hints, I suggest that this weak absorption at 4.4 eV in the vapor spectrum of NB is due to the $S(n_\pi \rightarrow \pi^*)$ excited state and not the $S(\pi \rightarrow \pi^*)$ state and, consequently, that the second excited singlet state of NB is a predominantly doubly excited state.

Turning to the energy of the lowest triplet states of NB, MOM-CCSD and MOM-CCSD(T) yield the same state ordering as ADC(3), but the energetic gap between $T(n_\pi \rightarrow \pi^*)$ and $T(n \rightarrow \pi^*)$ states is much smaller for MOM-CCSD (0.35 eV) and MOM-CCSD(T) (0.14 eV) than for ADC(3) (0.52 eV). Since the MOM-CCSD(T) result is presumably the most accurate one, the difference of the vertical energies of the lowest triplet states is in the order of 0.1 - 0.2 eV. Hence, structural relaxation in the excited states has to be taken into account to answer the question for the globally lowest triplet state. In any case, the $n \rightarrow \pi^*$ and $n_\pi \rightarrow \pi^*$ triplet states are most likely closer in energy than predicted at the ADC(3) level of theory.

4.4.6 Structural Relaxation in the Excited States

To account for nuclear relaxation, the geometries of all relevant excited states were optimized at the EOM-CCSD level of theory in C_{2v} symmetry using the cc-pVDZ basis sets. Subsequently, the geometries of the lowest singlet and two

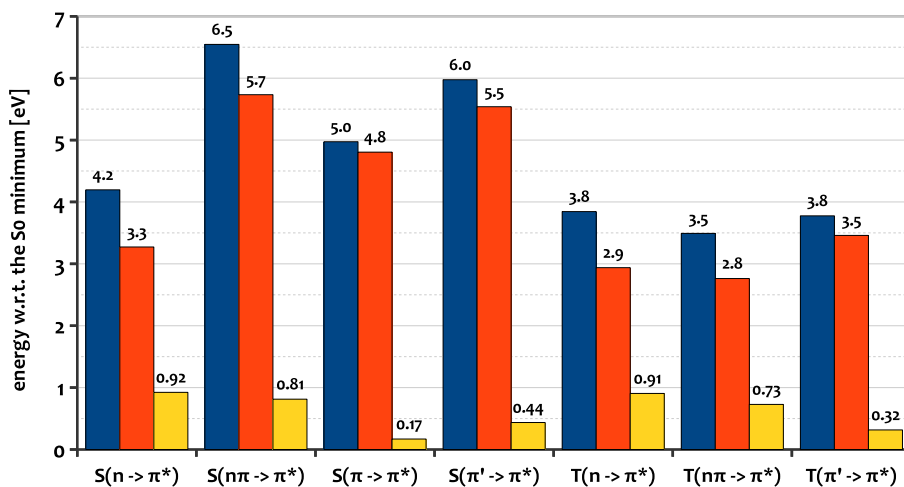


Figure 4.5: Vertical excitation energies (blue), energies of the equilibrium structures of excited states (red) and differences thereof (yellow) relative to the ground-state minimum of nitrobenzene at the EOM-CCSD/cc-pVDZ level of theory in C_{2v} symmetry. In general, the benefit of structural relaxation is larger for $n \rightarrow \pi^*$ excited states than for $\pi \rightarrow \pi^*$ excited states. The $T(n \rightarrow \pi^*)$ state exhibits a slightly larger relaxation than the $T(n_\pi \rightarrow \pi^*)$ excited state, reducing the energy difference between these states compared to the vertical excitation energies.

lowest triplet states were asymmetrically distorted and then reoptimized without molecular symmetry using the smaller SVP basis set to check whether the states have minima of lower symmetry. Only the $n_\pi \rightarrow \pi^*$ state has a C_s symmetric minimum with the oxygen atoms bent out of the molecular plane exhibiting an ONCO out-of-plane angle of 40° . This distortion, however, hardly affects the energy of the relaxed structure ($dE < 0.03$ eV), as can be seen in the relaxed scan along this ONCO out-of-plane coordinate (see fig. 4.8). Vertical excitation energies and energies of the equilibrium structures of the excited states obtained at the EOM-CCSD/cc-pVDZ level of theory are summarized in fig. 4.5.

In general, geometric relaxation is more pronounced for the $n \rightarrow \pi^*$ excited states of NB than for the $\pi \rightarrow \pi^*$ excited states. Focusing on the triplet states, the $n \rightarrow \pi^*$ excited state shows a slightly larger relaxation contribution than the $n_\pi \rightarrow \pi^*$ state (0.91 eV vs 0.73 eV). Combining these EOM-CCSD/cc-pVDZ relaxation energies with the MOM-CCSD(T) vertical excitation energies, these lowest triplet states are virtually degenerate. Taking into account the vertical excitation energies obtained with CAS-SCF/NEVPT2, DFT/MRCI, ADC(3), EOM-CCSD or TD-B2-PLYP, which all give the same state ordering as MOM-CCSD(T) but with a significantly larger energy gap, the $T(n_\pi \rightarrow \pi^*)$ state is obtained as the lowest triplet state with an energy gap to the minimum of the $T(n \rightarrow \pi^*)$ state in the order of -0.05 eV (switched ordering) to 0.5 eV. After all, the ordering of the lowest triplet state of NB in vacuum can not be determined conclusively. However, the $T(n \rightarrow \pi^*)$ and $T(n_\pi \rightarrow \pi^*)$ states are most likely very close in energy. For the investigation of non-radiative relaxation of NB, it is sufficient to know that these lowest states are almost degenerate. In such a

case, the actual ordering is of minor relevance since there is a conical intersection connecting the minima of the two states (see table 4.1).

Considering the fact that, as will be demonstrated below, the triplet manifold of NB is most likely accessed *via* ISC from the $S(n \rightarrow \pi^*)$ to the $T(n_\pi \rightarrow \pi^*)$ state, it is suggestive that the triplet population will end up in the $T(n_\pi \rightarrow \pi^*)$ minimum. From there, thermal population of the $T(n \rightarrow \pi^*)$ state may be possible, depending on the actual energy gap and the thermal energy available. However, to address such delicate dynamic questions conclusively, advanced quantum-dynamical simulations on highly accurate PES are required. These are, due to the time-scale of several hundreds of picoseconds, still out of reach even on most modern computers.

Table 4.1: Relative energies and structural parameters for the most relevant points of the potential energy surface of nitrobenzene at the (EOM-)CCSD/cc-pVDZ level of theory. Energies for each of the relevant points on the PES are given with respect to the lowest accessible minimum (low. min.) as well as the energies of S_1 and ground state (S_0) at the FranckCondon point. In this table, for the sake of compactness T_1 is used to abbreviate the $T(n_\pi \rightarrow \pi^*)$ state and T_2 for the $T(n \rightarrow \pi^*)$ state. The C_S symmetric structures exhibit ONCO out-of-plane bending angles of 48° (CI(S_1/S_0)), 38° (T_1) and 54° (X(T_1/S_0)).

point	sym.	low. min.	S_1 (FC)	S_0 (FC)	r(CN)	r(NO)	\angle (ONO)
S_0 min.	C_{2v}	-	-4.20	-	1.483	1.221	125.4
S_1 min.	C_{2v}	-	-0.92	3.27	1.392	1.293	106.3
CI(S_1/S_0)	C_{2v}	0.63 (S_1)	-0.29	3.91	1.357	1.324	88.2
CI(S_1/S_0)	C_S	0.43 (S_1)	-0.49	3.71	1.422	1.324	91.1
X(S_1/T_1)	C_{2v}	0.03 (S_1)	-0.89	3.31	1.383	1.289	102.1
T_1 min.	C_S	-	-1.44	2.76	1.426	1.307	115.9
T_2 min.	C_{2v}	0.18 (T_1)	-1.26	2.94	1.398	1.292	106.2
X(T_1/S_0)	C_S	0.22 (T_1)	-1.21	2.98	1.449	1.327	97.1
CI(T_1/T_2)	C_{2v}	0.19 (T_1)	-1.25	2.95	1.404	1.3	108.8

At this point it may thus help to consider the experimentally observed reactivity of nitroaromatics: On the one hand, it has been found that the nitro group can undergo excited-state intermolecular and intramolecular hydrogen-abstraction, e.g. in *ortho*-nitrotoluene, which is only possible in the $n \rightarrow \pi^*$ excited triplet but not in the $n_\pi \rightarrow \pi^*$ excited triplet state.⁶⁹ On the other hand, this reaction reduces the lifetime of the *ortho*-isomer of nitrotoluene (690 ps) only marginally compared to NB (770 ps).⁴⁴ Hence, one may conclude that the $n \rightarrow \pi^*$ state has to be thermally accessible from the minimum of the $n_\pi \rightarrow \pi^*$ state at room temperature, but also that either a significant energy gap or a barrier for hydrogen-transfer has to exist since otherwise, the triplet lifetime of *ortho*-nitrotoluene should be much lower than the one of NB. In chapters 3 and 2, this hydrogen transfer has been investigated for the cases of *ortho*-nitrobenzyl acetate (oNBA) and *ortho*-nitrophenylacetate (oNPA) at various levels of theory yielding substantial barrier of 0.4-0.5 eV.^{30;69} This suggests a rather small splitting of the lowest triplets, since otherwise the hydrogen transfer, for which the energy difference to the $T(n \rightarrow \pi^*)$ state and the barrier in this state have to be overcome, would presumably not take place at all. To finally answer this question, it will help to determine the temperature-dependent lifetimes of the three isomers of nitrotoluene experimentally and calculate the resulting barrier

via an Arrhenius ansatz.

4.4.7 Technical Details

Software

Calculations employing configuration-interaction singles (CIS), CIS with the iterative doubles correction CIS(D), coupled cluster singles, doubles and perturbative triples (CCSD(T)), equation-of-motion (EOM)-CCSD, maximum-overlap method (MOM)⁸⁷ and the algebraic-diagrammatic construction of second and third order (ADC(2), ADC(3))⁸⁹ were carried out using a development version of the Q-Chem 4.1 program package.⁹⁰ The complete active-space self-consistent field (CAS-SCF), n-electron valence-state perturbation theory (NEVPT2), B3-LYP^{91;92} and B2-PLYP⁹³ calculations were conducted using the ORCA 2.9.1 program package.⁵⁴ Perturbative coupled-cluster of second-order (CC2) and its linear-response variant (LR-CC2) calculations were done with the TURBOMOLE 6.3.1 software.⁴⁶⁻⁵⁰ Density-functional theory/multi-reference configuration interaction (DFT/MRCI) and spin-orbit coupling calculations were done with the DFT/MRCI and SPOCK-CI programs, respectively.⁹⁴⁻⁹⁷

Basis Sets

For all energy calculations along the NO stretching, ONO bending and ONCO out-of-plane coordinates the def2-TZVP(-f) basis set was employed,⁵⁷ which is obtained from the standard def2-TZVP basis set by deleting the computationally most expensive f-type polarization functions. For the ADC(3) calculations, this modification significantly reduces computational cost while it hardly affects the results ($\Delta E < 0.05$ eV). Calculations of the vertical excitation energies at the ground-state equilibrium geometry were carried out with the unmodified def2-TZVP basis set. The MOM-CCSD(T) single-point energy calculation for the $S(n_\pi \rightarrow \pi^*)$, $T(n_\pi \rightarrow \pi^*)$ and $T(n \rightarrow \pi^*)$ states were carried out with the def2-TZVP(-f) and cc-pVTZ⁹⁸ basis sets, since it was not possible to converge the unrestricted SCF reference in the calculation with def2-TZVP. The results of these calculations are lying within 0.02 eV for excitation energies and excitation energy differences. For the calculation of the $S(n \rightarrow \pi^*)$, $T(n \rightarrow \pi^*)$ and $T(n_\pi \rightarrow \pi^*)$ relaxed potential energy surface cuts along ONO bending and ONCO out-of-plane modes at EOM-CCSD level of theory, the basis set quality was reduced to def2-SVP to reduce the computational effort.

Symmetry

All calculations were carried out exploiting C_{2v} symmetry of the NB molecule. Only along the ONCO out-of-plane coordinate and for some of the excited state optimizations the symmetry was reduced to C_s and C_1 as mentioned in the text.

4.5 Mechanism of Non-Radiative Decay

4.5.1 Approach

By comparison of the ground- and excited-state equilibrium structures (see table 4.1) I identified the coordinates, which will presumably be relevant for the

non-radiative relaxation processes. The four coordinates exhibiting the largest changes between ground and excited state geometries of the lowest excited states are the NO and CN bond lengths as well as ONO-angle and the ONCO out-of-plane improper dihedral (given as the displacement from the planar structure: $\text{ONCO out-of-plane} = 180 - (\text{ONCO dihedral})$). Out of these coordinates, only the latter has been previously inferred to be relevant for NB photochemistry and investigated by Takezaki and Quenneville and coworkers (for a summary of the existing literature see section 4.2).⁶⁵

To obtain a coarse overview, rigid scans were carried out using the ground-state equilibrium structure as a starting point and ADC(3)/SVP single-point calculations to yield ground and excited-state energies (see supporting information of ref. 75). It was found that along the CN bond length as well as along the nitro group tilting (CCNO dihedral) coordinates the PES of ground and excited states are almost flat and virtually parallel, such that crossings between these states are absent. Hence, these coordinates were excluded from further investigations.

Along the unrelaxed ONO bending, ONCO out-of-plane and NO stretching coordinates, on the contrary, numerous crossings between all relevant states exist. To improve the theoretical description, the scans along the ONO bending and ONCO out-of-plane coordinates were refined. For this purpose, the unrelaxed structures of the preliminary calculations were optimized at the EOM-CCSD/SVP level of theory to obtain relaxed PES of the relevant states and coordinates. Along these relaxed scans, ADC(3)/def2-TZVP(-f) as well as DFT/MRCI/def2-TZVP single-point calculations were carried out to obtain energies and spin-orbit coupling (SOC) elements for the relevant excited states.

In the following, only the energies obtained with ADC(3) are shown and discussed, which is due to their much better agreement with experimental results and high-level calculations compared to DFT/MRCI (see section 4.4 and fig. 4.5 for details). For the latter, the excitation energies are too low compared to experimental values and high-level calculations, which is true in particular for the $S(n \rightarrow \pi^*)$ excited state (S_1). As a result from this erroneous description, one would expect ultra-fast deactivation *via* the artificially lowered S_1/S_0 CI (almost 1 eV below the experimental energy of the S_1 at the FC-point) along the ONO bending and hardly any population of the triplet state *via* ISC. Since this is obviously not the case, I will omit the PES calculated with DFT/MRCI in the discussion. The SOC elements calculated with DFT/MRCI, however, show reasonable agreement with those obtained with CAS-NEVPT2 for the ground-state equilibrium geometry.

The energies for the key points of the PES (crossing points, conical intersections and excited state minima) given in the text below have been obtained at EOM-CCSD/cc-pVDZ level of theory since this method allows for minimum energy crossing point (MECP) optimizations. These energies and geometric parameters for these point are summarized in tab. 4.1. For the respective values estimated from the ADC(3)/def2-TZVP(-f) PES, see 4.9.

4.5.2 Internal Conversion

Let me first turn to the theoretical investigation of the fastest, experimentally observed process, for which an upper limit of 100 fs has been reported.⁶⁵

For an excitation of the bright $S(\pi' \rightarrow \pi^*)$ state, one may speculate that this

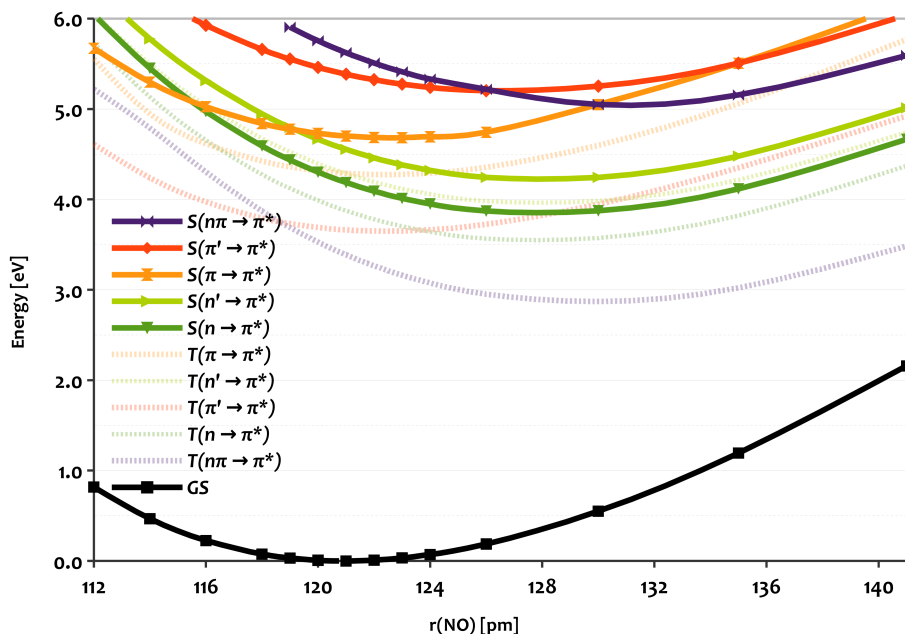


Figure 4.6: Unrelaxed potential energy surfaces along the symmetric NO-stretching mode at the ADC(3)/def2-TZVP(-f) level of theory. Singlet states are depicted as continuous lines, triplet states as transparent, dashed lines. Corresponding singlet and triplet states have the same color.

process could be IC to S_1 since there is a continuous path from the bright state to the lowest singlet state (fig. 4.6). This complete path is lying below the energy of the bright state at the FC point. Hence, if energy conservation is assumed, IC from the bright $S(\pi' \rightarrow \pi^*)$ to S_1 should be possible in the given time window that equals a few vibrational periods of the symmetric NO stretching mode. In this case, a large fraction of the initial excitation energy that is released during IC from the bright state to S_1 will end up in this symmetric NO stretching mode.

In their experiments, however, Takezaki and coworkers directly excited the S_1 state at 320 nm (see fig. 4.9) and there has to be another process causing this ultra-fast component. For cooling of the S_1 population, as inferred by Takezaki and coworkers, this process is at least an order of magnitude too fast. In similar aromatic molecules, internal vibrational equilibration (IVR) and cooling take place on time-scales of 1 and 10 ps, respectively.²⁵ Hence, I think this ultra-fast signal is caused by a fraction of the vibrationally excited S_1 population undergoing IC to the ground state *via* the S_1/S_0 CI along the ONO bending coordinate, which shown in fig. 4.7.

4.5.3 Inter-System Crossing into the Triplet Manifold or Internal Conversion to the Ground State

Eventually, the population has reached S_1 either *via* IC or directly *via* excitation of the weak $S(n \rightarrow \pi^*)$ band, like in the experimental investigations described in section 4.2. For the ISC into the triplet manifold with a quantum yield of

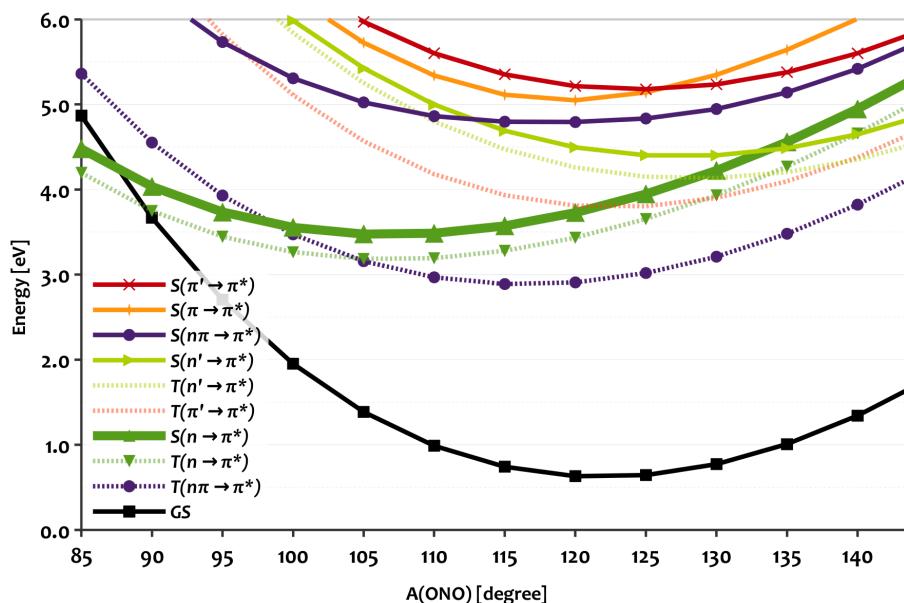


Figure 4.7: $S(n \rightarrow \pi^*)$ relaxed (thick green line) surface of the ONO-bending coordinate at the ADC(3)/def2-TZVP(-f)//EOM-CCSD/SVP level of theory. Right next to its minimum, the $S(n \rightarrow \pi^*)$ and $T(n_\pi \rightarrow \pi^*)$ states are degenerate, which together with the large spin-orbit coupling between those two states explains the fast and efficient inter-system crossing. At even larger distortions and higher energy the $S(n \rightarrow \pi^*)$ state also crosses the S_0 , which most likely is the channel for the observed 20% of the population that do not undergo ISC but IC.

80%, a time-scale of 6 ps has been reported, whereas the other 20% undergo IC back to the ground state. After 6 ps, it can be assumed that IVR and cooling of the population in S_1 is largely progressed. Hence, to explain for ISC on such a time-scale, one would expect an energetically accessible crossing between the $S(n \rightarrow \pi^*)$ and $T(n_\pi \rightarrow \pi^*)$ states in close proximity to the $S(n \rightarrow \pi^*)$ minimum exhibiting large SOC. Furthermore, a CI between the $S(n \rightarrow \pi^*)$ and the ground state should be present that is energetically and structurally further away but yet accessible immediately after the excitation to explain for the remaining 20% of the population that do not undergo ISC but instead IC.

This is exactly what is found for the S_1 optimized PES shown in fig. 4.7. The crossing between $S_1/T(n_\pi \rightarrow \pi^*)$ is found to be virtually degenerate with the S_1 minimum ($\Delta E < 0.03$ eV), while the S_1/S_0 CI is significantly higher in energy ($\Delta E = 0.63$ eV) but still below the energy of the S_1 at the FC point (FC point: 4.2 eV, S_1 minimum: 3.3 eV, see tab. 4.1 for all the data).

Accordingly, I suggest the following mechanistic picture: Due to the gradient in the S_1 state at the FC point, the population will reach the S_1 minimum with a momentum pointing in the direction of the crossings with the $T(n_\pi \rightarrow \pi^*)$ and the ground state. Regarding the initial excitation energy of the S_1 state at the FC point, which is only slightly below to the energy of the S_1/S_0 CI, IC to the ground state is possible *via* this CI is possible only immediately after the initial

excitation. Already about 100 fs later, too much energy may be dissipated *via* IVR and cooling, effectively trapping the population in the S_1 minimum. From there, only the crossing point with the $T(n_\pi \rightarrow \pi^*)$ state is accessible. At this crossing point, the SOC calculated at the DFT/MRCI level of theory is about 50 cm^{-1} , which causes the remaining population in S_1 to undergo ISC into the triplet manifold.

To verify this hypothesis, I suggest an experiment in which the excitation energy of NB is to be varied (e.g. by excitation of the bright $S(\pi' \rightarrow \pi^*)$ state instead of the $S(n \rightarrow \pi^*)$ state) while the quantum yield of the population undergoing either IC or ISC is to be measured. The outcome should be different depending on the excitation energy or in practice, which of the states of NB is excited. This is due to the fact that the vibrational excess energy available to the molecules immediately after the excitation discriminates between IC and ISC or in other words the S_1/S_0 and $S_1/T(n \rightarrow \pi^*)$ state crossings. To allow for more quantitative predictions of the outcome of these experiments, quantum-dynamics simulations should be performed.

Besides S_1/S_0 IC along the ONO bending coordinate, there is in principle another possibility for this IC along the ONCO out-of-plane coordinate as can be seen in fig. 4.8. Although the latter is optimized for $T(n_\pi \rightarrow \pi^*)$, the S_1 optimized surface is very similar. A S_1/S_0 IC along this CI involving the out-of-plane bending has been suggested by Quenneville and coworkers. According to EOM-CCSD/cc-pVDZ the position of this CI is 0.43 eV above the S_1 minimum, which is 0.2 eV lower than the C_{2v} symmetric CI along the ONO bending coordinate (see table 1). Nevertheless, I do not expect the IC along the ONCO coordinate to be of major relevance for two reasons. At first, the out-of-plane bending is not FC active as it experiences no gradient in any of the singlet excited states (the relaxed excited-state structures are all planar). Secondly, this out-of-plane bending is only weakly coupled to the FC active modes, since the latter are all in-plane modes. The ONO bending mode, on the contrary, is one of the two FC active coordinates exhibiting the largest gradient on the S_1 surface at the FC point (see fig. 4.7). Hence, immediately after excitation and IC to the S_1 mainly the ONO bending and NO stretching modes may be vibrationally excited and the primary internal-vibrational redistribution (IVR) does most likely not include the ONCO out-of-plane mode. Only *via* interaction with the solvent and indirect IVR, the ONCO out-of-plane mode may receive a fraction of the vibrational energy. After all, any process taking place mainly along the ONCO coordinate that involves crossing a barrier of 0.4 eV will presumably be much slower compared to a similar process along the ONO coordinate, although the barrier there is 0.6 eV.

4.5.4 Inter-System Crossing to the Ground State

After all, 80% of the population end up in the $T(n_\pi \rightarrow \pi^*)$ state, from which the ground state is regenerated *via* ISC within hundreds of picoseconds depending on solvent and temperature.⁶⁵ To investigate this second ISC back to the ground state, the $T(n_\pi \rightarrow \pi^*)$ optimized ONO bending and ONCO out-of-plane coordinates were calculated. For this second ISC process, one condition has changed compared to initial IC and ISC processes. When reaching the triplet manifold on a time-scale of 6 ps, the NB molecules will presumably be completely equilibrated internally as well as with the environment and consequently,

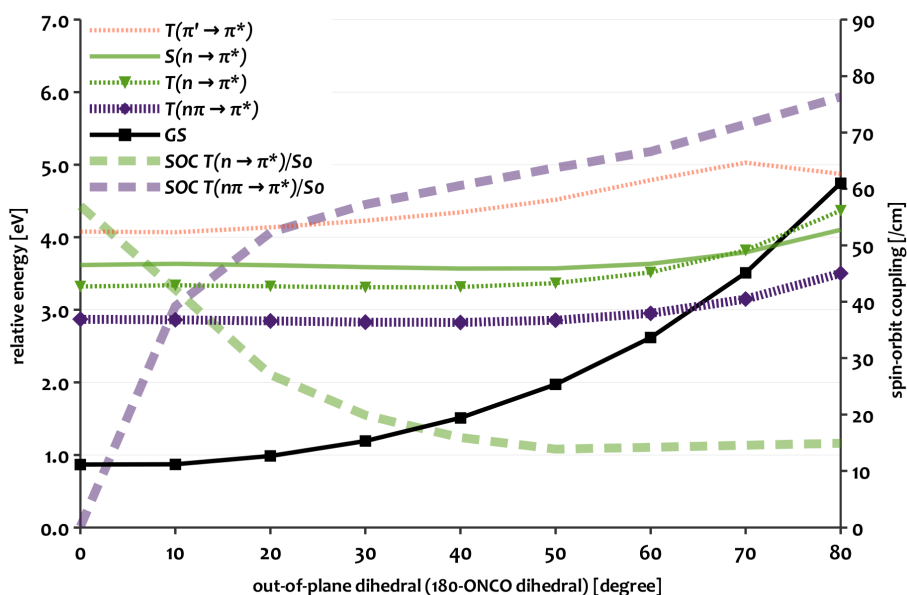


Figure 4.8: $T(n_{\pi} \rightarrow \pi^*)$ relaxed potential energy surface of the ONCO dihedral angle at the ADC(3)/def2-TZVP(-f)//EOM-CCSD/SVP level of theory in C_S symmetry. Additionally, the spin-orbit coupling elements (SOC) between the lowest triplets and the ground state (bold, transparent lines) obtained at DFT/MRCI level of theory are shown on a secondary y-axis (right).

the energy available will be equal or at least very close to the thermal energy. Hence, this second ISC should be seen as a classical thermo-chemical reaction which is corroborated by the temperature-dependent rate constant reported by Takezaki and coworkers.

Regarding the $T(n \rightarrow \pi^*)$ optimized PES along the ONCO coordinate (fig. 4.8), a thermal excitation to $T(n_{\pi} \rightarrow \pi^*)$ *via* the crossing along the ONO bending coordinate can be excluded at room temperature due to the large energy difference of about 0.5 eV between these states, at least at the ADC(3) level of theory. Remembering the results from section 4.3 and 4.4, which hint towards a much smaller energy gap as predicted by ADC(3), the $T(n \rightarrow \pi^*)$ state may be thermally accessible after all.

The actual energy gap and the state ordering are, however, irrelevant concerning the validity of this hypothesis. Along the ONCO out-of-plane mode, both lowest triplet states exhibit an energetically accessible crossing with the ground state at an ONCO out-of-plane angle of 65° and 70° , respectively. For both states the barrier towards the CI with the ground state is approximately the same. Hence, even if the lowest triplet states are energetically degenerate, the pathway for non-radiative relaxation is determined rather by the magnitude of SOC with the ground state.

Although the SOC between the $T(n_{\pi} \rightarrow \pi^*)$ state and the ground state is zero according to El-Sayed's rules and our calculations for the C_{2v} symmetric equilibrium geometry, this changes dramatically as soon as the molecule is distorted along this ONCO out-of-plane coordinate. For ONCO out-of-plane bending

angles larger than 10° the SOC between ground state and $T(n_\pi \rightarrow \pi^*)$ state is larger than that of the $T(n \rightarrow \pi^*)$ state (see fig. 4.8). Hence, the second ISC will presumably take place along the ONCO out-of-plane bending in the $T(n_\pi \rightarrow \pi^*)$ state in a classical thermo-chemical reaction and the barrier that has to be overcome is given as the difference between the $T(n_\pi \rightarrow \pi^*)/S_0$ crossing point and the $T(n_\pi \rightarrow \pi^*)$ minimum, which is 0.15 eV at the EOM-CCSD/cc-pVDZ level of theory in C_s symmetry (see tab. 4.1). To eliminate restrictions introduced by symmetry, the minimum-energy crossing point (MECP) was calculated also at the B2-PLYP level of theory using ORCA. Starting from the EOM-CCSD/SVP optimized geometry closest to the crossing point in fig. 4.8 (ONCO out-of-plane of 60°), the MECP optimization was carried out using the closed-shell variant of B2-PLYP for the ground state and the unrestricted open-shell variant for the $T(n_\pi \rightarrow \pi^*)$ state. B2-PLYP was chosen for this purpose due to its very good agreement with ADC(3) for the vertical excitation energy of $T(n_\pi \rightarrow \pi^*)$ (see fig. 4.3), which in combination with its low computational demands enables one to carry out vibrational analyses at the crossing point and respective minimum. In perfect agreement with the EOM-CCSD calculations in C_s symmetry (see tab. 4.1), the difference of the total energies between $T(n_\pi \rightarrow \pi^*)$ minimum and the MECP between $T(n_\pi \rightarrow \pi^*)$ and the ground state is 0.15 eV. Furthermore, it was found that this value is hardly affected by thermal and entropical corrections for RT (+0.01 eV).

Using the temperature-dependent lifetimes of the triplet state reported by Takezaki and coworkers to calculate the energy barrier of this reaction *via* a simple Arrhenius ansatz, one obtains an activation energy of approximately 0.084 eV, which is in very reasonable agreement with our theoretical results (for the calculation see supporting information of ref. 75).

Finally, one may ask why this second ISC process back to the ground state is two orders of magnitude slower than the ISC into the triplet manifold. I think there are three main reasons. At first, the molecule is much colder at the time of the second ISC, which is true in particular for the relevant ONCO out-of-plane coordinate, that is not Frank-Condon active at all. Secondly, the energetic distance of the crossing point to the minimum is much lower for the first ISC than for the second (0.03 eV *vs.* 0.15 eV) and finally, the ONCO out-of-plane coordinate is a large-amplitude motion that deforms the molecule out of its planar structure. Hence, this motion is hindered by solvent molecules, which might provide an explanation for the chain-length dependent rate-constant found by Takezaki and coworkers. The higher the viscosity of the solvent, the more energy is required for its displacement and hence also for this motion to be carried out.

4.6 Summary & Conclusion

Despite being subject of research for more than 100 years, there are still many open questions regarding the photochemical and photophysical processes as well as the underlying electronic structure of electronically excited nitro-aromatic compounds and their parent nitrobenzene (NB). On the experimental side, this was traced back to the non-radiative character of the relaxation processes in NB, while on the theoretical side, the involved electronic structure of NB complicates their computation.

Here, I reported an extensive theoretical investigation with the aim of establishing a reliable and accurate methodology for the description of NB (section 4.4). Subsequently, potential energy surfaces (PES) of NB were investigated employing high-level single and multi-reference *ab initio* as well as DFT methods featuring the recently implemented ADC(3) and DFT/MRCI (section 4.5), which allow for an accurate and balanced description of singly and doubly excited states as well as for a calculation of spin-orbit couplings (SOC).

The difficulties with the theoretical description of NB could be traced back to a low-lying singlet state with large double-excitation character of about 50% at an energy of 4.4 eV according to MOM-CCSD(T). In very good agreement with excitation energy, vibrational splitting and oscillator strength, this state was assigned to the lowest energy peak in the experimental absorption spectrum of NB vapor. It constitutes the second lowest excited singlet state of NB at the ground-state equilibrium geometry.

As a result of its large double excitation character and thus great importance of secondary (electronic) relaxation effects, the calculated vertical excitation energy of this $n_\pi \rightarrow \pi^*$ excited singlet state of B_1 symmetry ranges from 6.3 eV (EOM-CCSD) to 4.4 eV (MOM-CCSD(T)), with ADC(3) (5.4 eV) and DFT/MRCI (5.2 eV) in between. The difficulties in its theoretical description and the resulting inaccuracy persist for the corresponding 1^3B_1 triplet state. As a consequence, the riddle of the character of the lowest triplet state of NB, for which the 1^3A_2 $T(n \rightarrow \pi^*)$ and 1^3B_1 $T(n_\pi \rightarrow \pi^*)$ states are good candidates, could not be ultimately resolved. Concluding the results of the highest level single- and multi-reference calculations, it seems that the $T(n_\pi \rightarrow \pi^*)$ is slightly below the $T(n \rightarrow \pi^*)$ state at the Franck-Condon (FC) point (ΔE MOM-CCSD(T): 0.14 eV, CAS-NEVPT2(14/11): 0.18 eV). Including nuclear relaxation effects obtained at the EOM-CCSD level of theory, which favor the $T(n \rightarrow \pi^*)$ state a little bit more (-0.92 eV *vs.* -0.73 eV), the small energy difference is decreased even further, yielding two virtually degenerate triplet states. According to ADC(3), however, the difference is significantly larger at the Franck-Condon geometry (0.52 eV) and prevails when relaxation effects are included.

At this point, it is unclear whether ADC(3) or MOM-CCSD(T) and CAS-NEVPT2 yield more accurate results. There are valid arguments for and against all of these methods. Although MOM-CCSD(T) should in general be more accurate than ADC(3), it suffers from serious spin contamination of the reference and there exists not much experience on how this may affect the accuracy of the method. For any other than the $n_\pi \rightarrow \pi^*$ excited states of NB, however, MOM-CCSD(T) shows very good agreement with experimental values and other high level calculations despite spin contamination. For the CAS-NEVPT2 calculations, tweaking of the state averaging (e.g. equal weights for each class of states, equal weight for each state, inclusion of further/less states in the averaging scheme etc.) allows one to obtain almost any desired result within 0.1-0.3 eV. Hence, it is left to future studies employing even higher-order methods to determine the character of the lowest triplet state of NB. For the investigation of the non-radiative relaxation pathways of NB, it was sufficient to know the character of the lowest two triplet states and that they are almost degenerate.

To study the non-radiative relaxation processes, the relaxed PES of the relevant states along the symmetric NO stretching, ONO bending and ONCO out-of-plane bending coordinates of the NB molecule were calculated. For this pur-

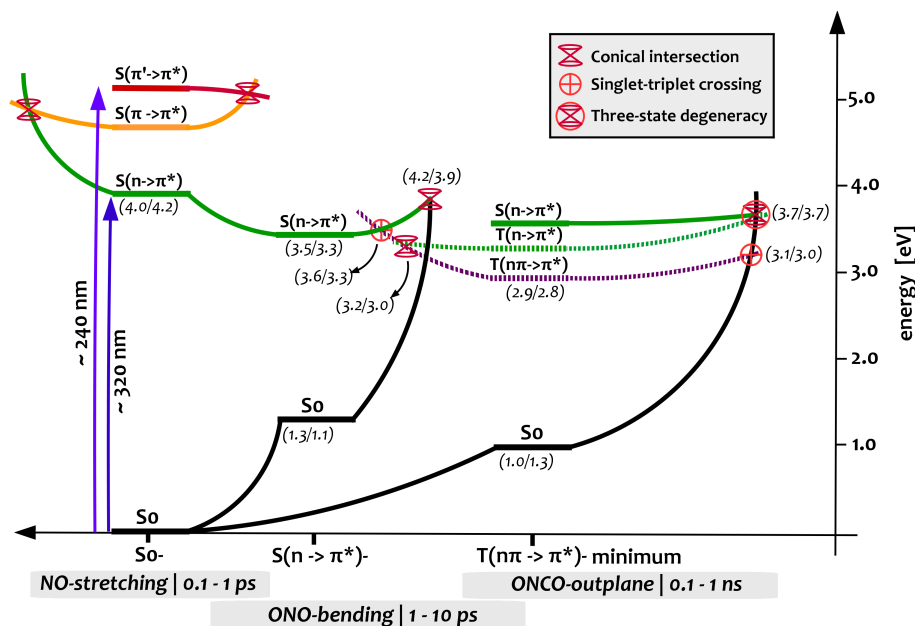


Figure 4.9: Schematic potential-energy surface of the non-radiative relaxation pathways of nitrobenzene based on the ADC(3) and EOM-CCSD calculations. This scheme summarizes the relaxed surface scans, relating conical intersections and singlet-triplet crossings to the coordinates and time-scales of the non-radiative relaxation processes. ADC(3) and EOM-CCSD energies in eV for the key points of the PES are given in parenthesis (ADC(3)/CCSD).

pose I have chosen the ADC(3) model for energies and DFT/MRCI to obtain spin-orbit-couplings (SOC), which are shown in fig. 4.9.

The first and fastest decay process is observed on a time-scale < 100 fs in the experimental investigation, in which the S_1 is directly excited. Based on the results of the calculations, I suggested this process to be the internal conversion (IC) of a fraction (about 20%) of the vibrationally excited S_1 population to the electronic ground state *via* an energetically high-lying conical intersection (CI) along the ONO bending coordinate. A few hundreds of femtoseconds later, too much energy is dissipated to reach the CI, effectively trapping the population in S_1 .

If NB is excited into its bright $S(\pi' \rightarrow \pi^*)$ state, IC to S_1 will presumably take place on a similar time-scale along the NO stretching coordinate, along which there exists a continuous pathway well below the initial excitation energy. Since there will be much more vibrational excess energy available to the molecules after IC to S_1 , I suggested that in case of excitation of the bright state, the fraction of the population undergoing IC instead of ISC will be significantly larger. Inter-system crossing (ISC) from S_1 to the triplet manifold was reported to occur on a 6 ps time-scale exhibiting a quantum yield of 80%. The calculations show that indeed, the $T(n_\pi \rightarrow \pi^*)$ state crosses the minimum of the S_1 along the ONO bending mode (ΔE 0.04 eV, see table 1). For the crossing point, one obtains a SOC in the order of 50 cm^{-1} , which explains for the unusually fast and efficient ISC of NB.

The second ISC from the triplet manifold back to the ground state has been found to occur on a time-scale of hundreds of picoseconds, depending on temperature and surprisingly also the chain length of the aliphatic solvent. Due to the much longer time-scales of this process, one can expect the molecules to be equilibrated with their environment. Our results corroborate the hypothesis of Takezaki and coworkers, who suggested this final relaxation to occur along the ONCO out-of-plane coordinate. In the $T(n_\pi \rightarrow \pi^*)$ relaxed PES along this coordinate, there are crossings between both low-lying triplet states with the ground state, for each of which there is significant SOC. Since, however, the SOC at the crossing points is about three times larger between the energetically favored $T(n_\pi \rightarrow \pi^*)$ state and the ground state than for the $T(n \rightarrow \pi^*)$ state (75 cm^{-1} vs. 15 cm^{-1} , see fig. 4.8), I suggested the second ISC to the ground state to occur from the $T(n_\pi \rightarrow \pi^*)$ state. Due to an almost flat run of the lowest two triplet states along this coordinate, the $T(n_\pi \rightarrow \pi^*)/S_0$ crossing is found at an energy only 0.15 eV above the relaxed $T(n_\pi \rightarrow \pi^*)$ minimum. This is in very reasonable agreement with the experimentally observed temperature dependency that translates into a barrier of 0.08 eV according to the Arrhenius formalism.

Finally, I want to point out a parallel between the failure of CC2 for NB and the problems concerning the description of ozone, which is isoelectronic to NO_2^- and hence related to the aromatic nitro group. The PES of NO_2^- has been investigated and compared to PES obtained with MP2, CCSD and CCSDT by Pabst and coworkers,⁹⁹ who discovered very similar problems leading to the same overestimation of the NO bond length by CC2 that was reported here. In their work, the problems are traced back to the structure of the CC2 model in combination with significant singlet double-radical character of ozone and NO_2^- . They emphasize that CC2 was developed aiming at the description of excited states, but not as an improvement over MP2 for ground-state geometries, for which the latter should be preferred. Regarding our results, I want to reface their warning and suggest not to use CC2 for optimization of systems containing an aromatic or aliphatic nitro group.

Chapter 5

PCM-Based *a Posteriori* Corrections for Excitation Energies in Solution

In this chapter, I describe development, implementation and evaluation of two perturbative, density-based *a posteriori* correction schemes for vertical excitation energies in solution calculated in the framework of a polarizable continuum model (PCM). Employing the algebraic-diagrammatic construction (ADC) scheme of up to third order as well as time-dependent density-functional theory (TD-DFT) I demonstrate and systematically evaluate the approach. For this purpose, I assembled a set of experimental benchmark data for solvatochromism in molecules (xBDSM) containing 44 gas-phase to solvent shifts for 17 molecules. These data are compared to solvent shifts calculated at the ADC(1), ADC(2), ADC(3/2) and TD-DFT/LRC- ω PBE levels of theory in combination with state-specific as well as linear-response type PCM-based correction schemes. Some unexpected trends and differences between TD-DFT, the levels of ADC, and variants of the PCM are observed and discussed. The most accurate combinations of QM/PCM reproduce experimental solvent-shifts resulting from the bulk electrostatic interaction with maximum errors in the order of 50 meV and a mean absolute deviation of 20 – 30 meV for the xBDSM set.

The project described above was motivated by the investigations of oNPA and oNBA, in which the lack of a solvation model for ADC as implemented in Q-Chem prevented its application. The work has been submitted to publication in *the Journal of Physical Chemistry A*, Tomasi-Festschrift (2014). The article has been written and composed by myself and includes only editorial contributions from the co-authors.

5.1 Introduction

Apart from atmospheric and interstellar chemistry, most photochemical problems occur in condensed phases, where the molecular environment may significantly affect the photophysical and photochemical processes. Any investigation of light-induced processes in a condensed-phase system should therefore include at least an estimate of the influence of the environment on the vertical excitations of the chromophore. The direct approach, which is to fully include the relevant environment explicitly in the quantum chemical calculation is not feasible due to the huge number of atoms that would be required to recover the bulk electrostatic interaction with the environment in combination with the steep exponential scaling of the computational effort for accurate quantum chemical methods with respect to system size. Hence, the approximate modeling of molecular environments in quantum-chemical problems in condensed phase is a very active field of research.^{62;100–106} This development culminated in the 2013 Nobel Prize for Chemistry, which was awarded to Karplus, Levitt and Warshel for their pioneering developments in the field of multiscale models for complex chemical systems.

For the purpose of modeling the environment, condensed phase problems may be subdivided into two groups: on the one hand chromophores embedded in an essentially isotropic environment (e.g. solvent, non-polar polymer matrix) and on the other hand, chromophores surrounded by an anisotropic environment (e.g. protein, polar polymer matrix). For the latter, polarizable continuum models (PCMs) are only of limited applicability, since specific interactions between chromophore and the anisotropic environment are usually of key relevance. Hence, an atomistic modelling of the environment is indispensable. This can be achieved using e.g. QM/MM,^{100;101;104;105} fragment-based,^{102;103} or symmetry-adapted perturbation-theoretical (SAPT) approaches.¹⁰⁶ In exchange for the ability to describe an explicit environment, these models are usually quite demanding with respect both, to time required for set-up and evaluation of numerous parameters like the e.g. force-field, embedding scheme, partitioning, cut-offs etc. Moreover, the computational demand for such explicit approaches is inherently many times higher than for a single quantum-chemical calculation *in vacuo*. This is due to the need for sampling, which means an averaging over tens to hundreds of explicit configurations to capture the thermal equilibration of the environment.

For chromophores in solution, for which the bulk electrostatic interaction usually is the most important one, PCMs offer an elegant way to include it at very limited extra cost. Since furthermore, only a few system-independent parameters that mainly concern the construction of the cavity are involved, they can be regarded as a black-box method. In many cases, the QM/PCM approach can be used to estimate the influence of the environment in one single calculation as it circumvents the problem of sampling: The equilibration of the solvent is already included in the dielectric constant ϵ , which is the single quantity used to describe the solvent. Since temperature and frequency dependency of ϵ are well known as they are experimentally accessible, a variation of ϵ allows for a straightforward investigation of these dependencies. Therefore, it is worth while to further pursue this approach despite its limitations, which will be discussed in the next section. An extensive survey of the field of continuum solvation models in quantum chemistry can be found in this review by Tomasi, Menucci and Cossi.⁶²

This work is organized as follows. In Section 5.2, I introduce the concept of PCMs and the extension to vertical excitations, discuss the accuracy of the model, and motivate an evaluation based on a comparison to experimental data. In Section 5.3, I introduce the formalism for quantum-chemical calculations of vertical excitation energies within a PCM framework. In Section 5.4, I describe the experimental results that are used to construct a benchmark data set. Finally, in Section 5.5 results of the ADC and TD-DFT calculations are discussed and compared to the xBDSM set.

5.2 General Considerations

5.2.1 Polarizable Continuum Model

The central idea underlying PCMs is to include the electrostatic interaction of a molecule with an isotropic environment (usually a solvent) using the macroscopic dielectric polarizability of the environment. For this purpose, one needs to partition the system into molecule (solute) and environment (solvent), which gives rise to the molecular cavity. The construction of the cavity is non-trivial and often critical for the accuracy of the PCM,¹⁰⁷ but it is not an issue that I will explore in this work.

For a classical charge distribution within the cavity, the solution of Poisson’s equation for the cavity embedded in a dielectric medium can be circumvented in favor of a boundary-element procedure that solves for the surface charge arising from the discontinuous change in the dielectric constant.¹⁰⁸ Volume polarization, arising from the tail of the quantum-mechanical density, is included approximately by modifying the apparent surface charge (ASC). Two procedures for this were developed independently and are now widely used in quantum chemistry: the “integral equation formulation” (IEF-PCM) of Cancés, Mennucci, and Tomasi,^{109;110} and the “surface and simulation of volume polarization for electrostatics” [SS(V)PE] approach developed by Chipman.^{111;112} Although these methods are formally equivalent,^{113;114} some differences arise when the integral equations are discretized for practical calculations.^{108;115} I use the “asymmetric” version of SS(V)PE, which is recommended in Ref. 115, as implemented in the Q-CHEM program⁹⁰ *via* an intrinsically smooth discretization procedure.¹¹⁶

For an investigation of vertical excitations in a PCM framework, the frequency dependence of the dielectric susceptibility must be considered, at least approximately. The response of the PCM environment depends on the time scale of the molecular process under investigation, since the dielectric polarization includes both slow (orientational and vibrational) components as well as fast (electronic) contributions. Since the atomistic environment is replaced by a continuum, and since the underlying quantum-chemical model is a time-independent one, the consequences of time-dependent polarization have to be introduced explicitly. The formalism is summarized in Section 5.3.2. For a complete and detailed derivation starting from basic electrostatics, see Ref. 117.

5.2.2 Considerations for Excited States

The accuracy of the PCM treatment of solvation effects is limited by a number of factors. First, only bulk electrostatic interactions are included at this level, and the accuracy will suffer when “specific” solvent effects are important. A

prototypical example is a chromophore with a phenolate group, for which strong ionic hydrogen bonding directly affects the aromatic core. This effect becomes notable already if there are slightly acidic protons, *e.g.* in 3- and 4-nitroaniline and a slightly Lewis-basic solvent such as diethyl ether (Et₂O) or acetonitrile (MeCN). Such cases can usually be handled by the introduction of few explicit solvent molecules to the quantum system. The impact of hydrogen-bonding as well as the introduction of explicit solvent molecules on the accuracy of the PCM have been examined in Section 5.5.8.

Second, excitonic coupling between multiple chromophores may alter excitation energies in cases where there are multiple bright excited states of similar energies. (This is the case for coumarin, which is part of the benchmark set.) It has been inferred that this effect can be described within the PCM formalism by the so-called linear-response approach,¹¹⁸ which is obtained when time-dependent perturbation theory is applied to the QM/PCM system.¹¹⁹ Ultimately, the excitonic coupling of the excited states is described by the interaction of the induced polarizations of the transition densities. However, this requires a modification of the secular matrix of the CI problem prior to diagonalization, which goes beyond an exclusively density-based *a posteriori* correction. An implementation of this approach in combination with the COSMO solvent model⁵¹ and the ADC(2) quantum chemistry approach has recently been reported.¹¹⁸

A third problem that has attracted much less attention in the literature is the limitation of PCMs due to the approximate nature of the underlying quantum chemical model. This becomes particularly relevant when approximate linear response methods such as TD-DFT or ADC(1) are used, especially in the context of highly-correlated or charge-transfer (CT) excited states. Although problems with CT excitation energies in TD-DFT^{79;80} have to a large extent been resolved by the introduction of range-separated functionals,^{120–123} it is not clear how well this correction performs for the excited-state densities that will afford the solvation correction.¹²⁴

A fourth issue concerning post-Hartree-Fock methods within the PCM framework is the choice of the reference state. For ADC(*n*) calculations, one usually employs the corresponding Møller-Plesset (MP*n*) ground state as a reference, which leads to several distinct ways how solvation effects can be included:^{60;125;126}

- (1) Use solvated Hartree-Fock (HF) orbitals for the MP2 calculation, in the so-called PerTurbation-Energy (PTE) scheme.
- (2) Obtain the final solvation energy from an additional PCM calculation with the gas-phase MP2 density (PerTurbation-Density or PTD scheme).
- (3) Iterate the PTD scheme until the MP2 density and solvent field are self-consistent (PerTurbation-Energy-and-Density or PTED scheme).

As pointed out by Àngyàn,⁶¹ only the PTE scheme yields an energy that is formally consistent with MP2 theory, while the PTED scheme involves higher-order terms. Furthermore, the PTED scheme is computationally more involved, in particular for ADC(3), for which an MP3 ground-state density would have to be calculated multiple times. Hence, I only examine results obtained with the PTE as well as a modification of the PTD scheme. (An implementation of the PTED scheme in combination with ADC(2) is described in Ref. 118) To the best of my knowledge, there exists neither a systematic investigation of the accuracy

of predicted solvent shifts with respect to the level of electronic structure theory nor with respect to the choice of the ground-state reference. The present work reports such tests, for a variety of ADC-based methods, along with TD-DFT.

A fifth issue, which is beyond the scope of this work is due to the influence of the solvent onto the vibrational transitions in the chromophore. Since the influence of solvation will affect the Franck-Condon factors, which determine the intensity of the optical spectrum, it can shift the maximum of the experimentally determined absorption peak. Unfortunately, this effect can not be accounted for with the presented methodology. Furthermore, it would require a computationally demanding calculation of the ground and excited-state vibrational frequencies in solution in the non-equilibrium reaction field of the excited state. To the best of my knowledge, no implementation capable of such a calculation exists today.

5.2.3 Evaluation of Solvent Models by Comparison to Experimental Solvatochromic Shifts

In comparing PCM solvent shifts to experimental ones, it is important to understand the various effects that contribute to the shift. In quantum chemical terms, these include:

- (1) differences between the ground-state equilibrium geometry in the gas *versus* solution phase;
- (2) “zeroth-order” contributions arising from the polarization of the ground-state wave function by the solvent,
- (3) “first-order” corrections arising from the fast, electronic component of the solvent’s dielectric susceptibility, and
- (4) non-electrostatic interactions that change upon electronic excitation.

The size of these contributions strongly depends on the particular molecule. For example, in molecules exhibiting negative solvatochromism (blue-shift upon increasing solvent polarity), geometrical contributions actually make up the blue part of the shift, whereas zeroth and first order contributions are usually negative (red shift). To keep geometrical contributions small, and thereby focus on the electrostatic contributions, I have exclusively selected molecules exhibiting solvatochromic red-shifts for the benchmark set, although the influence of geometry is taken into account in the calculations. Non-electrostatic contributions arise primarily from the energetic cost of cavity formation (“cavitation energy”), which may be expected to cancel for vertical excitation, and for changes in dispersion and Pauli repulsion energies upon electronic excitation, which are usually neglected.

Another problem in the evaluation of calculated solvent shifts becomes evident when one analyzes the various contributions of non-polar to polar (*e.g.*, cyclohexane to acetonitrile) solvent shifts. In doing so, one finds that these arise exclusively due to differences in the zeroth-order contributions, whereas the first-order contributions cancel quantitatively. This is traceable to the very small variation in the optical dielectric constant ($= n^2$, where n is the index of refraction) across common solvents, whereas the static dielectric constant varies significantly (see Table 5.1).

Table 5.1: Dielectric constants used in the calculations

Solvent	Static Dielectric, ϵ	Optical Dielectric, n^2
Hexane (Hex)	1.89	1.88
Cyclohexane (cyHex)	2.03	2.02
Dioxane (Diox)	2.21	2.02
Diethyl Ether (Et ₂ O)	4.32	1.83
Acetonitrile (MeCN)	36.7	1.81
Dimethylsulfoxide (DMSO)	46.7	2.07
Water (H ₂ O)	80.4	1.78

The small variations in n^2 suggest that a meaningful evaluation of PCM corrections must consider gas-phase to solution shifts, rather than solvent-to-solvent shifts. However, gas-phase data are scarce in the literature and place constraints upon the size and polarity of the molecules. Consequently, the benchmark set consists of small- to medium-sized organic compounds that can be evaporated under application of mild heat and/or low pressure. Moreover, each molecule needs to have a distinct absorption peak caused by a single transition that has no or little overlap with other transitions, since otherwise the analysis of the spectrum is significantly more complicated. These conditions are largely fulfilled for mono- and di-substituted nitroaromatics, for which experimental gas-phase and solvent excitation energies are available.^{127–130} In addition, I have recorded gas-phase and solvent spectra for the prototypical aromatic compounds pyridine (Py), benzofuran (Bf), coumarin (Cm) and nitrobenzene (NB).

5.3 Formalism & Implementation

In this section I present the PCM formalism for vertical excitation energies. For a more detailed derivation of the equation from basic electrostatic quantities, please be referred to ref. 117. The basic concept of the state-specific solvent correction was first introduced by Yomosa in 1974,¹³¹ and many subsequent formulations of the state-specific non-equilibrium formalism have since appeared.^{118;132–134} The “ptSS” formalism¹¹⁷ presented below is closely related to the corrected linear-response (cLR) approach of Caricato *et al.*¹³³ For a description of the ADC method, see section 1.6, ref. 21 or 89.

5.3.1 Ground-State Equilibrium PCM

The starting point for the calculation of excitation energies in solution is a converged HF or Kohn-Sham (KS) self-consistent field (SCF) calculation for a molecule in a cavity with the surface S subdivided into surface elements s . (In the implementation in Q-CHEM these are Lebedev grid points situated on atomic spheres.¹¹⁶) In this so-called self-consistent reaction field (SCRf) calculation, the effect of the PCM is contained in the reaction-field potential operator, $\hat{R}(0)$.

$$[\hat{H}^{\text{vac}} + \hat{R}(0)]|0\rangle = E_0|0\rangle, \quad (5.1)$$

which is

$$\hat{R}(i) \equiv \hat{R}_i \equiv \int_S \frac{\gamma_i(s)}{|r-s|} ds = \int_S \hat{V}(r,s) \gamma_i(s) ds . \quad (5.2)$$

For the sake of compactness, I introduced the operator $\hat{V}(r,s) = |r-s|^{-1}$, which formally corresponds to a measurement of the electrostatic potential (ESP) of the wave function on the position of the surface $s \in \{S\}$. The expression can be simplified even further by carrying out the implicit integration over r (eq. 5.3), which yields the function $V_0(s)$ for the ESP of the wave function $|0\rangle$ at the position s . The integration of the product of this function with the surface charge $\gamma_i(s)$ over the cavity surface S yields the interaction energy of $|0\rangle$ with the polarization induced by $|i\rangle$.

$$\begin{aligned} \langle 0 | \hat{R}_i | 0 \rangle &= \int_S \langle 0 | \hat{V}(r,s) | 0 \rangle \gamma_i(s) ds \\ &\equiv \int_S V_0(s) \gamma_i(s) ds \\ &= E_{0-i} \end{aligned} \quad (5.3)$$

If solute and solvent are in equilibrium, e.g. in case of a ground or long-lived excited state, the molecule interacts with its self-induced polarization and $|0\rangle$ and $|i\rangle$ in eq. (5.3) are identical. In practice, $\gamma(s)$ in \hat{R} is represented by a set of Gaussian-blurred point charges at the positions of the surface elements s , which enter the core-Hamiltonian (eq. 1.33) as additional terms similar to those for the electron-nuclear interaction (see fig. 5.1). In contrast to fixed point charges of e.g. a QM/MM calculation, the ASC in an SCRf calculation does itself depend on the molecular charge distribution, and is thus updated in every iteration. To obtain the ASC $\gamma(s)$ for a given wave function, one may formulate a surface-charge operator

$$\hat{Q} \equiv \int_S \hat{V}(r,s') A_\epsilon^{-1}(s,s') ds' , \quad (5.4)$$

which contains the so-called PCM kernel A_ϵ^{-1} . This kernel depends on the cavity geometry and the dielectric constant of the medium, and is what discriminates between various flavors of PCM. Formally, it is used to solve the Poisson problem, or in other words to convert the molecular ESP into an ASC $\gamma(s)$. Due to the self-interaction of the ASC, the kernel for the charge on a fraction s of the surface depends upon the molecular ESP as well as the ESP of the charge on the remaining surface $\gamma(s')$. Applied to a wave function $|i\rangle$, \hat{Q} yields the ASC $\gamma_i(s)$ resembling the polarization of the dielectric continuum with the dielectric constant ϵ .

$$\gamma_i(s) = \langle i | \hat{Q} | i \rangle = \int_S V_i(s') A_\epsilon^{-1}(s,s') ds' \quad (5.5)$$

It is important to stress that during the SCRf calculation the solute wave function and its reaction field are iterated to self-consistency. As a result, the polarized MOs building the reference-state wave function contain the interaction with the ASC in the form of orbital energies. Any post-HF procedure therefore includes the interaction with the equilibrated ground-state solvent field, just as the mean-field electron-electron interaction and/or any interaction with any classical point charges would be included, in a QM/MM calculation for example. This will become relevant for the discussion of non-equilibrium situations in the next section.

5.3.2 Vertical Excitations in a PCM Framework

Vertical excitation energies can be obtained *via* a CI-like procedure from the solvated ground-state reference wave function. To obey the Franck-Condon principle, only the fast (electronic) component of the polarization should be relaxed, while the slow (nuclear) component has to be kept frozen at its ground-state equilibrium. This is the so-called non-equilibrium limit for a very fast process in a PCM framework. To take this into account the reaction field is separated into fast (electronic) and slow (nuclear) components, starting with the operators. In the definitions of surface-charge and reaction-field operators (eqs. 5.2 and 5.4) the solvent is fully relaxed, which corresponds to the equilibrium case for the ground state. This means that the reaction field includes both fast (electronic) and slow (nuclear) contributions, which corresponds to ϵ as the (static) dielectric constant. In non-equilibrium situations, one needs to treat the fast component of the polarization separately. This can be achieved by replacing ϵ in A^{-1} (eq. 5.4) with the optical dielectric constant n^2 . The slow component of ϵ is replaced by $\epsilon - n^2$. Accordingly, one may split the reaction-field and surface-charge operators into fast and slow components:

$$\hat{Q}^{f+s} = \hat{Q}^f + \hat{Q}^s \quad (5.6a)$$

$$\hat{R}^{f+s} = \hat{R}^f + \hat{R}^s . \quad (5.6b)$$

A Hamiltonian for an out-of-equilibrium excited state $|i\rangle$ that is in accordance with the Franck-Condon principle can now be constructed:

$$E_i^{\text{NEq}} = \langle i | \hat{H}^{\text{vac}} + \hat{R}_0^s + \hat{R}_i^f | i \rangle . \quad (5.7)$$

This Hamiltonian is, however, not practical, as it is different for each excited state, and therefore sacrifices orthogonality between states as well as certain sum rules for oscillator strengths.¹³⁵ A solution to this problem is suggestive, if it is realized that the potential introduced through the fast polarization component is small with respect to the potential of the solute nuclei and furthermore the change in electron density upon excitation is small with respect to the whole solute density. Hence, the response of the solvent to excitation of the solute can be treated as a perturbation employing Rayleigh-Schrödinger perturbation theory described in section 1.5.1, whereas the zeroth-order Hamiltonian \hat{H}^0 includes the ground-state reaction field, and the perturbation \hat{V} is the difference between the latter and the excited-state reaction field

$$\begin{aligned} \hat{H}^0 &= H^{\text{vac}} + \hat{R}_0^{f+s} \\ \hat{V} &= \lambda(\hat{R}_i^f - \hat{R}_0^f) . \end{aligned}$$

Consequently, the perturbation-theoretical, state-specific Hamiltonian becomes

$$E_i^{\text{NEq}} = \langle i | \hat{H}^{\text{vac}} + \hat{R}_0^{f+s} + \lambda(\hat{R}_i^f - \hat{R}_0^f) | i \rangle , \quad (5.9)$$

which affords the following zeroth-order energy

$$E_i^{(0)} = \langle i^{(0)} | \hat{H}^0 | i^{(0)} \rangle = \langle i^{(0)} | \hat{H}^{\text{vac}} + \hat{R}_0^{s+f} | i^{(0)} \rangle , \quad (5.10)$$

and the respective first-order correction

$$E_i^{(1)} = \langle i^{(0)} | \hat{V} | i^{(0)} \rangle = \langle i^{(0)} | \hat{R}_i^f - \hat{R}_0^f | i^{(0)} \rangle . \quad (5.11)$$

Eventually, the problematic state-specific (SS) Hamiltonian (eq. 5.7) is converted into a perturbative correction, which can be computed *a posteriori* using the zeroth-order wave function $|i^{(0)}\rangle$. The latter is obtained from a CI-type calculation based on polarized ground-state MOs. To emphasize the perturbative nature of the approach, it will be denoted as perturbation-theoretical state-specific (ptSS)-PCM.

For the evaluation of eq. 5.11 one needs the fast polarization charges of the ground state. To compute these, the ground-state reaction field can be separated on the basis of the respective dielectric constants for fast (n^2) and slow (ϵ) polarization:¹¹⁹

$$\gamma^f = \left(\frac{n^2 - 1}{\epsilon - 1} \right) \gamma^{\text{total}} \quad (5.12a)$$

$$\gamma^s = \left(\frac{\epsilon - n^2}{\epsilon - 1} \right) \gamma^{\text{total}} = \gamma - \gamma^f \quad (5.12b)$$

When the charges are separated in this way, one must mind the self-interaction between fast and slow ground-state surface charges according to

$$E_{s-f} = \int_S \gamma_0^f(s) V_{\gamma_0^s}(s) ds, \quad (5.13)$$

where $V_{\gamma_0^s}(s)$ is the ESP of the slow, ground-state polarization charges at the position s . In analogy to the molecular ESP, it can be obtained by integrating the slow component of ASC resembling the ground-state polarization

$$V_{\gamma_0^s}(s) = \int_S \frac{\gamma_0^s(s')}{|s' - s|} ds'. \quad (5.14)$$

If the fast ASC obtained for the ground state is now replaced by the fast ASC of an excited state $\gamma_i^f(s)$, this interaction changes. To account for this, a charge-separation correction is introduced:

$$E_{cs} = \int_S \left(\gamma_i^f(s) - \gamma_0^f(s) \right) V_{\gamma_0^s}(s) ds. \quad (5.15)$$

5.3.3 Free Energy

Because the dielectric constant implicitly includes solvent averaging, the electrostatic energies in PCM theory are *free* energies, whereas up to this point I have introduced expressions for interaction energies only. To obtain free energies one must account for the work associated with polarizing the continuum, which amounts to half of the electrostatic interaction energy.^{136;137} Thus, the free energy of the equilibrated system in its ground state is

$$G^{\text{solv}} = \langle 0 | \hat{H}^{\text{vac}} + \frac{1}{2} \hat{R}_0 | 0 \rangle \quad (5.16)$$

For an excited state in the non-equilibrium limit, the derivation of the polarization work is more involved. It includes the charge-separation correction (eq. 5.15) as well as further terms for the polarization work involving the fast charges in both ground and excited states, thereby taking into account from

which state the polarization originated. For a detailed derivation and discussion of these terms, see Ref. 117. Finally, the first-order ptSS correction to the $|0\rangle \rightarrow |i\rangle$ excitation energy is given as

$$\begin{aligned}
 G_i^{\text{ptSS}} &= \langle i^{(0)} | \hat{R}_i^f | i^{(0)} \rangle - \langle i^{(0)} | \hat{R}_0^f | i^{(0)} \rangle \\
 &\quad - \frac{1}{2} \left(\langle i^{(0)} | \hat{R}_i^f | i^{(0)} \rangle - \langle 0 | \hat{R}_0^f | 0 \rangle \right) \\
 &\quad + \frac{1}{2} \int_S \left(\gamma_i^f(s) - \gamma_0^f(s) \right) V_{\gamma_0^s}(s) ds .
 \end{aligned} \tag{5.17}$$

Here, the interaction terms are collected in the first line whereas the remaining terms constitute the polarization work.

5.3.4 Electron Correlation in the PCM Framework

For calculations employing the PTE scheme, γ^{total} in eq. 5.12 refers to the ASC obtained for the ground-state HF or KS density. This introduces a systematic error in solvent shifts if the ground-state ESP is not well described at the HF level of theory because the ground-state reaction field enters the zeroth-order excitation energies *via* the polarized MOs. This is indeed the case for nitroaromatics, for which the total MP2 dipole moment is only 80% of the HF dipole moment. To account for this effect, I introduce the following correction to the zeroth-order excitation energy:

$$\begin{aligned}
 E_{\text{PTD}}^{(0)} &= \left(\langle i^{(0)} | \hat{R}_{0\text{MP}} | i^{(0)} \rangle - \langle 0^{\text{MP}} | \hat{R}_{0\text{MP}} | 0^{\text{MP}} \rangle \right) \\
 &\quad - \left(\langle i^{(0)} | \hat{R}_{0\text{HF}} | i^{(0)} \rangle - \langle 0^{\text{MP}} | \hat{R}_{0\text{HF}} | 0^{\text{MP}} \rangle \right) \\
 &= \langle i^{(0)} | \hat{R}_{0\text{MP}} - \hat{R}_{0\text{HF}} | i^{(0)} \rangle \\
 &\quad - \langle 0^{\text{MP}} | \hat{R}_{0\text{MP}} + \hat{R}_{0\text{HF}} | 0^{\text{MP}} \rangle .
 \end{aligned} \tag{5.18}$$

Adding this correction, the zeroth-order interaction of the difference density of the excited state with the polarization of the HF ground state ($|0^{\text{HF}}\rangle$, lower term) is replaced by the interaction of the difference density of the excited state with the polarization of the Møller-Plesset (MP) ground state ($|0^{\text{MP}}\rangle$, upper term). Within this scheme, the employed HF reaction field is obtained self-consistently, but the MP reaction field is calculated from the MP density computed with HF orbitals. Since the latter are overly polarized in the case of nitroaromatics, the MP reaction field contains the error due to the HF density. Hence, the correction will not be quantitative but presumably constitute a lower border to the error introduced by the HF reaction field. However, as compared to the iterative PTED scheme, this PTD correction has the advantage that it can be calculated *a posteriori*, which is in accordance with all other correction terms introduced above.

The first-order terms also differ between the PTE and PTD schemes, since the response of the polarization has to be calculated in the presence of the slow component of the ground-state reaction field (eq. 5.20). Consequently, γ^{total} in eq. (5.12) refers to the ASCs obtained for the MP ground state density. Accordingly, for the PTD scheme all other terms that explicitly depend upon the ASC

of the ground state (eqs. 5.2, 5.11, 5.15, 5.17, and 5.20) use MP densities. To distinguish between the PTE and PTD approaches for the ADC(2) and ADC(3/2), the abbreviation ptSS-PCM(PTE) and ptSS-PCM(PTD) will be used.

5.3.5 Perturbative Linear-Response-Type Corrections

In addition to the state-specific corrections described above, *perturbative* linear-response (LR) correction terms have been implemented. These are obtained by keeping only the diagonal elements of the original LR *ansatz* described in Ref. 138 for TD-DFT and in Ref. 118 for ADC. As compared to the latter formulation, I use a different partition of the Hamiltonian, in order to obtain the same formalism for the zeroth-order terms of the LR and SS approaches, which are indeed identical.¹³⁹ Consequently, the first two terms in the diagonal elements of the free energy matrix (eq. (17) in Ref. 118) can be identified as the zeroth-order energy (eq. (5.10) in this work). For the perturbative LR-type corrections (ptLR-PCM), the energy of the third term in eq. (17) of Ref. 118 is added to the zeroth-order result. Since all off-diagonal elements for my perturbative corrections are neglected, this term corresponds to the interaction of the transition density with the dielectric medium:

$$E_i^{\text{ptLR}} = \int_S \langle i^{(0)} | \hat{V}(r, s) | 0 \rangle \gamma_{lr}(s) ds \quad (5.19a)$$

$$\gamma_{lr}(s) = \int_S \langle i^{(0)} | \hat{V}(r, s') | 0 \rangle A_n^{-1}(s, s') ds' \quad (5.19b)$$

Although this ptLR correction is itself independent of the PTE and PTD schemes, one can combine these corrections with the zeroth-order terms for both, affording what I designate as the ptLR-PCM(PTE) and ptLR-PCM(PTD) schemes.

In the case of an isolated bright state, the ptLR-PCM approach yields results that are reasonably close to the full, self-consistent LR approach, as demonstrated below. The advantage is that the ptLR corrections can be calculated *a posteriori*, without a manipulation of the secular matrix of the CI problem. However, this approximation can break down if there are additional bright excited states in close proximity, as e.g. in case of coumarin.

5.3.6 Excited-State Densities

Excited-state densities are required to compute the ESP for $|i^{(0)}\rangle$. Formally, these can be obtained from the excited-state wave function, which corresponds to an unrelaxed density, or by computing the energy-derivative with respect to an electric field, yielding a relaxed density.¹⁴⁰ For linear-response methods, only the relaxed density corresponds to an observable quantity, since the response vectors themselves have no physical meaning. This is reflected in the results of the TD-DFT calculations, where unrelaxed densities yield first-order corrections that are too large. Consequently, the solvent shifts are systematically overestimated in all cases using unrelaxed TD-DFT densities, as shown in section 5.5.6. A recent study of 4-nitroaniline also confirms that only relaxed TD-DFT densities are in good agreement with multi-reference CI calculations.¹⁴¹ Hence, relaxed densities have been used for the TD-DFT calculations.

For ADC calculations, the densities are obtained *via* the intermediate state representation (ISR) formalism consistent to the given order in perturbation

theory.⁸⁹ ADC is not a linear response method, and these densities are not “relaxed” in the aforementioned sense *i.e.* they do not include explicitly calculated orbital relaxations. Nevertheless, they do contain significant orbital relaxation effects, as demonstrated recently at second order,^{142;143} and are inexpensive to compute. For this purpose, the converged ADC excited-state vectors are combined with the intermediate-state basis of the appropriate order, yielding an excited-state wave function. Eventually, the excited-state densities used for the PCM calculations are consistent to first order for ADC(1) and to second order for ADC(2). For ADC(3), an efficient implementation of the ISR of corresponding order is not yet available, so the ISR of second order is used in combination with the ADC(3) state vectors. This is the definition of the mixed ADC(3/2) approach.

5.3.7 Technical Details of the Implementation

After convergence of the SCRF calculation (eq. 5.1), the ground state reaction field is split into fast and slow components according to eq. (5.12). Using the polarized MOs, a CI-type calculation (ADC or TD-DFT in this chapter) is carried out, which affords the correlated ground-state density as well as the zeroth-order excited-state vectors and excitation energies (eq. 5.10). To obtain the first-order corrections, the terms in eq. (5.17) have to be calculated. For this purpose, \hat{R}_i^f needs to be build, which in turn requires the ASC resembling the fast component of the polarization for the excited state $|i^{(0)}\rangle$. This is obtained using a modified version of the surface-charge operator eq. (5.4), in which ϵ is replaced by n^2 and the ESP of the slow ground-state polarization charges (eq. 5.14) is added to the molecular ESP, $V_{i(0)}(s')$:^{119;134}

$$\gamma_i^f(s) = \int_S \left(V_{\gamma_0^f}(s') + V_{i(0)}(s') \right) A_{n^2}^{-1}(s, s') ds'. \quad (5.20)$$

Having the surface charges, \hat{R}_i^f can be constructed and all first-order interaction and polarization terms can be evaluated. The numerical procedure is sketched for the example nitrobenzene in fig. 5.1.

To obtain corrected vertical excitation energies for the PTE scheme, the first-order corrections are just added to the zeroth-order excitation energies. However, for calculation of the fast polarization and first-order terms within the PTD scheme, the ground-state polarization of the correlated ground-state is required. To obtain it, eq. 5.4 is solved for the correlated MP density, which in contrast to the original PTD scheme is calculated using the polarized HF MOs. The zeroth-order PTD corrections (eq. 5.18) contain additional terms. These are the interaction of the excited-state densities with the ground-state polarization of both the MP and HF ground states, as well as the interaction of the MP density with the HF reaction field. All these terms are calculated after the CI calculation-type using the respective reaction fields.

5.4 Methodology

5.4.1 Technical Details

Gas-phase as well as solvent-relaxed geometries were obtained at the B2-PLYP/def2-TZVP level of theory,^{57;93} in combination with Grimme’s D3 dispersion cor-

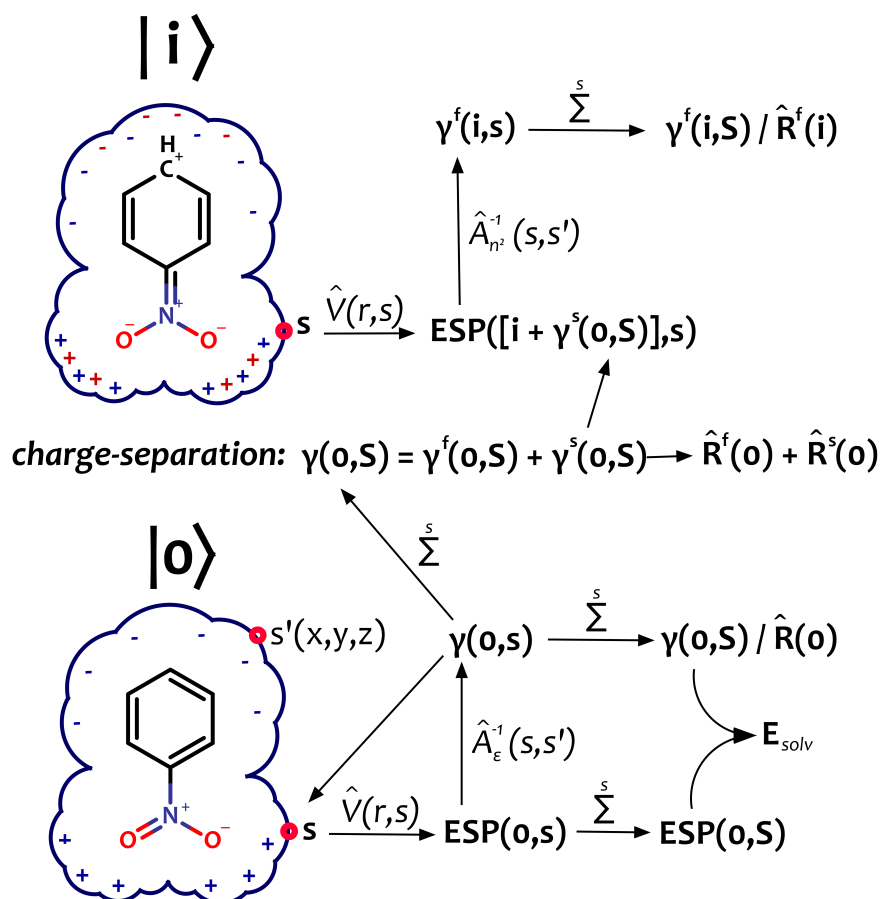


Figure 5.1: Flowchart of the numerical procedure of a non-equilibrium state-specific PCM calculation for a vertical excitation from the ground state $|0\rangle$ to the excited state $|i\rangle$. The integration over S is replaced by a finite sum over the surface elements. The ground-state polarization of the surface-charges is depicted in blue, the response of the fast component to the increased dipole moment of the excited state in red. The notation is very similar to the article, except for the electro-static potential for which I use the notation $\text{ESP}(\text{state},s)$ instead of $V_0(s)$.

rection¹⁴⁴ and the COSMO solvation model¹⁴⁵ as implemented in ORCA 3.0.1.⁷ This level of theory has previously been found to provide good agreement with experiment for prototypical nitrobenzene, whereas MP2-, CC2-, and CCSD-optimized geometries deviated significantly.⁷⁵ In the case of the amino-methoxy disubstituted nitroaromatics, I find that the dispersion correction systematically improves the predicted solvent shifts, for all QM/PCM combinations considered here.

All CI-type calculations (ADC and TD-DFT) were carried out using a locally-modified version of Q-CHEM 4.2,⁹⁰ and employ the cc-pVDZ basis set.⁹⁸ For the TD-DFT/LRC- ω PBE calculations, the range-separation parameter was tuned such that the HOMO and LUMO energy equal the ionization potential and electron affinity, respectively.¹⁴⁶ This procedure leads to ω values of 0.27 – 0.32 for the molecules in the xBDSM set, which is close to the standard value of 0.3. The cavity for the PCM calculations in Q-CHEM is obtained using a smooth Lebedev-grid based construction algorithm,¹¹⁶ with Bondi’s atomic van-der-Waals radii^{147;148}, which are as usual scaled by a factor of 1.2.

5.4.2 Experimental Data

Experimental data for the *meta*- and *para*-substituted nitroaromatic compounds were obtained from Ref. 128. Data for the methoxy-nitroanilines were taken from Ref. 129. Data for 4-nitrophenolate and 4-(4-nitrophenyl)-phenolate were obtained from Ref. 149.

For nitrobenzene, benzofuran, coumarin, pyridine and 4-nitroaniline UV/VIS spectra were recorded in the gas-phase and in Hex, MeCN, and for 4-nitroaniline also in dioxane. The UV/VIS-transmission spectra were recorded using a Perkin Elmer - Lambda 750 spectrometer operated at a resolution of 0.5 nm. A 10 mm quartz glas (suprasil - Hellma) was used. The average concentration of the compounds (purities grade > 99%) in solution has been adjusted between 0.1 mM and 0.01 mM. To obtain transmission spectra in the gas phase, a small quantity of the compound was filled into the sealable cuvette or, in case of pyridine, a gaseous injection was taken from the original bottle. In case of coumarin, mild heat was applied to achieve a sufficient concentration in the gas phase. The peak-finding algorithm implemented in the Perkin Elmer Spectra Suite software was used to determine maxima and solvent shifts. In case of coumarin and benzofuran, whose absorption spectra exhibit vibrational structure, the differences were determined between the most distinct features of the respective peaks. This is sufficient since the relevant quantities here are not the absolute excitation energies, but in the solvent-induced shifts thereof.

5.5 Results & Discussion

5.5.1 Characterization of the Excited States

The experimental data for the mono-substituted nitroaromatics always refer to the first peak in the absorption spectrum. For all but two of the nitroaromatic molecules, the calculations reveal that the first bright state is closely related to the $2A_1 \pi \rightarrow \pi^*$ excited state of nitrobenzene (NB), which is almost exclusively characterized by the HOMO-1 to LUMO transition. This excited state has significant CT character, with a dipole moment that increases from 4.3 D in the ground state to 10.0 (8.9) D in the excited state at the MP2/ADC(2) (ADC(3,2)) level of theory. Only in the *meta*-substituted isomers of the push-pull systems 3-nitroanisole (3-methoxy-NB) and 3-nitroaniline (3-amino-NB) a different state is responsible for the first peak. In these two cases, it is related to the $1B_1 \pi \rightarrow \pi^*$ state of NB, which is symmetry forbidden in the parent NB. In molecules with an electron-pushing substituent in the *meta* position, however, it has enough oscillator strength to appear in the spectrum. This state is characterized by the HOMO \rightarrow LUMO transition, whereas the dipole moment is increased to 5.8 (6.3) D at the ADC(2) (ADC(3,2)) level of theory for NB. A details analysis and examination of the excited states of NB can be found in chapter 4.

In pyridine, benzofuran and coumarin I investigate the shifts of the lowest $\pi \rightarrow \pi^*$ excitation(s). In pyridine, the ground state dipole moment of 2.0 D is slightly decreased in the first bright state (S_3 , 1.8 D, HOMO \rightarrow LUMO and HOMO-1 \rightarrow LUMO+1 transition). In benzofuran, the ground-state dipole moment of 0.6 D is hardly affected in the first bright state (S_1 , 0.7 D, HOMO-1 \rightarrow LUMO and HOMO \rightarrow LUMO+1 transition), and slightly increased in the second bright state (S_2 , 3.3 D, HOMO \rightarrow LUMO and HOMO-1 \rightarrow LUMO+1). In coumarin, the ground-state dipole moment of 4.2 D is hardly affected in the first bright state (S_1 , 4.7 D, HOMO \rightarrow LUMO, HOMO-1 \rightarrow LUMO) and slightly increased in second bright state (S_3 , 5.9 D, HOMO-1 \rightarrow LUMO, HOMO \rightarrow LUMO+1). All values correspond to gas-phase ADC(2)/cc-pVDZ single-point calculations using B2-PLYP+D3/def2-TZVP structures.

5.5.2 Composition of the xBDSM Set

From the data available in the literature for mono-substituted nitroaromatics, I have chosen cyclohexane (cyHex), diethyl ether (Et₂O) and acetonitrile (MeCN) as representative solvents. According to eq. (5.12), only the fast electronic polarization is relevant for the ground-state polarization cyHex ($\gamma^f = 99\%$ of γ^{total}), whereas for Et₂O both fast and slow components contribute significantly ($\gamma^f = 25\%$ of γ^{total}), while for MeCN the slow nuclear component is dominant ($\gamma^s = 98\%$ of γ^{total}).

For the analysis of the results, the experimental data points are divided into three subgroups depending on molecule/solvent interactions and character of the excited-states.

- (1) **Exclusively electrostatic cases.** This largest subgroup consists of the data points for nitrobenzene (NB) and the *meta*- and *para*-isomers of nitrotoluene (methyl-NB), nitroanisole (methoxy-NB), and nitrochlorobenzene (chloro-NB) in cyHex, Et₂O and MeCN, as well as for *meta*- and *para*-nitroaniline (amino-NB) and the methoxy-nitroanilines (NH₂-MeO-NB) in

cyHex. For this selection, the gas-phase to solvent shifts are for isolated bright transitions. Hence, the solvatochromic shift is almost exclusively due to the bulk electrostatic interaction, which should be accurately described by a proper PCM formalism.

On the basis of these examples, the accuracy of the first-order treatment of the fast response of the polarization is evaluated and the composition of the solvent shifts with respect to geometric, zeroth-, and first-order contributions is analysed. Moreover, the performance of the ptSS and ptLR approaches with respect to the level of electronic structure theory is examined and studied how the treatment of correlation effects in the solvent model (PTE vs. PTD) affects the results.

- (2) **Cases involving hydrogen bonding.** These cases are also examples dominated by electrostatic effects but they also involve hydrogen bonding with solvent molecules. The data points in this set comprise 4-nitroaniline in Et₂O, MeCN, dioxane (Diox) and dimethylsulfoxide (DMSO), as well as 4-nitrophenolate (4-NP) and 4-(4'-nitrophenyl)-phenolate (44-NPP) in water. Based on these examples, the impact of hydrogen bonding on the accuracy and is quantified and furthermore, it is demonstrated how well this can be corrected-for by introduction of few explicit solvent molecules.
- (3) **Non-electrostatic cases.** This set includes molecules which exhibit hardly any experimental shift at all that have multiple bright excited states close in energy. These are pyridine, benzofuran, and coumarin in hexane and MeCN. This subset demonstrates how the ptLR correction behaves in difficult situations.

5.5.3 Basis-Set Dependence

I recalculated solvent shifts for nitrobenzene in cyHex, Et₂O and MeCN at the ADC(2)/ptSS-PCM and ADC(2)/ptLR-PCM levels of theory using the (aug-)cc-pVDZ and (aug-)cc-pVTZ basis sets. Examining the results shown in fig. 5.2, one finds that the ptLR terms increase by more than 65% (0.3 eV *vs.* 0.2 eV) for the augmented basis sets. The ptSS-corrections, on the contrary, are less affected by the augmentation (+20%, 0.11 eV *vs.* 0.09 eV), but show a larger increase for the cc-pVTZ basis (15% increase for ptSS *vs.* 4% increase for ptLR).

Also the zeroth-order contributions of the shifts exhibit a basis set dependence. The augmentation of the cc-pVDZ basis causes an increase of about 13% (0.18 eV *vs.* 0.16 eV for cyHex, 0.40 eV *vs.* 0.45 eV for MeCN), while the triple- ζ basis yields zeroth-order shifts that are about 8% bigger than those obtained with the double- ζ basis. For the ptSS approach, the differences between the medium (cc-pVTZ, aug-cc-pVDZ) and largest (aug-cc-pVDZ) basis sets are smaller, which indicates a convergence of the results.

Ultimately, the complete shifts obtained with the largest aug-cc-pVTZ for the ptSS-approach are increased by 18% (0.43 eV *vs.* 0.37 eV for Et₂O) compared to the smallest cc-pVDZ. Very similar changes are obtained for cyHex (20%) and MeCN (18%). For the ptLR approach, the differences between cc-pVDZ and aug-cc-pVTZ are even larger and there is more variation amongst the solvents. For cyHex, the shifts increase by 50% (0.55 eV *vs.* 0.37 eV), for Et₂O the increase is 37% (0.64 eV *vs.* 0.47 eV) and for MeCN it is 32% (0.78 eV *vs.* 0.59 eV).

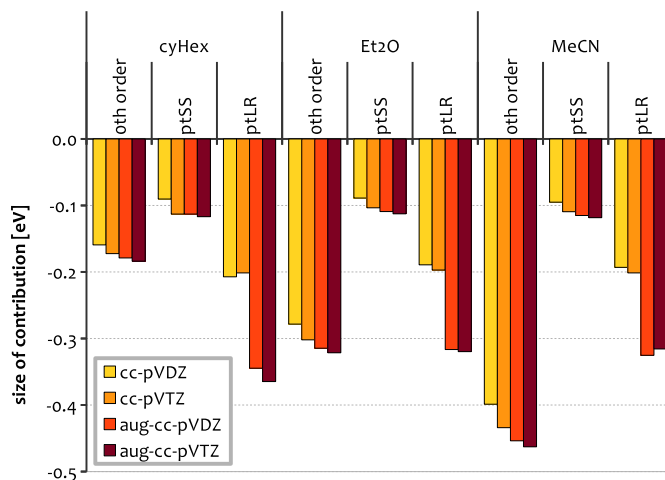


Figure 5.2: Components of the calculated solvent shifts with ADC(2)/ptSS- and ptLR-PCM for the cc-pVDZ, aug-cc-pVDZ, cc-pVTZ and aug-cc-pVTZ basis sets.

The reason for this pronounced basis-set dependence of the results is presumably the charge-transfer character of the excited states under investigation. Due to a surplus of negative charge located at the nitro group in the excited-states, the description of these states profits tremendously from the introduction of diffuse functions and the additional flexibility of a triple- ζ basis. This is corroborated by the calculated gas-phase excitation energies and their agreement with the experimental values. At the ADC(2) level of theory, the difference between calculated and experimental excitation energies decreases from +0.66 eV (cc-pVDZ) to +0.23 eV (aug-cc-pVTZ), while ADC(3) is off by +0.37 eV with cc-pVDZ and quantitative with aug-cc-pVTZ (+0.05 eV). Hence, for a reasonable description of the states and their solvatochromism, the use of larger basis sets is advisable. This would, however, lead to prohibitively expensive calculations at the ADC(3) level of theory. To retain comparability between the methods, the cc-pVDZ basis was used throughout this chapter and the results from this basis-set study will be considered in the discussion.

5.5.4 Composition of Calculated Shifts

In this section, the composition of solvent shifts is examined using ADC(2)/ptSS-PCM(PTD) as a representative level of theory. An inspection of fig. 5.4 reveals that geometrical contributions to the shifts are small compared to the sum of zeroth- and first-order contributions. Although for clarity only a limited number of examples is shown in fig. 5.4, this applies to all molecules in the benchmark set. Only for 4-nitroaniline (termed 4-Amino-NB, far right in fig. 5.4), the geometric contribution is larger than 0.1 eV, which can be traced back to a solvent-dependent variation of the NH₂ out-of-plane bending. Another result that stands out is that differences between non-polar cyHex, intermediate-polarity Et₂O, and highly-polar MeCN are exclusively due to a variation in the zeroth-order contributions, whereas the first-order contributions are virtu-

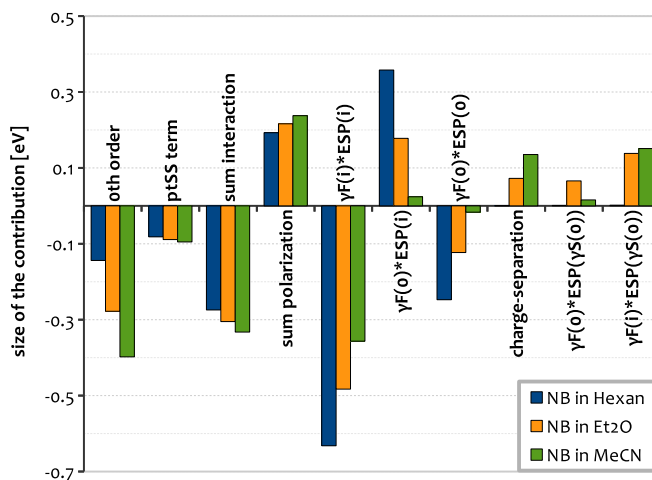


Figure 5.3: Breakdown of the first-order contributions into the single terms (see eq. 5.17) and the sums of all interaction and polarization term for nitrobenzene in cyclohexane, diethyl ether and acetonitrile. Despite large differences in the separate terms, the final first-order corrections are virtually identical for all three solvents

ally identical for all three solvents. This finding holds for all of the molecules investigated in this chapter and is independent of the level of QM theory employed. The mean absolute deviation between the first-order terms for the same molecule in different solvents is smaller than 4 meV for the complete data set at the ADC(2)/ptSS-PCM level of theory.

Considering the large variation of the single terms contributing to the first-order correction shown in fig. 5.3, the similarity of the first-order contributions is even more remarkable. Obviously, a meaningful evaluation of the latter should involve gas-phase to solvent shifts. However, the small variation in the optical dielectric constant among typical solvents ($n^2 = 1.75 - 2.25$) causes the differences in calculated first-order terms to be too small for a meaningful evaluation. If an evaluation of zeroth-order terms is desired, *e.g.*, for the comparison of PTE and PTD schemes in the next section, a comparison involving solvents of different polarity is advisable.

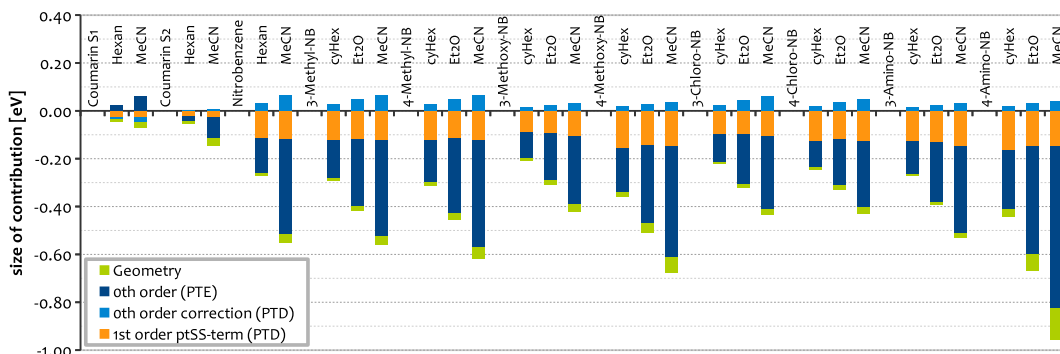


Figure 5.4: Breakdown of the calculated solvent shifts into geometrical, zeroth-, and first-order contributions for selected examples at the ADC(2)/ptSS-PCM level of theory. In each case, the identity of the chromophore (coumarin S_1 , coumarin S_2 , nitrobenzene, etc.) is followed by a series of bar graphs representing different solvents.

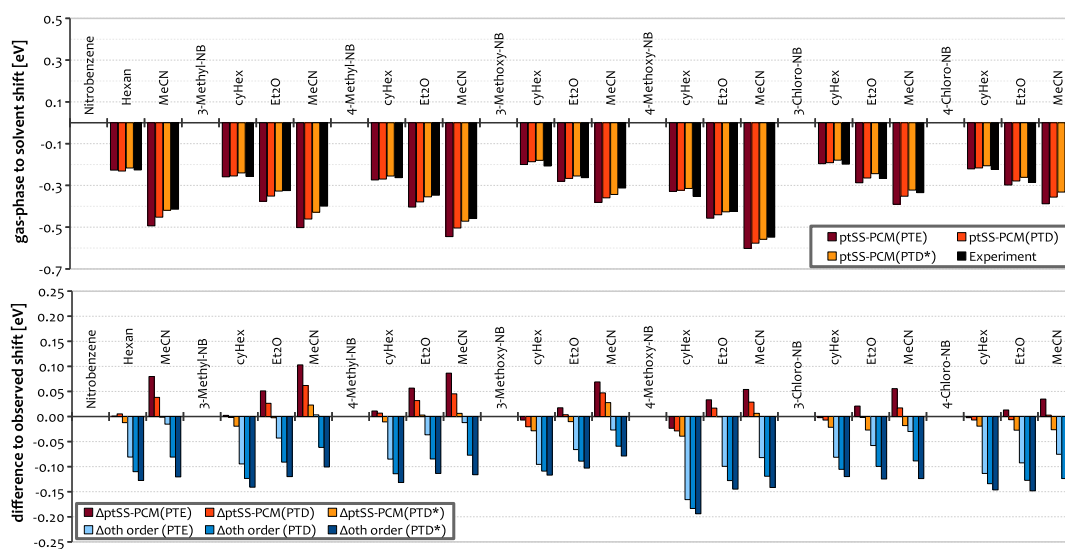


Figure 5.5: *Top*: Experimental and calculated solvent shifts for a selection of molecules in the exclusively electrostatic subgroup of xBDSM. Solvent shifts are computed at the ADC(2)/ptSS-PCM level of theory with the PTE, PTD and scaled PTD* approaches. *Bottom*: Differences between experimental and calculated solvent shifts for the PTE, PTD and scaled PTD* approaches including also the zeroth-order terms.

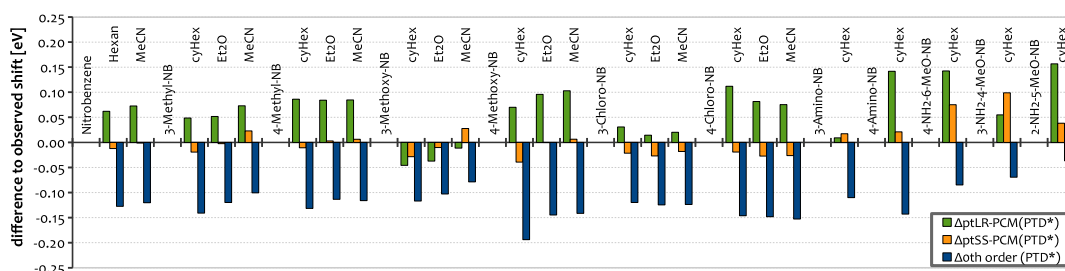


Figure 5.6: Differences between calculated and experimental solvent shifts at the ADC(2) level of theory using either the ptSS or ptLR scheme, in conjunction with the empirically-scaled PTD* zeroth-order contribution.

5.5.5 PTE vs. PTD

To evaluate the PTD correction, calculated solvent shifts for a selection of molecules from the first (exclusively electrostatic) subgroup of the xBDSM set in cyHex, Et₂O and MeCN are compared to the respective experimental values. The calculations were carried out at the ADC(2) and ADC(3/2) levels of theory using the ptSS-PCM approach and results are shown in fig. 5.5 for ADC(2) and fig. 5.8 for ADC(3/2). It is found that solvent shifts computed using the PTE scheme are overestimated by an amount proportional to the solvent polarity. On a molecular level, this systematic error can be traced back to the poor description of the ground state at the Hatree-Fock level of theory, which is the level at which the ESP of the solute is computed in the PTE approach. In particular, the dipole moment of the nitrobenzyl moiety is overestimated by about 20% at the HF level as compared to the unrelaxed MP2 dipole moment. For polar solvents that exhibit a large nuclear component of the polarization, this error gives rise to a systematic overestimation of the solvent-shifts as the slow component of the ground-state polarization enters the calculation of the excitation energies in zeroth order. For unpolar solvents there is a similar overpolarization, but it only affects the fast component of the ground-state polarization, whose interaction with the excited state is, however, subtracted in the first-order terms (see eq. (5.17), second term in the first line).

As supposed in Section 5.3.4, the PTD corrections systematically reduce the errors but don't eliminate them quantitatively. To compensate for this empirically, I have scaled the zeroth-order PTD correction by a factor of 1.6, such that the systematic error for ADC(2) is completely eliminated (fig. 5.5). This scaled approach is denoted PTD*.

For ADC(3/2) already the unscaled PTD correction overcompensates the error introduced by the HF-reaction field (see fig. 5.8). Apparently, the optimal scaling factor is different for ADC(3/2), which is presumably because the higher-order of perturbation theory does in part correct for the errors in the HF reaction field. Using the same procedure as for ADC(2), one finds that a scaling factor of 0.5 largely eliminates the systematic error. Hence, in the following, a scaling factor of 0.5 will be used for the ADC(3/2)/ptSS-PCM(PTD*) approach.

5.5.6 ptSS and ptLR with ADC and TD-DFT

To compare the accuracy and investigate the relation of the perturbative, state-specific corrections and linear-response-type corrections, solvent shifts for the exclusively electrostatic subgroup at the ADC(1), ADC(2), ADC(3/2) and TD-DFT/LRC- ω PBE levels of theory have been calculated. For the isolated bright excited states of the mono-substituted nitroaromatics, the results of the ptLR corrections are quite close to the original, self-consistent LR formalism.¹⁵⁰ In the case of nitrotoluene, for example, the self-consistent LR solvent shifts are 0.185, 0.251, and 0.325 eV in cyHex, Et₂O and MeCN, respectively, whereas the same shifts computed with the ptLR approach are 0.186, 0.259, and 0.325 eV.

ADC(2)

ADC(2) results using either the ptLR or ptSS scheme are shown in fig. 5.6. In general, the accuracy of the solvent shifts calculated at the ADC(2)/ptSS-PCM(PTD*) level of theory is remarkable. Most errors are well below 0.05 eV,

with a mean error of 2 meV, and the largest deviation is 0.08 eV. The root-mean-square deviation (RMSD) is 32 meV, which is most likely comparable to the experimental uncertainty. This agreement demonstrates that a first-order treatment of the fast solvent response is sufficient. The improved accuracy of the PTD approach falls into place from a theoretical point of view, since all corrections are based on densities computed at a consistent order of perturbation theory, whereas for the PTE approach, excitation energies and correction terms obtained at second-order are combined with a solvent field obtained for a first-order (HF) ground-state wave function.

Considering the increase of the solvent shifts observed for larger basis sets (section 5.5.3), the very good agreement observed here benefits from some error compensation. For the aug-cc-pVTZ basis set, one would presumably observe a slight but systematic overestimation of the solvent shifts.

The combination of ADC(2)/PCM(PTD*) zeroth-order energies with the ptLR correction is not nearly as accurate as the ptSS-approach. The shifts are systematically overestimated (mean error = 58 meV, MAD = 73 meV, RMSD = 81 meV), and in three of the examples the zeroth-order correction actually lies closer to (or as close to) the experimental result than the full ptLR result. Moreover, the accuracy of the ptLR results seems to depend on the character of the excited state: shifts obtained for states that are related to the $2 A_1$ (HOMO-1 \rightarrow LUMO) state of NB are generally too large, whereas shifts are accurate or slightly underestimated for states related to the $1 B_1$ (HOMO \rightarrow LUMO) transition, as in 3-methoxy-NB and 3-amino-NB.

ADC(1)

ADC(1) results (fig. 5.7) are in sharp contrast to those obtained using ADC(2). For ADC(1), the ptSS correction terms are systematically too small (mean error = -127 meV, MAD = 127 meV, RMSD = 148 meV), while the ptLR-PCM is balanced and much more accurate than for ADC(2) (mean error = 10 meV, MAD = 50 meV, RMSD = 63 meV). In general, the average deviation in the solvent shifts at the ADC(1)/ptLR-PCM level of theory is much smaller than for ADC(2)/ptLR-PCM(PTD*) and rather compares to that of ADC(2)/ptSS-PCM(PTD*). Surprisingly, the deviations in the shifts calculated at the ADC(1)/ptLR-PCM level of theory are systematic with respect to solvent polarity, but follow an inverse pattern (smaller shifts for polar solvents) as compared to those observed for ADC(2) in combination with the PTE approach.

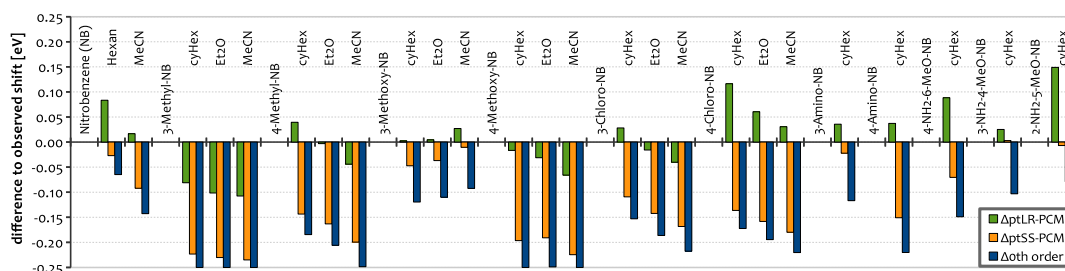


Figure 5.7: Experimental and calculated solvent shifts for the exclusively electrostatic subgroup of xBDSM calculated at the ADC(1)/ptSS-PCM and ADC(1)/ptLR-PCM levels of theory.

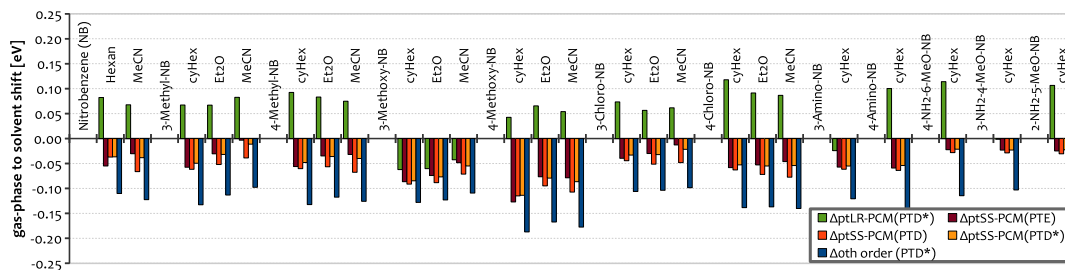


Figure 5.8: Differences between experimental and calculated solvent shifts for the exclusively-electrostatic subgroup of xBDSM computed at the ADC(3/2)/ptSS-PCM and ADC(3/2)/ptLR-PCM levels of theory in combination with the PTE, PTD and PTD* schemes.

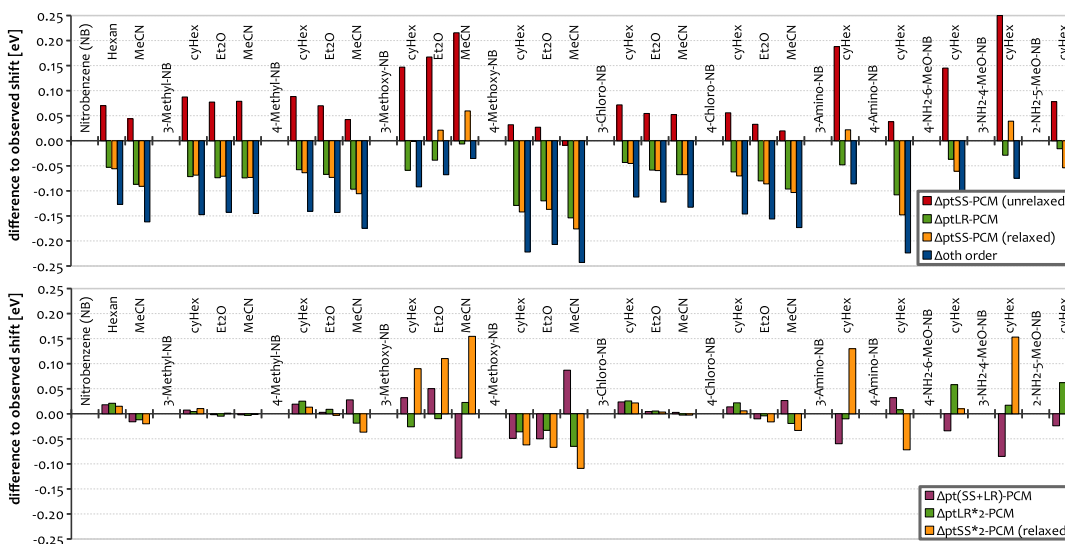


Figure 5.9: *Top*: Differences between calculated and experimental solvent shifts for ptSS and ptLR approaches as well as the zeroth-order contribution at the LRC- ω PBE/ptSS-PCM and /ptLR-PCM levels of theory. *Bottom*: Differences between calculated and experimental solvent shifts for the empirically-scaled ptSS*2 and ptLR*2 approaches as well as the combined pt(LR+SS) approach.

ADC(3/2)

Surprisingly, the accuracy of the shifts calculated with ADC(3/2) and the ptSS-PCM(PTD*) scheme does not improve compared to ADC(2). On the contrary, the shifts calculated with ADC(3/2)/ptSS-PCM(PTD*) are systematically too low (mean error = -49 eV, MAD = 49 meV, RMSD = 54 meV). A detailed analysis and comparison of zeroth- and first-order contributions to those obtained for ADC(2) reveals that this is mainly due to smaller ptSS correction terms (77 meV, on average, *versus* 123 meV), whereas the zeroth-order contributions (PTD*) are very similar (mean deviation = -126 meV *versus* -120 meV). Probably due to fortuitous error compensation, the ptSS corrections yields a better agreement with the experiment in combination with ADC(3/2) zeroth-order energies obtained with the PTE scheme (mean error = -47 meV, MAD = 47 meV, RMSD = 52 meV). The differences to ADC(3/2)/ptSS-PCM(PTD*) are, however, negligibly small.

Regarding the very systematic underestimation of the solvent shifts observed for ADC(3/2)/ptSS-PCM one should bear in mind the basis-set dependence of the shifts. Obtained with augmented and/or triple- ζ basis sets, the solvent shifts might be about 20% larger, which would yield something much closer to quantitative agreement with experiment.

The ptLR corrections in combination with ADC(3/2)/PCM(PTD*) zeroth-order energies yield consistently too large solvent shifts (mean error = 63 meV, MAD = 71 meV, RMSD = 81 meV). As in case of ADC(2)/ptLR-PCM, the results of the ptLR approach seem to depend on the character of the excited state. While the shifts are overestimated for those states related to the 2 A_1 state of nitrobenzene, the shifts for the 1 B_1 cases (3-methoxy-NB and 3-amino-NB) are slightly too low.

TD-DFT

The TD-DFT/LRC- ω PBE results are different from any of the ADC/PCM combinations, in particular regarding the ptLR approach. The shifts predicted by the latter are systematically too *small* (mean error = -69 meV, MAD = 69 meV, RMSD = 77 meV). The same applies to the TD-DFT/ptSS-PCM corrections (mean error = -64 meV, MAD = 76 meV, RMSD = 86 meV). Regarding the very similar underestimation of the solvent shifts with the ptSS approach for ADC(1), one may suggest that first-order excited-state densities are not accurate enough for ptSS calculations, and that at least second-order excited-state densities are needed to obtain accurate first-order corrections to the solvent-shifts with the ptSS approach.

For TD-DFT, the first-order terms of ptLR and ptSS approaches are virtually identical for most of the molecules in the xBDSM set. The cases where they differ include 3-methoxy-NB and 3-amino-NB (excitations related to the 1 B_1 state of nitrobenzene), along with the *para*-substituted isomers of 3-amino-NB (see fig. 5.9). The connection between these cases are the strong electron-pushing substituents ($-\text{NH}_2$ and $-\text{OMe}$), and as such one would expect the largest degree of CT character in these cases. This offers a hint that CT character may explain differences between the ptSS and ptLR approaches. Considering the much better agreement with experiment for the ptLR approach (see below), one may conclude that even with range-separated functionals like LRC- ω PBE, and a systematic adaptation of the range-separation parameter, the excited-state density is not

properly described when there is significant CT character. A recent investigation of this issue can be found in Ref. 124.

Since the deviations from the experiment are systematic underestimation, the first-order terms can be scaled up pragmatically. Surprisingly, with a scaling factor of exactly 2.0 the ptLR*2-PCM approach yields the most accurate description of the solvatochromic shifts in this investigation (mean error = 1 meV, MAD = 21 meV, RMSD = 28 meV), with virtually no mean deviation and a maximum error of only 60 meV (see fig. 5.9, bottom). Although scaling with the same factor does also improve the ptSS results dramatically, the resulting ptSS*2-PCM approach is not nearly as accurate as the scaled ptLR approach. In particular, one finds a large overestimation of the shifts for the CT examples, for which the ptSS and ptLR first-order terms differ (mean error = 10 meV, MAD = 45 meV, RMSD = 68 meV, with several large errors of about 0.15 eV). Motivated by previous work,¹¹⁸ and the idea that the state-specific and linear-response approaches describe different physical effects, the combination of first-order terms of the ptSS and ptLR approaches has also been studied. Indeed, also this pt(SS+LR) approach improves the results significantly, but is not as accurate as the scaled ptLR approach (mean error = -4 meV, MAD = 32 meV, RMSD = 47 meV).

5.5.7 Discussion of the Relation of SS and LR Formalisms

A statistical analysis of the error for the investigated QM/PCM methods, as applied to the electrostatically-dominated subset of xBDSM, is given in Table 5.2 and plotted in fig. 5.10. The most accurate methods are clearly TD-DFT/ptLR*2-PCM, TD-DFT/pt(SS+LR)-PCM as well as ADC(2)/ptSS-PCM(PTD*), and if the basis-set dependency is considered also ADC(3/2)/ptSS-PCM.

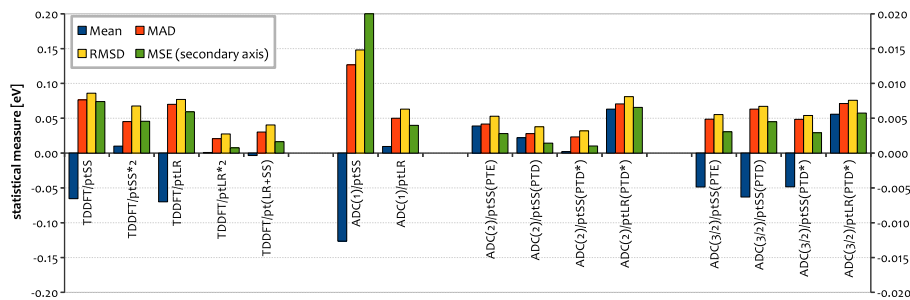


Figure 5.10: Statistical errors in various QM/PCM schemes as applied to the electrostatically-dominated subset of xBDSM. For the sake of completeness, the results for the scaled ptSS*2 and combined pt(SS+LR) approaches in combination with TD-DFT are given.

First, it bears pointing out the perturbative ptLR corrections are formally *not* identical to the self-consistent LR-PCM formalism described in the literature.^{118;119} Nevertheless, for nitrotoluene the ptLR scheme affords results that are essentially identical to those obtained using the self-consistent LR-PCM procedure as implemented in Q-CHEM.¹⁵⁰

Let me begin the discussion with an interpretation of the results regarding the relation of the ptLR and ptSS formalisms. The zeroth-order (static polarization)

Table 5.2: Statistical errors for the electrostatically-dominated subset of the xBDSM set.

	mean	MAD	RMSD
—zeroth order—			
LRC- ω PBE	-141	141	149
ADC(1)	-185	185	198
ADC(2) (PTE)	-67.3	67.7	77.5
ADC(2) (PTD)	-101	101	105
ADC(2) (PTD*1.6)	-120	120	124
ADC(3/2) (PTE)	-111	111	114
ADC(3/2) (PTD)	-140	140	142
ADC(3/2) (PTD*0.5)	-126	126	128
—ptLR-PCM—			
LRC- ω PBE	-70.0	70.0	77.3
LRC- ω PBE (ptLR*2)	0.9	20.7	27.5
ADC(1)	9.5	50.1	63.1
ADC(2) (PTD*1.6)	66.4	73.4	83.0
ADC(3/2) (PTD*0.5)	55.8	71.1	75.8
—ptSS-PCM—			
LRC- ω PBE	-65.6	76.4	86.0
LRC- ω PBE (ptSS*2)	10.0	45.2	67.6
ADC(1)	-126.5	-126.7	148.1
ADC(2) (PTE)	38.9	41.7	52.9
ADC(2) (PTD)	22.0	27.9	37.8
ADC(2) (PTD*1.6)	2.1	23.2	31.9
ADC(3/2) (PTE)	-48.7	48.7	55.3
ADC(3/2) (PTD)	-63.1	63.1	67.1
ADC(3/2) (PTD*0.5)	-48.5	48.5	54.1
—pt(SS+LR)-PCM—			
LRC- ω PBE	-3.5	30.2	40.4

energy is identical in both cases, but the first-order terms are generally regarded as describing different physical phenomena. Specifically, the first-order ptSS contribution is associated with the dynamical response of the fast component of the polarization, whereas the first-order LR correction has been suggested to relate to excitonic coupling¹¹⁸ or dispersion effects.^{139;151} Here, however, it is found that for the case of TD-DFT, the ptLR and ptSS corrections (as formulated here) afford similar values in cases where the solvatochromic shift is dominated by electrostatic effects. However, the relation between the ptLR and ptSS corrections also depends on the underlying QM level of theory. For ADC(2) and ADC(3/2), the ptLR corrections are about twice as large as the ptSS corrections (mean 0.19 eV *vs.* 0.11 eV for ADC(2), 0.18 eV *vs.* 0.08 eV for ADC(3/2)).

With respect to the accuracy of the ptSS and ptLR approaches for the first xBDSM subset, there are only negligible differences if one compares the best-performing QM/PCM combinations (see fig. 5.11). The results indicate that the ptSS correction is more sensitive with respect to the level of theory, *i.e.* more sensitive to the quality of the excited-state densities. Taking into account the

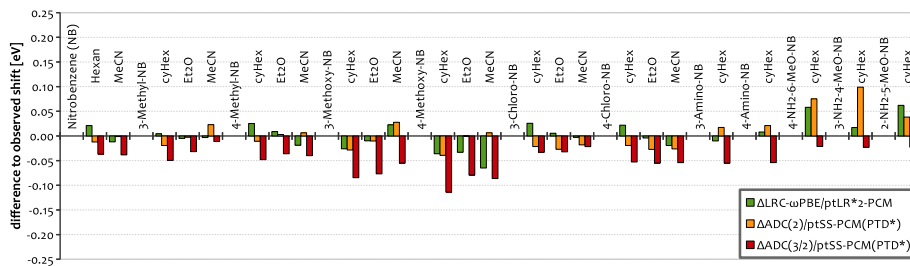


Figure 5.11: Direct comparison of the errors of the most accurate QM/PCM combinations for the first xBDSM subset.

basis-set dependence of the shifts, the accuracy of the ptSS-PCM combinations with ADC(2) and ADC(3/2) is presumably very similar. In combination with the CIS-related ADC(1) and TD-DFT, however, one finds a systematic underestimation of the solvent shifts.

For the ptLR-PCM approach, the exact opposite is the case. It affords the most accurate solvatochromic shifts when combined with TD-DFT (upon empirical scaling by a factor of 2.0), and also with ADC(1) the predicted shifts are balanced and accurate (without a scaling). For ADC(2) and ADC(3/2), however, the ptLR correction terms are too large to suite the zeroth-order excitation energies, which are closer to the experimental shifts for ADC(2) and ADC(3/2) (mean deviation about -0.125 eV) than for ADC(1) (mean deviation -0.155 eV). The ptLR corrections are, however, very similar for ADC(1) (mean 0.19 eV), ADC(2) (mean 0.19 eV) and ADC(3/2) (0.18 eV).

Despite these differences between the ptSS and ptLR corrections, I conclude that the electrostatic information relevant to the fast solvent response seems to be encoded in the *transition density*, not just in the excited-state density. As such, the ptLR and the ptSS formalisms constitute different ways to extract this information and translate it into an energy correction. If the ptLR formalism would indeed describe an entirely different physical effect, it should not give rise to any sizeable contribution for the nitroaromatic compounds, whose solvatochromism is apparently well-described with the purely electrostatic ptSS-PCM approach.

A recent series of articles of Plasser, B appler and coworkers,^{142;143} in which they presented a detailed analysis of the density matrices occurring within the ADC computational framework might help to guide this discussion. They demonstrated that the transition-density matrix simply represents the orbital transitions contained in the ADC response vector, while the excited-state densities are characterized by additional contributions deriving from secondary orbital-relaxation effects, which are present whenever significant charge shifts occur.¹⁴³ With these results in mind, one may suggest that the essential difference between ptLR and ptSS correction is that the ptSS correction terms do include orbital relaxation *via* the respective densities, while the former, transition-density based ptLR corrections do not. This is in line with the better agreement and much more systematic errors of the ptSS-approach in combination with ADC(2) and ADC(3/2). Since for the latter, the relaxation effects are also included in the zeroth-order energies, the ptLR correction terms are just too large. Hence, for correlated higher-order methods, the ptSS approach should be preferred over the

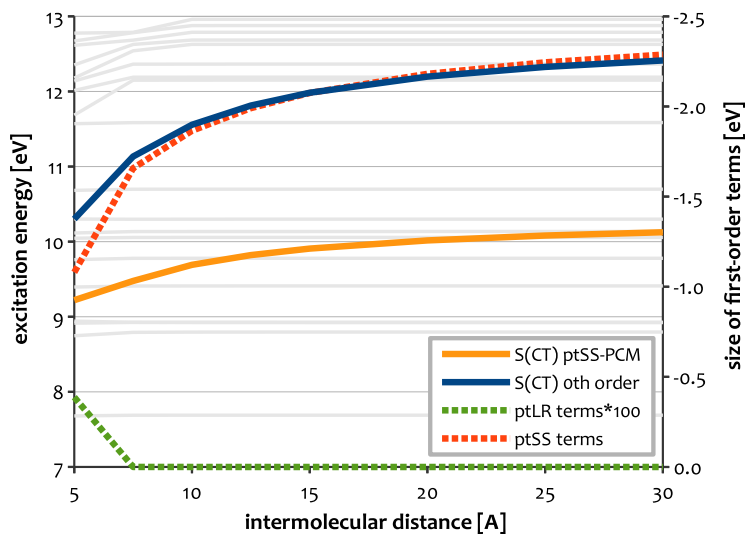


Figure 5.12: Zeroth- and first-order energy of the electron-transfer excitation of the $\text{C}_2\text{H}_4/\text{C}_2\text{F}_4$ complex in MeCN, computed at the ADC(2)/ptSS-PCM(PTD) and ADC(2)/ptLR-PCM levels of theory. The magnitude of the first-order ptLR and ptSS terms can be read from the vertical axis on the right. As the intermolecular separation increases, only the ptSS approach affords a physically-correct description, whereas the fast solvent response vanishes at the ptLR level.

ptLR approach.

For first-order methods like TD-DFT or ADC(1), which do not include any orbital relaxation in the excitation energies, the ptLR-approach constitutes a short-cut to obtain the response of the solvent polarization that circumvents the explicit calculation of the excited-state wavefunction. From this perspective, also the agreement of ptLR and ptSS-terms for linear-response method TD-DFT falls into place. A drawback of the ptLR-PCM approach is due to the mathematical structure of the transition density as product of electron and hole orbitals. For CT excitations associated with large electron-hole separation the transition density becomes zero and so do the ptLR correction terms. As a concrete example, I choose the lowest CT excitation of the $\text{C}_2\text{H}_4/\text{C}_2\text{F}_4$ complex⁷⁹ (see fig. 5.12). Obviously, the transfer of an electron should give rise to a pronounced response of the fast component of the polarization since two full charges are created in the process, but due to negligible overlap between initial and final orbitals, the transition density for this excitation vanishes, and so does the ptLR correction. In this and comparable situations, only the ptSS approach affords a physically correct description.

5.5.8 Examples Involving Hydrogen Bonding

The PCM describes only the (long-range) electrostatic interaction with the bulk solvent, but no specific interactions such as hydrogen bonds. In the previous section, the accuracy of the ADC(2)/ptSS-PCM(PTD*) and LRC- ω PBE/ptLR*2-PCM approaches has been established to be ~ 50 meV for cases in which the solvatochromic shift is dominated by electrostatic effects. Here, I examine how

these approaches behave for cases in which hydrogen bonding affects the excitation energy and how this can be included in the model by adding few explicit solvent molecules.

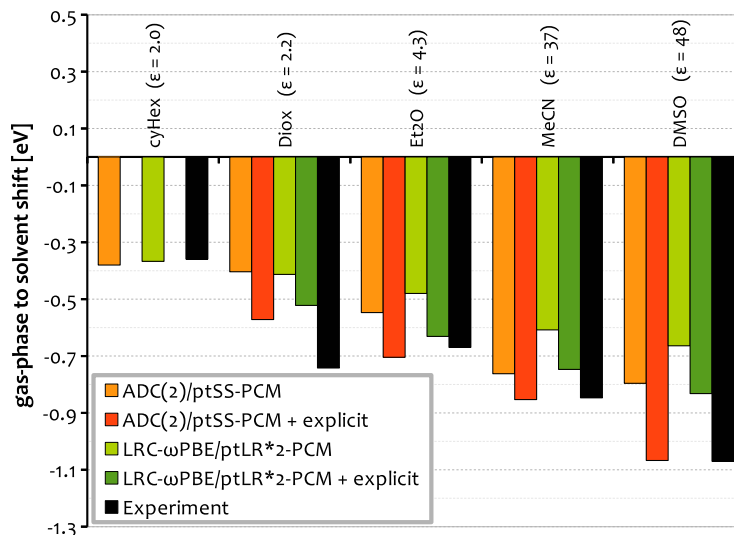


Figure 5.13: Experimental and calculated solvent shifts for *para*-nitroaniline (4-amino-NB) at the ADC(2)/ptSS-PCM(PTD*) and LRC- ω PBE/ptLR*2-PCM levels of theory. Results are shown both with an without a single explicit solvent molecule in the QM region.

Consider the moderately-strong H-bonding case of *para*-nitroaniline (pNA). Already for the weakly Lewis-acidic solvents Et₂O and MeCN, inclusion of explicit solvent molecules has a notable influence onto the excitation energy (fig. 5.13), as coordination to the solvent stabilizes the positive charge at the amine that is created in the excited state, and thus lowers the excitation energy. This effect is even more pronounced for the non-polar, but more Lewis-basic solvent dioxane ($\epsilon = 2.25$). The excitation energy in dioxane (3.50 eV) is actually closer to that observed in the polar solvent MeCN ($\epsilon = 36.7$, 3.39 eV) than it is to the excitation energy in cyclohexane ($\epsilon = 2.03$, 3.88 eV). Thus, the influence of hydrogen bonding to pNA in dioxane is actually larger than the effect of the bulk electrostatic interactions. Inclusion of one explicit solvent molecule within the QM region does generally move the calculated solvent shifts in the right direction, as shown in fig. 5.13. In particular with the ADC(2)/ptSS-PCM(PTD*), the inclusion of a single solvent molecule restores the accuracy quantitatively for all cases but dioxane.

For cases such as charged chromophores in water that exhibit very strong, ionic hydrogen bonds, a calculation of reliable solvent shifts is more involved. Especially in systems where the chromophore has more than one H-bonding site, one may need to sample over conformations of the explicit solvent molecules.¹⁵² In my experience, a practical approach is to: (1) successively include water molecules at one H-bond donor or acceptor site after another, (2) optimize the structure with a method appropriate for the description of intermolecular interactions (*e.g.*, B2-PLYP+D3) using a PCM, and (3) calculate the excitation

energies and see if and how the results converge with the number of explicit solvent molecules.

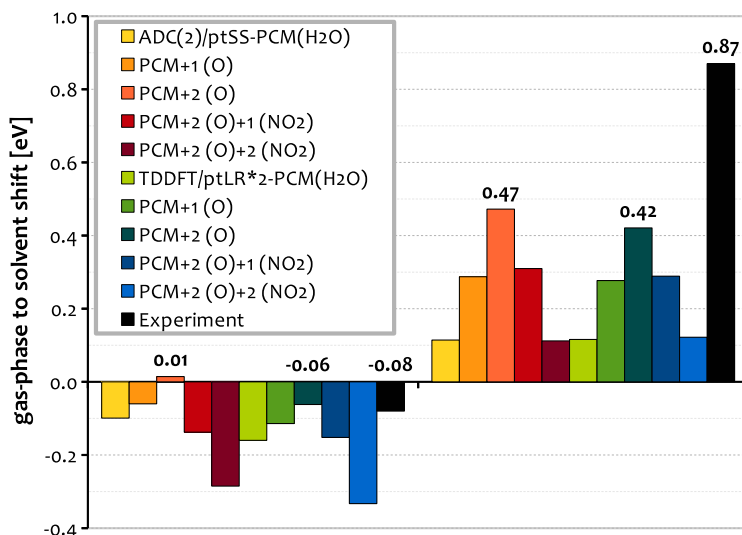


Figure 5.14: Experimental and calculated solvent shifts for 4-nitrophenolate (on the left) and 4-(4'-nitrophenyl)phenolate (on the right) at the ADC(2)/ptSS-PCM(PTD) and LRC- ω PBE/ptLR*2-PCM levels of theory with up to two explicit water molecules at the phenolate group and up to two more at the nitro group.

Following this protocol, I investigated the vacuum-to-water solvatochromic shifts in 4-nitrophenolate (4-NP) and 4-(4'-nitrophenyl)phenolate (44-NPP), which differ (-0.08 eV vs. 0.87 eV, respectively),¹⁴⁹ despite the similar structure of the two molecules. I successively added up to four water molecules, two each at the phenolate and nitro groups, optimized the structures, and then calculated the excited states at the ADC(2)/ptSS-PCM(PTD) and LRC- ω PBE/ptLR*2-PCM levels of theory (see fig. 5.14).

Despite the apparent presence of strong ionic hydrogen bonding, both methods yield a reasonable, qualitatively correct estimate of the observed solvent shifts even without explicit solvent molecules. While the introduction of explicit water molecules to the phenolate improves the agreement with the experiment, additional water molecules at the nitro group decrease the accuracy of the model. One may conclude that the explicit interactions of the solvent with the ionic phenolate are much stronger and thus more important compared to those with the nitro group. This is corroborated by the fact that nitrobenzene itself is, despite its large dipole, virtually insoluble in water. Due to an apparently imbalanced explicit solvation scheme, none of the methods yields a quantitative answer for both molecules.

All together, one may conclude that ADC(2)/ptSS-PCM is more robust with respect to the introduction of explicit solvent molecules. In particular for the examples involving 4-nitroaniline, the results for the explicitly solvated systems are as accurate as for the cases without explicit interactions.

5.5.9 Non-Electrostatic Examples

The lowest electronic transitions in pyridine as well as the lowest two in benzofuran and coumarin exhibit only a very small (or zero) solvatochromic shift between the gas phase, hexane and acetonitrile. This makes these cases very different from the electrostatically-dominated examples discussed thus far. To investigate how the best-performing QM/PCM combinations work for these cases, I calculated solvent shifts at the ADC(2) and LRC- ω PBE levels of theory in combination with the ptSS-PCM and ptLR-PCM approaches. For ADC(2), I used PTD zeroth-order energies and for TD-DFT I used the empirically-scaled ptSS*2 and ptLR*2 schemes.

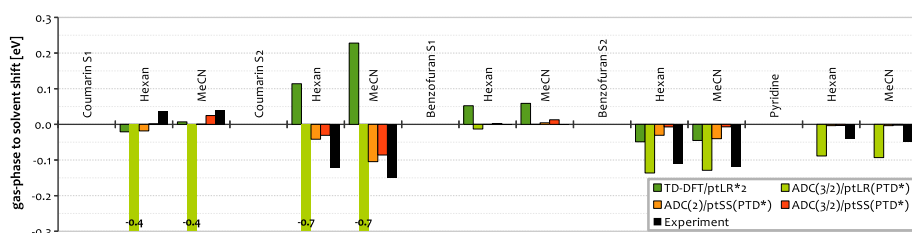


Figure 5.15: Experimental and calculated solvent shifts for the subset of non-electrostatic examples, for ADC(2) and LRC- ω PBE calculations in combination with the ptSS and ptLR schemes.

Inspecting the results in fig. 5.15, one finds a dramatic failure of the ptLR approach in the case of coumarin. Surprisingly, ADC(2) and TD-DFT deviate in opposite directions. An examination of the shifts reveals that in case of TD-DFT, the large blue-shift is due to the zeroth-order term (+0.23 eV in case of MeCN), whereas the ptLR term only -0.003 eV. In contrast, ADC(2) yields a much smaller contribution in the zeroth-order terms in MeCN (0.04 eV for PTD, -0.09 eV for PTE), whereas the ptLR correction is very large (-0.61 eV). For the case of ADC(2), this failure of the ptLR approach is most certainly due to the perturbative character of the ptLR approach, which neglects coupling elements between excited states. A preliminary investigation of this particular example using the self-consistent implementation of the LR formalism for ADC(2)/COSMO in TURBOMOLE¹¹⁸ revealed that, indeed, the predicted solvent shift is much smaller (< 0.1 eV) than the one obtained here. At the TD-DFT level of theory, however, the problem is present already at the stage of the TD-DFT calculation. The ptSS formalism in combination with ADC(2) yields the most accurate predictions for these non-electrostatic cases.

5.6 Summary & Conclusions

I have presented a systematic evaluation of two new, PCM-based corrections for vertical excitation energies by comparison to experimental gas-phase to solvent shifts. For this purpose, I composed the eXperimental Benchmark Data for Solvatochromism in Molecules (xBDSM) set including 44 gas-phase to solvent shifts for 17 molecules in three subgroups as well as the respective gas-phase and solvent-relaxed geometries. The first subgroup consists of examples whose solvatochromism is dominated by the bulk electrostatic interaction. The data points of this group can thus be accurately reproduced by the QM/PCM approach. In the second group, there are cases involving weak to strong hydrogen bonding. Its purpose is to study how hydrogen bonding affects the accuracy and how explicit solvent molecules in the QM subsystem can be used to overcome the shortcomings of pure PCMs. The third group consists of examples that exhibit very weak solvatochromism but have multiple bright excited states in close proximity. In this sense the third set is orthogonal to the former two and was used to demonstrate the limitations of the ptLR correction terms.

The presented PCM-based approaches are derived from the state-specific and linear-response formalisms. Termed perturbation-theoretical state-specific (ptSS)-PCM and perturbation-theoretical linear-response type (ptLR)-PCM, the correction terms depend solely on the zeroth-order excited state or transition densities, respectively. Hence, the correction terms can just be added to the zeroth-order excitation energy, which is the same for both approaches. It can be obtained *via* an configuration-interaction (CI)-type calculation employing the polarized ground-state Hartree-Fock molecular orbitals as a reference. Consequently, the transfer of the approaches to other CI-type excited state methods is straightforward.

By comparison to the xBDSM set, the performance of the ptSS-PCM and ptLR-PCM approaches was examined in combination with ADC of first to third order as well as TD-DFT/LRC- ω PBE. It is found that the ptLR-PCM method affords good accuracy in particular in combination with first-order methods. The ptSS-PCM approach, on the contrary, apparently requires accurate excited-state densities and in turn yields the most accurate results only in combination with correlated methods such as ADC(2) and ADC(3/2).

The statistically most accurate prediction of solvatochromism for the first xBDSM subset is obtained with the ptLR approach in combination with TD-DFT/LRC- ω PBE (see Table 5.2 and fig. 5.10 for summaries of the error statistics for various methods). To achieve this accuracy, however, the ptLR corrections (first-order terms) have to be scaled by an empirically determined factor of 2.0 to eliminate a systematic underestimation (see fig. 5.9). Although this scaling improves the results for all but one example in the xBDSM set, the generality of this scaling has to be questioned and should be investigated more thoroughly in the future. An almost as accurate model can be obtained for TD-DFT if the ptSS and ptLR correction terms are both added to the zeroth-order excitation energy. In contrast to the up-scaling of the ptLR terms, the combination of the ptSS and ptLR corrections can be physically motivated, if it is assumed that the two approaches describe different physical effects. However, this assumption is questionable regarding the almost identical first-order terms of the two methods for many of the examples.

For some of the examples in the third xBDSM subset, the TD-DFT/ptLR*2-

approach fails to yield even a qualitatively correct description. These are on the one hand coumarin, for which the zeroth-order excitation energies are by far too large, and on the other charge-transfer excitations with large electron-hole separation, for which the ptLR corrections become zero due to a vanishing transition density.

The ptSS-PCM approach yields a very accurate description of solvatochromism in combination with the correlated ADC(2) and ADC(3/2) methods. This is true in particular for the PTD variants of the methods, in which the zeroth-order excitation energies are corrected for deficiencies in the HF solvation field (see sections 5.3.4 and 5.5.5). While the agreement with ADC(2) is quantitative with the rather small cc-pVDZ basis set, the combination with ADC(3/2)/cc-pVDZ yields a systematic underestimation of the shifts. If, however, diffuse functions and/or larger triple- ζ basis sets are employed, the calculated shifts are increased by about 20% (see section 5.5.3), which would largely eliminate the systematic error for ADC(3/2) and in turn yield a systematic overestimation for ADC(2). Concerning the total excitation energies instead of just the solvent shifts, ADC(3/2)/ptSS-PCM(PTD*) is certainly the most accurate for the prediction of vertical excitation energies in solution in this investigation, in particular if larger basis sets (e.g. aug-cc-pVTZ) are employed.

For the H-bonded examples including explicit solvent molecules, ADC(2)/ptSS-PCM(PTD*) is more accurate than the scaled LRC- ω PBE/ptLR*2-PCM. Moreover, the ptSS-approach yields a physically sound description of solvatochromism in cases with large electron-hole separation and does not fail qualitatively for any of the examples studied. For molecules in which the solvent shift is *not* dominated by electrostatic interactions, the PTE variant of ADC(2)/ptSS-PCM is more accurate. This is probably due the fact that the solvent reaction field is iterated to self-consistency alongside the ground-state density, and furthermore the differences between the HF and MP2 ground state are much smaller than for the nitroaromatics. In combination with TD-DFT and ADC(1) the ptSS correction terms are systematically too small, which was traced back to poor excited-state densities.

Concerning the relation of the linear-response and state-specific approaches, I conclude that both approaches essentially describe the same electrostatic effect (response of the fast component of the polarization to an electronic excitation) within the perturbative formulation presented here. The main difference is that the ptSS approach allows to include orbital-relaxation effects *via* the respective excited-state densities, while the ptLR approach, on the contrary, does not. This was traced back to the fact that the transition density itself does, in contrast to the excited-state density, not contain any orbital relaxation effects, even if computed with correlated methods such as ADC(2) and ADC(3/2).¹⁴³

Along this line of thought, the good agreement obtained with the ptLR approach in combination with first-order methods such as TD-DFT and ADC(1) falls into place. Neither ADC(1) nor TD-DFT include orbital relaxation effects in the excitation energies. Hence, the latter are consistent with the “unrelaxed” ptLR correction terms. For ADC(2) and ADC(3/2), whose excitation energies do contain orbital relaxation effects, the ptLR correction terms are too large. For these correlated methods, also the first-order corrections need to include orbital-relaxation effects, which can only be achieved *via* the ptSS approach in combination with proper excited-state densities. Hence, for correlated methods the ptSS approach is required to obtain a balanced description of solvent effects.

Since the implementation of ADC in Q-CHEM 4 in combination with the ISR formalism offers a very efficient way to obtain accurate excited-state densities directly from the excited-state vectors, *i.e.* without the need to calculate the orbital response explicitly (see Section 5.3.6), the ptSS corrections can be calculated at essentially no extra computational cost compared to the respective excitation energies.

For TD-DFT, on the contrary, the ptLR*2-PCM approach seems to be the most accurate, in particular for bright excited states with large charge-transfer character. For the latter, the ptLR and ptSS correction terms differ significantly, whereas the scaled ptLR*2-PCM approach consistently yields a slightly better agreement with the experimental values than the combination of both approaches pt(SS+LR) (see Section 5.5.6). Hence, I suggest to use the scaled ptLR*2-PCM approach in combination with TD-DFT.

After all, one may question whether the xBDSM data set, which mainly consists of nitroaromatic compounds is as diverse as it should be to provide representative error estimates for various PCM approaches. Unfortunately, this lack of diversity is mainly due to the combined limitations of the experiments and the calculations, which place tight constraints on the size of molecules that can be computed (with ADC methods) and the types of chromophores that yield unambiguous experimental solvent shifts. It would be useful to expand the size of this data set in the future, in particular the third subset of non-electrostatic examples. Despite the limitation, this first systematic evaluation of PCM-based solvent models by comparison to the xBDSM set provides valuable insights in the relation between SS and LR formalisms, and uncovered unexpected differences between density- and wave function-based methods within a PCM framework.

Chapter 6

Conclusion

6.1 Global Summary & Outlook

In the previous chapters I have given a brief introduction to selected quantum-chemical methods as well as the field of photochemistry and presented the research conducted during the time of my Ph.D. in chronological order. Here, I will briefly summarize the most important results and point out the relations between the projects.

Complementing the research of my master thesis, the first project was the investigation of the photo-decarboxylation (PDC) of nitro-phenylacetate (NPA). The aim of the combined experimental and theoretical investigation was to explain the differences between the three isomers, which either exhibit a slow release on a time-scale of 200 ps with a quantum yield of about 60% in the *para* isomer (pNPA), a fast release on a sub-ps time-scale with a quantum yield < 10% in the *ortho* isomer (oNPA) or a combination of both for the *meta* isomer (mNPA). However, prior to the actual investigation of the PDC, a thorough consideration of the influence of solvation onto the electronic structure of anionic NPA was found to be required and realized using explicit and implicit models of solvation as well as combinations thereof.

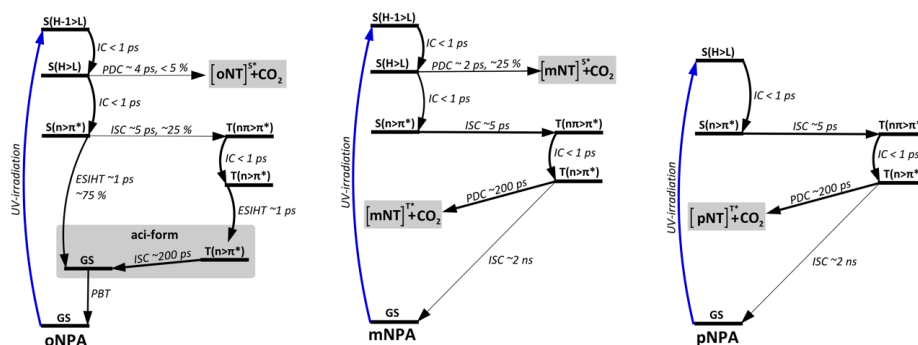


Figure 6.1: Reaction schemes summarizing the photo-decarboxylation mechanism of oNPA (left), mNPA (middle) and pNPA (right). The time-scales are estimated based on computational and experimental results. (ESIHT: excited-state intra-molecular hydrogen-transfer, IC: internal conversion, ISC: inter-system crossing, PBT: proton back-transfer).

Inspecting the relaxed potential energy surfaces (PES) along the C-CO₂ bond cleavage, the fast channel of CO₂ release could be traced back to the presence of a repulsive singlet excited state in oNPA and mNPA, which is absent in pNPA. The slow release was found to occur from a repulsive triplet state that exhibits significant charge-transfer character. In turn, the energetic ordering of the lowest triplet states was found to depend on the details of the applied solvation model. Due to the time-scale of hundreds of picoseconds, the solvent will fully relaxed to the excited-state charge-distribution. This relaxation exerts a large influence onto the energy of the reactive triplet state, which may thus become the lowest excited state. Hence, it was suggested that solvent-related fluctuations of the geometry dictate the time-scale of this slow release. In oNPA, the slow component was found to be quenched by a competing excited-state intra-molecular hydrogen transfer (ESIHT), which is succeeded by a proton back-

transfer in the ground state and thus allows for non-radiative decay to the ground state on a time-scale of few picoseconds. The mechanism for the three isomers is concluded in fig. 6.1 This hypothesis is corroborated by the results of UV-pump vis-probe experiments, which have a time-resolution < 200 fs. An inspection of the transient-absorption data clearly shows the build up of the triplet population as well as the aci-form, which could be assigned conclusively by means of the calculated excited-state absorption.

Interestingly, the non-destructive quenching channel of oNPA constitutes the initial step of the photo-deprotection mechanism in closely related ortho-nitrobenzylic (oNB) photolabile protecting groups, which is commonly referred to as *uncaging*. Hence, within my next project, I investigated the ESIHT of ortho-nitrobenzylacetate (oNBA), which constitutes a prototypical example for oNB photolabile protecting groups to study the relation between these processes. In the existing literature, the interplay of inter-system crossing (ISC) and the ESIHT, which may occur in the singlet as well as the respective triplet states, had not been addressed before. However, during my investigation of oNPA, I found that the singlet and triplet mechanisms afford a different distribution of photo-products, which in turn might influence the quantum yield of the uncaging reaction. The outcome of the investigation of oNBA corroborated my hypothesis: Since the singlet channel for ESIHT leads to a conical intersection (CI) with the ground state, it yields a hot ground state population of the so-called aci-form, in which a hydrogen has been transferred to the nitro group. Since the aci-form is separated from the energetically much lower nitroaromatic form only by a relatively small barrier, a very efficient proton back-transfer is possible, which explains the efficient quenching of CO_2 release observed in oNPA. If, however, ESIHT takes place on the triplet surface, the conversion to the ground state is spin forbidden and thus about three orders of magnitude slower. Consequently, the equilibrium between nitroaromatic and aci-form is established in the triplet manifold, where the aci-form is energetically favored and can be expected to yield the desired aci-form with higher quantum yield (see fig. 6.2). This could be exploited to increase the quantum-yield of oNB cages. For this purpose one would need to slow down ESIHT to allow a larger fraction of the molecules to undergo ISC prior to ESIHT. Indeed, oNB compounds with substituents in the benzylic position that slow down initial singlet ESIHT exhibit an almost twice as large uncaging quantum yield. An example for such compounds are α -carboxy oNB compounds.

After the above-described investigations of the photochemistry of nitrobenzylic compounds, an open question concerning the non-radiative decay of nitroaromatic compounds remained. In the absence of substituents in *ortho*-position, the excited-state population decays to the ground state on a very stable time-scale of 1-2 nanoseconds (ns), which is a surprisingly short life time for a non-reactive and non-radiative triplet state. Moreover, this life time is on the one hand almost independent of solvent polarity, but on the other influenced by the chain-length of e.g. aliphatic solvents. Regarding the prototypical nature of nitrobenzene (NB) as the smallest nitroaromatic compound and the fact that it constitutes the parent compound of the previously investigated molecules and many other photo-active systems, I decided to conduct an investigation of its photochemistry and excited states and the mechanism of non-radiative decay. Due to its small size and high C_{2v} symmetry, it was possible to employ a hierarchy of very sophisticated *ab initio* methods including multi-reference (CAS-

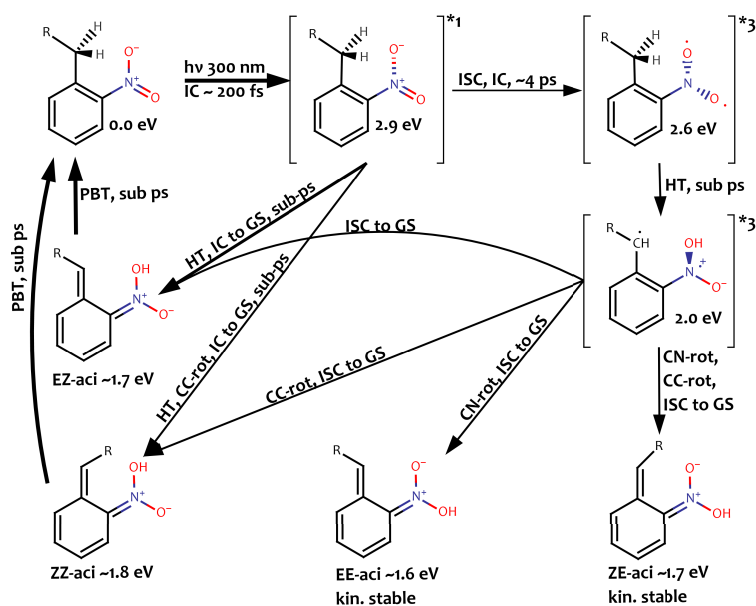


Figure 6.2: Photochemistry of oNBA after UV excitation into S_4 . Although ESIHT can occur via both singlet and triplet pathways, only the triplet route yields kinetically stable aci-isomers. The singlet route, on the contrary, leads into a conical intersection and thus mainly to non-radiative decay to the electronic ground state.

SCF(14/11) with NEVPT2, DFT/MRCI) as well as high-level single-reference methods (EOM-CCSD, MOM-CCSD(T), ADC(3)). An important first result of this investigation was that the electronic structure of the simple molecule NB is more problematic than expected. A comparison between calculated and experimental gas-phase geometries of NB revealed that the perturbative coupled-cluster singles and doubles (CC2) method fails to predict an accurate ground-state geometry. Only because of a fortuitous error compensation between the excitation energies calculated with the linear response variant of CC2 and the faulty geometry, the excitation energies are in good agreement with the experiment. This finding questions the credibility of the previous investigations of oNPA and oNBA, in which CC2 has been employed as well. Particularly, CC2 predicts a different ordering of the lowest triplet states as well as different ground and excited-state geometries compared to higher-order methods. Since this presumably also impacts the shape of the PES of ESIHT, it is suggestive to confirm the results of these investigations using a more sophisticated methodology such as EOM-CCSD or CAS-SCF.

Concerning the non-radiative decay, potential energy surfaces along the ONO bending and ONCO out-of-plane bending angles of nitrobenzene computed at the EOM-CCSD (geometries) and ADC(3) (energies) levels of theory revealed an energetically feasible deactivation mechanism. The calculated energy barrier for the ISC from the lowest triplet state to the ground state agrees well with the reported temperature dependency. Furthermore, a low-energy large-amplitude motion of the oxygen atoms out of the molecular plane, which is

of the polarization of the environment. Eventually, I derived and implemented two different, perturbative formalisms that account for the shift of the electron density due to an excitation. To evaluate the performance of these so-called perturbation-theoretical linear-response-type (ptLR) and perturbation-theoretical state-specific (ptSS) formalisms I composed a set of experimental benchmark-data for solvatochromism in molecules (xBSDM). Subsequently, the ptLR and ptSS formalisms were employed in combination with long-range corrected time-dependent density functional theory (LRC TD-DFT), *i.e.* ω PBE as well as the algebraic diagrammatic construction (ADC) of first through third order. This first systematic evaluation of calculated solvent shifts by comparison to experimental data demonstrated the convincing accuracy of the model in particular in combination with ADC(2) and ADC(3) as shown in fig. 6.4 and furthermore revealed a number of surprising and unexpected results.

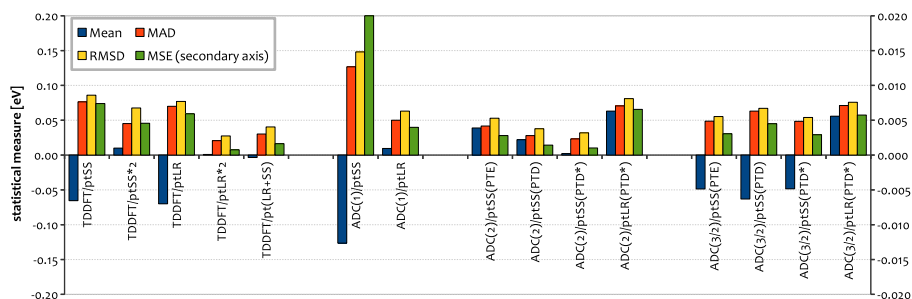


Figure 6.4: Summary of the statistical errors of solvatochromic shifts predicted with various combinations of quantum-chemical models (TD-DFT, ADC(1), ADC(2) and ADC(3)) and PCM formalisms (perturbative linear-reponse-type (ptLR) and perturbative state-specific (ptSS)) I derived and implemented in the scope of this work. The errors are with respect to the electrostatically dominated subgroup of the experimental data contained in the xBSDM set.

Most notably, I was able to shed light onto the relation of transition-density based ptLR and difference-density based ptSS formalisms. In good agreement with the findings of F. Plasser and S. B appler on the relation of transition and differences densities in the ADC framework, the transition density based ptLR corrections do not include orbital-relaxation effects, while the difference-density based ptSS corrections do include orbital-relaxation as far as these are present in the respective excited-state densities. Consequently, the ptLR formalism is well suited to be used in combination with first-order methods, for which it constitutes a short-cut avoiding the explicit calculation of excited-state densities. For second- and higher-order methods, however, the ptSS formalism in combination with proper excited-state densities is required to obtain correction terms that suite the respective excitation energies, which also include orbital-relaxation effects. In combination with ADC(2) and ADC(3), the ptSS formalism quantitatively reproduced the experimental solvent shifts with maximum deviations of about 50 meV. Similar accuracy was achieved by the ptLR approach in combination with TD-DFT when the respective correction terms were scaled by an empirical factor of two.

After all, I have present applications of quantum-chemical methods to study photochemical processes of NPA, oNBA and nitrobenzene in condensed phase

as well as the development of PCM-based corrections for vertical excitation energies in solution. To enable a thorough exploration of photochemical processes and the respective excited-state potential-energy surfaces and in solution, the QM/PCM methodology should be extended to allow for full relaxation of solute and solvent. For this purpose, ADC excited-state gradients are required, which have recently be implemented in a development version of Q-CHEM. In this context, particularly the calculation of fluorescence energies is interesting, because they offer another possibility for the evaluation of the PCM solvation model by comparison to experimental fluorescence data.

6.2 Danksagung

Für die Tatsache, dass ich jetzt diese Danksagung schreiben muss, sind viel mehr Leute verantwortlich als ich hier erwähnen kann. Ein paar wenige, ganz besonders Verantwortliche, möchte ich hier jedoch namentlich nennen und kurz vorstellen. Da wäre zunächst mein Doktorvater *Prof. Dr. Andreas Dreuw*, der seit dem ich bei ihm vor gut sechs Jahren meine Bachelorarbeit begonnen habe, immer genau die richtige Mischung aus freundschaftlichem Umgang, Chef und begeistertem Wissenschaftler gefunden hat, die nötig war um mich zu motivieren und anzuspornen. *Danke, für die ausgezeichnete Betreuung, all die Freiheiten und ganz besonders für die vielen Weisheiten des alltäglichen und wissenschaftlichen Lebens!*

Weiterhin möchte ich *Dr. Michael Wormit* danken, für die Einführung in den Quelltext von ADCman, die vielen, aufschlussreichen Diskussionen über den PCM-Formalismus im Kontext von ADC und die unerschöpfliche Geduld mit der er den wiederkehrenden Fragen eines Chemikers über die hohe Kunst des Programmierens in Klassen und Strukturen begegnete.

Die Interpretation der hier vorgestellten Ergebnisse und deren optisch ansprechende Aufbereitung wurden auf zahllosen Zugfahrten zwischen Frankfurt und Heidelberg ausgiebig mit *Herrn Dr. Felix Plasser* diskutiert. Diese zielführenden Diskussionen über Elektron- und Übergangsdichten, Methoden und Moleküle waren mir beim Erstellen dieser Arbeit eine große Hilfe. Letztlich hat auch Felix jüngstes Projekt „Theodore“ zu dieser Arbeit beigetragen. *Danke Felix.*

The work on the topic of solvation models would not have been possible in the presented form without a very productive visit in the Group of *Prof. John Herbert* at Ohio State University in Columbus. I specifically want to thank *Zhi-Qiang You* for his time, his patient explanations and the introduction to the PCM code. Im Zusammenhang mit dem PCM-Projekt möchte ich mich auch bei *Thomas Kriesche* bedanken, der mir bei der Erzeugung von experimentellen Referenzdaten für das xBDSM Set sehr geholfen hat.

Allerdings fing meine wissenschaftliche Karriere viel früher an als mit der Promotion oder dem Studium. Ich war mir sicher, dass es Chemie werden soll lange bevor der Gong meine ersten Chemiestunde beendete. Verantwortlich dafür ist *Herr Dr. Friedel*, der uns in der Chemie AG der Goetheschule aufopferungsvoll betreute und mit damit erste Einblicke in die Chemie ermöglichte. In diesem Zusammenhang gilt mein Dank auch *Frau Anders*, die mich im Leistungskurs Chemie gut auf die akademische Laufbahn vorbereitet hat.

Schon meine Eltern mussten sich mit meiner Neugier an meiner Umwelt im Rahmen ausgedehnten Frage-und-Antwort Marathons auseinandersetzen. Als ich schließlich auf die Chemie kam, haben sie sich wahrscheinlich nicht nur einmal gewünscht, dass ich früher auf theoretische Modelle und computerbasierte Experimente umgestiegen wäre und im Gegenzug dafür weniger praktische Experimente in ihrem Keller durchgeführt hätte. Nichtsdestotrotz, ohne ihre Unterstützung und Geduld wäre ich nie so weit und diese Arbeit niemals zustande gekommen. *Danke Eltern, für einfach alles!*

Zu guter letzt möchte ich meine tiefste Dankbarkeit gegenüber *Stefanie Böppler* zum Ausdruck bringen, die mir in den letzten Zügen der Anfertigung dieser Arbeit tatkräftig und moralisch zur Seite stand. *Danke Steffi, für die ganz besondere Unterstützung, vor allem in der „heißen Phase“ meiner Promotion sowie für die allgemeine Versüßung meines Lebens.*

List of Figures

- 1.1 Shape of (from left to right) $1s$, $2s$, $3s$ and $4s$ as well as one of the (below) $2p$, $3p$ and $4p$ orbitals of elemental Argon calculated at the Hartree-Fock/def2-TZVP level of theory and visualized using isovalue surfaces. The latter are a very common tool for visualization of densities in quantum-chemistry. Each of the three surfaces encases a specific fraction of the global density of the respective orbital (solid surface: 80%, transparent: 90% and diffuse: 95%) and furthermore, all points of one surface have the same local value of the density (isovalue). The plots nicely show the internal nodal structure of the orbitals with increasing principle quantum number n , which is due to the $r^{(n-1)}$ term in the radial part of the orbital. Also, the orbitals become more and more diffuse, as indicated by the increase of transparent and diffuse surfaces in the higher orbitals to the right. 5
- 1.2 Comparison between the Slater-type and Gaussian (STO-1G) $1s$ orbital for the hydrogen atom (eq. 1.7) as well as linear combinations of two (STO-2G) to five (def2-TZVP) primitive Gaussian functions according to eq. (1.9). While the linear plot on the left exposes the different shape of the Slater and Gaussian functions close to the core, the logarithmic plot on the right also shows differences for large electron-nuclear distances. 8
- 1.3 Selected valence molecular orbitals of CO (carbon left, oxygen right) during a HF-SCF/def2-TZVP calculation using the DIIS algorithm. The first row corresponds to the initial guess, which was in this case obtained using only the one-electron part of the Hamiltonian (H^{core}). Apparently, in absence of the inter-electronic repulsion the electrons accumulate at the oxygen atom due to its higher nuclear charge, which causes the oxygen atom to accumulate a (Mulliken) charge of -1.4 (Löwdin -2.1). In the first SCF step including also the mean-field potential depicted in the second row, this is over-corrected and the center of the electron-distribution is shifted to the carbon atom. Already the orbitals from the second step including v^{HF} shown in the third row closely resemble the final, converged MOs (after 12 further steps, convergence threshold 10^{-6} Hartree) shown in the last row. This can be regarded as a demonstration of the efficiency of the DIIS algorithm. Note that the phases of the orbitals change randomly during the calculation and the coloring is thus inconsistent. . . . 17

1.4	Block-structure of the hermitian ISR matrix of zeroth and first order (left) as well as second and third order (middle). Apparently, the zeroth and first-order matrix as well as the second- and third-order matrix have an identical structure. The differences between these levels of theory arise from the order of perturbation theory at which the matrix elements in the singles (a), doubles (c) and coupling blocks between singles/doubles (b) are obtained, which is shown for ISR(0) through ISR(3) in the table on the right. . .	36
2.1	Molecular structure of anionic <i>ortho</i> -, <i>meta</i> - and <i>para</i> -nitrophenylacetate.	46
2.2	Generic deprotection-mechanism of photo-labile protecting groups (cages) of the <i>ortho</i> -nitrobenzyl type	47
2.3	a) Absorption transients of o-, m-, and pNPA at the characteristic triplet absorption of 667 nm. b) Absorption transients of oNPA at 450 and 400 nm as well as their difference.	50
2.4	Coordination geometries of micro-solvated clusters of (from left to right) oNPA, mNPA and pNPA including seven water molecules.	55
2.5	Difference-density plots of the $n \rightarrow \pi^*$ (top), $Bz(\pi) \rightarrow \pi^*$ (middle) and $Bz(\pi') \rightarrow \pi^*$ (bottom) state of o-, m- and pNPA (from left to right) at the CIS/def2-TZVP level of theory. The transparent surfaces are rendered using an isovalue of 0.002 (to include minor contributions), while the opaque surfaces correspond to an isovalue of 0.01 (to show major contributions). Regions of increasing density are blue, while red areas show a decrease in density. .	60
2.6	Cut through the relaxed potential energy surfaces along the decarboxylation coordinate of mNPA. The Figure includes the ground state (blue) as well as $Bz(\pi) \rightarrow \pi^*$ (termed S(H>L), red) and $n \rightarrow \pi^*$ (green) excited singlet (dotted) and triplet (dashed) states at the riCC2/def2-TZVP/COSMO level of theory and furthermore the $Bz(\pi) \rightarrow \pi^*$ (termed T(H>L)) and $n \rightarrow \pi^*$ triplet states at the uPBE0/def2-TZVP level of theory. Except for the excited states close to the Franck-Condon point, the curves correspond to the relaxed surfaces obtained using non-equilibrium solvation for riCC2 and equilibrium solvation for uPBE0. All curves are shown relative to the optimized ground state geometry.	62
2.7	Cut through the relaxed potential energy surfaces along the decarboxylation coordinate of pNPA. Displayed is the ground state (blue) as well as $Bz(\pi) \rightarrow \pi^*$ (termed, S(H>L), red) and $n \rightarrow \pi^*$ (green) excited singlet (dotted) and triplet (dashed) states at the riCC2/def2-TZVP/COSMO level of theory and furthermore the $Bz(\pi) \rightarrow \pi^*$ (termed, T(H>L)) and $n \rightarrow \pi^*$ triplet states at the uPBE0/def2-TZVP level of theory. Except for the excited states close to the Franck-Condon point, the curves correspond to the relaxed surfaces obtained using non-equilibrium solvation for riCC2 and equilibrium solvation for uPBE0. All curves are shown relative to the optimized ground state geometry.	65

-
- 2.8 Cut through the ground-state optimized potential energy surface of $Bz(\pi) \rightarrow \pi^*$ excited (red curves) and $n \rightarrow \pi^*$ excited (green curves) singlet (solid curves) and triplet (dashed curves) states along the decarboxylation coordinate of oNPA at the riCC2/def2-TZVP/COSMO level of theory using non-equilibrium solvation. 66
- 2.9 Cut through the relaxed potential energy surface along the H-transfer coordinate of oNPA. Singlet as well as triplet $n \rightarrow \pi^*$ excited states allow for an almost barrierless H-transfer eventually leading to a conical intersection with the electronic ground state. 67
- 2.10 Suggested photochemistry of oNPA after UV excitation. Although H-transfer may occur *via* a singlet or triplet pathway, mainly the triplet route yields stable aci-isomers, while the initial photo products of singlet H-transfer largely undergo proton-backtransfer. 69
- 2.11 Energy profile of the H-transfer (O-H scan) and C=N rotation (CCNO dihedral scan from EZ-aci to ZE-aci) in T_1 as well as proton-backtransfer including syn-EZ-aci to anti-EZ-aci isomerization (C-H scan) in the GS for oNPA at the uPBE0/def2-TZVP level of theory using COSMO equilibrium solvation. For comparison, the results of corresponding CC2 calculations using non-equilibrium solvation are also shown (orange curve). In the top-right corner the maximum-energy structure along the H-transfer coordinate is given. 70
- 2.12 Reaction schemes for the photo-decarboxylation of oNPA (left), mNPA (middle) and pNPA (right). The time-scales are estimated based on computational and experimental results. (ESIHT: excited-state intra-molecular hydrogen-transfer, IC: internal conversion, ISC: inter-system crossing, PBT: proton back-transfer). 74
- 3.1 Molecular equilibrium structures of ortho-nitro-benzylacetate (oNBA) in its electronic ground state (left), the first excited singlet S_1 (middle) and triplet T_1 (right) states obtained at the riCC2/def2-TZVP(-f) level of theory. The radical character of the lowest excited states can be related to the structural changes in the nitro-group. Compared to the ground-state structure, one of the NO bonds is significantly stretched in S_1 due to a reduced bond order, while in T_1 both NO bonds are elongated and the oxygen-atoms are furthermore bent out-of-plane hinting towards a free electron-pair at the nitrogen atom. 77
-

-
- 3.2 Comparison of the photochemical processes of oNPA (left) and oNBA (right) after excitation. The given time constants and yields marked with a star (*) are estimates for NBA based on experimental data for oNPA showing similar theoretical results. In both cases the main channel is the deactivation via internal conversion (IC), excited-state intramolecular hydrogen-transfer (ESIHT) and finally proton back-transfer (PBT). For oNPA it was inferred that a fraction of approximately 25% of the excited molecules undergo inter-system crossing (ISC) into the triplet manifold instead of ESIHT from S_1 . Since these photochemical processes are a common feature of the *ortho*-nitrobenzylic moiety, they are relevant for all oNB cages in general, since the subsequent formation of the aci-form is more efficient in the triplet manifold. 78
- 3.3 Relaxed difference density (negative part: red; positive part: blue) of the lowest singlet $S(n \rightarrow \pi^*)$ state (left) and $S(\pi' \rightarrow \pi^*)$ state (right) of oNBA obtained at the riCC2/def2-TZVP(-f) level of theory. These plots clearly show the purely local character of the S_1 as well as the charge-transfer character of initially excited S_4 state. 81
- 3.4 Relaxed scans of the potential energy surfaces of the electronic ground state, S_1 and T_1 along the ESIHT coordinate of oNBA at the riCC2-def2-TZVP level of theory. S_1 as well as T_1 are $n \rightarrow \pi^*$ excited states and allow for ESIHT (from left to right) eventually leading to crossings with the electronic ground state (GS). On the right, fully relaxed energies of the H-transfer products EZ- and ZZ-aci-oNBA are given for GS and T_1 . For comparison, also the curves obtained at the uPBE0/def2-TZVP level of theory for GS, S_1 and T_1 are plotted, which are similar to those obtained with riCC2. The shown structures refer to the ground-state optimized nitro-aromat, Z-aci-isomer and E-aci-isomer (bottom from left to right) as well as the triplet-optimized Z-aci-isomer (top right). . . 82
- 3.5 Energy profile of the ESIHT process (O-H scan) and subsequent C=NOOH isomerization, which includes N-OH rotation (CNOH dihedral scan from anti (180°) to syn (0°)) and C=NOOH rotation (CCNOH dihedral scan from EZ-aci to EE-aci) in T_1 and GS at the uPBE0/def2-TZVP level of theory with and without COSMO equilibrium solvation. The syn-anti isomerization is possible in both states, whereas the Z-aci to E-aci conversion can only take place in T_1 . Here, the double-radical character of the molecule allows for C=NOOH rotation yielding EE-aci isomers. This can not occur in the electronic ground state, since it would involve the rotation of a double bond. 84
- 3.6 Photochemistry of oNBA after UV excitation into S_4 . Although ESIHT can occur via both singlet and triplet pathways, only the triplet route yields kinetically stable aci-isomers. The singlet route, on the contrary, leads into a conical intersection and thus mainly to non-radiative decay to the electronic ground state. 85
-

4.1	Isosurfaces for attachment (top, blue) and detachment (top, red) densities for the energetically lowest excited singlet states and the $n_\pi \rightarrow \pi^*$ triplet state at the ADC(3) level of theory as well as the relevant molecular orbitals (bottom) of nitrobenzene calculated with the def2-TZVP basis for the B2-PLYP/def2-TZVP geometry. For all states apart from the $n_\pi \rightarrow \pi^*$ state, attachment and detachment densities of singlet and respective triplet states are hardly distinguishable. The isosurfaces were rendered with the isovalues 0.018 (opaque), 0.006 (colored transparent) and 0.002 (transparent) for the att./det. densities and 0.1, 0.05 and 0.025 for the orbitals. The use of three surfaces instead of only one allows to distinguish between major contributions (opaque surfaces) and minor ones and furthermore to estimate the gradient of the density from the distance of the three surfaces.	93
4.2	Composition of the $n_\pi \rightarrow \pi^*$ excited singlet and triplet states ADC(3)/def2-TZVP//B2-PLYP/def2-TZVP level of theory. Doubly excited determinants are shown in blue. Over-all, they make up for about 50% of the contributions to the excitation vector of this state.	95
4.3	Plot of the vertical excitation energies calculated with single-reference methods of increasing accuracy. The level of theory increases from yellow (first order) over red (second-order) to purple (third order), DFT results are green. Regarding the states for which experimental data is available, ADC(3) outperforms EOM-CCSD. For the $S(n \rightarrow \pi^*)$ excited state, ADC(3) yields excitation energies that are little too high and ADC(2) is superior. All calculation were carried out for the B2-PLYP/def2-TZVP equilibrium geometry with the def2-TZVP basis set.	97
4.4	Vertical excitation energies calculated with the maximum-overlap method in combination with CCSD/CCSD(T) as well as DFT/MRCI and CAS-SCF/NEVPT2 for the B2-PLYP/def2-TZVP equilibrium geometry. While all methods shown here predict the $T(n_\pi \rightarrow \pi^*)$ state to be the lowest triplet state, the critical energy gap to the next higher $T(n \rightarrow \pi^*)$ state varies from 0.13 eV (MOM-CCSD(T)) to 0.72 eV (NEVPT2) with ADC(3) (0.52 eV) and EOM-CCSD (0.3 eV) in between.	99
4.5	Vertical excitation energies (blue), energies of the equilibrium structures of excited states (red) and differences thereof (yellow) relative to the ground-state minimum of nitrobenzene at the EOM-CCSD/cc-pVDZ level of theory in C_{2v} symmetry. In general, the benefit of structural relaxation is larger for $n \rightarrow \pi^*$ excited states than for $\pi \rightarrow \pi^*$ excited states. The $T(n \rightarrow \pi^*)$ state exhibits a slightly larger relaxation than the $T(n_\pi \rightarrow \pi^*)$ excited state, reducing the energy difference between these states compared to the vertical excitation energies.	103
4.6	Unrelaxed potential energy surfaces along the symmetric NO-stretching mode at the ADC(3)/def2-TZVP(-f) level of theory. Singlet states are depicted as continuous lines, triplet states as transparent, dashed lines. Corresponding singlet and triplet states have the same color.	107

4.7	$S(n \rightarrow \pi^*)$ relaxed (thick green line) surface of the ONO-bending coordinate at the ADC(3)/def2-TZVP(-f)//EOM-CCSD/SVP level of theory. Right next to its minimum, the $S(n \rightarrow \pi^*)$ and $T(n_\pi \rightarrow \pi^*)$ states are degenerate, which together with the large spin-orbit coupling between those two states explains the fast and efficient inter-system crossing. At even larger distortions and higher energy the $S(n \rightarrow \pi^*)$ state also crosses the S_0 , which most likely is the channel for the observed 20% of the population that do not undergo ISC but IC.	108
4.8	$T(n_\pi \rightarrow \pi^*)$ relaxed potential energy surface of the ONCO dihedral angle at the ADC(3)/def2-TZVP(-f)//EOM-CCSD/SVP level of theory in C_S symmetry. Additionally, the spin-orbit coupling elements (SOC) between the lowest triplets and the ground state (bold, transparent lines) obtained at DFT/MRCI level of theory are shown on a secondary y-axis (right).	110
4.9	Schematic potential-energy surface of the non-radiative relaxation pathways of nitrobenzene based on the ADC(3) and EOM-CCSD calculations. This scheme summarizes the relaxed surface scans, relating conical intersections and singlet-triplet crossings to the coordinates and time-scales of the non-radiative relaxation processes. ADC(3) and EOM-CCSD energies in eV for the key points of the PES are given in parenthesis (ADC(3)/CCSD).	113
5.1	Flowchart of the numerical procedure of a non-equilibrium state-specific PCM calculation for a vertical excitation from the ground state $ 0\rangle$ to the excited state $ i\rangle$. The integration over S is replaced by a finite sum over the surface elements. The ground-state polarization of the surface-charges is depicted in blue, the response of the fast component to the increased dipole moment of the excited state in red. The notation is very similar to the article, except for the electro-static potential for which I use the notation ESP(state,s) instead of $V_0(s)$	127
5.2	Components of the calculated solvent shifts with ADC(2)/ptSS- and ptLR-PCM for the cc-pVDZ, aug-cc-pVDZ, cc-pVTZ and aug-cc-pVTZ basis sets.	131
5.3	Breakdown of the first-order contributions into the single terms (see eq. 5.17) and the sums of all interaction and polarization term for nitrobenzene in cyclohexane, diethyl ether and acetonitrile. Despite large differences in the separate terms, the final first-order corrections are virtually identical for all three solvents	132
5.4	Breakdown of the calculated solvent shifts into geometrical, zeroth-, and first-order contributions for selected examples at the ADC(2)/ptSS-PCM level of theory. In each case, the identity of the chromophore (coumarin S_1 , coumarin S_2 , nitrobenzene, etc.) is followed by a series of bar graphs representing different solvents.	133

5.5	<i>Top:</i> Experimental and calculated solvent shifts for a selection of molecules in the exclusively electrostatic subgroup of xBDSM. Solvent shifts are computed at the ADC(2)/ptSS-PCM level of theory with the PTE, PTD and scaled PTD* approaches. <i>Bottom:</i> Differences between experimental and calculated solvent shifts for the PTE, PTD and scaled PTD* approaches including also the zeroth-order terms.	133
5.6	Differences between calculated and experimental solvent shifts at the ADC(2) level of theory using either the ptSS or ptLR scheme, in conjunction with the empirically-scaled PTD* zeroth-order contribution.	133
5.7	Experimental and calculated solvent shifts for the exclusively electrostatic subgroup of xBDSM calculated at the ADC(1)/ptSS-PCM and ADC(1)/ptLR-PCM levels of theory.	136
5.8	Differences between experimental and calculated solvent shifts for the exclusively-electrostatic subgroup of xBDSM computed at the ADC(3/2)/ptSS-PCM and ADC(3/2)/ptLR-PCM levels of theory in combination with the PTE, PTD and PTD* schemes.	136
5.9	<i>Top:</i> Differences between calculated and experimental solvent shifts for ptSS and ptLR approaches as well as the zeroth-order contribution at the LRC- ω PBE/ptSS-PCM and /ptLR-PCM levels of theory. <i>Bottom:</i> Differences between calculated and experimental solvent shifts for the empirically-scaled ptSS*2 and ptLR*2 approaches as well as the combined pt(LR+SS) approach.	136
5.10	Statistical errors in various QM/PCM schemes as applied to the electrostatically-dominated subset of xBDSM. For the sake of completeness, the results for the scaled ptSS*2 and combined pt(SS+LR) approaches in combination with TD-DFT are given.	138
5.11	Direct comparison of the errors of the most accurate QM/PCM combinations for the first xBDSM subset.	140
5.12	Zeroth- and first-order energy of the electron-transfer excitation of the C ₂ H ₄ /C ₂ F ₄ complex in MeCN, computed at the ADC(2)/ptSS-PCM(PTD) and ADC(2)/ptLR-PCM levels of theory. The magnitude of the first-order ptLR and ptSS terms can be read from the vertical axis on the right. As the intermolecular separation increases, only the ptSS approach affords a physically-correct description, whereas the fast solvent response vanishes at the ptLR level.	141
5.13	Experimental and calculated solvent shifts for <i>para</i> -nitroaniline (4-amino-NB) at the ADC(2)/ptSS-PCM(PTD*) and LRC- ω PBE/ptLR*2-PCM levels of theory. Results are shown both with an without a single explicit solvent molecule in the QM region.	142
5.14	Experimental and calculated solvent shifts for 4-nitrophenolate (on the left) and 4-(4'-nitrophenyl)phenolate (on the right) at the ADC(2)/ptSS-PCM(PTD) and LRC- ω PBE/ptLR*2-PCM levels of theory with up to two explicit water molecules at the phenolate group and up to two more at the nitro group.	143
5.15	Experimental and calculated solvent shifts for the subset of non-electrostatic examples, for ADC(2) and LRC- ω PBE calculations in combination with the ptSS and ptLR schemes.	144

6.1	Reaction schemes summarizing the photo-decarboxylation mechanism of oNPA (left), mNPA (middle) and pNPA (right). The time-scales are estimated based on computational and experimental results. (ESIHT: excited-state intra-molecular hydrogen-transfer, IC: internal conversion, ISC: inter-system crossing, PBT: proton back-transfer).	150
6.2	Photochemistry of oNBA after UV excitation into S_4 . Although ESIHT can occur via both singlet and triplet pathways, only the triplet route yields kinetically stable aci-isomers. The singlet route, on the contrary, leads into a conical intersection and thus mainly to non-radiative decay to the electronic ground state.	152
6.3	Schematic summary of the part of the potential-energy surface of nitrobenzene relevant for the non-radiative decay. Energies of the respective points calculated with ADC(3) and EOM-CCSD are given in eV for the key points of the PES are given in parenthesis (ADC(3)/EOM-CCSD).	153
6.4	Summary of the statistical errors of solvatochromic shifts predicted with various combinations of quantum-chemical models (TD-DFT, ADC(1), ADC(2) and ADC(3)) and PCM formalisms (perturbative linear-reponse-type (ptLR) and perturbative state-specific (ptSS)) I derived and implemented in the scope of this work. The errors are with respect to the electrostatically dominated subgroup of the experimental data contained in the xBDSM set.	154

List of Tables

2.1	Summary of the time-constants derived from the global fit analyses of o-, m- and pNPA.	49
2.2	Vertical excitation energies (ω_{ex}) [eV] and oscillator strength (f , in parenthesis) as well as character ^a of the first four excited states of mNPA and mNPAA with and without COSMO at the CIS(D)/def2-TZVP level of theory.	52
2.3	Vertical excitation energies (ω_{ex}) [eV] and oscillator strengths (f , in parenthesis) of the first four excited singlet states of o-, m- and pNPA*7 H ₂ O at the ground state equilibrium geometries at the riCC2/def2-TZVP(-f) level of theory.	56
2.4	Influence of the model of solvation on the vertical excitation energies (ω_{ex}) [eV] and oscillator strengths (f , in parenthesis) of mNPA at the riCC2/def2-TZVP(-f) level of theory. The calculations were performed with and without COSMO (C) for bare mNPA as well as the complex including two and seven explicit water molecules.	56

2.5	Vertical calculated excitation energies (ω_{ex}) [eV] and oscillator strengths (f , in parenthesis) of the first four excited singlet states of o-, m- and pNPA at their equilibrium geometries at the riCC2/def2-TZVP level of theory.	58
3.1	Excitation energies (ω_{ex}) and oscillator strengths (f) of the energetically lowest singlet and triplet states of oNBA at its ground-state equilibrium structure at the riCC2/def2-TZVP and EOM-CCSD level of theory. For the triplet states, also the energy difference to the corresponding singlet state is given.	80
4.1	Relative energies and structural parameters for the most relevant points of the potential energy surface of nitrobenzene at the (EOM-)CCSD/cc-pVDZ level of theory. Energies for each of the relevant points on the PES are given with respect to the lowest accessible minimum (low. min.) as well as the energies of S_1 and ground state (S_0) at the FranckCondon point. In this table, for the sake of compactness T_1 is used to abbreviate the $T(n_\pi \rightarrow \pi^*)$ state and T_2 for the $T(n \rightarrow \pi^*)$ state. The C_S symmetric structures exhibit ONCO out-of-plane bending angles of 48° (CI(S_1/S_0)), 38° (T_1) and 54° (X(T_1/S_0)).	104
5.1	Dielectric constants used in the calculations	120
5.2	Statistical errors for the electrostatically-dominated subset of the xBDSM set.	139

Bibliography

- [1] P. DIRAC. “Quantum Mechanics of Many-Electron Systems”. *Proceedings of the Royal Society of London*, 123 (1929).
- [2] R. J. BARTLETT AND M. MUSIAL. “Coupled-cluster theory in quantum chemistry”. *Reviews of Modern Physics*, 79 (2007) page 291.
- [3] A. D. BECKE. “Perspective: Fifty years of density-functional theory in chemical physics”. *J. Chem. Phys.*, 140 (2014) page 18A301.
- [4] P. G. SZALAY, T. MULLER, G. GIDOFALVI, H. LISCHKA AND R. SHEPARD. “Multiconfiguration self-consistent field and multireference configuration interaction methods and applications”. *Chemical reviews*, 112 (2011) pages 108–181.
- [5] A. SZABO AND N. S. OSTLUND. *Modern Quantum Chemistry*. McGraw-Hill Publishing Company, New-York, first, revised edition (1989).
- [6] A. J. GARZA AND G. E. SCUSERIA. “Comparison of self-consistent field convergence acceleration techniques”. *J. Chem. Phys.*, 137 (2012) 054110. doi:10.1063/1.4740249.
- [7] F. NEESE. “The ORCA program system”. *WIREs Comput. Mol. Sci.*, 2 (2012) pages 73–78.
- [8] R. HARRISON AND N. HANDY. “Full CI calculations on BH, H₂O, NH₃, and HF”. *Chemical Physics Letters*, 95 (1983) pages 386 – 391. doi:10.1016/0009-2614(83)80579-X.
- [9] J. B. FORESMAN, M. HEAD-GORDON, J. A. POPLE AND M. J. FRISCH. “Toward a systematic molecular orbital theory for excited states”. *The Journal of Physical Chemistry*, 96 (1992) pages 135–149. doi:10.1021/j100180a030.
- [10] S. A. BÄPPLER, F. PLASSER, M. WORMIT AND A. DREUW. “Exciton analysis of many-body wave functions: Bridging the gap between the quasiparticle and molecular orbital pictures”. *Physical Review A*, 90 (2014) page 052521.
- [11] E. R. DAVIDSON. “The iterative calculation of a few of the lowest eigenvalues and corresponding eigenvectors of large real-symmetric matrices”. *Journal of Computational Physics*, 17 (1975) pages 87 – 94. doi:10.1016/0021-9991(75)90065-0.
- [12] C. LANCZOS. “An iteration method for the solution of the eigenvalue problem of linear differential and integral operators”. *Journal of Research of the National Bureau of Standards*, 45 (1950) page 255.
- [13] C. MØLLER AND M. S. PLESSET. “Note on an Approximation Treatment for Many-Electron Systems”. *Phys. Rev.*, 46 (1934) pages 618–622. doi:10.1103/PhysRev.46.618.

-
- [14] S. GRIMME. “Improved second-order MllerPlesset perturbation theory by separate scaling of parallel- and antiparallel-spin pair correlation energies”. *J. Chem. Phys.*, 118 (2003) pages 9095–9102. doi:10.1063/1.1569242.
- [15] M. GERENKAMP AND S. GRIMME. “Spin-component scaled second-order Mller-Plesset perturbation theory for the calculation of molecular geometries and harmonic vibrational frequencies”. *Chemical Physics Letters*, 392 (2004) pages 229 – 235. doi:10.1016/j.cplett.2004.05.063.
- [16] S. GRIMME. “Accurate Calculation of the Heats of Formation for Large Main Group Compounds with Spin-Component Scaled MP2 Methods”. *The Journal of Physical Chemistry A*, 109 (2005) pages 3067–3077. doi:10.1021/jp050036j. PMID: 16833631.
- [17] I. HYLA-KRYSPIŃ AND S. GRIMME. “Comprehensive Study of the Thermochemistry of First-Row Transition Metal Compounds by Spin Component Scaled MP2 and MP3 Methods”. *Organometallics*, 23 (2004) pages 5581–5592. doi: 10.1021/om049521b.
- [18] M. PITOK, P. NEOGRDY, J. ERN, S. GRIMME AND P. HOBZA. “Scaled MP3 Non-Covalent Interaction Energies Agree Closely with Accurate CCSD(T) Benchmark Data”. *ChemPhysChem*, 10 (2009) pages 282–289. doi:10.1002/cphc.200800718.
- [19] R. SEDLAK, K. E. RILEY, J. EZ, M. PITOK AND P. HOBZA. “MP2.5 and MP2.X: Approaching CCSD(T) Quality Description of Noncovalent Interaction at the Cost of a Single CCSD Iteration”. *ChemPhysChem*, 14 (2013) pages 698–707. doi:10.1002/cphc.201200850.
- [20] J. SCHIRMER AND F. MERTINS. “Review of biorthogonal coupled cluster representations for electronic excitation”. *Theoretical Chemistry Accounts*, 125 (2010) pages 145–172. doi:10.1007/s00214-009-0597-x.
- [21] J. SCHIRMER. “Beyond the random-phase approximation: A new approximation scheme for the polarization propagator”. *Phys. Rev. A*, 26 (1982) pages 2395–2416.
- [22] P. H. P. HARBACH, M. WORMIT AND A. DREUW. “The third-order algebraic diagrammatic construction method (ADC(3)) for the polarization propagator for closed-shell molecules: Efficient implementation and benchmarking”. *J. Chem. Phys.*, 141 (2014) 064113. doi:10.1063/1.4892418.
- [23] A. B. TROFIMOV, G. STELTER AND J. SCHIRMER. “Electron excitation energies using a consistent third-order propagator approach: Comparison with full configuration interaction and coupled cluster results”. *J. Chem. Phys.*, 117 (2002) pages 6402–6410. doi:10.1063/1.1504708.
- [24] A. JABL OŃSKI. “Efficiency of Anti-Stokes Fluorescence in Dyes”. *Nature*, 131 (1933) pages 839–840. doi:10.1038/131839b0.
- [25] T. ELSAESSER AND W. KAISER. “Vibrational and Vibronic Relaxation of Large Polyatomic Molecules in Liquids”. *Annual Review of Physical Chemistry*, 42 (1991) pages 83–107. doi:10.1146/annurev.pc.42.100191.000503.
- [26] M. KASHA. “Characterization of Electronic Transitions in Complex Molecules”. *Discussions of the Faraday Society*, 9 (1950) pages 14–19.
- [27] M. A. ELSAYED. “SpinOrbit Coupling and the Radiationless Processes in Nitrogen Heterocyclics”. *J. Chem. Phys.*, 38 (1963) pages 2834–2838. doi: 10.1063/1.1733610.
-

BIBLIOGRAPHY

- [28] K. NEUMANN, M.-K. VERHOEFEN, J.-M. MEWES, A. DREUW AND J. WACHTVEITL. "Investigating the CO₂ uncaging mechanism of nitrophenylacetates by means of fs-IR spectroscopy and quantum chemical calculations". *Phys. Chem. Chem. Phys.*, 13 (2011) pages 17367–17377. doi:10.1039/C1CP21721F.
- [29] J.-M. MEWES, K. NEUMANN, M.-K. VERHOEFEN, G. WILLE, J. WACHTVEITL AND A. DREUW. "Molecular Mechanism of Uncaging CO₂ from Nitrophenylacetate Provides General Guidelines for Improved ortho-Nitrobenzyl Cages". *ChemPhysChem*, 12 (2011) pages 2077–2080. doi:10.1002/cphc.201100322.
- [30] J.-M. MEWES, E. PEPLER, J. WACHTVEITL AND A. DREUW. "Combined Theoretical and Experimental Investigation of the Photodecarboxylation of Nitrophenylacetates and Its Implications for the Design of Improved ortho-Nitrobenzyl Caging Groups". *J. Phys. Chem. A*, 116 (2012) pages 11846–11862. doi:10.1021/jp3071629.
- [31] A. P. PELLICCIOLI AND J. WIRZ. "Photoremovable protecting groups: reaction mechanisms and applications". *Photochem. Photobiol. Sci.*, 1 (2002) pages 441–458. doi:10.1039/B200777K.
- [32] G. C. ELLIS-DAVIES. "Caged compounds: photorelease technology for control of cellular chemistry and physiology". *Nature methods*, 4 (2007) pages 619–628.
- [33] C. BRIEKE, F. ROHRBACH, A. GOTTSCHALK, G. MAYER AND A. HECKEL. "Lichtgesteuerte Werkzeuge". *Angewandte Chemie*, 124 (2012) pages 8572–8604. doi:10.1002/ange.201202134.
- [34] J. BARLTROP AND P. SCHOFIELD. "Photosensitive Protecting Groups". *Tetrahedron Letters*, 3 (1962) pages 697 – 699. doi:10.1016/S0040-4039(00)70935-X.
- [35] J. H. KAPLAN, B. FORBUSH AND J. F. HOFFMAN. "Rapid photolytic release of adenosine 5'-triphosphate from a protected analog: utilization by the sodium:potassium pump of human red blood cell ghosts". *Biochemistry*, 17 (1978) pages 1929–1935. doi:10.1021/bi00603a020.
- [36] J. ENGELS AND E. J. SCHLAEGER. "Synthesis, structure, and reactivity of adenosine cyclic 5'-phosphate-benzyltriesters". *Journal of Medicinal Chemistry*, 20 (1977) pages 907–911. doi:10.1021/jm00217a008.
- [37] J. ENGELS AND R. REIDYS. "Synthesis and application of the photolabile guanosine 3',5'-phosphoric-o-nitrobenzylester". *Experientia*, 34 (1978) pages 14–15. doi:10.1007/BF01921871.
- [38] C.-H. PARK AND R. S. GIVENS. "New Photoactivated Protecting Groups. 6. p-Hydroxyphenacyl: A Phototrigger for Chemical and Biochemical Probes^{1,2}". *Journal of the American Chemical Society*, 119 (1997) pages 2453–2463. doi:10.1021/ja9635589.
- [39] A. MOMOTAKE, N. LINDEGGER, E. NIGGLI, R. J. BARSOTTI AND G. C. ELLIS-DAVIES. "The nitrodibenzofuran chromophore: a new caging group for ultra-efficient photolysis in living cells". *Nature methods*, 3 (2005) pages 35–40.
- [40] G. CIAMICIAN AND P. SILBER. "Chemische Lichtwirkungen". *Berichte der deutschen chemischen Gesellschaft*, 34 (1901) pages 2040–2046. doi:10.1002/cber.190103402118.
- [41] J. D. MARGERUM AND C. T. PETRUSIS. "Photodecarboxylation of nitrophenylacetate ions". *Journal of the American Chemical Society*, 91 (1969) pages 2467–2472. doi:10.1021/ja01038a012.

-
- [42] K. LOMMEL, G. SCHÄFER, K. GRENADER, C. RULAND, A. TERFORT, W. MÄNTELE AND G. WILLE. “Caged CO₂ for the Direct Observation of CO₂-Consuming Reactions”. *ChemBioChem*, 14 (2013) pages 372–380. doi:10.1002/cbic.201200659.
- [43] B. B. CRAIG, R. G. WEISS AND S. J. ATHERTON. “Picosecond and nanosecond laser photolyses of p-nitrophenylacetate in aqueous media: a photoadiabatic decarboxylation process?” *The Journal of Physical Chemistry*, 91 (1987) pages 5906–5912. doi:10.1021/j100307a019.
- [44] R. W. YIP, D. K. SHARMA, R. GIASSON AND D. GRAVEL. “Picosecond excited-state absorption of alkylnitrobenzenes in solution”. *The Journal of Physical Chemistry*, 88 (1984) pages 5770–5772. doi:10.1021/j150668a004.
- [45] T. SCHMIERER, F. BLEY, K. SCHAPER AND P. GILCH. “The early processes in the photochemistry of ortho-nitrobenzyl acetate”. *J. Photochem. Photobio. A: Chemistry*, 217 (2011) pages 363 – 368. doi:10.1016/j.jphotochem.2010.11.006.
- [46] O. CHRISTIANSEN, H. KOCH AND P. J. RGENSEN. “The second-order approximate coupled cluster singles and doubles model {CC2}”. *Chemical Physics Letters*, 243 (1995) pages 409 – 418. doi:10.1016/0009-2614(95)00841-Q.
- [47] C. HÄTTIG AND F. WEIGEND. “CC2 excitation energy calculations on large molecules using the resolution of the identity approximation”. *J. Chem. Phys.*, 113 (2000) pages 5154–5161. doi:10.1063/1.1290013.
- [48] R. AHLRICHS, M. BÄR, M. HÄSER, H. HORN AND C. KÖLMEL. “Electronic structure calculations on workstation computers: The program system turbomole”. *Chemical Physics Letters*, 162 (1989) pages 165 – 169. doi:10.1016/0009-2614(89)85118-8.
- [49] C. HÄTTIG. “Geometry optimizations with the coupled-cluster model CC2 using the resolution-of-the-identity approximation”. *J. Chem. Phys.*, 118 (2003) pages 7751–7761. doi:10.1063/1.1564061.
- [50] A. KÖHN AND C. HÄTTIG. “Analytic gradients for excited states in the coupled-cluster model CC2 employing the resolution-of-the-identity approximation”. *J. Chem. Phys.*, 119 (2003) pages 5021–5036. doi:10.1063/1.1597635.
- [51] A. KLAMT AND G. SCHÜÜRMAN. “COSMO: A new approach to dielectric screening in solvents with explicit expressions for the screening energy and its gradient”. *J. Chem. Soc. Perkin Trans. 2*, (1993) pages 799–805.
- [52] M. HEAD-GORDON, R. J. RICO, M. OUMI AND T. J. LEE. “A doubles correction to electronic excited states from configuration interaction in the space of single substitutions”. *Chemical Physics Letters*, 219 (1994) pages 21 – 29. doi:10.1016/0009-2614(94)00070-0.
- [53] S. GRIMME. “Improved second-order MllerPlesset perturbation theory by separate scaling of parallel- and antiparallel-spin pair correlation energies”. *J. Chem. Phys.*, 118 (2003) pages 9095–9102. doi:10.1063/1.1569242.
- [54] F. NEESE. “The ORCA program system”. *WIREs Comput. Mol. Sci.*, 2 (2012) pages 73–78.
- [55] J. P. PERDEW, K. BURKE AND M. ERNZERHOF. “Generalized Gradient Approximation Made Simple”. *Phys. Rev. Lett.*, 77 (1996) pages 3865–3868. doi:10.1103/PhysRevLett.77.3865.
-

BIBLIOGRAPHY

- [56] C. ADAMO AND V. BARONE. “Toward reliable density functional methods without adjustable parameters: The PBE0 model”. *J. Chem. Phys.*, 110 (1999) pages 6158–6170. doi:10.1063/1.478522.
- [57] F. WEIGEND AND R. AHLRICHS. “Balanced basis sets of split valence, triple zeta valence and quadruple zeta valence quality for H to Rn: Design and assessment of accuracy”. *Phys. Chem. Chem. Phys.*, 7 (2005) pages 3297–3305.
- [58] A. D. BECKE. “A new mixing of HartreeFock and local densityfunctional theories”. *J. Chem. Phys.*, 98 (1993) pages 1372–1377. doi:10.1063/1.464304.
- [59] A. KARTON, A. TARNOPOLSKY, J.-F. LAMRE, G. C. SCHATZ AND J. M. L. MARTIN. “Highly Accurate First-Principles Benchmark Data Sets for the Parametrization and Validation of Density Functional and Other Approximate Methods. Derivation of a Robust, Generally Applicable, Double-Hybrid Functional for Thermochemistry and Thermochemical Kinetics”. *The Journal of Physical Chemistry A*, 112 (2008) pages 12868–12886. doi:10.1021/jp801805p.
- [60] F. J. OLIVARES DEL VALLE AND J. TOMASI. “Electron correlation and solvation effects. I. Basic formulation and preliminary attempt to include the electron correlation in the quantum mechanical polarizable continuum model so as to study solvation phenomena”. *Chem. Phys.*, 150 (1991) pages 139–150.
- [61] J. ÁNGYÁN. “Choosing between alternative MP2 algorithms in the self-consistent reaction field theory of solvent effects”. *Chem. Phys. Lett.*, 241 (1995) pages 51–56.
- [62] J. TOMASI, B. MENNUCCI AND R. CAMMI. “Quantum mechanical continuum solvation models”. *Chem. Rev.*, 105 (2005) pages 2999–3093.
- [63] R. IMPROTA, G. SCALMANI, M. J. FRISCH AND V. BARONE. “Toward effective and reliable fluorescence energies in solution by a new state specific polarizable continuum model time dependent density functional theory approach”. *J. Chem. Phys.*, 127 (2007) 074504. doi:10.1063/1.2757168.
- [64] R. HURLEY AND A. C. TESTA. “Triplet-state yield of aromatic nitro compounds”. *Journal of the American Chemical Society*, 90 (1968) pages 1949–1952. doi:10.1021/ja01010a004.
- [65] M. TAKEZAKI, N. HIROTA AND M. TERAZIMA. “Nonradiative Relaxation Processes and Electronically Excited States of Nitrobenzene Studied by Picosecond Time-Resolved Transient Grating Method”. *The Journal of Physical Chemistry A*, 101 (1997) pages 3443–3448. doi:10.1021/jp963095t.
- [66] J. C. S. N. J. TURRO, V. RAMAMURTHY. *Modern Molecular Photochemistry of Organic Molecules*. University Science Books, CA (2010).
- [67] I. R. DUNKIN, J. GEBICKI, M. KISZKA AND D. SANIN-LEIRA. “Phototautomerism of o-nitrobenzyl compounds: o-quinonoid aci-nitro species studied by matrix isolation and DFT calculations”. *J. Chem. Soc., Perkin Trans. 2*, (2001) pages 1414–1425. doi:10.1039/B009630J.
- [68] J. W. WALKER, J. A. MCCRAY AND G. P. HESS. “Photolabile protecting groups for an acetylcholine receptor ligand. Synthesis and photochemistry of a new class of o-nitrobenzyl derivatives and their effects on receptor function”. *Biochemistry*, 25 (1986) pages 1799–1805.

-
- [69] J.-M. MEWES AND A. DREUW. “On the role of singlet versus triplet excited states in the uncaging of ortho-nitrobenzyl caged compounds”. *Physical Chemistry Chemical Physics*, 15 (2013) pages 6691–6698.
- [70] J. KOHL-LANDGRAF, F. BUHR, D. LEFRANCOIS, J.-M. MEWES, H. SCHWALBE, A. DREUW AND J. WACHTVEITL. “Mechanism of the Photoinduced Uncaging Reaction of Puromycin Protected by a 6-Nitroveratryloxycarbonyl Group”. *Journal of the American Chemical Society*, 136 (2014) pages 3430–3438. doi: 10.1021/ja410594y.
- [71] K. SCHAPER, M. ETINSKI AND T. FLEIG. “Theoretical Investigation of the Excited States of 2-Nitrobenzyl and 4,5-Methylenedioxy-2-nitrobenzyl Caging Groups”. *Photochemistry and Photobiology*, 85 (2009) pages 1075–1081. doi: 10.1111/j.1751-1097.2009.00560.x.
- [72] C. HÄTTIG AND P. JØRGENSEN. “Derivation of coupled cluster excited states response functions and multiphoton transition moments between two excited states as derivatives of variational functionals”. *J. Chem. Phys.*, 109 (1998) pages 9219–9236. doi:10.1063/1.477581.
- [73] H. LISCHKA, R. SHEPARD, I. SHAVITT, R. PITZER, M. DALLOS, T. MÜLLER, P. SZALAY, F. BROWN, R. AHLRICHS, H. BOEHM *et al.* “COLUMBUS, an ab initio electronic structure program, release 5.9.1”. *Wien, Austria*, (2006).
- [74] D. R. Y. W. DOMCKE AND H. KÖPPEL. *Conical Intersections: Theory, Computation and Experiment*. World Scientific (2011).
- [75] J.-M. MEWES, V. JOVANOVIĆ, C. M. MARIAN AND A. DREUW. “On the molecular mechanism of non-radiative decay of nitrobenzene and the unforeseen challenges this simple molecule holds for electronic structure theory”. *Phys. Chem. Chem. Phys.*, 16 (2014) pages 12393–12406.
- [76] G. CIAMICIAN AND P. SILBER. “Chemische Lichtwirkungen”. *Berichte der deutschen chemischen Gesellschaft*, 35 (1902) pages 1992–2000. doi: 10.1002/cber.190203502148.
- [77] J. HENZL, M. MEHLHORN AND K. MORGENSTERN. “Amino-nitro-azobenzene dimers as a prototype for a molecular-level machine”. *Nanotechnology*, 18 (2007) page 495502.
- [78] S. NAGAKURA, M. KOJIMA AND Y. MARUYAMA. “Electronic spectra and electronic structures of nitrobenzene and nitromesitylene”. *Journal of Molecular Spectroscopy*, 13 (1964) pages 174 – 192. doi:10.1016/0022-2852(64)90066-9.
- [79] A. DREUW, J. L. WEISMAN AND M. HEAD-GORDON. “Long-range charge-transfer excited states in time-dependent density functional theory require non-local exchange”. *J. Chem. Phys.*, 119 (2003) pages 2943–2946.
- [80] A. DREUW AND M. HEAD-GORDON. “Failure of time-dependent density functional theory for long-range charge-transfer excited-states: The zincbacteriochlorin–bacteriochlorin and bacteriochlorophyll–spheroidene complexes”. *J. Am. Chem. Soc.*, 126 (2004) pages 4007–4016.
- [81] A. DREUW AND M. HEAD-GORDON. “Single-reference ab initio methods for the calculation of excited states of large molecules”. *Chem. Rev.*, 105 (2005) pages 4009–4037.
-

- [82] A. DOMENICANO, G. SCHULTZ, I. HARGITTAI, M. COLAPIETRO, G. PORTALONE, P. GEORGE AND C. BOCK. “Molecular structure of nitrobenzene in the planar and orthogonal conformations”. *Structural Chemistry*, 1 (1990) pages 107–122. doi:10.1007/BF00675790.
- [83] M. TAKEZAKI, N. HIROTA AND M. TERAZIMA. “Relaxation of nitrobenzene from the excited singlet state”. *J. Chem. Phys.*, 108 (1998) pages 4685–4686. doi:10.1063/1.475883.
- [84] M. TAKEZAKI, N. HIROTA, M. TERAZIMA, H. SATO, T. NAKAJIMA AND S. KATO. “Geometries and Energies of Nitrobenzene Studied by CAS-SCF Calculations”. *The Journal of Physical Chemistry A*, 101 (1997) pages 5190–5195. doi:10.1021/jp970937v.
- [85] J. QUENNEVILLE, M. GREENFIELD, D. S. MOORE, S. D. MCGRANE AND R. J. SCHARFF. “Quantum Chemistry Studies of Electronically Excited Nitrobenzene, TNA, and TNT”. *J. Phys. Chem. A*, 115 (2011) pages 12286–12297. doi:10.1021/jp204104j.
- [86] H. GORNER. “Effects of 4,5-dimethoxy groups on the time-resolved photoconversion of 2-nitrobenzyl alcohols and 2-nitrobenzaldehyde into nitroso derivatives”. *Photochem. Photobiol. Sci.*, 4 (2005) pages 822–828. doi:10.1039/B506393K.
- [87] A. T. B. GILBERT, N. A. BESLEY AND P. M. W. GILL. “Self-Consistent Field Calculations of Excited States Using the Maximum Overlap Method (MOM)”. *J. Phys. Chem. A*, 112 (2008) pages 13164–13171. doi:10.1021/jp801738f.
- [88] J. F. STANTON. “On the extent of spin contamination in openshell coupled-cluster wave functions”. *J. Chem. Phys.*, 101 (1994) pages 371–374. doi:10.1063/1.468144.
- [89] A. DREUW AND M. WORMIT. “The algebraic diagrammatic construction scheme for the polarization propagator for the calculation of excited states”. *WIREs Comput. Mol. Sci.*, (2014).
- [90] Y. SHAO, Z. GAN, E. EPIFANOVSKY, A. T. B. GILBERT, M. WORMIT, J. KUSSMANN, A. W. LANGE, A. BEHN, J. DENG, X. FENG *et al.* “Advances in molecular quantum chemistry contained in the Q-Chem 4 program package”. *Mol. Phys.*, (2014).
- [91] A. D. BECKE. “Densityfunctional thermochemistry. III. The role of exact exchange”. *J. Chem. Phys.*, 98 (1993) pages 5648–5652. doi:10.1063/1.464913.
- [92] P. J. STEPHENS, F. J. DEVLIN, C. F. CHABALOWSKI AND M. J. FRISCH. “Ab Initio Calculation of Vibrational Absorption and Circular Dichroism Spectra Using Density Functional Force Fields”. *J. Phys. Chem.*, 98 (1994) pages 11623–11627. doi:10.1021/j100096a001.
- [93] F. NEESE, T. SCHWABE AND S. GRIMME. “Analytic derivatives for perturbatively corrected “double hybrid” density functionals: Theory, implementation, and applications”. *J. Chem. Phys.*, 126 (2007) page 124115.
- [94] S. GRIMME AND M. WALETZKE. “A combination of KohnSham density functional theory and multi-reference configuration interaction methods”. *J. Chem. Phys.*, 111 (1999) pages 5645–5655. doi:10.1063/1.479866.
- [95] M. KLEINSCHMIDT, C. M. MARIAN, M. WALETZKE AND S. GRIMME. “Parallel multireference configuration interaction calculations on mini-carotenes and -carotene”. *J. Chem. Phys.*, 130 (2009) 044708. doi:10.1063/1.3062842.

-
- [96] M. KLEINSCHMIDT, J. TATCHEN AND C. M. MARIAN. “Spin-orbit coupling of DFT/MRCI wavefunctions: Method, test calculations, and application to thiophene”. *Journal of Computational Chemistry*, 23 (2002) pages 824–833. doi:10.1002/jcc.10064.
- [97] M. KLEINSCHMIDT AND C. M. MARIAN. “Efficient generation of matrix elements for one-electron spinorbit operators”. *Chemical Physics*, 311 (2005) pages 71 – 79. doi:10.1016/j.chemphys.2004.10.025. Relativistic Effects in Heavy-Element Chemistry and Physics. In Memoriam Bernd A. Hess (19542004).
- [98] T. H. DUNNING, JR. “Gaussian basis sets for use in correlated molecular calculations. I. The atoms boron through neon and hydrogen”. *J. Chem. Phys.*, 90 (1989) pages 1007–1023.
- [99] M. PABST, A. KÖHN, J. GAUSS AND J. F. STANTON. “A worrisome failure of the {CC2} coupled-cluster method when applied to ozone”. *Chemical Physics Letters*, 495 (2010) pages 135 – 140. doi:10.1016/j.cplett.2010.06.023.
- [100] R. A. FRIESNER AND V. GUALLAR. “Ab initio quantum chemical and mixed quantum mechanics/molecular mechanics (QM/MM) methods for studying enzymatic catalysis”. *Annu. Rev. Phys. Chem.*, 56 (2005) pages 389–427.
- [101] H. M. SENN AND W. THIEL. “QM/MM methods for biomolecular systems”. *Angew. Chem. Int. Ed. Engl.*, 48 (2009) pages 1198–1229.
- [102] D. G. FEDOROV AND K. KITaura. “Extending the power of quantum chemistry to large systems with the fragment molecular orbital method”. *J. Phys. Chem. A*, 111 (2007) pages 6904–6914.
- [103] M. S. GORDON, D. G. FEDOROV, S. R. PRUITT AND L. V. SLIPCHENKO. “Fragmentation methods: A route to accurate calculations on large systems”. *Chem. Rev.*, 112 (2012) pages 632–672.
- [104] M. W. VAN DER KAMP AND A. J. MULHOLLAND. “Combined quantum mechanics/molecular mechanics (QM/MM) methods in computational enzymology”. *Biochem.*, 52 (2013) pages 2708–2728.
- [105] L. D. JACOBSON, R. M. RICHARD, K. U. LAO AND J. M. HERBERT. “Efficient monomer-based quantum chemistry methods for molecular and ionic clusters”. *Annu. Rep. Comput. Chem.*, 9 (2013) pages 25–56.
- [106] K. U. LAO AND J. M. HERBERT. “Accurate and efficient quantum chemistry calculations of non-covalent interactions in many-body systems: The XSAPT family of methods”. *J. Phys. Chem. A*, submitted as an invited Feature Article (2014).
- [107] V. BARONE, M. COSSI AND J. TOMASI. “A new definition of cavities for the computation of solvation free energies by the polarizable continuum model”. *J. Chem. Phys.*, 107 (1997) pages 3210–3221.
- [108] J. M. HERBERT AND A. W. LANGE. “Polarizable continuum models for (bio)molecular electrostatics: Basic theory and recent developments for macromolecules and simulations”. In Q. CUI, P. REN AND M. MEUWLY, editors, “Many-Body Effects and Electrostatics in Multi-Scale Computations of Biomolecules”, Pan Stanford Publishing (2014).
- [109] E. CANCELÉS, B. MENNUCCI AND J. TOMASI. “A new integral equation formalism for the polarizable continuum model: Theoretical background and applications to isotropic and anisotropic dielectrics”. *J. Chem. Phys.*, 107 (1997) pages 3032–3041.
-

- [110] J. TOMASI, B. MENNUCCI AND E. CANCÈS. “The IEF version of the PCM solvation method: An overview of a new method addressed to study molecular solutes at the QM ab initio level”. *J. Mol. Struct. (Theochem)*, 464 (1999) pages 211–226.
- [111] D. M. CHIPMAN. “Charge penetration in dielectric models of solvation”. *J. Chem. Phys.*, 106 (1997) pages 10194–10206.
- [112] D. M. CHIPMAN. “Reaction field treatment of charge penetration”. *J. Chem. Phys.*, 112 (2000) pages 5558–5565.
- [113] E. CANCÈS AND B. MENNUCCI. “Comment on “Reaction field treatment of charge penetration” [J. Chem. Phys. 112, 5558 (2000)]”. *J. Chem. Phys.*, 114 (2001) pages 4744–4745.
- [114] D. M. CHIPMAN. “Comparison of solvent reaction field representations”. *Theor. Chem. Acc.*, 107 (2002) pages 80–89.
- [115] A. W. LANGE AND J. M. HERBERT. “Symmetric versus asymmetric discretization of the integral equations in polarizable continuum solvation models”. *Chem. Phys. Lett.*, 509 (2011) pages 77–87.
- [116] A. W. LANGE AND J. M. HERBERT. “A smooth, non-singular, and faithful discretization scheme for polarizable continuum models: The switching/Gaussian approach”. *J. Chem. Phys.*, 133 (2010) pages 244111:1–18.
- [117] Z.-Q. YOU, J.-M. MEWES, A. DREUW AND J. M. HERBERT. “General formulation of an *a posteriori*, state-specific correction for vertical excitation energies within the polarizable continuum framework”.
- [118] B. LUNKENHEIMER AND A. KÖHN. “Solvent effects on electronically excited states using the conductor-like screening model and the second-order correlated method ADC(2)”. *J. Chem. Theory Comput.*, 9 (2013) pages 977–994.
- [119] M. COSSI AND V. BARONE. “Separation between fast and slow polarizations in continuum solvation models”. *J. Phys. Chem. A*, 104 (2000) pages 10614–10622.
- [120] Y. TAWADA, T. TSUNEDA, S. YANAGISAWA, T. YANAI AND K. HIRAO. “A long-range corrected time-dependent density functional theory”. *J. Chem. Phys.*, 120 (2004) pages 8425–8433.
- [121] M. A. ROHRDANZ, K. M. MARTINS AND J. M. HERBERT. “A long-range-corrected density functional that performs well for both ground-state properties and time-dependent density functional theory excitation energies, including charge-transfer excited states”. *J. Chem. Phys.*, 130 (2009) pages 054112:1–8.
- [122] T. STEIN, L. KRONIK AND R. BAER. “Reliable prediction of charge transfer excitations in molecular complexes using time-dependent density functional theory”. *J. Am. Chem. Soc.*, 131 (2009) pages 2818–2820.
- [123] T. STEIN, L. KRONIK AND R. BAER. “Prediction of charge-transfer excitations in coumarin-based dyes using a range-separated functional tuned from first principles”. *J. Chem. Phys.*, 131 (2009) pages 244119:1–5.
- [124] H. LI, R. NIEMAN, A. J. A. AQUINO, H. LISCHKA AND S. TRETIAK. “Comparison of LC-TDDFT and ADC(2) methods in computations of bright and charge transfer states in stacked oligothiophenes”. *J. Chem. Theory Comput.*, 10 (2014) pages 3280–3289.

-
- [125] M. A. AGUILAR, F. J. OLIVARES DEL VALLE AND J. TOMASI. "Electron correlation and solvation effects. II. The description of the vibrational properties of a water molecule in a dielectric given by the application of the polarizable continuum model with inclusion of correlation effects". *Chem. Phys.*, 150 (1991) pages 151–161.
- [126] F. J. OLIVARES DEL VALLE, R. BONACCORSI, R. CAMMI AND J. TOMASI. "Electron correlation and solvation effects: Part 3. Influence of the basis set and the chemical composition on the solvation energy components evaluated with the quantum mechanical polarizable continuum model". *J. Mol. Struct. (Theochem)*, 230 (1991) pages 295–312.
- [127] S. MILLEFIORI, G. FAVINI, A. MILLEFIORI AND D. GRASSO. "Electronic spectra and structure of nitroanilines". *Spectrochim. Acta A*, 33 (1977) pages 21–27.
- [128] S. MILLEFIORI, F. ZUCCARELLO AND G. BUEMI. "Excited state dipole moments of nitrobenzene derivatives". *J. Chem. Soc. Perkin Trans. 2*, (1978) pages 849–852.
- [129] G. BUEMI, S. MILLEFIORI, F. ZUCCARELLO AND A. MILLEFIORI. "Excited state properties of nitrobenzene derivatives". *Can. J. Chem.*, 57 (1979) pages 2167–2171.
- [130] F. ZUCCARELLO, S. MILLEFIORI AND G. BUEMI. "Electronic spectra of nitrobenzene derivatives". *Spectrochim. Acta A*, 35 (1979) pages 223–227.
- [131] S. YOMOSA. "Theory of the excited state of molecular complex in solution". *J. Phys. Soc. Jpn.*, 36 (1974) pages 1655–1660.
- [132] A. KLAMT. "Calculation of UV/Vis spectra in solution". *J. Phys. Chem.*, 100 (1996) pages 3349–3353.
- [133] M. CARICATO, B. MENNUCCI, J. TOMASI, F. INGROSSO, R. CAMMI, S. CORNI AND G. SCALMANI. "Formation and relaxation of excited states in solution: A new time dependent polarizable continuum model based on time dependent density functional theory". *J. Chem. Phys.*, 124 (2006) page 124520.
- [134] D. M. CHIPMAN. "Vertical electronic excitation with a dielectric continuum model of solvation including volume polarization. I. Theory". *J. Chem. Phys.*, 131 (2009) pages 014103:1–10.
- [135] L. D. JACOBSON AND J. M. HERBERT. "A simple algorithm for determining orthogonal, self-consistent excited-state wave functions for a state-specific Hamiltonian: Application to the optical spectrum of the aqueous electron". *J. Chem. Theory Comput.*, 7 (2011) pages 2085–2093.
- [136] C. J. F. BOTTCHER, O. V. BELLE, P. BORDEWIJK AND A. RIP. *Theory of Electric Polarization*, volume 1 of *Dielectrics in Static Fields*. Elsevier (1973).
- [137] L. D. JACOBSON, C. F. WILLIAMS AND J. M. HERBERT. "The static-exchange electron-water pseudopotential, in conjunction with a polarizable water model: A new Hamiltonian for hydrated-electron simulations". *J. Chem. Phys.*, 130 (2009) pages 124115:1–18.
- [138] R. CAMMI AND B. MENNUCCI. "Linear response theory for the polarizable continuum model". *J. Chem. Phys.*, 110 (1999) pages 9877–9886.

- [139] R. CAMMI, S. CORNI, B. MENNUCCI AND J. TOMASI. “Electronic excitation energies of molecules in solution: State specific and linear response methods for nonequilibrium continuum solvation models”. *J. Chem. Phys.*, 122 (2005) pages 104513:1–12.
- [140] J. GAUSS. “Molecular properties”. In J. GROTEENDORST, editor, “Modern Methods and Algorithms of Quantum Chemistry”, volume 3 of *NIC Series*. John von Neumann Institute for Computing, Jülich, second edition (2000). pages 541–592.
- [141] E. RONCA, C. ANGELI, L. BEMPASSI, F. DE ANGELIS, F. TARANTELLI AND M. PASTORE. “Density relaxation in time-dependent density functional theory: Combining relaxed density natural orbitals and multireference perturbation theories for an improved description of excited states”. *J. Chem. Theory Comput.*, 10 (2014) pages 4014–4024.
- [142] F. PLASSER, M. WORMIT AND A. DREUW. “New tools for the systematic analysis and visualization of electronic excitations. I. Formalism”. *J. Chem. Phys.*, 140 (2014) pages 024106:1–13.
- [143] F. PLASSER, S. A. BÄPPLER, M. WORMIT AND A. DREUW. “New tools for the systematic analysis and visualization of electronic excitations. II. Applications”. *J. Chem. Phys.*, 141 (2014) pages 024107:1–12.
- [144] S. GRIMME, J. ANTONY, S. EHRLICH AND H. KRIEG. “A consistent and accurate *ab initio* parameterization of density functional dispersion correction (DFT-D) for the 94 elements H–Pu”. *J. Chem. Phys.*, 132 (2010) pages 154104:1–19.
- [145] A. KLAMT AND V. JONAS. “Treatment of the outlying charge in continuum solvation models”. *J. Chem. Phys.*, 105 (1996) pages 9972–9981.
- [146] T. STEIN, L. KRONIK AND R. BAER. “Reliable Prediction of Charge Transfer Excitations in Molecular Complexes Using Time-Dependent Density Functional Theory”. *J. Am. Chem. Soc.*, 131 (2009) pages 2818–2820. doi: 10.1021/ja8087482.
- [147] A. BONDI. “Van der Waals volumes and radii”. *J. Phys. Chem.*, 68 (1964) pages 441–451.
- [148] R. S. ROWLAND AND R. TAYLOR. “Intermolecular nonbonded contact distances in organic crystal structures: Comparison with distances expected from van der Waals radii”. *J. Phys. Chem.*, 100 (1996) pages 7384–7391.
- [149] M.-B. S. KIRKETERP, M. Å. PETERSEN, M. WANKO, L. A. E. LEAL, H. ZETTERGREN, F. M. RAYMO, A. RUBIO, M. B. NIELSEN AND S. B. NIELSEN. “Absorption spectra of 4-nitrophenolate ions measured *in vacuo* and in solution”. *ChemPhysChem*, 10 (2009) pages 1207–1209.
- [150] J. LIU AND W. LIANG. “Analytical second derivatives of excited-state energy within the time-dependent density functional theory coupled with a conductor-like polarizable continuum model”. *J. Chem. Phys.*, 138 (2013) pages 024101:1–10.
- [151] S. CORNI, R. CAMMI, B. MENNUCCI AND J. TOMASI. “Electronic excitation energies of molecules in solution within continuum solvation models: Investigating the discrepancy between state-specific and linear-response methods”. *J. Chem. Phys.*, 123 (2005) pages 134512:1–10.
- [152] T. SCHWABE, K. SNESKOV, J. M. H. OLSEN, J. KONGSTED, O. CHRISTIANSEN AND C. HÄTTIG. “PERI-CC2: A polarizable embedded RI-CC2 method”. *J. Chem. Theory Comput.*, 8 (2012) pages 3274–3283.